



Provided by the author(s) and University of Galway in accordance with publisher policies. Please cite the published version when available.

Title	Characterisation of rotationally moulded polymer liners for low permeability cryogenic applications in composite overwrapped pressure vessels
Author(s)	Murray, Brendan R.
Publication Date	2016-09-20
Item record	<a href="http://hdl.handle.net/10379/6036">http://hdl.handle.net/10379/6036</a>

Downloaded 2024-04-24T18:18:16Z

Some rights reserved. For more information, please see the item record link above.



**Characterisation of Rotationally Moulded Polymer  
Liners for Low Permeability Cryogenic Applications  
in Composite Overwrapped Pressure Vessels**

Brendan R. Murray

**Supervisors:**

Prof. Conchúr M. Ó Brádaigh, University of Edinburgh.

Prof. Sean B. Leen, Mechanical Engineering, National University of  
Ireland Galway.



**NATIONAL UNIVERSITY OF IRELAND, GALWAY**

College of Engineering and Informatics

Department of Mechanical and Biomedical Engineering

Thesis submitted to the National University of Ireland as fulfillment of the  
requirements for the Degree of Doctor of Philosophy

September 2016

# Table of Contents

<b>Abstract.....</b>	<b>v</b>
<b>Acknowledgements.....</b>	<b>vii</b>
<b>List of Publications.....</b>	<b>ix</b>
<b>Nomenclature .....</b>	<b>x</b>
<b>1. Introduction.....</b>	<b>1</b>
1.1. Composite Overwrapped Pressure Vessels (COPVs).....	1
1.2. COPV History .....	2
1.3. COPVs in Space.....	4
1.4. COPV Failure Mechanisms .....	6
1.5. Background and Motivation.....	11
1.6. Project Objectives and Methodology .....	13
1.7. Thesis Outline .....	15
<b>2. Literature Review .....</b>	<b>16</b>
2.1. History of Standards Governing COPVs .....	16
2.2. Rotational Moulding .....	20
2.3. Polymer Structure .....	31
2.4. Permeation .....	34
2.5. Diffusion .....	37

2.6.	Sorption.....	43
2.7.	Time Lag Method.....	46
2.8.	Temperature Effects on Permeability Coefficients.....	48
2.9.	Heterogeneous Permeability .....	49
2.10.	Polymer Permeability.....	52
2.11.	Laser Assisted Tape Placement (LATP).....	58
<b>3.</b>	<b>Materials &amp; Methods.....</b>	<b>60</b>
3.1.	Chapter Overview .....	60
3.2.	Polymer Liner Material Characterisation.....	60
3.3.	Polymer Materials Selected .....	61
3.4.	Composite Materials Tested.....	63
3.5.	Specimen Manufacture .....	63
3.6.	Test Methods.....	70
3.7.	Conclusions.....	101
<b>4.</b>	<b>Material Characterisation and Permeability Testing .....</b>	<b>102</b>
4.1.	Chapter Overview .....	102
4.2.	Material Characterisation.....	103
4.3.	Permeability Tests – NUI Galway .....	108
4.4.	Permeability Tests – ÉireComposites .....	116
4.5.	Predicted Leak Rates for Demonstrator Tank.....	125
4.6.	Conclusions.....	129
<b>5.</b>	<b>Heterogeneous Modelling.....</b>	<b>131</b>
5.1.	Chapter Overview .....	131
5.2.	Polyethylene Void Analysis.....	131
5.3.	Finite Element Mass Diffusion Analysis .....	137
5.4.	Permeability Prediction Model .....	146

5.5.	Conclusions .....	149
<b>6.</b>	<b>Integrally Heated Rotomoulding Tooling Development .....</b>	<b>151</b>
6.1.	Chapter Overview .....	151
6.2.	Modified Rotational Moulding Process .....	151
6.3.	Initial Design Considerations.....	155
6.4.	Detailed Tooling Design and Fabrication .....	155
6.5.	Process Optimisation and Demonstrator Part Production.....	165
6.6.	Conclusions.....	175
<b>7.</b>	<b>Liner and Overwrap Cryogenic Testing.....</b>	<b>176</b>
7.1.	Chapter Overview .....	176
7.2.	Cryogenic Cycling of Polymer Composite Welds .....	176
7.3.	Dynamic Mechanical Analysis (DMA) .....	191
7.4.	Thermal Mechanical Analysis (TMA).....	195
7.5.	X-ray CT Analysis of Hot Plate Formed PEEK-CF/PEEK Joints.....	197
7.6.	Conclusions.....	199
<b>8.</b>	<b>Cryogenic Cycling and Final Layup Testing.....</b>	<b>202</b>
8.1.	Chapter Overview .....	202
8.2.	Polymer Liner Formation and LATP Tape-Placement .....	203
8.3.	Permeability Testing with Cryogenic Cycling.....	208
8.4.	X-ray CT Scanning of CF/PEEK-PEEK Samples .....	211
8.5.	Microscopy and Nano-Indentation of LATP CF/PEEK-PEEK Welds....	223
8.6.	Conclusions.....	226
<b>9.</b>	<b>Conclusions and Future Work .....</b>	<b>228</b>
9.1.	Conclusions.....	228
9.2.	Future Work .....	231
9.3.	Final Conclusions.....	234

<b>Appendices</b> .....	<b>236</b>
A.1. Original COPV Designs .....	237
A.2. Rotomoulding Tooling Drawings.....	242
B.1. DSC Graphs of As-Delivered Powders .....	244
C.1. Python Scripting Code.....	245
D.1. DMA Test Results .....	249
D.2. TMA Test Results.....	257
<b>Bibliography</b> .....	<b>259</b>

# Abstract

Composite overwrapped pressure vessels (COPVs) have become a critical component in satellite and space applications due to their ability to store highly permeating fuels at high pressures and under cryogenic conditions. Their main drawback is the associated cost of manufacturing the inner metallic liner which has hindered their integration across other forms of industry. Polymers have been identified as a prospective replacement material for titanium liners in COPV applications. The work presented here assesses the ability of polymer materials to fulfil the requirements of a functioning COPV liner (via helium permeability testing and cryogenic environment testing) while also developing a manufacturing method for COPV production using a modified rotational moulding process and laser assisted tape placement of a thermoplastic carbon fibre tape.

Prospective liner materials have been permeability tested to assess their ability to resist permeation from helium gas. Permeability coefficients have been measured from helium leak rates and used to rank prospective materials based on their ability to resist permeation. These measured coefficients have then been used to predict the ability of each material tested to perform as a permeation barrier in a demonstrator COPV, with PA11 and PVDF showing significant promise. These results have been verified by permeability testing PA11 samples at a 5 bar (0.5 MPa) pressure difference (which is indicative of the final operating conditions) and has shown acceptable levels of fuel containment. The effect of variations in processing conditions on permeability in the chosen manufacturing method has also been

## Abstract

assessed, with internal void contents and defects giving higher permeation coefficients and valuable insights into liner formations studies.

The effect of air voids on permeability has also been assessed with a three dimensional finite element mass diffusion analysis of void distributions in rotomoulded samples. Using polyethylene, a microscopic study of the effects of temperature on void distributions has shown lower void contents in samples manufactured at higher temperatures. The correlation between the maximum forming temperature and the void volume fraction and void radius has been used to assess the forming conditions which produce the lowest permeability. The finite element analysis has shown that higher void contents lead to an increase in permeability. Models with larger voids have lower leak rates than models with smaller voids (for equal void volume fractions) due to the smaller voids forming leak paths throughout the sample. This has led to recommendations for using higher forming temperatures for polymer liner formations to reduce void contents and hence permeability.

A modified rotational moulding tool has been used to produce demonstrator liners for proof of concept testing for the current project. The tooling was designed and fabricated as part of this project and has proven versatile in the production of polyethylene, nylon, polyvinyl-difluoride and poly(ether ether ketone) liners using the same tooling for each formation. The use of segregated heating lines has increased control of temperature distributions (specifically in the flange region, the area of highest heat loss) and has increased the dimensional accuracy of the formed parts. This has been demonstrated via thermal imaging analysis and has also been confirmed via wall thickness consistency measurements in demonstrator parts produced using the aforementioned tooling.

A number of material properties have also been measured with thermal and dynamic mechanical analyses. This has been coupled with studies of bonding properties between the polymer liner and the thermoplastic carbon fibre overwrap, which has been applied using the laser assisted tape placement process. The effect of cryogenic cycling on cracking in the liner-overwrap bond region has been assessed in detail with X-ray CT scanning, while nano-indentation has been used to map the effects of the laser welding process on the bond between the polymer liner and carbon fibre overwrap.

# Acknowledgements

First I would like to thank my supervisors, Prof. Conchúr Ó Brádaigh and Prof. Sean Leen. Words cannot describe the debt of gratitude I owe you both. Your technical knowledge and constant encouragement has been the cornerstone of my work and I will always remember and appreciate the help you have given me. I have learned so much from you both, and I can't begin to thank you enough for all you have done for me.

Next I would like to thank my funders, the Irish Research Council (IRC), the European Space Agency (ESA), ÉireComposites Teo., the College of Engineering and Informatics at the National University of Ireland Galway (NUI Galway), the Irish Centre for Composites Research (ICOMP), and Airbus Defence & Space, for their support and backing throughout my research.

From ESA's ESTEC facility I would like to thank Christopher Semprimoschnig for his technical support and input which has been immensely important throughout my PhD. I would also like to extend my thanks to everybody in TEC-QTE, specifically Cathal Mooney, Laurence Tu-Mai, Catalin Fotea, Jason Williamson, Graham Harris, Roman Gerrard and Kristien Bentley. Thanks also to everybody in the YGT office including, Derek, Ornella, Ana, Helena, Cédric, Leonidas, Ricardo, Nuno, Bruno, Premysl, Kenneth and the ESTEC Irish contingent for bestowing me with an incredibly warm welcome and some great memories.

I would like to thank the entire staff at ÉireComposites, specifically PJ Feerick, Adrian Doyle, Thomas Flanagan, Jean-Marie Bocquel, Derrick Doyle, Fintan Doyle, Kenneth O'Toole, Mike Flanagan, Bryan Weafer, Keith Doyle, Mike Walls and

## Acknowledgements

Mark Logan. My research would not have been possible without all of their help and I am eternally grateful for the opportunity that the company has given me. Special thanks also to Vincent, Tommy and Ronan for always pointing me in the right direction when I needed help.

From NUI Galway I'd like to thank the secretarial staff, Jane Bowman, Sharon Gilmartin and Michelle Broderick for looking after all of my administrative affairs, and the technical staff, William Kelly, Pat Kelly, Bonaventure Kennedy, Myles Meehan and Dave Connolly, for all of the rigs, jigs and fixtures over the past four years. You have saved my proverbial bacon more times than I can count and for that I am incredibly grateful. I'd also like to thank Dr. Annette Harte for lending me the thermal imaging camera from the Civil Engineering Department and Reyhaneh Neghabat for help with the nano-indentation testing.

From ICOMP I would like to thank Terry McGrail, for facilitating the use of the University of Limerick's (UL) LAMP unit, and David Jones for taking the time and care to fabricate parts for me.

On a personal level I'd like to thank David Grogan, who has shared the burden of PhD suffering with me since I started and has always been there for a talk, a drink and an adventure near and afar. To my office colleagues, Alan, Des, Edelle, Conan, Eanna, Kev, Brian Sexton, Brian Sheil, Gary, Colm, Dan, Karlo, Luka, Will, Kelly, Emma, Con, Shane, James Maguire, James Murray, Collette, John, Ger, Fiona and the rest of the people on the 2<sup>nd</sup> and 3<sup>rd</sup> floor, I thank you for all the lunches, laughs and memories that made my PhD life so enjoyable.

Finally, and most importantly, I would like to thank my friends and family. To Ian, Mark, Eamon, David, Maebh, and Caoimhe, I thank you for helping to keep my sanity intact throughout the highs and lows of PhD life. To my sister Katie, I thank you for always looking out for me. I owe you more than you'll ever know. To my parents, Rita and Nial, to whom this thesis is dedicated, I thank you for your constant and unwavering support. It has made me the person I am today (for better or worse, I'll let you decide!) and I know I would not have been able to do this without you. You are a constant force in my life for which I will always be grateful. You are everything I aspire to be and hope to become.

# List of Publications

The work presented here has been published in the following journal articles:

**Chapter 4:** Murray, B.R., Leen S.B., Semprimoschnig C.O.A., Ó Brádaigh C.M. Helium permeability of polymer materials as liners for composite overwrapped pressure vessels. *Journal of Applied Polymer Science*. 2016, vol. 133, no. 29, DOI: 10.1002/app.43675.

**Chapter 5:** Murray, B.R., Leen S.B., Ó Brádaigh C.M. Void distributions and permeability prediction for rotationally moulded polymers. *Journal of Materials: Design and Applications*. 2015, vol. 229, no. 5, pp. 403-418. DOI: 10.1177/1464420714525135.

The following conference papers have been derived from the work presented:

**Chapters 5 and 6:** Murray, B.R., Leen S.B., Semprimoschnig C.O.A., Ó Brádaigh C.M. Tooling. A study of air void formations in a modified rotational moulding process for COPV liners in hydrogen fuel tanks. *IMC-29*, Belfast, Northern Ireland, UK, August 29-30, 2012.

**Chapters 5 and 6:** Murray, B.R., Leen S.B., Semprimoschnig C.O.A., Ó Brádaigh C.M. Tooling. Rotational moulding of polymer liners for composite overwrapped pressure vessels in cryogenic fuel storage applications. *ISMSE-12*, ESA/ESTEC, Noordwijk, the Netherlands, September 24-28, 2012.

**Chapters 4, 6, 7 and 8:** Murray, B.R., Leen S.B., Semprimoschnig C.O.A., Ó Brádaigh C.M. Polymer lined COPVs formed using an integrally heated rotational moulding tool and laser assisted tape placement *SAMPE2016*, Long Beach, CA, USA, May 23-26, 2016.

**Note:** B.R. Murray is the primary author of all publications.

# Nomenclature

$A$	Area ( $m^2$ )
$\alpha$	Geometric Indenter Constant
$B$	Thickness (m)
$B$	Temperature Dependent Material Constant
$\beta$	Indenter Dependent Correction Factor
$C$	Concentration ( $scc/m^3$ )
$C_d$	Solubility Governed by Henry's Law
$C_H$	Solubility Governed by Langmuir Isotherm
$D$	Diffusion Coefficient ( $m^2/s$ )
$D_i$	Average Particle Size
$D_m$	Mean Particle Size ( $\mu m$ )
$E_d$	Activation Energy of Diffusion
$E_p$	Activation Energy of Permeation
$E_r$	Reduced Modulus (GPa)
$E_i$	Indenter Modulus (GPa)
$E_{IT}$	Elastic Modulus (GPa)
GTR	Gas Transmission Rate ( $scc/m^2s$ )
$h$	Indenter Depth (nm)
$\Delta H_s$	Heat of Sorption
$J$	Mass Flux, Mass Flow Rate or Leak Rate ( $scc/m^2s$ )
$L$	Time Lag (s)
LR	Leak Rate ( $scc/m^2.s$ )
$\lambda$	Permeability Ratio
$l$	Thickness (m)
$m$	Power Law Index
$n$	Moles (mol)
$\eta$	Viscosity (Pa.s)

## Nomenclature

$P$	Applied Load (N)
$P$	Permeability Coefficient (scc/m.s,bar)
$P_i$	Percentage Material Retained
$P_m$	Matrix Permeability
$P_r$	Relative Permeability
$p$	Pressure (Pa)
$\Delta p$	Pressure Difference (bar)
$\Phi$	Volume Fraction of Dispersed Phase
$\Phi_m$	Maximum Packing Volume
$R$	Gas Constant (L.Pa/mol.K)
$R_v$	Average Void Radius ( $\mu\text{m}$ )
$S$	Solubility Coefficient (scc/m <sup>3</sup> bar)
$t$	Time (s)
$\tau$	Shear Stress (Pa)
$T$	Temperature ( $^{\circ}\text{C}$ or $^{\circ}\text{K}$ )
$T_m$	Melt Temperature ( $^{\circ}\text{C}$ )
$T_g$	Glass Transition Temperature ( $^{\circ}\text{C}$ )
$u$	Chemical Potential
$V$	Total Volume of Gas (scc)
$V_f$	Void Volume Fraction
$\nu$	Poisson's Ratio
$\dot{\gamma}$	Strain Rate ( $\text{s}^{-1}$ )
$X_c$	Crystallinity (%)
$x$	Thickness (m)

# 1. Introduction

## 1.1. Composite Overwrapped Pressure Vessels (COPVs)

COPVs have become a critical component in satellite and space applications since their initial introduction in the early 1970s [1, 2]. Their ability to store highly permeating fuels at high pressures under cryogenic conditions (below  $-200\text{ }^{\circ}\text{C}$ ) makes them an integral part of propulsion systems, breathing systems and specialised research and analysis equipment aboard rockets, satellites and spacecraft [3-5]. COPVs have replaced traditional metallic tanks due to their significant reduction in weight and dimensional flexibility which has reduced the cost of sending COPVs to space [6, 7].

While new materials and configurations have been developed for COPVs, the core design principles have remained unchanged. They consist of two distinct layers, the outer high strength fibre overwrap and the inner low permeability liner. The outer fibre overwrap absorbs the stresses generated by the containment of the high pressure fuel within and consists of a composite structure with fibres such as Kevlar, carbon or glass dispersed in a polymer matrix [8]. The thin inner liner contains the fuel and limits permeation through the tank wall with materials such as titanium and aluminium being used in most high end applications, due to their good specific strength, excellent barrier properties and resistance to chemical attack [7, 9, 10].

COPVs usually take the form of a spherical or cylindrical tank with domed/elliptical ends as shown in Fig. 1.1, with a two stage process used in the formation of the liner

and subsequent overwrap [11, 12]. For the liner, the cylindrical sections are typically fabricated from rolled sheet stock while the dome sections are formed using various forming methods including hydroforming, spin forming and deep drawing techniques, with assembly performed by welding processes using specialised tooling [13-15].



*Figure 1.1. A cross section image of a COPV along with a variety of COPV tanks consisting of spherical and cylindrical structures [11, 12].*

These liners, once fabricated, are overwrapped with a thermoplastic tape using an automatic tape placement (ATP) machine and an autoclave to consolidate the overwrap to the liner [16, 17]. The ATP process uses the preformed liner as a rotating mandrel to apply a wound composite tape to the outer liner surface in a variety of patterns (helical, polar, hoop) with the chosen heating method providing in-situ consolidation of the tape to produce a finished COPV tank structure [16, 18]. While COPV fabrication and automated overwrapping processes are common techniques in manufacturing plants today, the development of COPV technologies has only occurred over the past 40 years with COPVs gradually replacing traditional all metal tanks in the space industry over that time period.

## 1.2. COPV History

With the advent of spaceflight in the early 1960s, and an emphasis on intelligent design of spacecraft, new pressure vessel designs were needed to replace the bulkier and heavier metallic tanks with new vessels of reduced weight and increased functionality. Traditionally, metallic spherical vessels were the normal fuel-

## Introduction

containment unit aboard spacecraft and satellites. These vessels occupied a large volume of space and so vessel designs were altered to make longer but thinner diameter cylindrical tanks to fit into specific compartmentalised regions. This increased hoop stresses in the cylindrical part of the vessel, requiring thicker and heavier wall sections increasing the overall weight of the tank. In the 1970s a technology transfer program between the National Aeronautics and Space Administration (NASA) and Firefighters in major American cities provided the solution to this problem in the form of the initial designs for COPVs.

This program aimed to use NASA's knowledge of breathing and respiratory systems, garnered from the Apollo missions, to help design and develop a new breathing apparatus for their Firefighters Breathing System Program [19]. Before this program, breathing systems consisted of a pressure vessel formed from conventional steel or aluminium [19]. A number of trade studies by this program highlighted that the main problems were the weight of the tank, its operational duration and the standard face mask apparatus [20]. This program focused on reducing the weight of the tanks by incorporating an aluminium liner, overwrapped with fibre glass, to produce a low weight, high strength, durable vessel [21].

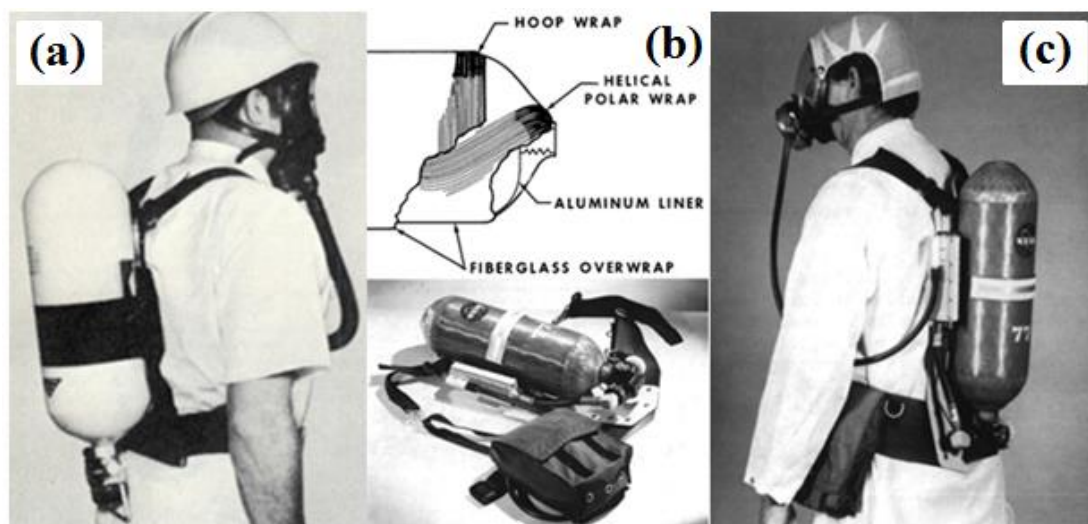


*Figure 1.2. COPV designs for the Firefighter Breathing System Program from (a) the original metallic tank to (b) the improved designs and (c) the final COPV demonstrator [21, 22].*

The aluminium liner material provided the impermeable layer to contain the oxygen and ensure against leakages while the fibre glass overwrap provided the strength to

contain the pressure and resist rupture. Fig. 1.2 shows the improved designs in the breathing system from start to finish. Design changes resulted in a 50% weight reduction, while other secondary issues such as comfort and operational length were also improved [21, 22]. The reduction in weight alone increased the operational life of the vessel due to the reduced rate of oxygen consumption by users which was associated to the increased comfort and ease of use [22].

### 1.3. COPVs in Space

Following on from these initial designs for breathing systems, larger COPVs were designed and manufactured for various fuel storage applications and rapidly incorporated into systems aboard satellites and spacecraft. The Orbiter Space Shuttle had over twenty-four COPV tanks performing a variety of tasks and operations [23]. The construction and design of these COPVs was critical, as failure during flight could lead to significant damage and loss of the vessel and crew. These vessels incorporated a titanium liner, in conjunction with an overwrap consisting of Kevlar® 49 fibres in an epoxy resin with a polyurethane coating, and successfully stored highly permeating gases, such as nitrogen and helium, in a variety of tank sizes [24].

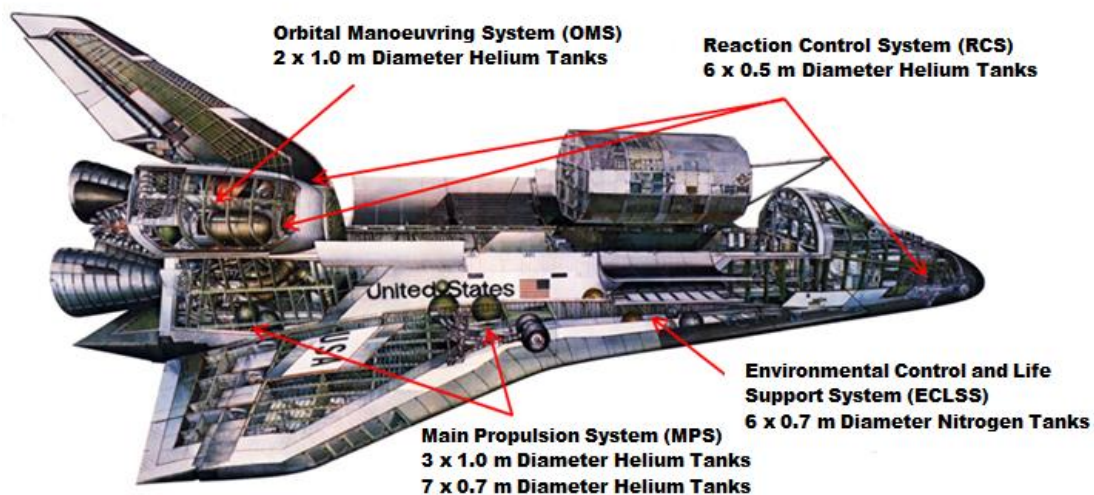


*Figure 1.3. Location of COPVs in NASA's Space Orbiter [25].*

Fig. 1.3 shows a number of COPVs which were used on board the Orbiter space craft during its operation [25]. While some are for breathing systems and environmental control, others are for fuel containment, mechanical systems and experimental equipment [23, 26]. These tanks were initially designed for a 10 year life span, but

## Introduction

subsequent testing and recertification extended the lifetime to over 20 years [24]. While this demonstrates that the design tolerances and safety factors used in their construction were quite conservative, it also highlights the relative unknowns associated with their failure mechanisms and lifetime assessments at the time.

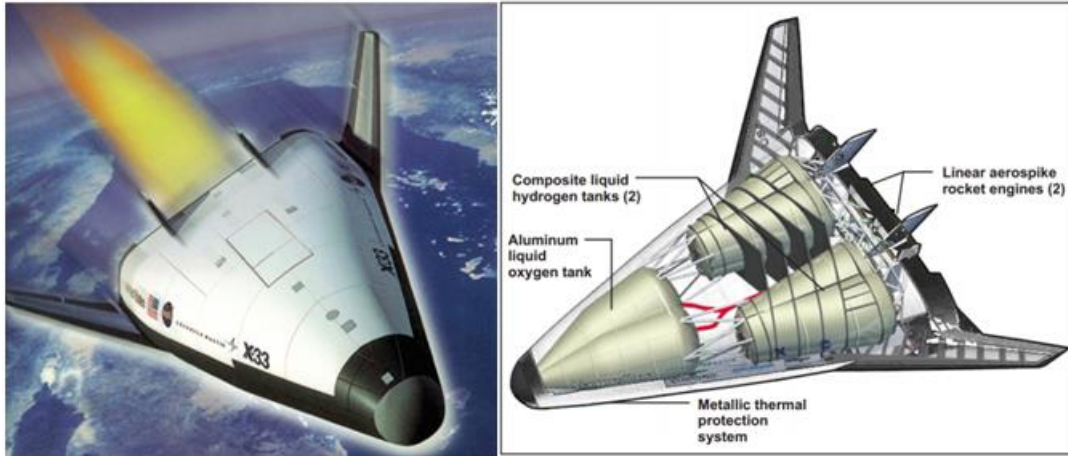


*Figure 1.4. Composite liquid hydrogen tank orientations in the X-33 vehicle [27, 28].*

The X-33 reusable launch vehicle, Fig. 1.4, was developed in the late 1990s as one of the first reusable launch vehicles to attempt the storage of cryogenic fuels in COPV fuel tanks. This suborbital space plane, developed by Lockheed Martin in conjunction with NASA, was in development from 1996 until 2001 when a critical failure in one of the composite storage tanks caused debonding of the composite face sheet from the tank structure during ground testing at cryogenic temperatures [29]. The failures associated with the project and the leakage it experienced during ground testing of its LH2 tanks has been widely reported [29-31].

The composite tank wall consisted of a carbon fibre laminate and metallic honeycomb sandwich structure. Failure occurred due to microcracking of the composite material and subsequent leakage of the liquid hydrogen (LH2) into the interior honeycomb structure [30]. However, a final project review of the X-33 noted that the composite cryogenic tank was a huge advancement in innovative COPV technologies and held significant promise for future endeavours [31].

While the X-33 project was eventually shelved in 2001, it sparked significant research in the area of COPV technologies. Studies on barrier materials, structural

testing and an analysis of the effects of cryogenic environments on vessel integrity have significantly increased the understanding of COPVs and their operation. The X-33 project and the issues highlighted by the recertification of the COPVs aboard the Orbiter space shuttles were the main driving forces behind extensive research in COPV technologies. The designs, materials and fabrication methods utilised for COPV production have been scrutinised due to these issues to obtain a greater understanding of their failure mechanisms and to better predict the lifetime of these critical space components.

### **1.4. COPV Failure Mechanisms**

Although COPVs had early success in high pressure storage among space and satellite applications, there remained a lack of knowledge in regards to their failure criteria. Originally, COPVs were qualified using testing methods that were developed for metallic vessels. This would have been adequate for metal to metal comparisons but the design and characteristics of COPVs makes them quite different to metallic pressure vessels and so analysis techniques had to be developed and restructured to incorporate the differences between metallic vessels and COPVs [32].

- Unlike metallic vessels, minor surface damage significantly affects the structural strength of COPVs due to the load bearing relationship between the thin inner liner and the outer fibre overwrap. Minor surface damage could cause the formation of leakage paths within the vessel wall which would lead to early leakage of the fuel contained within, while also acting as a crack initiation point due to fibre breakage which could lead to overall failure of the vessel.
- COPVs are subject to a failure mechanism known as static rupture, where failure occurs in the fibre overwrap at its normal operating pressure. Static rupture is directly related to the operational time of the vessel and can lead to significant damage and failure of the tank if not properly addressed in the design stage of the manufacturing process.
- The techniques used for analysing thick-walled metal vessels are generally not applicable to COPVs as the thin liner and composite overwrap must be analysed in conjunction with each other and cannot be treated as a single entity. New non-destructive examination techniques had to be developed for qualification of COPV structures.

## Introduction

Because of the significant differences in operating principles and failure mechanisms between metallic vessels and COPV designs, a different method of predicting failures in COPV tanks had to be developed. Fleet leader programs were one such method used to act as precursors to failures of critical pressure vessels aboard spacecraft for different missions [33]. In these programs a COPV vessel similar to the one in use was subjected to enhanced operating conditions, usually increased pressure and temperature, to act as an identifier for critical failures in the COPV tanks. In this way the fleet leader COPV vessels were used as predictive alarms for critical failures in COPV tanks aboard the spacecraft.

If a fleet leader vessel failed or ruptured under these enhanced conditions then an adequate amount of time would be allowed for pre-emptive repair of COPV tanks aboard the shuttle to ensure that failure did not occur and that systems remained fully operational. These fleet leader practices do not need to be incorporated into metallic vessel analyses as their designs and failure mechanisms are better understood. While COPVs are usually designed to exhibit leak-before-burst characteristics, there is always a risk of burst failure which can lead to catastrophic failure of the tank and the subsequent loss of the shuttle and crew. These burst failures result in the rapid release of fuel and can involve fragmentation of tank components into surrounding systems. Burst failures can be caused by over-pressurisation of the COPV whereby pressure build up in the tank exceeds that of the design requirements and results in rapid failure of the liner and overwrap, Fig. 1.5.

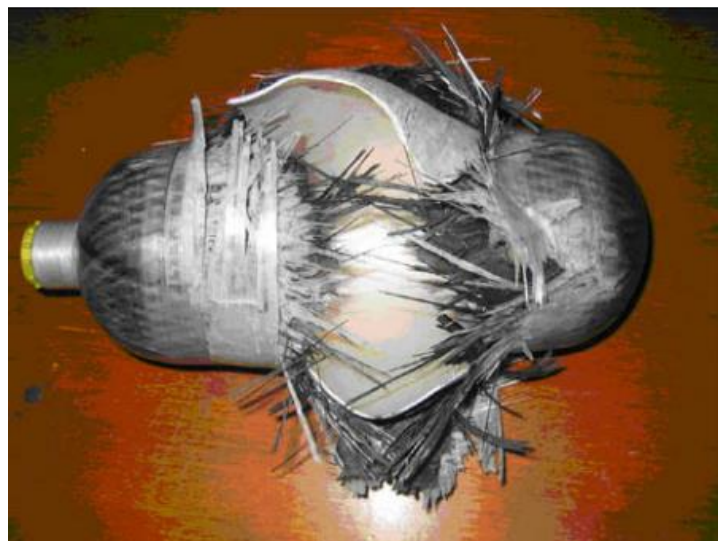


*Figure 1.5. Burst failure due to over pressurisation in a COPV tank [34].*

## Introduction

The risks associated with burst failure can be minimised by proper selection of materials and allowing for conservative estimates of burst pressure failure limits either by proof pressurisation testing or burst testing during the acceptance stage of COPV design [32]. Other causes of burst failures can usually be attributed to failures in either the inner liner or the outer composite overwrap. A combination of time, the cyclic behaviour of multiple pressurisation cycles and prolonged operation at the maximum expected operating conditions can result in leakage or burst failure of the COPV structure.

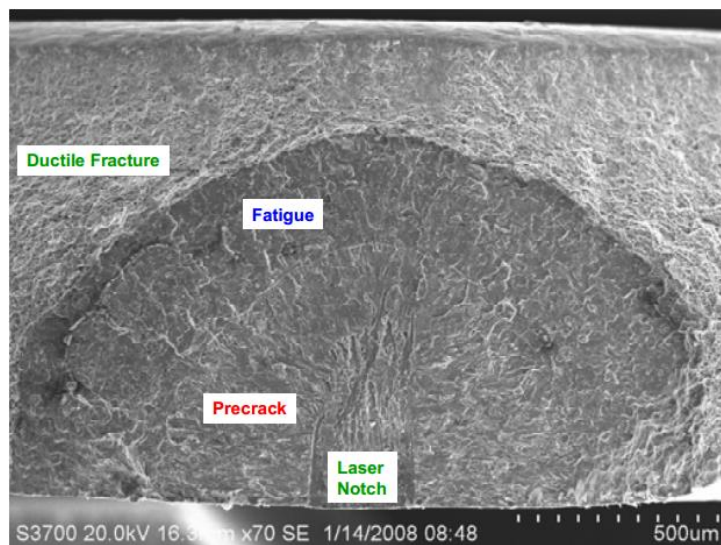


*Figure 1.6. Representative fracture surface of a fatigue crack in aluminium resulting in fracture once a critical crack size is reached [36].*

Failure of the inner metallic liner is usually attributed to fatigue or buckling whereby general pressurisation operations, environmental conditions or manufacturing processes contribute to the failure of the vessel during operation. Fatigue can be described as failure due to crack growth in the liner from the cyclic loading effects of the pressurisation cycle [35]. This repeated cyclic loading causes small cracks to grow over time until a critical crack size is reached and results in failure of the vessel, Fig. 1.6 [36]. It can be alleviated by testing liner materials to determine fatigue characteristics and non-destructive examination of the liner during proof testing to ensure that flaws in the liner structure or welds are not present (Eddy Current Testing) [37, 38].

Buckling is another form of liner failure whereby ripples, depressions or anomalies in the liner can result in the creation of cracks, shape deformation or failure of the

## Introduction

vessel itself, Fig 1.7. Buckling usually occurs during the autofrettage cycle whereby the COPV is subjected to an elevated pressure cycle inducing yielding in the metal liner [40]. This yielding is beneficial for COPV liners as it places the liner in a residual compressive state when it is depressurised. Thus the subsequent pressurisation of the vessel, back to its operating pressure, results in a lower level of stress in the liner during operation.

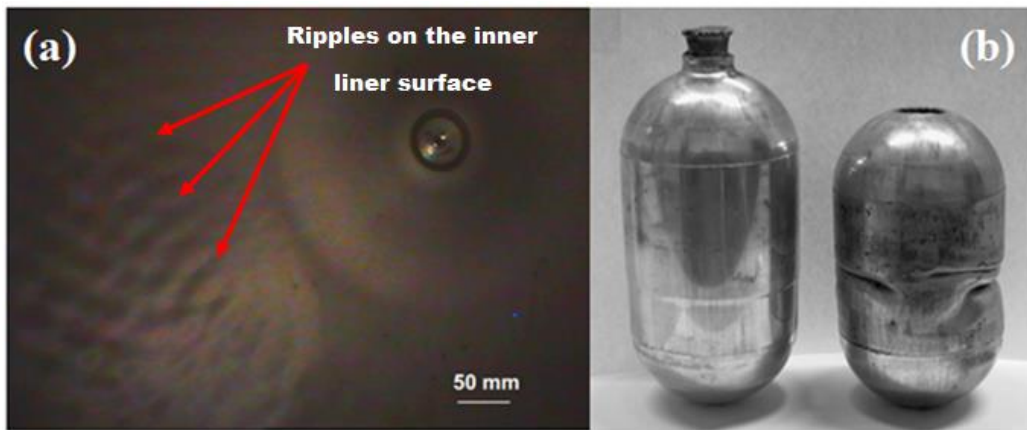


*Figure 1.7. Buckling in the form of (a) ripples on the inner surface of the metal liner and (b) shape deformation in metallic liners and tanks [35, 39].*

This elevated pressure causes the liner to plastically yield into the composite overwrap and induces a residual compressive stress in the liner after depressurisation which results in improved fatigue properties of the thin metal liner [41, 42]. But, if the bond strength between the liner and overwrap is insufficient then buckling occurs due to the residual stress instability in the liner and debonding of the liner from the overwrap occurs [42]. Buckling can even occur after the autofrettage cycle in instances where temperature differences are excessive due to the difference in thermal expansion coefficients between the liner and overwrap material [41, 42]. Buckling can be reduced by assuring that adequate bond strength exists between the metal liner and composite overwrap over the operating temperature range of the vessel, although it is still important to monitor these tanks for microcracks after the autofrettage cycle.

Unlike liner failure mechanisms, failures in the composite overwrap are not associated with the cyclic pressurisation of the vessel. Failure of the overwrap is instead due to an intrinsic phenomenon known as stress rupture, where the COPV is

## Introduction

held at high pressures (near its maximum expected operating pressure (MEOP)) for extended periods of time [43]. Also known as static rupture, it is attributed to creep induced failure over time and is dependent upon the loading history of the tank and its environmental conditions. Elevated temperatures increase the chance of stress rupture significantly [43, 44]. Stress rupture has been a serious cause for concern since the first analyses of this phenomenon were investigated as part of the recertification of the Orbiter COPVs mentioned earlier due to the already prolonged use of these COPVs aboard the shuttle.

A large amount of research has been conducted to study stress ruptures in COPV overwraps, with large scale pressure vessel tests being conducted (over periods of up to 10 years from 1974 to 1998) to determine contributing factors to stress rupture failure and to provide long term statistical data for analysis and modelling [45]. While these tests encompassed pressure testing of some 300 COPVs, the failings of these programs were in the inconsistency of pressure monitoring, inadequate temperature control and variance in the design of vessels tested, leaving a large amount of questions unanswered in relation to the causes of stress rupture failures [45]. Further testing of Kevlar overwrapped COPVs in 2004 with improved environmental controls and monitoring equipment led to more significant statistical data for model simulations. Non-destructive examination (NDE) techniques for COPVs such as Raman spectroscopy, laser shearography and laser profilometry were also developed in conjunction with this testing [46].

The prediction of stress rupture life has also seen a significant amount of research. Models developed using a Weibull power law for lifetime predictions of carbon/epoxy failure form the basis of most models to describe damage in a composite versus the stress level [47]. Phoenix and Glaser models have formed the basis for the prediction of stress rupture life of COPVs on board the Orbiter space shuttle, with both models exhibiting similar statistical outputs for predicted probabilities of failure [26]. All of this research, including testing data and stress rupture life predictions, has highlighted the need for COPV designers to understand the entire tank structure, not just single tank requirements such as burst pressure. New test standards and safety certifications have been developed as a result of these findings and the lessons learned have been incorporated into subsequent designs for new space missions.

## 1.5. Background and Motivation

As already discussed, the traditional design for COPVs has centred on the use of a titanium liner with a composite overwrap. While this design meets all the requirements needed for fuel containment, the cost of a precision machined titanium liner can reach almost €80,000 (\$90,000) for a 500 mm diameter spherical vessel [48]. This is one reason why COPVs have not been incorporated into new technology designs. Manufacturing runs of COPVs are also quite low which reduces the return on investments made in any tooling used in their production. A number of studies have been conducted on replacing titanium liners with alternative materials which can still provide all of the functionality needed. The main candidates under investigation for this purpose are polymers.

Polymers are low-cost, low weight, and easy to handle materials, with low permeability properties, high resistances to chemical attack and good compatibility with highly permeating fuels. Their ability to withstand cryogenic temperatures without cracking makes them suitable candidates as alternative liner materials and has led to the commissioning of a number of studies into their characteristic properties as liner materials. Astrium Space Transportation (now Airbus Defence & Space) are one manufacturer leading the way in the use of polymer liners having recently produced a 300 L tank with a polymer liner via an injection blow moulding process, Fig. 1.8 [49].

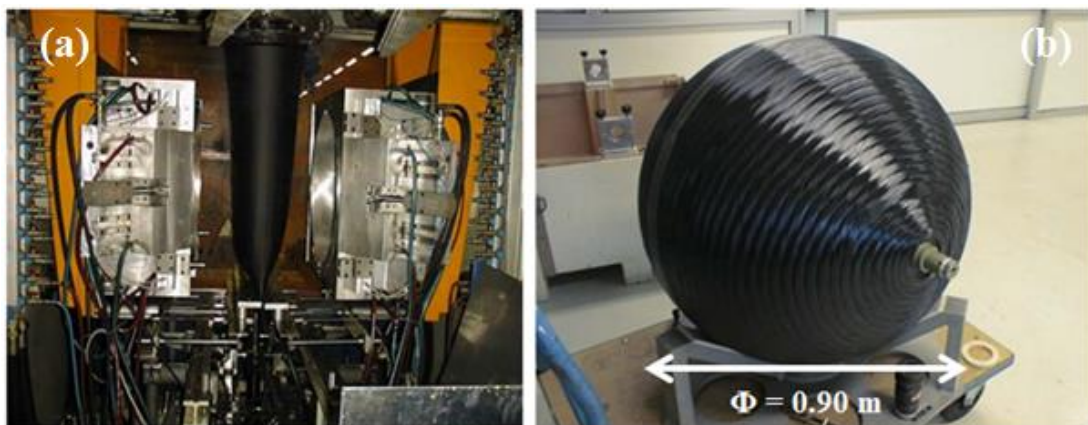


Figure 1.8. (a) Injection blow moulding process for (b) a polymer lined COPV [49].

While this illustrates that a shift towards cheaper and alternative liners is currently underway, no definitive manufacturing process has been chosen for the production of

## Introduction

polymer liners for future COPVs. Rotational moulding is another manufacturing process that produces hollow polymer parts of uniform wall thickness at a reduced cost. It uses a polymer powder, a biaxially rotating arm and the application of heat to coat the entire inner surface in a uniform layer of material. In comparison to the previously mentioned blow injection moulding process it has a number of benefits, but also some drawbacks, as outlined in Table 1.1 [50, 51].

*Table 1.1. Comparison of factors between blow injection moulding and rotational moulding [50, 51].*

Factor	Injection Blow Moulding	Rotational Moulding
Materials Available	Extensive	Limited
Feedstock	Pellets	Powder
Mould Pressure	<1.0 MPa	<0.1 MPa
Mould Cost	High	Moderate
Wall Thickness Uniformity	Tends to be Non-Uniform	Uniformity Possible
Residual stress	Moderate	Low
Cycle Time	Fast	Slow
Dual Layering	Easy	Difficult

Rotational moulding forms parts with lower residual stress, more uniform wall thicknesses, and with lower mould tooling costs due to the lack of an applied pressure during processing. But, in comparison, blow injection moulding uses pellets for its forming material which increases the number of materials available for the process, has lower cycle times increasing its efficiency, and can produce multi-layer parts with ease. While there are ancillary benefits to using both processes, the main differentiating factor is the presence of thinning in the corner regions of blow injection moulded parts which lead to weaknesses in load bearing areas. In rotational moulding, the opposite occurs, where corner regions have thicker wall sections due to the pick-up of powder particles in these areas. This, coupled with the capital intensive nature of blow injection moulding (whereby precision machined pathways have to be constructed throughout the tool for coolant flow and a large amount of

performing and stretching of the liner itself is required prior to manufacturing [52, 53]), is why the current research presented focuses on rotational moulding as a prospective liner manufacturing method.

Research into the use of rotational moulding for polymer liner production for COPV applications has not yet been undertaken, so the focus of this thesis is to test polymer materials for fuel storage applications and determine the viability of this manufacturing process as a liner production method. This project has been undertaken in conjunction with Airbus Defence and Space (formally Astrium ST), ÉireComposites Teo. and the European Space Agency (ESA) to develop a 90L COPV tank to the specifications listed in Table 1.2.

*Table 1.2. Tank requirements for proposed structure.*

Parameters	Requirements
Tank Capacity	90 L
Dimensions	950.4 mm × 402.6 mm
Operating Pressure	5.0 bar (0.50 MPa)
Burst Pressure	7.5 bar (0.75 MPa)
Operating Temperature Range	90 to 323 K (-183 °C to 49 °C)
Maximum No. of Thermal Cycles	50 cycles
Max He Leak Rate	$1 \times 10^{-3}$ scc/s at MEOP
Weight Target	-30% compared to equivalent metallic tank
Fuel Compatibility	Liquid Hydrogen and Liquid Oxygen

## 1.6. Project Objectives and Methodology

The main objectives of this project are as follows:

- To investigate the permeability of a number of polymer materials, formed using rotational moulding techniques, to determine their suitability as liner materials for the containment of highly permeating fuels in COPV structures

## Introduction

- To develop a rotational moulding process that can produce low permeability polymer liners, demonstrating proof of concept, and facilitate subsequent testing to prove the viability of the process as a manufacturing method
- To design, develop and manufacture a polymer liner that can be overwrapped with a tape placed composite in an ATP process for out-of-autoclave manufacturing to demonstrate the effectiveness of the liner manufacturing method for producing future COPVs
- To test a polymer liner that is overlaid with a tape placed composite for mechanical properties and permeability rates after cryogenic cycling to prove the viability of the chosen COPV design

The methodology followed to achieve these objectives is as follows. Low permeability polymer materials were identified from literature and industrial sources, and these materials were then down selected for further testing. A permeability apparatus was constructed for bulk testing of prospective liner materials, to determine sufficiently low permeabilities for hydrogen storage, using gaseous helium permeability testing. Subsequent permeability testing in a mass spectrometer test apparatus was also conducted as a validation of the previously measured results.

A study of the effects of void distributions on permeability is presented to identify optimum processing conditions with respect to minimisation of void volume fraction. A modified rotational moulding tool was fabricated in conjunction with an industrial sponsor to allow for the rotational moulding of demonstrator components, while also producing samples for overwrapping test trials. After these initial trials, a material screening process was undertaken to down-select materials for further study. A full analysis of material properties is presented, including an analysis of cryogenic effects on expansion coefficients and changes in material stiffness.

A laser assisted tape placement (LATP) process was employed to overlay CF/PEEK composite tape on polymer liner samples including an investigation of processing effects. These LATP liner-overwrap samples were permeability tested and cryogenically cycled to determine the effects of the environment on their steady state leak-rate. Microcracking studies were conducted via X-ray CT scanning on cycled laminates to determine the effects of thermal cycling on structural integrity.

## 1.7. Thesis Outline

This thesis is divided into a number of sections as follows:

- Chapter 2 provides a literature review which includes a discussion of the regulations governing COPV design, rotational moulding, polymers, permeability, laser assisted tape placement, composites and cryogenic cycling
- Chapter 3 details the materials and forming methods used, including preparation methods and test methods for all testing conducted within this thesis
- Chapter 4 presents permeability test results for a range of polymer materials tested in both the NUI Galway permeability test apparatus, developed in-house, and the ÉireComposites permeability test apparatus, using a mass spectrometer
- Chapter 5 describes the experimental analysis of void dispersions and the finite element analysis conducted to determine the effect of air voids on permeability
- Chapter 6 describes the design and construction of the rotomoulding tooling with detailed descriptions of tooling designs, fabrication and subsequent demonstrator moulding formations included
- Chapter 7 presents the results for thermal mechanical analysis (TMA) and dynamic mechanical analysis (DMA) testing of the down-selected materials, with analysis of the effects of cryogenic cycling on liner-overwrap specimens included
- Chapter 8 discusses the final permeability results of the tape-laid liner samples, while also demonstrating the effects of cryogenic cycling on the final configuration
- Finally, Chapter 9 summarises the main findings of this thesis, their applications and recommendations for future work

## **2. Literature Review**

### **2.1. History of Standards Governing COPVs**

While COPVs have been in use aboard rockets and satellites since the 1970s, the standards that have governed their design and operation have undergone a number of changes over the past forty years. The design and operation of COPVs used by NASA was initially governed by the American military standard, MIL-STD-1522 [54] released in 1972. This standard covered safe design and operation of pressurised missiles, space systems and ground support systems and was one of the first standards to acknowledge the need for governance of COPVs aboard rockets and satellites. This standard encompassed all activities relating to COPV design and required a systematic analysis of the vessel and its components to ensure that the operation of the vessel did not result in unsafe conditions for the craft and flight personnel.

The standard begins with a definition of the load-pressure-temperature history for the lifetime of the vessel, which determined the test conditions under which the vessel would be qualified so that it could be cleared for use in the defined mission. The safe life of the vessel was also set at four times that of the designed service life which added a significant factor of safety to the vessels integrity. A detailed inspection plan was also compulsory for all COPVs falling under this standard, which encompassed the entire manufacturing process. From initial material procurement to final proof pressure testing, milestones throughout the life of the COPV were used to monitor the vessel integrity and to ensure that proper procedures were followed at all times.

## Literature Review

The failure of the Mars Observer in 1992 was the initiation of a move towards more detailed standards governing COPV safety and design. All communication was lost with the Mars Observer on the 22nd of August 1992 after pressurisation of the propulsion systems was undertaken in a planned portion of the mission outline. The satellite never registered telemetry after this point and it was with great difficulty that an investigative board concluded that the most probable cause was a catastrophic failure of the pressurisation system via an unintended mixing of stored gases aboard the Observer [55]. This was probably one of the main drivers towards redevelopment of test standards and resulted in a number of updates over the following years even though MIL-STD-5012 was still used for pressure vessels aboard the international space station via SSP-30558 [56].

The US Air Force also released a standard governing COPV design and development in 1994, AFSPCMAN 91-710, which detailed range safety for launch vehicles, payloads and ground support systems [57, 58]. While this standard placed a larger focus on the safety of ground systems and range conditions, there were also significant improvements in the requirements for COPV designs. Updated testing of COPVs was included with a mandatory analysis of shear and in-plane stresses of the composite using laminate theory. A buckling analysis of the liner was also included with the first mention of a crack growth analysis in the COPV included. The requirement for a safe life of four times that of the service life was kept as a standard requirement and a renewed focus of contamination mitigation was included.

The next test standard to define upgrades in COPV qualification testing was NASA-STD-5019 which was released in 2008 [59]. This standard covered fracture control requirements for a number of systems, not just COPVs, and was a significant upgrade on previous attempts at ensuring COPV safety. It required a requalification of all vessels currently in use for any and all recertification purposes, while also placing a greater focus on fracture characterisation and analysis of parts. COPVs were defined as fracture critical components and so damage tolerances had to be based on initial flaw sizes obtained from increasingly sensitive NDE techniques. This standard defined that the qualification of all COPVs was to follow that of ANSI/AIAA-S-081A as set by the American Institute of Aeronautics and Astronautics [60].

## Literature Review

ANSI/AIAA-S-081A has become the standard for COPV qualification over the last number of years with NASA using it as a requirement for all COPVs involved in the new commercial crew program to the international space station [61, 62]. While the other standards covered a large range of safety and fracture requirements, this standard is solely focused on COPVs and is tailored specifically to their design, fabrication, testing, inspection, operation and maintenance procedures.

The general requirements as defined by this standard fall into a number of categories including [58]:

- System Analysis Requirements
- General Design Requirements
- Material Requirements
- Fabrication and Process Control Requirements
- Quality Assurance Requirements
- Operations and Maintenance Requirements
- Data Retention

The verification of the COPV for certification and use involved:

- Verification by Analysis
- Verification by Testing
- Acceptance Test Requirements
- Qualification Test Requirements

This adds a significant layer of analysis to COPV designs and qualifications and is aimed at ensuring that the risk of failure is minimised to a level which ensures the safety of any flight and crew utilising COPVs in future launches. The evolution of test standards noted here follows an enhanced knowledge of COPVs with the rapid inclusion of fracture characterisation and modelling included in the later test standards as more information became available about COPV characteristics. The specific tailoring of standards to COPVs alone also shows that they have become an

integral part of operations in space applications with the need for specific analyses tailored to their working environments.

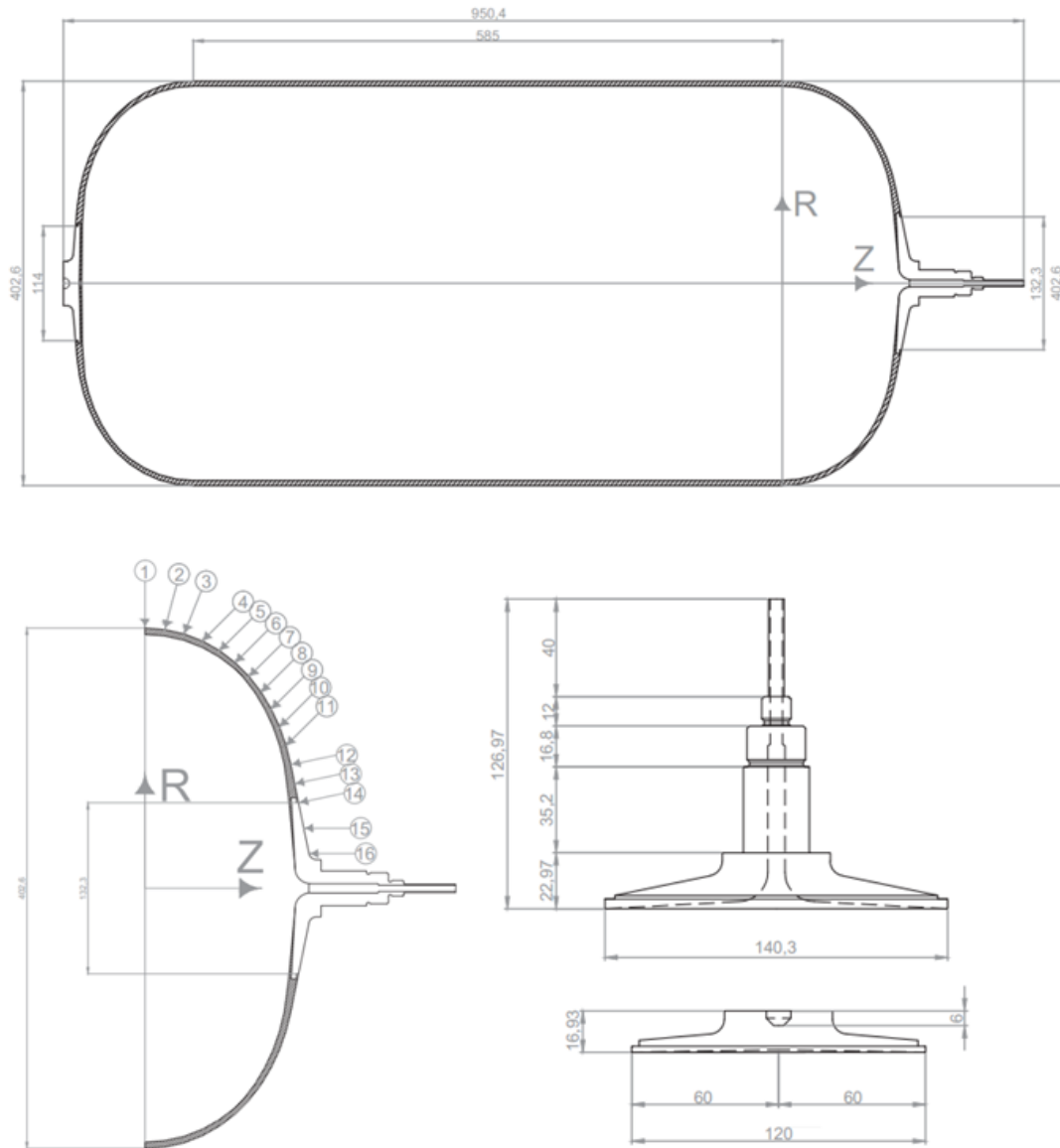


*Figure 2.1. Representation of the metallic pressure vessel accompanied with images of the dome curvature and the compulsory inserts. Detailed schematics supplied in Appendices A.1.*

Dimensions for a metallic tank have been provided by Airbus Defence and Space as a comparison for the COPV designed in this thesis. Dimensions have also been supplied for both polar boss inserts in the COPV but they can be tailored to suit the design requirements, specifically in the area of anchoring mechanisms in the tank. The standard tank dimension are included in Fig. 2.1 (with a full overview included in Appendix A.1) to outline the dimensions of the metallic pressure vessel.

Dimensions for the polar boss inserts and the specific dome curvature at both ends of the pressure vessel have also been included in Appendix A.1. These drawings will be used for comparative purposes and for the design considerations of all subsequent operations.

### **2.2. Rotational Moulding**

As has already been highlighted in Chapter 1, a number of production methods have already been used for forming polymer liners in COPV applications. These methods are quite capital intensive and so an alternative manufacturing method that reduces costs, in regards to both production and material usage, could provide a significant benefit for future polymer-lined COPVs. Rotational moulding is an inexpensive processing method that has the capability of producing polymer liners at a reduced cost while still providing the necessary part quality and so has formed the basis for trial analyses in this thesis for polymer liner formation.

Rotational moulding is a manufacturing method used to produce hollow, single piece plastic parts at high temperatures and low pressures. It utilises a specially ground polymer powder placed in a metal or ceramic mould in conjunction with a biaxially rotating arm and the application of heat to produce hollow parts of uniform and consistent wall thickness. It finds its origins in slip casting production methods and has been used as a plastic forming method since the early 1940s [50]. While it was originally used mostly for producing children's toys, it has been adapted as a major manufacturing method for the production of fuel tanks, canoes, boats, air ducts and automotive parts, offering significant advantages over similar processing methods such as injection moulding and blow moulding [50, 63]. The lack of applied pressure minimises the residual stress build up in the plastic part while the use of a powder polymer material removes costly preforming processes from the production cycle.

The rotational moulding process is conventionally contained within a large heating oven and can be broken down into four major steps as outlined in Fig. 2.2 [50, 63, 64]. In step 1, the hollow metal mould is charged with the powder for forming the part. The amount of powder inserted into the mould is controlled by the internal volume of the mould and the desired wall thickness of the part, with the volume of the part and the density of the powder used to determine the required mass of

polymer powder needed. In step 2, the mould is closed and heat is applied as the mould rotates biaxially, causing the powder polymer to melt and stick to the mould surface. The rotational speed used here is quite low ( $< 12$  rpm) as the heated tool surface is the driving force behind wall thickness build up and not centrifugal force. The speed of each axis can also be altered to control wall thicknesses in different locations of the part as the time spent passing through the powder pool at the bottom of the mould during heating also controls the part thickness.

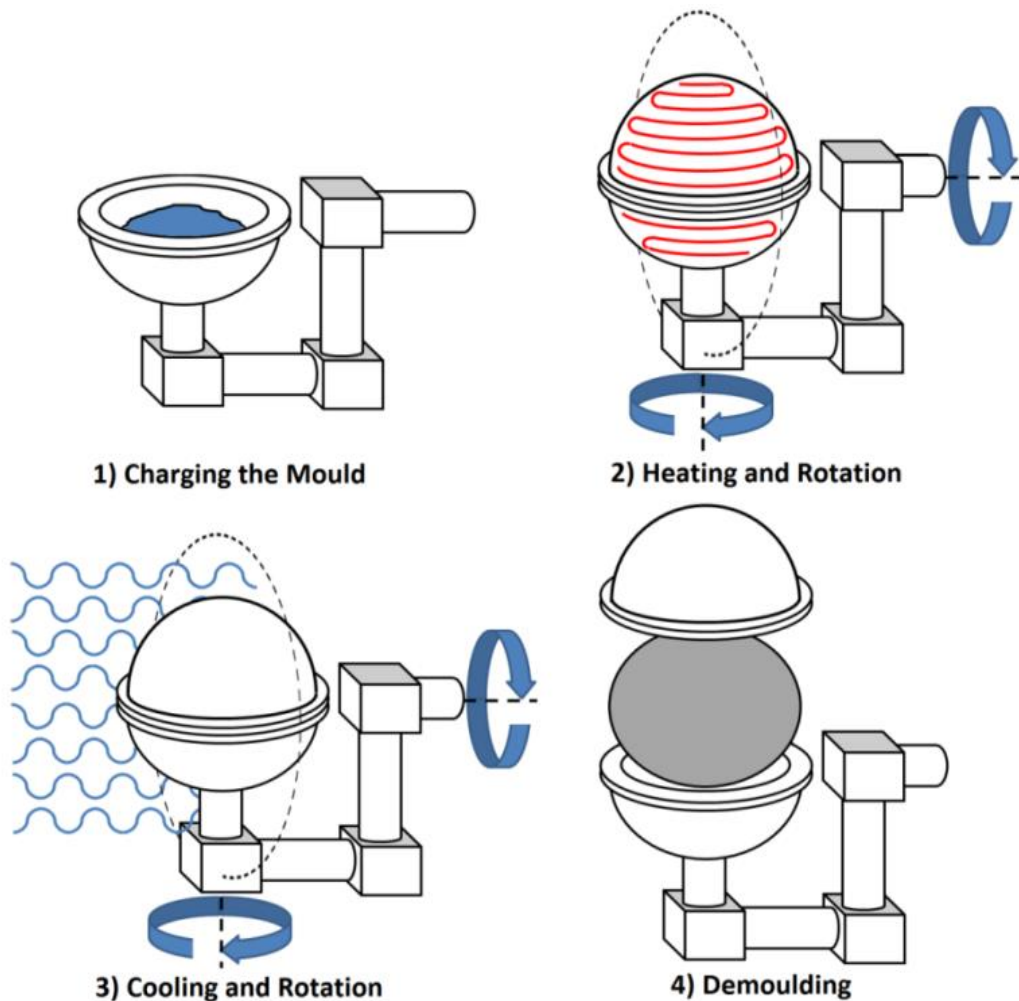


Figure 2.2. An outline of the main steps in the rotational moulding process [64].

For step 3 the mould is removed from the oven and allowed to cool as it continues to spin. External cooling systems such as air fans and water jet systems can be used to increase cooling rates and decrease cycle times after the part has solidified, to reduce warpage in the part cross section [50, 63]. In step 4 the mould reaches a sufficiently low temperature such that the tool can be opened and the part can be removed, so that the process can be repeated for further part production.

### 2.2.1. Standard Rotomoulding Heating Cycle

While the physical steps, as outlined above, are quite simple, monitoring these stages in rotomoulding is quite difficult. This is because the placement of the mould tooling inside an oven introduces a high temperature environment which is detrimental to conventional monitoring equipment. This limits the thermal analyses of the tooling, without the use of expensive heat resistant equipment, and so part quality is usually based on two measured factors; oven temperature and mould inner air temperature. These two temperatures relay a large amount of information about the mould tooling and provide feedback for determining the state of the part during the rotomoulding process. A typical heating cycle is outlined in Fig. 2.3 and demonstrates the different stages the part undergoes, A – F, during formation with the process steps also listed from 1 – 4.

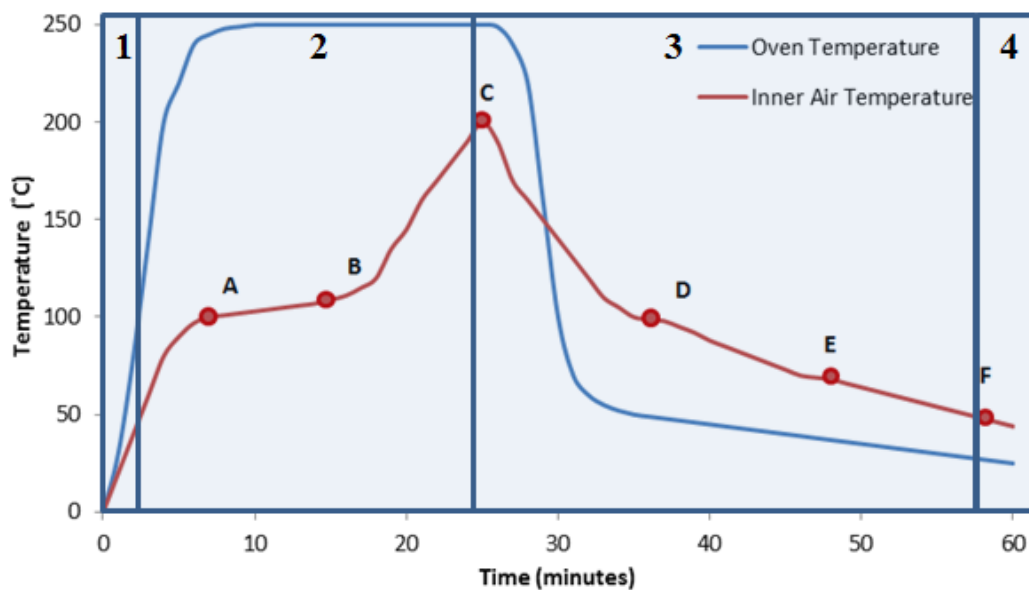


Figure 2.3. Typical heating cycle graph for a rotational moulding process with the physical stages listed from 1 - 4.

In a typical rotomoulding heating cycle [50, 63], the mould is charged and introduced to the oven causing the inner air temperature to rise from that of the ambient air. At point A, the polymer powder within the mould starts to melt and stick to the inner mould wall. The temperature remains quite constant between A and B as the powder absorbs the heat input to change from a solid to molten-like state, as its crystal structure is broken down. At point B the powder has completely melted

## Literature Review

and sticks to the mould wall in a thin consistent layer. The heat input is no longer being used by the powder to change into a molten melt and so again the inner air temperature starts to increase rapidly.

From stages B to C the powder particles continue to coalesce and densification of the polymer melt continues. When point C is reached the mould is removed from the oven and the desired cooling regime is applied [50, 63]. Most rotomoulding processes will incorporate water jet or air fan cooling to reduce cycle times and increase manufacturing efficiency. While this is beneficial for increasing efficiency in a high volume process it will also affect the material properties and crystallinity of the polymer part, the latter of which is an important factor in permeability.

At point D the molten plastic starts to crystallise and release stored energy in the form of heat so that the polymer can form an ordered solid structure. This heat is released within the mould and causes the inner mould temperature to remain quite consistent as the crystallisation process takes place. Once the polymer has completely solidified the temperature starts to decrease at a rate similar to before as it moves to point E [50, 63].

When the temperature within the mould reaches point E the rate of temperature change decreases again as the part starts to demould from the surface of the mould tooling. This demoulding is due to the difference in thermal expansion coefficients of both the plastic part and mould tooling materials [50, 63]. This creates an insulating barrier of air between the plastic part and mould tooling reducing the rate of heat loss further. The final step of this process is point F where the part is removed from the mould and the process is repeated.

One major issue with rotomoulding is its efficiency. Rotational moulding processes are traditionally less than 10% efficient in terms of the energy input into the system [65]. This is due to the loss of heat from the oven and the need to heat the entire oven space regardless of part size. Part removal from the oven is the most significant loss of energy as opening the oven releases all of the stored heat, causing the temperature within to reduce dramatically and necessitating the need for reheating. This wastes vast amounts of energy and reduces the effectiveness of this processing method as an inexpensive alternative to traditional manufacturing operations.

## Literature Review

A number of rotational moulding methods have been developed for the mass production of rotomoulded parts. These include carousel machines, shuttle machines, clamshell machines and rock and roll machines (all pictured in Fig. 2.4) which can employ a number of different heating methods including oven heating, electrical heating, circulating oil heating and open flame heating [50].

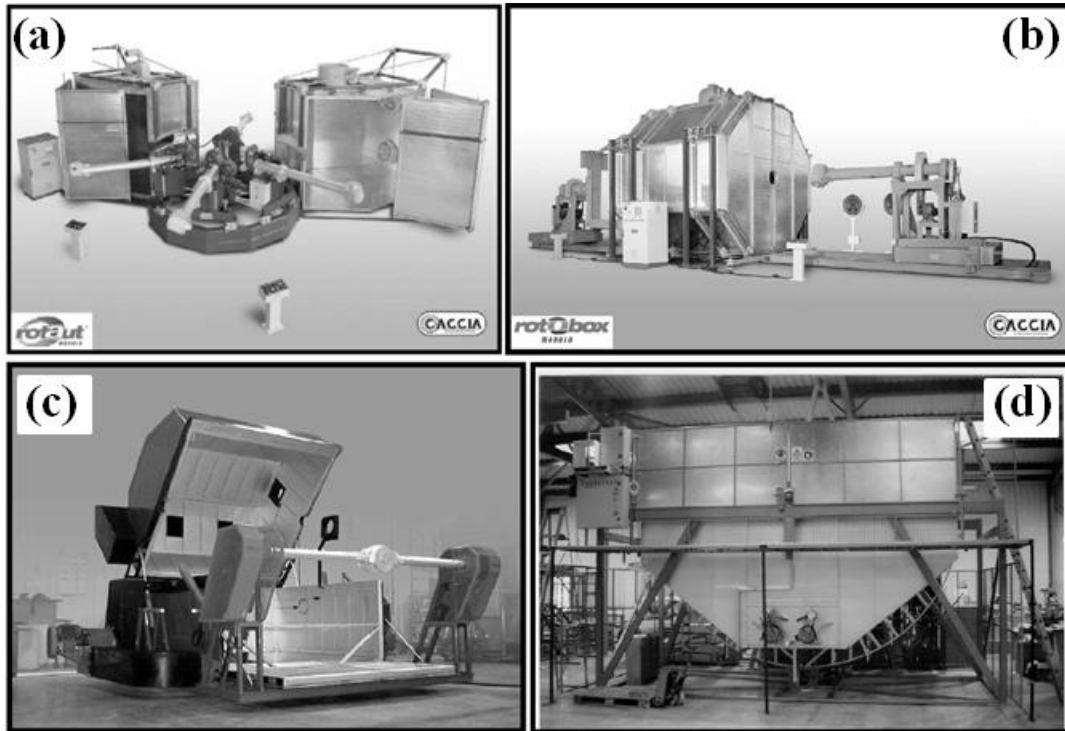


Figure 2.4. Standard rotomoulding processes including (a) carousel machines, (b) shuttle machines, (c) clamshell machines, and (d) rock and roll machines [50].

Electrical heating has been chosen for the current project as it offers a significant increase in temperature control within the tool to create uniform temperature distributions across the tool surface, and hence a more uniform part with consistent wall thickness. While the control offered is the most significant factor in this decision, a number of other factors affect the usage of the heating methods listed. Direct flame heating cannot provide the level of thermal control needed as it creates hot spots at specific burner locations. Oil heating, which involves the circulation of heated oil around the tool, could lead to leaks in the system at the extreme temperatures needed for the current liner formation (with moulding temperatures exceeding 400 °C). Traditional oven heating has also been excluded as it has an extremely low thermal efficiency due to the heat losses from the oven (while again not providing the control needed) [50, 65].

While low thermal efficiency can limit the effectiveness of rotational moulding processes a modified rotational moulding apparatus has been developed for the purpose of liner formation throughout this project. This modified process aims to eliminate the disadvantages associated with traditional processes while increasing the accuracy of part formation through significant improvements in process control and temperature distribution. This is described in detail in Chapter 6.

### **2.2.2. Polymer Powder**

The material used for rotational moulding of plastic parts is usually in liquid or powder form. The use of powder particles aids the rotational moulding process and ensures that the increase in wall thickness is slow and consistent over time as the powder is melted and adheres to the wall in a thin layer during each rotation. The powder quality is important to rotational moulding, with factors such as particle size, distribution and shape playing an important role in quality part formation [50, 63]. All of these factors are controlled by the grinding process for producing the polymer powder where shearing the material at high speeds produces powder particles of the desired shape and size.

The optimal shape of a powder particle is a cuboid with rounded edges such that the particle retains good heat transfer properties while also preserving its flow properties [66]. The optimal average diameter for a rotomoulding powder particle is 300  $\mu\text{m}$  with a maximum size of 500  $\mu\text{m}$  and a particle size distribution of 95% < 500  $\mu\text{m}$  and 15% < 150  $\mu\text{m}$  [66, 67]. This ensures that the presence of gaps between powder particles is minimised, that an optimal packing volume of the powder is achieved and that the flow properties of the particles are consistent.

The grinding process has a number of factors which affect the quality of the powder produced with the most important being the grinding temperature [60, 63, 66-68]. It is important to keep the grinding temperature below that of the polymer melt temperature so that fusion of particles does not occur during the shearing process. A grinding process which exceeds the melt temperature of the polymer material can experience a meltdown, where the polymer particles adhere together, clogging the machine and forcing it to shut down while the blockage is removed and the system cleaned. Grinding below the polymer melt temperature can be aided by cooling the

grinding wheel or by precooling the powder in liquid nitrogen. The downside to cooling in the grinding process is the formation of tails and fibrils with particle shapes becoming distorted and non-uniform in the processed powder [60, 63, 66-68] as demonstrated by Fig. 2.5. This can be mitigated by grinding near the softening temperature of the polymer and by using grinding wheels with sharp edges.



*Figure 2.5. Presence of tails and fibrils in a PEEK 2000P polymer powder signifying grinding at low temperatures or the use of blunt shearing blades.*

### **2.2.3. Air Void Formation**

The main drawback to rotational moulding is the formation of air voids in the part wall, due to the melt rheology and inherent shape of the powder particles which allow air to circulate between gaps in the powder particles prior to melting [50, 63]. Part solidification in rotational moulding follows a similar pattern to metals in that sintering of particles occurs whereby they melt and coalesce together at their contact points, creating a three dimensional network which propagates through the powder [69]. This network then collapses into the space between particles as densification of the part occurs. The air gaps between particles are then trapped in the powder and create pockets of air in the part wall, Fig. 2.6. The presence of tails and fibrils in polymer powders directly affects the rotomoulded part quality as these thinner sections inhibit close contact between particles [66, 70]. This leads to lower bulk

density, as the fibrils melt first during the rotomoulding process creating large spaces between particles, thus reducing the part quality and increasing the void volume content.

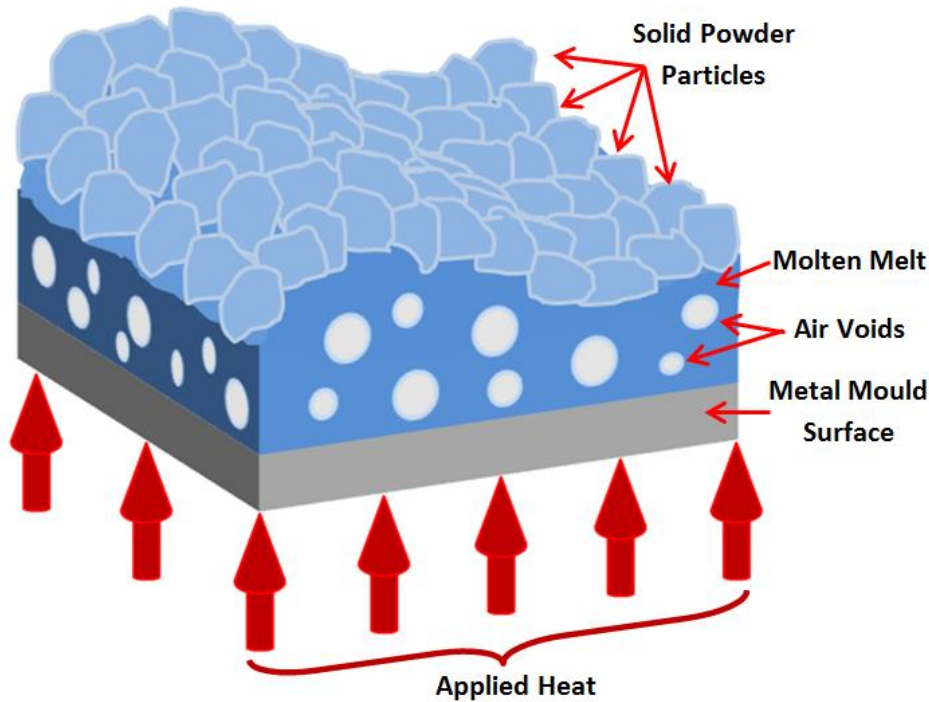


*Figure 2.6. Bubble formation in rotomoulded parts due to gaps between powder particles.*

The removal of air voids from rotomoulded parts has been a topic of extensive research from a number of different authors. The movement of bubbles due to buoyancy factors plays no part in air void removal, as demonstrated by Gogos [71]. The latter calculated that the movement of voids in LDPE was less than  $1.2 \mu\text{m}/\text{min}$  for a  $200 \mu\text{m}$  diameter air void. This calculated movement is consistent with observations reported by Kelly who observed an air void migration speed of  $0.8 \mu\text{m}/\text{min}$  for an average sized void in a polyethylene sample [72]. Thus it can be assumed that voids in the polymer melt are relatively stationary and that the natural mechanism for void removal in rotomoulded parts is the diffusion of air into the surrounding polymer melt [70, 71]. Industrial manufacturers have traditionally relied on elevated processing temperatures and longer cycle times to remove voids from rotomoulded parts, as the increased heat input increases the rate of diffusion while also increasing the amount of time available for the diffusion process to take place

[66, 70, 73]. While this is an effective means of void removal, the increase in cycle times and possible degradation of the polymer under elevated temperatures has led many manufacturers to use alternative methods of void removal.

### **2.2.4. Mould Pressure Control**

The use of an applied positive pressure in rotational moulds has shown significant benefits for air void removal in rotationally moulded parts with a number of ancillary benefits also present [74-77]. A positive pressure is applied after the powder has melted and has adhered to the mould wall and is maintained until near the end of the cool down cycle [74]. This positive pressure compresses the polymer melt which decreases the diameter of the voids within it and thus increases the pressure within the air void increasing the rate of diffusion and void removal [75]. Applied pressures of as little as 0.5 bar have shown to result in significant void removal in samples almost 9 mm thick, with complete removal of voids observed in the case of polyethylene trials [75].

While applied pressure is beneficial for reducing void contents, it also results in increases in the mechanical strength of the material, as parts rotomoulded with an applied pressure give increased bulk densities, which in turn increases measured impact strengths by 25% and tensile strength by 5% in rotomoulded parts [75]. The application of pressure also limits shrinkage and warpage of the part during cooling as the positive pressure holds the part against the mould wall giving greater dimensional accuracy [74, 75]. This also decreases cycle times as early demoulding of the part from the mould wall creates a pocket of air between the part and tool, which inhibits heat transfer during cool down as already explained [74, 75]. The application of pressure must be controlled to limit the existence of blow holes in the part line caused by over pressurisation of the mould, in turn leading to significant flash at the parting line [74]. The pressurisation of the mould also introduces residual stress to the part as its movement is inhibited during cool down and it is unable to shrink away from the mould naturally.

### **2.2.5. Venting and Cooling**

In traditional rotomoulding processes the pressure in the mould tool was assumed to be constant at atmospheric pressure, as facilitated by the inclusion of a vent pipe in

## Literature Review

the mould tooling, which negated any pressure build up in the tool due to increased temperatures in an enclosed volume. The vent pipe reduces the presence of blowholes and excessive flash at the parting line while also mitigating the risk of damage to the tool due to over pressurisation [77]. Therefore it is important to choose a vent pipe of sufficient diameter such that the flow of air is adequate for equilibrating the pressure with the surrounding environment.

Nugent showed that based on standard gas equations an 80 °C change in mould temperature equated to an increase in internal pressure of 0.2 bar, or a 20% increase in volume [77]. This means that larger moulds must have larger vents and the size of the mould is a determining factor in choosing the vent pipe diameter. Many authors have quoted a simple standard reference of a minimum vent diameter of 10-14 mm per m<sup>3</sup> of internal mould volume [50, 77-79]. While this calculation sets the minimum vent size, it is usually beneficial to use as large a vent as possible to ensure proper pressure equalisation with the external environment. The effects of part thickness can also contribute to vent size estimates and there are also a number of more advanced methods of calculating the proper vent size based on air flow measurements and part thickness effects [63, 77].

Cooling has also taken on an advanced role in rotational moulding operations, often being used in conjunction with pressurisation to reduce cycle times and increase output [80]. Air cooling, water jet cooling and internal mould cooling have all been proposed as methods of reducing cycle times, with reductions of almost 50% achieved in certain cases [80, 81]. Liquid cooling has been shown to offer significant advantages over gaseous cooling due to the enhanced heat transfer achieved, but distortions in part shape and increased warpage can be present in water jet cooled parts [80]. The rate of cooling can also affect the material properties of the rotomoulded part as crystallisation of the plastic is affected by the cooling rate. While this shows that rotational moulding can be used to manufacture the liner, the processing conditions used throughout the process will determine the overall liner quality in regard to both the dimensional consistency and barrier properties achievable.

### 2.2.6. Warpage and Shrinkage

Warpage and shrinkage are two different factors which have distinct impacts on rotomoulded parts. Rotomoulded parts undergo shrinkage during cooling due to the solidification of the molten melt causing the volume of the structure to reduce as thermal energy is expended. The shrinkage is usually controlled by the crystal growth in the material whereby polymers with higher crystallinity tend to induce higher levels of shrinkage as their ordered structure results in a polymer of reduced volume. This has a knock on effect on warpage, as the differences in crystal growth and shrinkage through the thickness of the parts wall cross section (due to the differences in cooling rates either side of the part) can lead to warpage and bending. Fig. 2.7 shows the cooling regime of rotomoulded parts whereby the section in contact with the mould wall cools faster than the internal surface and so the part at the mould wall side will have a lower crystallinity and hence less shrinkage. In comparison the internal surface will have slower cooling, higher crystallinity and higher shrinkage. This difference in shrinkage rates between the outer and inner wall sections imparts a residual stress on the wall cross section and causes the wall to warp towards the surface of higher shrinkage causing bending in the part wall as shown [50].

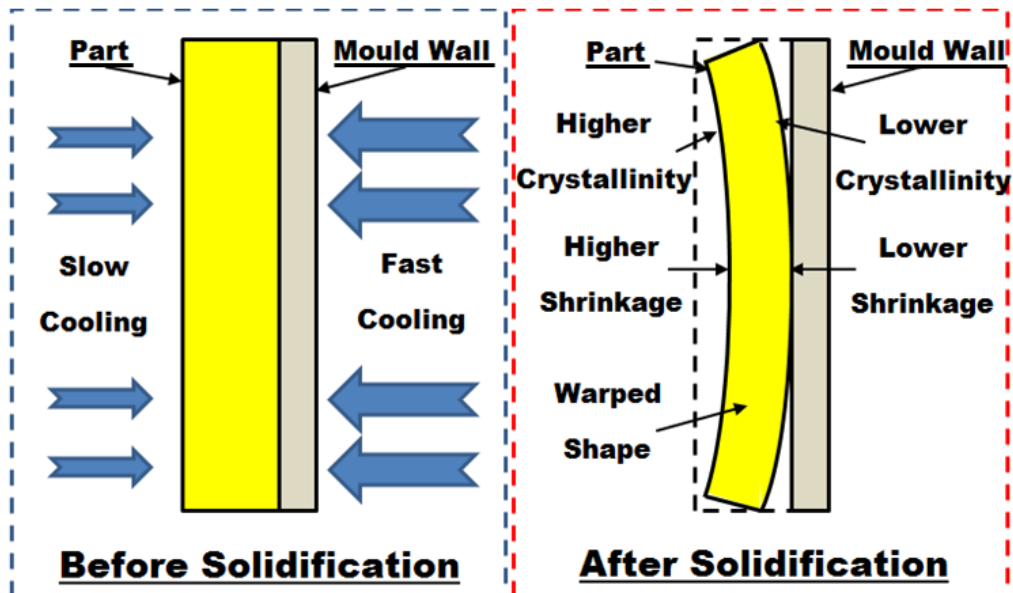


Figure 2.7. The cooling regimes of rotomoulded parts and the effects this has on crystallinity, part shrinkage and hence warpage of the final part [50].

### 2.2.7. Melt Rheology

Melt rheology is the study of the flow characteristics of molten polymer materials. It measures the viscoelastic behaviour of polymers in their molten state by applying a shear force to the sample and assessing its characteristic flow characteristics. Viscosity is defined as the ratio of stress to flow rate. Materials with low viscosity flow easily under an applied stress, while high viscosity materials resist deformation and have a much slower response to the applied stress. When a fluid is under stress, the ratio of the shear stress,  $\tau$ , to the strain rate  $\dot{\gamma}$ , is the shear viscosity  $\eta$  [51]:

$$\frac{\tau}{\dot{\gamma}} = \eta \quad (2.1)$$

For Newtonian fluids the viscosity is constant and so an increase in shear stress results in an equal and proportional increase in strain rate. However, polymer melts are non-Newtonian and so their response to an applied shear stress is non-linear; with increases in shear rate leading to decreases in viscosity [51]. The molecular weight of the polymer chains in the melt is one of the main characteristics which affects flow properties and hence a materials viscosity [82].

Polymers with low molecular weights (shorter chains) will not include chain entanglement which impinges on the motion of surrounding polymer chains and so their viscosities will be quite low. However, at a certain molecular weight, the chain entanglement becomes a larger factor and movement of chains is inhibited leading to an increase in viscosity [83]. Branching of polymer chains can also affect the melt viscosity with the branched chains impeding movement and increasing the materials viscosity. The melt viscosity and molecular weight of materials tested within this research has been found from the literature (only possible for the PEEK materials tested), to give a better understanding of their characteristic flow properties. This information (included in Chapter 3) has then been used to assess air void growth in the polymer samples based on melt flow characteristics in later chapters

## 2.3. Polymer Structure

Polymer permeability analysis spans a vast array of fields of study, not only in engineering but also in material science, the medical device industry and membrane science technologies. The rate of permeation of a penetrant through a polymer

material is directly related to the structure of the material under investigation. Unlike metals, which have highly compact crystal structures, polymers consist of long chain molecules with a carbon backbone and a single repeating structure at the core of the chains composition, Fig. 2.8 [84-88].

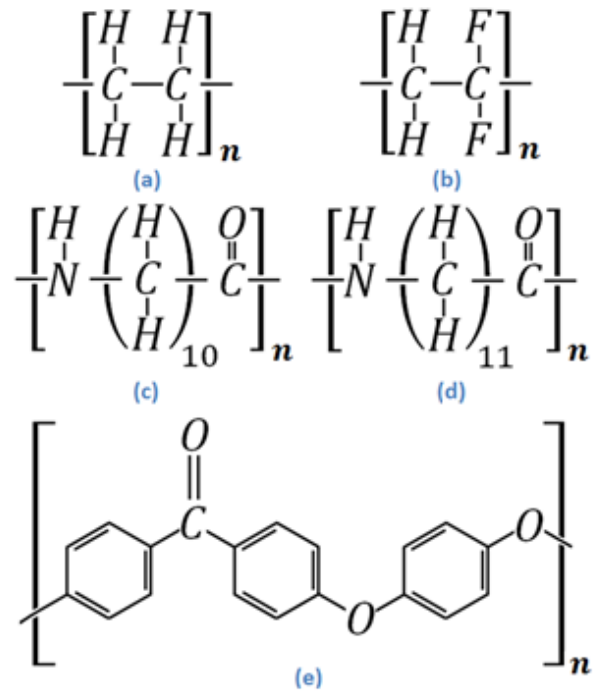
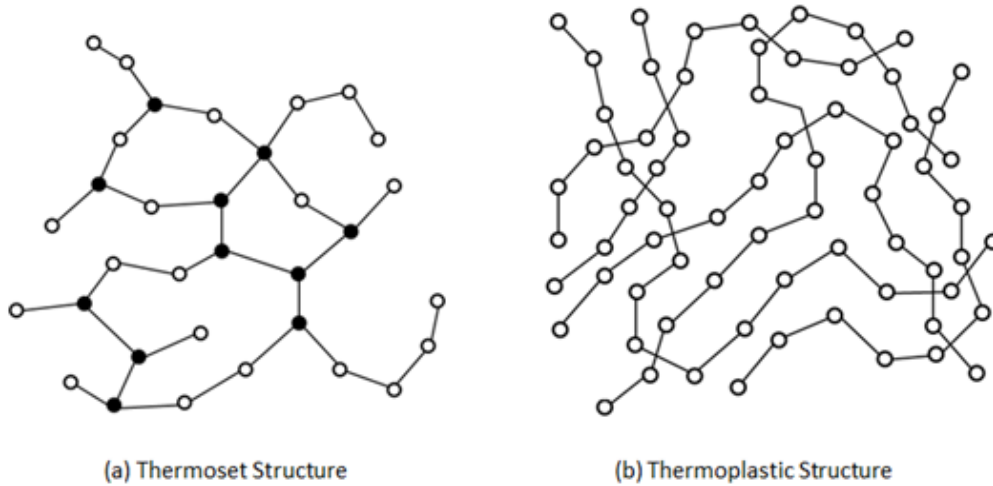


Figure 2.8: Monomer unit structure for a number of polymer materials including (a) polyethylene (PE) [84], (b) polyvinylidene difluoride (PVDF) [85], (c) polyamide 11 (PA11) [86], (d) polyamide 12 (PA12) [87] and (e) polyetheretherketone (PEEK) [88].

These core repeating units, or monomers, determine the structure of the polymer and govern the close packing of chains together in the material. Van der Waals forces and the introduction of covalent bonds between different chains create strong flexible materials with crosslinking and chain entanglement leading to varying polymer characteristics in regards to strength and toughness [89].

While there are a large number of polymer materials available for use in engineering applications, they usually fall into two categories, thermosets and thermoplastics, Fig. 2.9. Thermoset materials are characterised by their long chain molecules which can interlink together through branching and the formation of strong covalent bonds between adjacent polymer chains. This makes the polymer rigid and increases

strength with a networked structure prevalent in the bulk material. These polymers, once formed, cannot be reheated or reshaped as the bonds between chains cannot be broken down and so the application of heat degrades these materials after they have been formed. Examples include rubber, epoxies, phenol formaldehyde and some polyesters [51, 90].



*Figure 2.9. Molecular structure of thermosets and thermoplastics with crosslinking highlighted.*

Thermoplastic materials are identified by their highly linear chains which are held together by relatively weak Van der Waals forces. Their chain structures have little to no branching and are devoid of crosslinking which gives them the ability to be reheated and reshaped over a number of cycles without degradation of properties [88]. Examples include polyethylene, nylon, polyvinyl chloride, polypropylene and fluoropolymers [51, 89]. The structures of thermoplastics can consist of amorphous regions of random chain orientations or crystalline regions of ordered repeating structures with the polymer structure and forming history governing the prevalence of both regions in the bulk material [51].

Amorphous materials consist of polymer chains with a random structure (yet they can still have orientation bias), whereas crystalline materials have a uniform repeating structure displaying three dimensional and organised features. Semi crystalline materials consist of a balance of amorphous and crystalline regions with forming history and cooling rates affecting the overall percentage crystallinity.

Crystalline polymers can usually be differentiated from amorphous materials by the presence of spherulites within the material [51].

Crystal growth begins in regions where some form of ordered polymer chain structure is present, growing into spherulites within the polymer; with their size dependent upon material properties, cooling regime and proximity to other spherulites within the melt. Slow cooling rates result in a small number of spherulites with large crystals being developed over time. Rapid cooling leads to the initiation of crystal growth in a large number of spherulites or nucleation points, resulting in smaller crystal formation [51].

Research has shown that crystallinity has a significant effect on the permeability of polymer materials with the percentage crystallinity, dispersion and orientation of crystals being the most prominent factors controlling permeation rates [91-94]. In general, higher crystallinity percentages result in lower permeabilities and so cooling rates can be altered to influence the crystallinity percentage in materials to improve their barrier properties.

## 2.4. Permeation

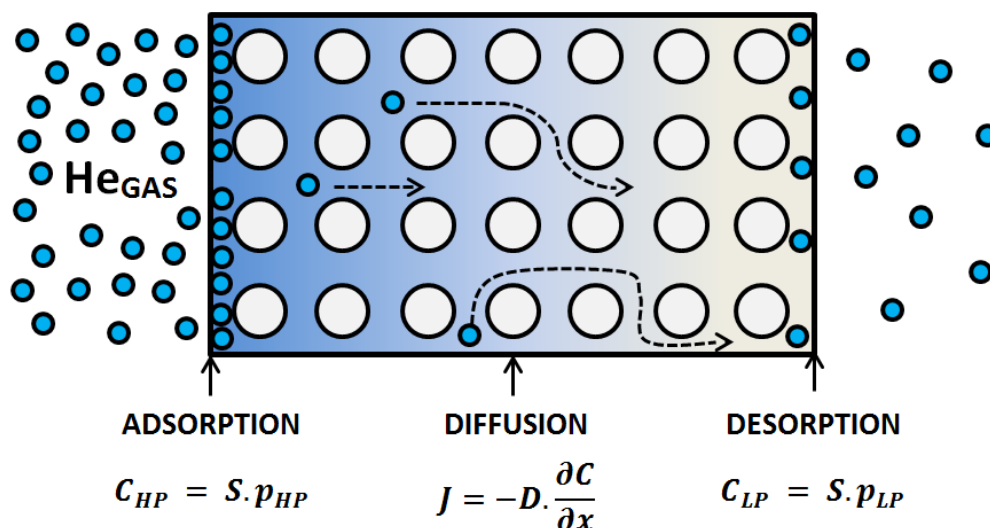


Figure 2.10. Image representing the entire process of gas permeation covering the three steps of adsorption, diffusion and desorption.

Permeation encompasses the entire process of a gas or liquid crossing a membrane or barrier due to an applied force. It consists of three main steps, shown in Fig. 2.10,

including (1) adsorption of the permeant into the membrane surface, (2) diffusion of the penetrant across the membrane thickness and then finally (3) desorption of the penetrant on the opposite side of the membrane [95]. These three steps govern the entire permeation process and can be broken down into their constituent parts for analysis.

### 2.4.1. The Solution Diffusion Model

This three step process was first proposed by Thomas Graham who used his observations in gas transport phenomena from 1829 to 1866 to propose a permeation model which has evolved today into what is more commonly known as the Solution-Diffusion Model [96-99]. The Solution-Diffusion Model forms the basis for the phenomenological descriptions of permeation in a number of materials and has been used extensively in the modelling of transport phenomena across polymer membranes [100-104].

The derivation for the equations governing the Solution-Diffusion Model, while based on phenomenological observations, is rooted in thermodynamics and is based on the premise that the driving forces behind permeation (pressure, temperature and concentration) are interrelated and that the overall driving force is the chemical potential gradient [105, 106]. This means that the flux,  $J$ , across a component,  $i$ , is related to the chemical potential,  $\mu_i$ , across the thickness of the component  $x$ :

$$J_i = -L_i \frac{d\mu_i}{dx} \quad (2.2)$$

where  $L_i$  is a constant of proportionality that links the chemical potential gradient to the flux. The flux is a negative quantity as the direction of flow is towards the region of lower chemical potential. In gas permeation analyses the only driving forces of note are the concentration and pressure which alter the chemical potential gradient to become [105, 106]:

$$d\mu_i = RT d\ln(\gamma_i c_i) + v_i dp \quad (2.3)$$

where  $R$  is the gas constant,  $T$  is the temperature,  $c_i$  is the molar concentration of component  $i$ ,  $\gamma_i$  is the activity coefficient that links the concentration to the activity,  $p$  is the pressure and  $v_i$  is the molar volume of the component  $i$ . In a solid membrane

the volume of the membrane does not change with pressure, so Eq. 2.3 can be integrated with respect to concentration and pressure to give [105, 106]:

$$\mu_i = \mu_i^0 + RT \ln(\gamma_i c_i) + v_i(p - p_i^0) \quad (2.4)$$

where  $\mu_i^0$  is the chemical potential of pure  $i$  at a reference pressure  $p_i^0$ , also known as the saturation vapor pressure of  $i$ .

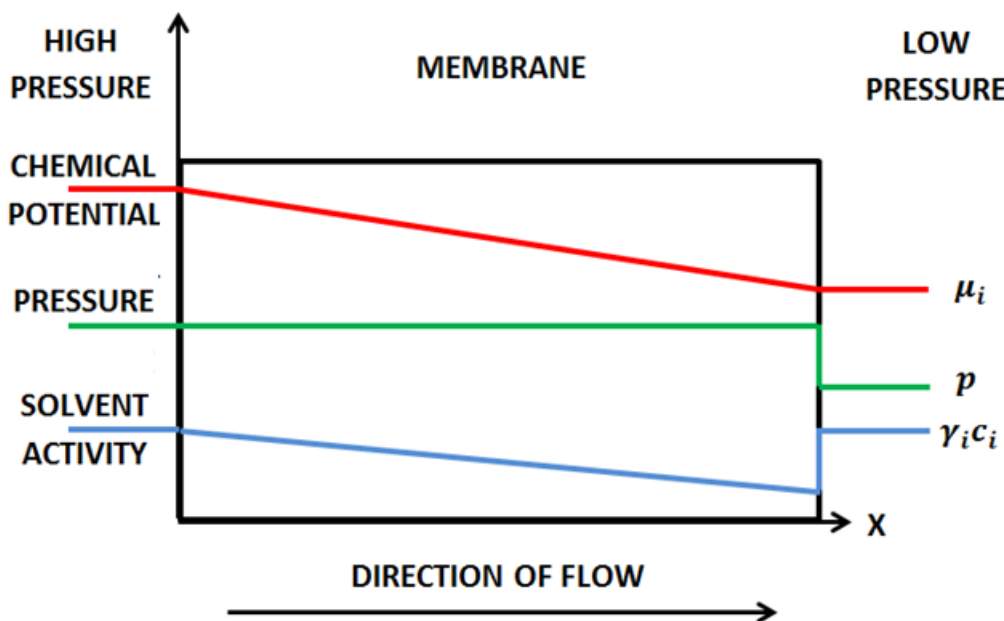


Figure 2.11. Overview of the Solution-Diffusion Model including a representation of the main factors governing the flux [104, 105].

The Solution-Diffusion model makes two main assumptions that differentiate it from other pore flow models and that allow it to calculate the flux from phenomenological observations. It assumes a continuous chemical gradient across the membrane by assuming the permeating fluid is in equilibrium either side of the membrane. This implies that the rate of adsorption and desorption of permeant molecules in the membrane is greater than the rate of the diffusion of these molecules across the membrane. It also assumes that the pressure across the membrane is constant and equal to the applied pressure on the upstream side of the membrane as shown in Fig 2.11. The chemical potential gradient is therefore expressed by the solvent activity alone in Eq. 2.3 as the lack of a pressure gradient causes Eq. 2.2 to be expressed as [105, 106]:

$$J_i = -\frac{RTL_i}{c_i} \frac{dc_i}{dx} \quad (2.5)$$

### 2.4.2. Permeability Coefficient

The permeability coefficient  $P$  is another measure of permeability and defines the rate at which a penetrant molecule can pass through a material. While closely linked to the flux and leak rate, the permeability coefficient is a better representation for ranking different materials against each other, in comparison to leak rate measurements, as it takes thickness and pressure into account and so eliminates discrepancies between materials by using units of scc/m.s.bar. It can be found by dividing the flux,  $J$ , through the material by the pressure difference,  $\Delta p$ , across the membrane and multiplying by the membrane thickness,  $l$ , as shown in Eq. 2.6 [107]:

$$P = \frac{J}{\Delta p} \cdot l \quad (2.6)$$

While the permeability coefficient alone cannot be used for qualification of COPV tanks it does differentiate between materials to define those which have the lowest permeability and so the permeability coefficient will be used in this thesis to rank materials for COPV liner applications.

## 2.5. Diffusion

While adsorption defines the surface interactions in permeation processes, the transfer of molecules through the membrane is governed by diffusion. As already discussed, diffusion is driven by a chemical gradient (in this case a concentration gradient provided by an applied pressure) which causes the dissolved molecules to move through the bulk material.

### 2.5.1. Fick's Law of Diffusion

Eq. 2.5 is more commonly referred to as Fick's first law of diffusion and is expressed more conveniently as [110]:

$$J_i = -D_i \frac{dc_i}{dx} \quad (2.7)$$

where the  $RTL_i/c_i$  term has been replaced with the diffusion coefficient  $D_i$ . It was first proposed by Adolf Fick in 1855 when he adopted it from the heat conduction equation derived by Joseph Fourier and related the mass flux to the concentration gradient and a diffusion coefficient [108, 109]. Fick's first law forms the basis for steady state permeation studies and has been used extensively in describing the mass flux through materials [110, 111]. While Eq. 2.7 governs one dimensional steady state flux, it can be expanded to incorporate three dimensional flux under transient conditions.

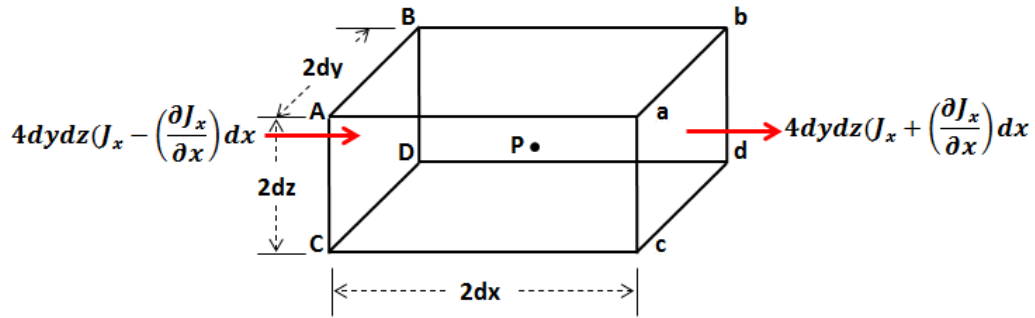


Figure 2.12. Representation of diffusion in a box element for Fick's second law of diffusion.

Consider diffusion into a box shaped element in Cartesian coordinates. A point,  $P$ , is located at the centre of the element and the box has element edge lengths of  $2dx$ ,  $2dy$  and  $2dz$  as shown in Fig. 2.12. If there is a flux gradient  $\partial J / \partial x$  such that the flux in the  $x$  direction at point  $P$  is  $J_x$  then the flux at the face  $ABCD$  is  $(J_x - (\partial J_x / \partial x))dx$  and at the face  $abcd$  is  $(J_x + (\partial J_x / \partial x))dx$ . This means that by multiplying the flux by the face area, the amount of material moving through the box at a unit time is  $4dydz(J_x - (\partial J_x / \partial x))dx$  at  $ABCD$  and  $4dydz(J_x + (\partial J_x / \partial x))dx$  at  $abcd$ . Thus the accumulation of material,  $R_x$ , in the element is that entering face  $ABCD$  less that exiting face  $abcd$  such that [110, 111]:

$$R_x = -8dxdydz \left( \frac{\partial J_x}{\partial x} \right) \quad (2.8)$$

and from the other faces in the  $y$  and  $z$  directions is:

$$R_y = -8dxdydz \left( \frac{\partial J_x}{\partial y} \right) \quad (2.9)$$

$$R_z = -8dxdydz \left( \frac{\partial J_x}{\partial z} \right) \quad (2.10)$$

But the rate at which the amount of diffusing substance increases in the element is also given by:

$$8dxdydz \left( \frac{\partial c}{\partial t} \right) \quad (2.11)$$

such that:

$$\frac{\partial c}{\partial t} = -\frac{\partial J_x}{\partial x} - \frac{\partial J_y}{\partial y} - \frac{\partial J_z}{\partial z} \quad (2.12)$$

Substitution of Eq. 2.7 into Eq. 2.12 becomes [110, 111]:

$$\frac{\partial c}{\partial t} = D \left( \frac{\partial^2 c}{\partial x^2} + \frac{\partial^2 c}{\partial y^2} + \frac{\partial^2 c}{\partial z^2} \right) \quad (2.13)$$

This reduces to Eq. 2.14 for diffusion in a single dimension and is better known as Fick's second law of diffusion for transient flow.

$$\frac{\partial c}{\partial t} = D \left( \frac{\partial^2 c}{\partial x^2} \right) \quad (2.14)$$

This equation governs all interactions before steady state conditions are reached and inserts a time dimension into the calculation of the flux. It was used by Daynes in 1920 to determine the diffusion coefficient via the "time lag method" which is still the most common method of diffusion coefficient calculation in use today [112].

### 2.5.2. Free Volume

A number of theoretical models have been developed to describe the diffusion processes in polymers, the most successful of which is free volume theory. Free volume theory was first introduced by Cohen and Turnbull [113] when they applied it to a liquid composed of solid spheres in a cage lattice where the total volume was composed of the occupied volume (hard spheres) and free volume (intermittent space between spheres). The spheres were free to vibrate but were unable to move unless a hole of equal size was located adjacent to the cage. In this manner, hard spheres were

## Literature Review

transported through the material through natural fluctuations in the free volume and not through displacements caused by changes in activation energy [114].

Work by Cohen and Turnbull has been readily applied to studies of diffusion in polymer materials [115, 116] where free volume holes are formed in polymers from the migration of polymer chain segments to create holes of sufficient size to accommodate diffusing molecules. Two types of free volume have been defined, the interstitial free volume and the hole free volume [116]. The interstitial free volume requires a large amount of energy to be redistributed throughout the polymer and so does not readily contribute to mass transport. The hole free volume however can be easily redistributed throughout the polymer and so governs the majority of mass transport operations in polymers [117].

Polymer materials can usually be grouped into one of two states, rubbery or glassy. At higher temperatures they usually fall into the rubbery state where polymer chains are free to rotate about their backbone and so thermal fluctuations combined with imperfect packing of the chains leads to high diffusion rates through the material [105, 117]. As the temperature is decreased, and the polymer cools, the specific volume of the polymer falls due to a reduction in the vibrational energy of the polymer chains. But at a certain temperature, known as the glass transition temperature  $T_g$ , the polymer chains become locked in place as there is not enough thermal energy to overcome the steric hindrance between chains and so free volume elements become trapped in the polymer [105, 117].

This non-equilibrium state is referred to as the glassy region and includes the trapping of hole free volume in the polymer material. This limits diffusion in the material as free volume can no longer redistribute throughout the polymer to aid the diffusion process. As the temperature decreases the reduction in vibrational energy will lead to a decrease in diffusion, but it will no longer be as pronounced as the rate above  $T_g$  as the trapped free volume restricts the level of shrinkage of the specific volume of the polymer in this non-equilibrium state [105, 117].

The graph in Fig. 2.13 displays the specific volume,  $V_g$ , of a glassy polymer material, which is greater than that of an equivalent rubbery material,  $V_l$ , whose value has been extrapolated from the specific volume data above the polymer's glass transition temperature,  $T_g$ . The non-equilibrium excess free volume is a direct result of the

freezing of the polymer chains in the glassy polymer and their inability to rearrange in a manner which would allow them to obtain a state of equilibrium below  $T_g$  with a lower specific volume [118].

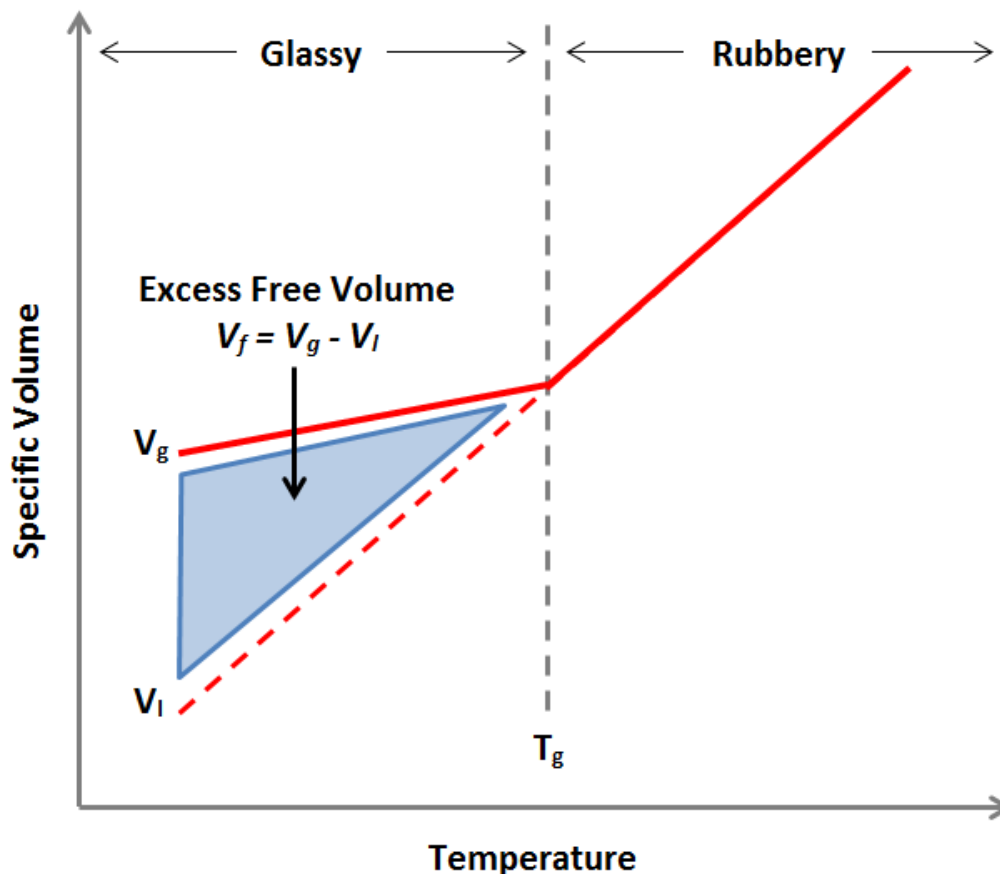


Figure 2.13. Graphical representation of the dual mode sorption model for the specific volume of a glassy polymer material [103, 118].

### 2.5.3. Diffusion Coefficient

The Diffusion Coefficient  $D$  is a measure of the frequency with which a penetrant molecule moves throughout a membrane while also quantifying the size of the movement [105]. Often measured in units of  $\text{cm}^2/\text{s}$  or  $\text{m}^2/\text{s}$ , it is directly dependent on the material properties of the membrane and on the size of the penetrant molecule. Each polymer material will have a different diffusion coefficient for each individual gas that passes through it as the gas size determines how restrictive the surrounding polymer chains are to movement. The change in location of penetrant molecules due to fluctuations in polymer chains has been modelled using statistical

fluctuations to demonstrate the diffusion of molecules through polymer materials and also to theoretically estimate the diffusion coefficient [119].

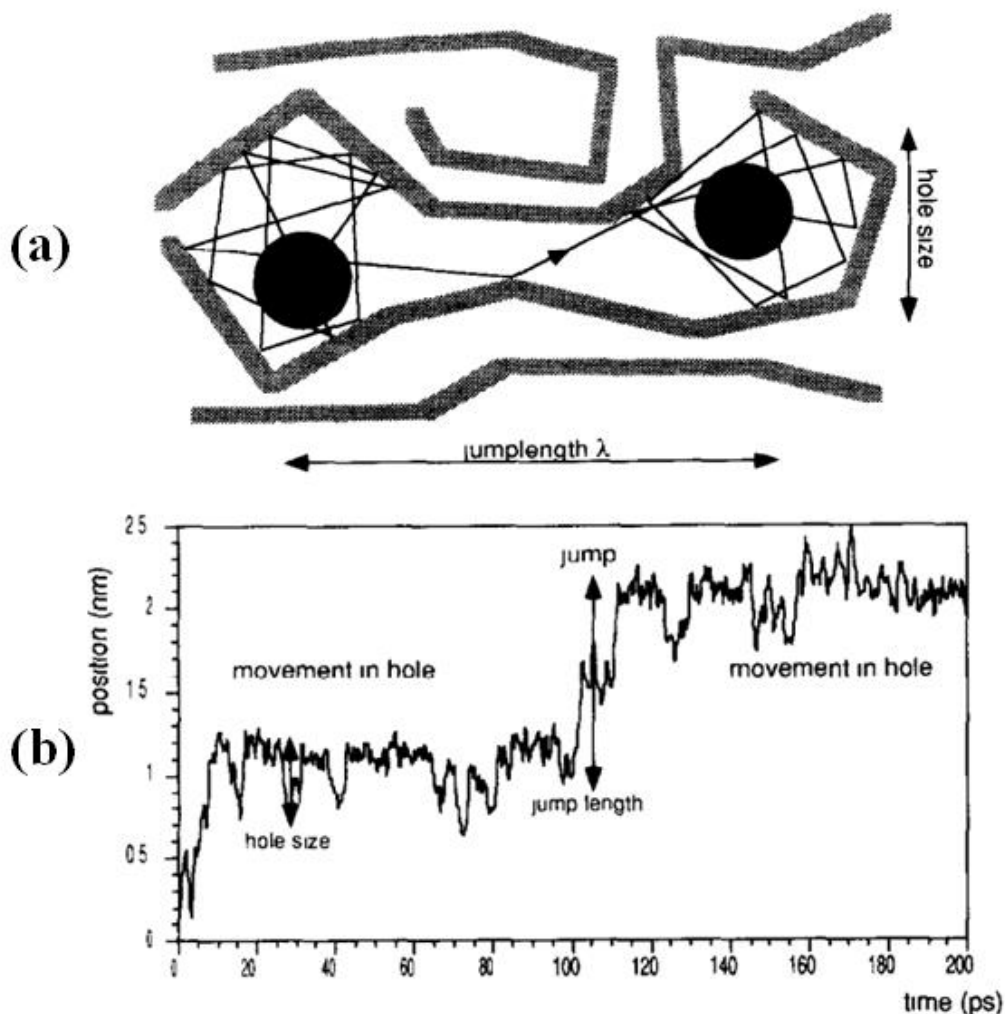


Figure 2.14. (a) Demonstration of the movement of penetrant molecules in the polymer accompanied with (b) a measurement of the distance travelled by the molecule based on its jump between microcavities [119].

These models create small microcavities over time through sparse polymer chain movements which the penetrant molecules can move into when a sufficient amount of space is present. By repeating this simulation for a large amount of similar cases, an average distance moved can be calculated for the penetrant molecule and a diffusion coefficient can be calculated based on these theoretical models of the jump length. Fig. 2.14 demonstrates one such calculation whereby the jump length between cavities is measured using a numerical simulation.

## 2.6. Sorption

Sorption covers both the adsorption and desorption of penetrant molecules into and out of a membrane and encompasses all interactions of the penetrant molecules with the membrane surface. For polymer materials interacting with inert gases such as helium, adsorption is governed by a physisorption process whereby the penetrant molecules impact the membrane surface and adhere to it through weak Van-der-Waals forces [120].

### 2.6.1. Henry's Law

There are a number of representations for describing the interactions of penetrant molecules with the membranes surface for sorption behaviour. These models usually pertain to both mono-layer or multi-layer adsorption and incorporate significant differences in their determination of the rate of sorped molecules. The simplest mono-layer isotherm is described by Henry's Law whereby a single layer of molecules is deposited on to a two dimensional surface where no interaction between adsorbed molecules occurs.

This law governs a linear increase in concentration,  $C$ , at the surface of the membrane with increases in pressure,  $p$ , and is generally only valid for systems with low occupancy at the membrane surface, consisting mostly of rubber materials. The concentration and pressure are linked via a solubility coefficient,  $S$ , as defined in the relationship in Eq. 2.15 [120-122].

$$C = S.p \quad (2.15)$$

### 2.6.2. Langmuir Isotherm

A more advanced mono-layer model is the Langmuir Isotherm. Again, like Henry's Law, only a single layer of molecules is adsorbed and there is no interaction between molecules. However the Langmuir model takes the coverage of the surface into account using a coverage grade,  $\theta$ , which is a value between 0 and 1 (with 1 = full coverage) and which leads to definition of the Langmuir Isotherm [120-122]:

$$\theta = \frac{Bp}{1 + Bp} \quad (2.16)$$

where B is a temperature dependent material constant that covers the bond strength of the solute. Because the coverage grade is proportional to concentration this equation can be linked back to concentration as shown:

$$C = \frac{S^* B p}{1 + B p} \quad (2.17)$$

It can also be noted that in the limiting case of low pressure the Langmuir model reverts back to Henry's Law as the denominator approaches unity.

### 2.6.3. Brunauer-Emmett-Teller (BET) Isotherm

Unlike mono-layer adsorption, multi-layer adsorption is usually defined by the BET model. In this model the surface possesses uniform localised sorption sites where adsorption on one sites does not affect neighbouring sites (molecules are independent of each other), subsequent layers can only grow on fully covered underlying layers and up to  $n$  layers can be adsorbed where the surface area of the  $n^{th}$  layer is equal to the coverage of the  $n-1$  layer [120-122]. The BET model also defines a surface coverage factor such that:

$$\theta = \frac{r_{BET} p}{(p_0 - p)[1 + (r_{BET} - 1)p/p_0]} \quad (2.18)$$

$$C = \frac{S^{**} r_{BET} p}{(p_0 - p)[1 + (r_{BET} - 1)p/p_0]} \quad (2.19)$$

where  $r_{BET}$  is the sticking times of adsorption and condensation layer and  $p_0$  is the vapor saturation pressure. Again this can be changed to concentration values via its intrinsic proportionality where  $S^{**}$  is a material constant.

### 2.6.4. Dual Mode Sorption

While all of these models can be relevant for certain materials and systems, it is the combination of Henry's Law and the Langmuir isotherm which is most widely used to describe sorption in glassy polymer materials, also known as the dual mode sorption model. This is because glassy polymers are not in a thermodynamically steady state and so the transference between Henry's law and the Langmuir isotherm is needed to define the sorption characteristics of glassy polymers. The graph in Fig.

2.13 has already shown the presence of excess free volume in the polymer due to the restriction of chain movement below the glass transition temperature.

The dual mode sorption model allows for these dual regions of sorption characteristics by utilising Henry's law in the equilibrium state (the rubbery region) and the Langmuir isotherm in the non-equilibrium state (glassy region where sorption is in holes frozen in the polymer material below  $T_g$ ) where the sorption is described by [123]:

$$C = C_D + C_H = Sp + \frac{S^*Bp}{1 + Bp} \quad (2.20)$$

where  $C$  is the total concentration of gas in a glassy polymer,  $C_D$  covers the ordinary dissolution with Henry's law and  $C_H$  covers the sorption into microvoids or holes via the Langmuir Isotherm,  $S$  is the Henry's Law coefficient, and  $B$  and  $S^*$  are the Langmuir hole affinity and capacity parameters respectively [123]. The sorption models described previously are all pressure dependent and so Fig. 2.15 displays the effects of concentration versus pressure for each of the four models discussed [121].

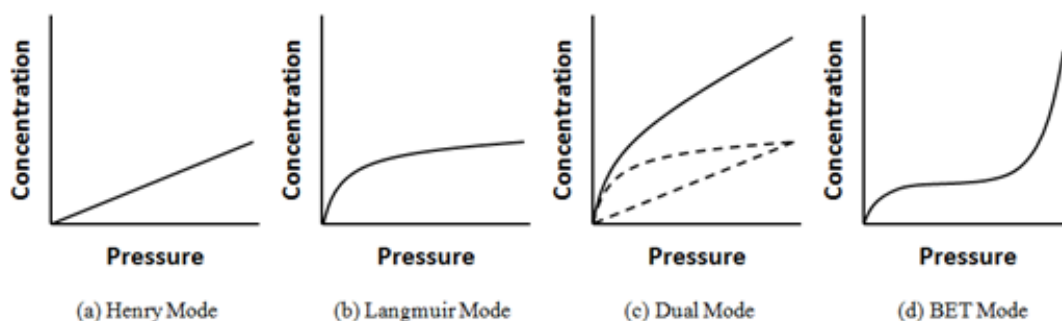


Figure 2.15. Graphical representations of the different sorption models.

### 2.6.5. Solubility Coefficient

The solubility coefficient  $S$  is a measure of a material's ability to store or adsorb a penetrating gas and defines the concentration of the diffusing substance in the material as a function of the applied pressure. It can be calculated by dividing the concentration of the penetrant in the membrane surface by the applied pressure to obtain the solubility coefficient in units of  $\text{scc/m}^3 \cdot \text{bar}$  through a rearrangement of Henry's law. The solubility coefficient is affected by a number of parameters

including the penetrant size, the presence of free volume in the polymer and penetrant-polymer interactions; most solubility coefficients remain constant for a constituent polymer family of the membrane [105, 124-126].

## 2.7. Time Lag Method

The time lag method is a permeability measurement technique that is used to define permeability,  $P$ , diffusion,  $D$ , and solubility,  $S$ , coefficients for a polymer material. It is based on the measurement of the gas that has passed through a sample due to an applied pressure gradient and allows for effective measurement of the coefficients by monitoring the leak rate and time taken to reach steady state conditions. Through Fick's Second Law of Diffusion, Eq. 2.14, the following boundary conditions are defined for the sample [110, 111]:

$$\begin{aligned} t < 0 & \quad 0 \leq x \leq l & \quad C = 0 \\ t \geq 0 & \quad x = 0 & \quad C = C_{2,m} = Sp_2 \\ t \geq 0 & \quad x = l & \quad C = \partial C / \partial t = 0 \end{aligned}$$

where  $l$  is the membrane thickness and  $x$  is any value less than or equal to the membrane thickness. This defines an initial concentration of  $C=0$  for the start of the test and then defines the application of a concentration  $C_{2,m}$  at  $x=0$  for the driving force and then defines transient conditions at the opposing end of the membrane  $l$  as a function of time  $t$ . The solution for these conditions, assuming that the diffusion coefficient is constant, is given by [110, 111]:

$$\frac{Q}{lC_2} = \frac{Dt}{l^2} - \frac{1}{6} - \frac{2}{\pi^2} \sum_{n=1}^{\infty} \frac{(-1)^n}{n^2} \exp\left(-\frac{Dn^2\pi^2 t}{l^2}\right) \quad (2.21)$$

where  $Q$  is the total amount of permeant passing through the membrane,  $l$  is the membrane thickness and all other variables are as previously defined. This equation governs the flow across the entire sample through transient conditions to steady state. If we assume the system has reached steady state and the time  $t$  is equal to infinity, then the summation term in Eq. 2.21 is equal to zero such that:

$$\frac{2}{\pi^2} \sum_{n=1}^{\infty} \frac{(-1)^n}{n^2} \exp\left(-\frac{Dn^2\pi^2 t}{l^2}\right) \Bigg|_{t \rightarrow \infty} = 0 \quad (2.22)$$

Steady state conditions can be defined such that:

$$\frac{Q}{lC_2} = \frac{Dt}{l^2} - \frac{1}{6} \quad (2.23)$$

Rearranging Eq. 2.23 to isolate the total amount of permeant passing through the membrane  $Q$  the equation then becomes:

$$Q = \frac{DC_2 t}{l} - \frac{lC_2}{6} = \frac{DC_2}{l} \left( t - \frac{l^2}{6D} \right) = \frac{DC_2}{l} (t - L) \quad (2.24)$$

where the time lag  $L$  is defined as [110, 111]:

$$L = \frac{l^2}{6D} \quad (2.25)$$

The measurement of the increase in gas accumulation  $Q$  leads to a plot of the total volume of gas that has passed through the sample versus time, to produce a graph similar to that shown in Fig. 2.16. In this graph there are two distinct sections, the unsteady transient region and the linear steady state region as defined by Eq. 2.25.

Both regions provide distinct information for coefficient definition in permeability studies with the time lag being defined as the point at which an extension of the linear portion of the graph intersects the time axis. This defines the time lag  $L$  with the solution to Eq. 2.25 allowing for the determination of the diffusion coefficient  $D$ . The permeability coefficient,  $P$ , is defined as the slope of the steady state region also outlined in Fig. 2.16.

The determination of  $D$  and  $P$  finally allows for the calculation of the solubility coefficient  $S$  which is defined by Eq. 2.26 and rounds out the definition of all coefficients related to permeability [110, 111]:

$$S = P/D \quad (2.26)$$

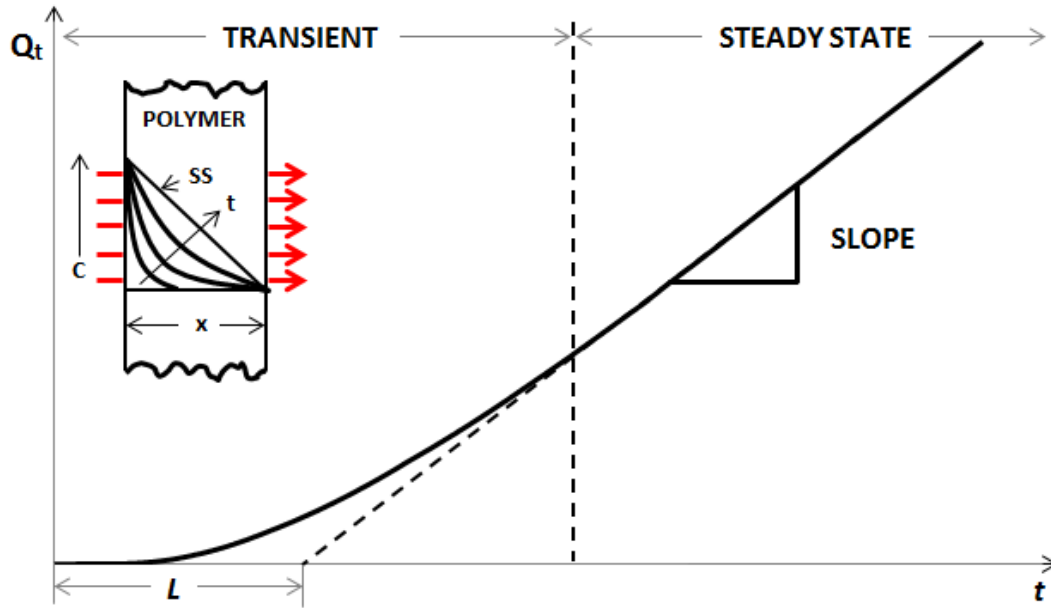


Figure 2.16. Graphical representation of the leakage of permeant for coefficient calculation in the time lag method [121].

## 2.8. Temperature Effects on Permeability Coefficients

Transport coefficients are inherently related to temperature, as has already been demonstrated by the effects of the glass transition temperature on free volume properties. An Arrhenius equation can be used to define a relationship between permeability, diffusion and solubility coefficients and temperature using a myriad of other factors [100, 127, 128]:

$$S = S_0 \exp\left(\frac{-\Delta H_s}{RT}\right) \quad (2.27)$$

$$D = D_0 \exp\left(\frac{-E_d}{RT}\right) \quad (2.28)$$

$$P = P_0 \exp\left(\frac{-E_p}{RT}\right) \quad (2.29)$$

where the pre-exponential terms  $S_0$ ,  $D_0$ , and  $P_0$  represent the limit values of their corresponding coefficients for an infinite molecular agitation (as  $T \rightarrow \infty$ ),  $R$  is the universal gas constant,  $T$  is the temperature,  $\Delta H_s$  is the heat of sorption,  $E_d$  is the activation energy of diffusion and  $E_p$  is the activation energy of permeation which is also equal to the algebraic sum of  $E_d$  and  $\Delta H_s$  [127, 128]:

$$E_p = E_d + \Delta H_s \quad (2.30)$$

These parameters are dependent upon the polymer morphology, including the crystal structure and the penetrant gas and polymer material characteristics [127]. The heat of sorption  $\Delta H_s$  can be equated to a two-step process via [100, 127]:

$$\Delta H_s = \Delta H_{condensation} + \Delta H_{mixing} \quad (2.31)$$

These steps involve the condensation of the gas molecule in the polymer,  $\Delta H_{condensation}$ , and the creation of a molecular scale gap,  $\Delta H_{mixing}$ , which holds the penetrant molecule [129]. For weak interactions between the gas molecule and the polymer, the change in enthalpy of mixing is positive, which leads to an increase in solubility coefficient as temperature increases. For condensable gases however the change in enthalpy of condensation is negative, such that solubility decreases with increasing temperature [100]. The gas activation term  $E_d$  is dependent on the size of the penetrant molecules with increases in temperature leading to increases in the diffusion coefficient [128]. These equations can be used to obtain the values for the activation energy and pre-exponential functions of each parameter, from the values at two different temperatures.

## 2.9. Heterogeneous Permeability

While Fick's Laws of Diffusion applies to mass flux through homogeneous membranes for steady and transient flow, the inclusion of air voids in polymers causes the materials to become heterogeneous in nature and therefore cannot be explained by this fundamental equation. It is for this reason that heterogeneous studies have been incorporated into mass diffusion studies by modelling the properties of both the continuous and dispersed phase to predict mass flow rates through the material.

A large amount of work has been conducted on the analysis of heterogeneous materials using predictive equations based on idealised models. These models have been used to predict the electrical resistance [130-133], elastic modulus [134] and heat transfer properties [135-139] of heterogeneous materials and have been applied directly to permeability studies [140-150] due to their analogous relationship with permeability. Most models use a resistance based approach and an idealised unit cell

to differentiate between the homogeneous matrix material and the dispersed heterogeneous phase, with predictions based on the relationship between the volume fraction of the dispersed phase, the particle shape and the permeability ratio of both materials.

### 2.9.1. Maxwell Model

The Maxwell model was one of the first models developed for analysing heterogeneous materials [130, 131]. It uses a resistance based approach to model the electrical potential and flux through a particulate filled composite and has been adapted to permeability studies for mass flux predictions [140-144]. The Maxwell equation uses intrinsic material properties to predict a relative permeability,  $P_r$ , which is defined by [144]:

$$P_r = \frac{P}{P_m} = \frac{1 + 2\Phi(\lambda_{dm} - 1)/(\lambda_{dm} + 2)}{1 - \Phi(\lambda_{dm} - 1)/(\lambda_{dm} + 2)} \quad (2.32)$$

where  $P$  is the permeability of the heterogeneous material,  $P_m$  is the permeability of the matrix material,  $\Phi$  is the volume fraction of dispersed particles in the matrix and  $\lambda_{dm}$  is the permeability ratio between the dispersed phase  $P_d$  and matrix phase  $P_m$ . The Maxwell model provides a good approximation for the permeability of heterogeneous materials at lower volume fractions ( $\Phi < 0.2$ ) but does not take account of the particle shape (assumes spherical particles) and the maximum packing limit of particles and so its accuracy is compromised at higher volume fractions [142-144].

### 2.9.2. Bruggeman Model

The Bruggeman model [132] was developed to predict dielectric constants for particulate filled composites, and has been adapted to permeability studies to predict the heterogeneous permeability via Eq. 2.33 using the same factors as defined in the Maxwell model [132, 144]:

$$(P_r)^{1/3} \left[ \frac{\lambda_{dm} - 1}{\lambda_{dm} - P_r} \right] = (1 - \Phi)^{-1} \quad (2.33)$$

While this provides a similar approximation to the Maxwell model, it deviates from it by altering the treatment of the volume fraction and is more accurate than the

Maxwell model at higher volume fractions. However it still does not account for particle size and shape and the form of the equation means that numerical methods must be employed to determine the relative permeability as this value is not a single entity in the equation [144].

### 2.9.3. Lewis-Nielsen Model

The Lewis Nielsen model was originally developed to estimate the elastic modulus of particulate filled composites [134] and then applied directly to studies of thermal and electrical properties of particulate filled composites [135] but has since been applied to permeability studies due to the analogous relationship between Fourier and Fick's Laws to predict the heterogeneous permeability via [143, 144]:

$$P = \left[ \frac{1 + 2((\lambda_{dm} - 1)/(\lambda_{dm} + 2))\Phi}{1 - ((\lambda_{dm} - 1)/(\lambda_{dm} + 2))\Phi\psi} \right] \quad (2.34)$$

$$\psi = 1 + \left( \frac{1 - \phi_m}{\phi_m^2} \right) \quad (2.35)$$

The Lewis Nielsen model deviates from those previously mentioned through the use of a maximum packing volume,  $\phi_m$ . This defines the maximum amount of particles which can be held in the heterogeneous material ( $\approx 0.66$  for spherical particles) and uses the calculation of the packing volume fraction,  $\psi$ , to incorporate this value into the equation. This sets a maximum limit for the inclusion of particles in the material and so is more accurate for higher volume fractions but it reduces to the Maxwell model when  $\phi_m = 1$  [142-145].

### 2.9.4. Felske Model

The Felske model is another predictive model which focuses on the thermal conductivity of a core shell particle in a composite matrix [136] and has been applied to permeability studies for mass flux predictions via [144]:

$$P_r = \frac{P}{P_m} = \frac{2(1 - \Phi) + (1 + 2\Phi)(\beta/\gamma)}{(2 + \Phi) + (1 - \Phi)(\beta/\gamma)} \quad (2.36)$$

$$\beta = (2 + \delta^3)\lambda_{dm} - 2(1 - \delta^3)\lambda_{lm} \quad (2.37)$$

$$\gamma = (1 + 2\delta^3) - 1(1 - \delta^3)\lambda_{dl} \quad (2.38)$$

Where  $\lambda_{lm}$  is the permeability ratio between the intermediary phase,  $I$ , and the matrix phase,  $m$ ,  $\lambda_{dl}$  is the permeability ratio between the dispersed phase,  $d$ , and the intermediary phase  $I$ ,  $\delta$  is the ratio of radii between the intermediary layer and core layer and all other values are as previously defined.

It individualises itself from previously mentioned models with the inclusion of an intermediary region around the dispersed particle which adds an extra layer of control in modelling a contact resistance or intermediary zone between the dispersed particles and matrix phases. It reduces to the Maxwell model when  $\delta = 1$  and so has similar limitations in the sense that it does not take account of the maximum packing volume and so is only accurate at low volume fractions [142-145].

### **2.9.5. Modified Models and Resistance Models**

While the models mentioned previously usually form the basis for heterogeneous permeability studies, these models have been expanded over time to include extra functionality and to eliminate some of their weaknesses with the addition of the maximum packing volume and particle shape parameters. Pal, who has conducted extensive work in modifying permeability models [133, 137, 144], and others [145-150] have used them to predict properties in heterogeneous materials with excellent correlation between experimental and theoretical data. Computer simulations mapping mass flux through dual phase materials have also been integrated into heterogeneous studies due to the increased utilisation of modelling software to determine the effects of randomisation on the dispersed phase and the overall permeability [64, 151]. It is with this in mind that finite element analyses of heterogeneous materials will be undertaken in the current work.

## **2.10. Polymer Permeability**

### **2.10.1. Penetrant Gas**

The choice of penetrant test gas is limited as the qualification of COPVs is stringently curtailed to be consistent with the envisaged application of the COPV. The desired storage of hydrogen in the present study is significantly hampered by the size of the  $H_2$  molecule, as smaller penetrants equate to larger diffusion coefficients

and hence higher permeation rates [152-155] and so the storage of fuels in COPVs is directly dependent on the size of the penetrant molecule.

While the desired applications for the COPVs designed here is the storage of liquid hydrogen, all permeability testing and qualification of liner materials will be conducted with a helium test gas. This is because hydrogen gas is highly flammable and so is dangerous to use or store in the testing apparatus. Helium has been used as a substitute test gas due to its inert qualities, which mitigate the risk of fires (although in enclosed spaces it can cause asphyxiation so proper ventilation is needed) and, more importantly, due to its comparable molecular size to that of hydrogen as shown in Table 2.1 [156-158].

*Table 2.1. Molecular diameter comparison of helium and hydrogen [158].*

Type of Gas	Molecular diameter (cm)		
	From Viscosity	From van der Waal's equation	From heat conductivity
Helium	$1.9 \times 10^{-8}$	$2.6 \times 10^{-8}$	$2.3 \times 10^{-8}$
Hydrogen	$2.4 \times 10^{-8}$	$2.3 \times 10^{-8}$	$2.3 \times 10^{-8}$

The comparable molecular size allows for helium permeation tests to be compared to hydrogen permeation tests with most cases showing that helium has a higher permeation rate than that of hydrogen [31, 159]. However, the issue with these comparisons is that, although the molecular size of helium is comparable, hydrogen still has a higher solubility coefficient in some polymer materials [160] which could lead to higher leak rates in the final COPV design.

Testing of composite panels with helium and hydrogen by Goetz [31] showed that the permeability of both gases in the same test sample was equivalent with both gases exhibiting similar permeation rates. While the hydrogen test gas did not always have the highest permeation rates (samples 1, 4 and 5 specifically in Fig. 2.17), on average helium has a higher permeation rate (average of  $17 \times 10^{-7}$  scc.m/m<sup>2</sup>sbar) of almost four times that of the hydrogen test gas (average of  $4.4 \times 10^{-7}$  scc.m/m<sup>2</sup>sbar).

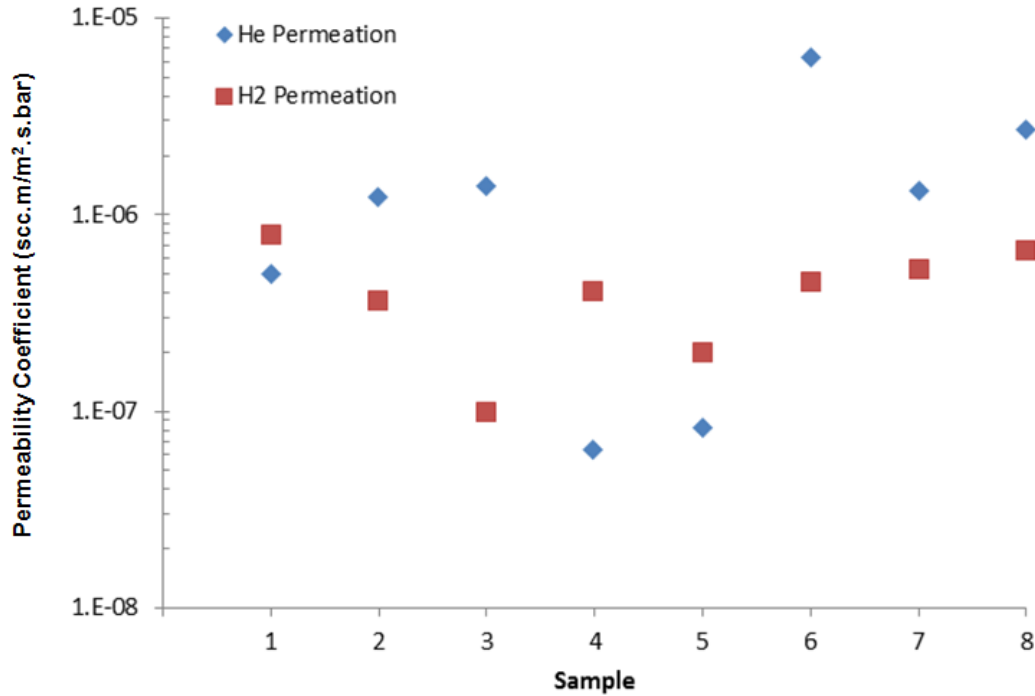


Figure 2.17. Permeability coefficient results for multiple graphite epoxy composite samples tested with both helium and hydrogen test gases [31, 121].

### 2.10.2. Allowable Leak Rates

The testing of leak rates through COPVs is important to limit permeation through the tank wall and to ensure proper storage of the fuel. An amount of fuel will permeate through the COPV, regardless of the precautions or system implemented, and the challenge is to quantify the allowable leak rate through the tank wall. This is quite difficult to accomplish on a broad scale as allowable leak rates vary with COPV applications, architecture (surface area and size), location and mission specific issues. The failure of the X-33 composite hydrogen tank [31] due to debonding from LH2 leakage was one of the main drivers behind research into allowable leak rates of hydrogen for mission specific applications.

The issues associated with the differences in allowable permeation rates of hydrogen have been addressed by an analysis of the amount of acceptable loss of fuel, set at 0.25% of the total volume, prior to flight engagement [161, 162]. Robinson has given estimations of the allowable leak rate for different tank configurations, with limited data, where most calculations show that the acceptable leak rate was above that previously stated as the maximum allowable by industry partners [161, 162]. It

has been reported by a number of authors that the minimum percentage of hydrogen in air that is flammable is 4%, with detonation occurring at the higher percentage of around 20% where by ignition causes propagation of the flame throughout the hydrogen mixture and can result in catastrophic failure [163-165]. Robinson has shown through test cases that the likelihood of achieving a hazardous mixture in tank structures is quite low and risks can be mitigated through small changes in operating procedures and analysis of allowable leak rates based on the surface area of tank structures [161,162].

### **2.10.3. Low Permeability Polymers**

The use of polymer materials as COPV liner materials is linked to the initial failings of the aforementioned X-33 composite cryogenic tank and is demonstrated by some of the initial work following these failures, in identifying polymer liner materials for mitigating permeation in composite tanks. A large amount of work has been conducted on the permeability testing of composite materials, with most of this work centred on increased permeability due to microcracks forming in the laminates, as a result of the mismatch of thermal expansion coefficients in the matrix under thermal cycling conditions [31, 156, 157, 166-170].

Grimsley [171] was one of the first to start this work by testing PET (polyethylene terephthalate), polyimides, liquid crystal polymers and lined composite materials with argon gas. While the PET was coated with a layer of aluminium in a vapor deposition process, the results obtained were still encouraging as the polyimide films also exhibited low permeability characteristics. This initial work was followed by that of Herring [172] who tested the helium permeability of polyimides, polyesters, polyvinyl fluorides, and polyurethanes for low permeability cryogenic liner applications. The fluoropolymer materials displayed the lowest permeability of all materials tested and also performed well under subsequent mechanical analysis testing [172].

Significant work has been conducted by other authors in testing helium and hydrogen permeabilities of prospective polymer liner materials in other areas of industry including oil and gas piping (PE, PA11, PVDF) [173], silicon wafer production (PEEK, PFA, PTFE) [174-176], and the medical device industry (PEEK) [177] as outlined in Table 2.2.

Table 2.2. Permeability coefficients for polymer materials from literature [173-177].

Material	Gas	Temp. (°C)	Pressure (bar)	Thickness (mm)	P ( $10^{-7}$ scc/m.s.bar)	Ref.
LDPE	He	41	40	1.81	64	[173]
MDPE	He	41	100	1.93	28	[173]
HDPE	He	40	100	2.11	19	[173]
PA11	He	41	40	1.87	21	[173]
PVDF	He	41	100	2.1	14	[174]
PFA	H <sub>2</sub>	25	2-6	0.13	920	[174]
PFA/PTFE	H <sub>2</sub>	25	2-6	0.13	510-1200	[175]
PEEK	H <sub>2</sub>	25	2-6	0.13	87-102	[176]
PEEK	He/Ar	N/A	0.4	0.25	25-50 x $10^5$	[177]

#### 2.10.4. Polymer Liners in COPVs

While these initial results are encouraging for polymer liner adoption in future COPV architectures, a number of industry partners have already commenced the production and testing of polymer-lined COPVs, Fig. 2.18. Airbus Defence and Space (formerly known as EADS ST) have designed and constructed a 300 L helium tank with a thermoplastic liner to replace the standard titanium lined tank for the ARIANE 5 launcher [178]. This new technology aimed to reduce costs and lead times significantly, with a total savings of 30% over previous tank models. It utilised a blow injection moulding process with a preformed thermoplastic material to produce liners for overwrapping with a tape placed composite. Lead times were significantly reduced by up to 60%, with the tank demonstration tests operating at 400 bar and leakage below  $5 \times 10^{-3}$  scc/s, proving the tank as a viable storage option for cryogenic fuels aboard future missions [179].

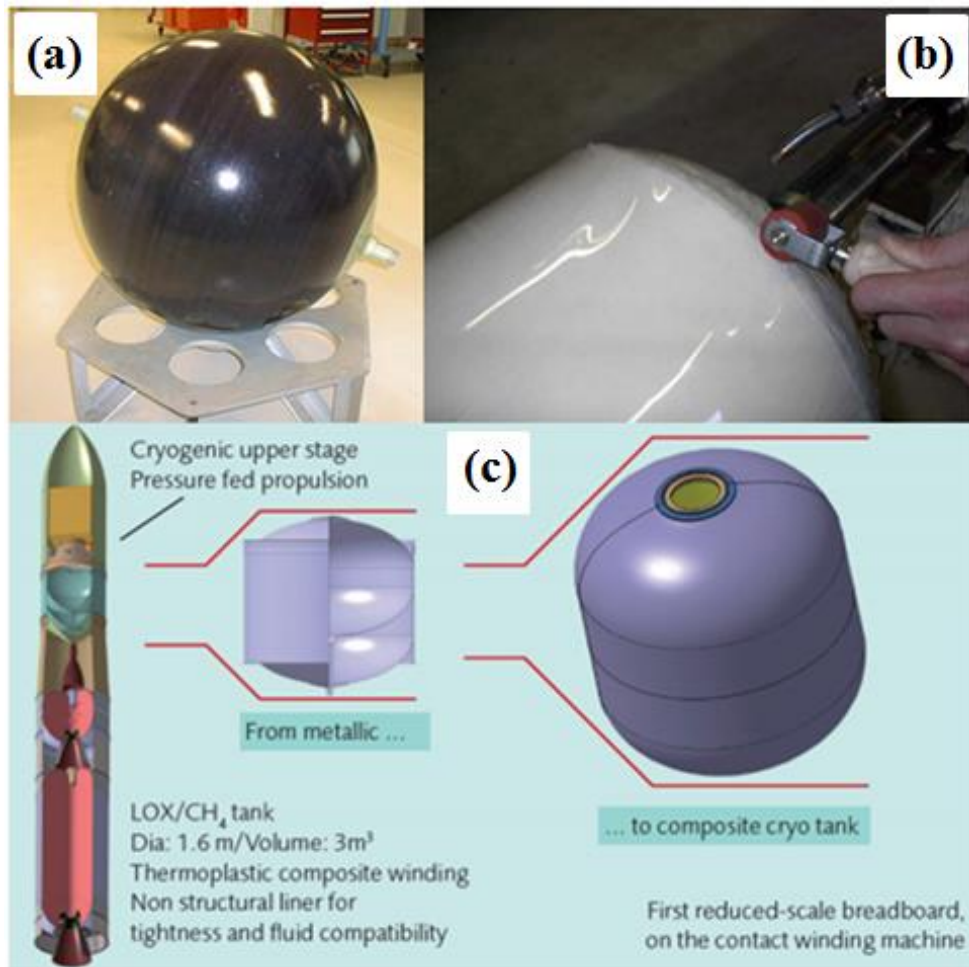


Figure 2.18. Images of (a) the 300 L thermoplastic lined COPV manufactured by EADS ST [178, 179], (b) the thermal welding of the fluoropolymer liner by AVIO [180], and (c) the envisaged usage of polymer materials by Astrium ST in the upper stage of a future launch structure [181].

AVIO, an Italian based manufacturing company, have also endeavoured to develop polymer lined cryogenic fuel tanks. They conducted extensive research into prospective liner materials including silicon rubbers and fluoropolymers. Fluoropolymers were shown to exhibit enhanced barrier properties with an ETFE grade demonstrating a sufficient operational temperature range making it the ideal choice for the liner material [180]. A small tank structure was thermally welded together and then overwrapped with a tape placed composite with subsequent tests carried out on the effectiveness of the tank as a LOX storage unit.

The subsequent testing of these tanks encountered a number of issues with tanks being damaged due to improper handling before testing and bursting of the structure

during testing after a number of cryogenic cycles. While this is a concern for the tank structure design, the liner itself met all barrier requirements and so was a positive outcome for polymer materials in low permeability applications [180].

Following on from initial work carried out by EADS ST in 2003, Astrium ST (now Airbus Defence and Space) also continued researching viable polymer materials for liner applications. Claudel et al. [181] investigated a number of polymer materials for barrier properties to gaseous helium in an effort to identify a possible liner material for large scale tanks with volumes ranging from 3 to 5 m<sup>3</sup> for the next generation of space launchers. Polymer materials identified throughout this research included liquid crystal polymers, nylons and fluoropolymers which exhibited low permeation properties to gaseous helium [181].

## **2.11. Laser Assisted Tape Placement (LATP)**

Laser Assisted Tape Placement (LATP) is an innovative manufacturing method that utilises a robotic arm and an infrared laser welder to apply a thermoplastic composite tape onto a tool surface. It benefits from in-situ consolidation of the composite tape as it is applied, removing the need for post-autoclave processing and decreasing the cost of part formation. It can be used to make a variety of shapes including flat plates, square, rectangular and cylindrical sections using a rotating mandrel and the continuous winding of the tape onto a predefined surface.

The process works using four distinct phases as indicated in Fig. 2.19, and includes (a) irradiation of the substrate with the laser, (b) the creation of a shadow region under the roller, (c) the consolidation of the heated tape to the substrate and finally (d) the post consolidation and cooling of the tape [182, 183]. The laser moves ahead of the tape and heats the already-laid tape surface to the required processing temperature. The tape is then immediately placed down over the heated area to form a bond between the already-laid tape and the incoming tape through the melted layer. A roller then presses over the tape to ensure consolidation and proper bonding of the tape to the already-laid tape material. The tape placement happens at about 8-12 m/min [183, 184] and so the process is quite rapid and equivalent to comparative automated tape placement methods such as hot gas heating and infrared lamp heating (3-9 m/min) [185-187].

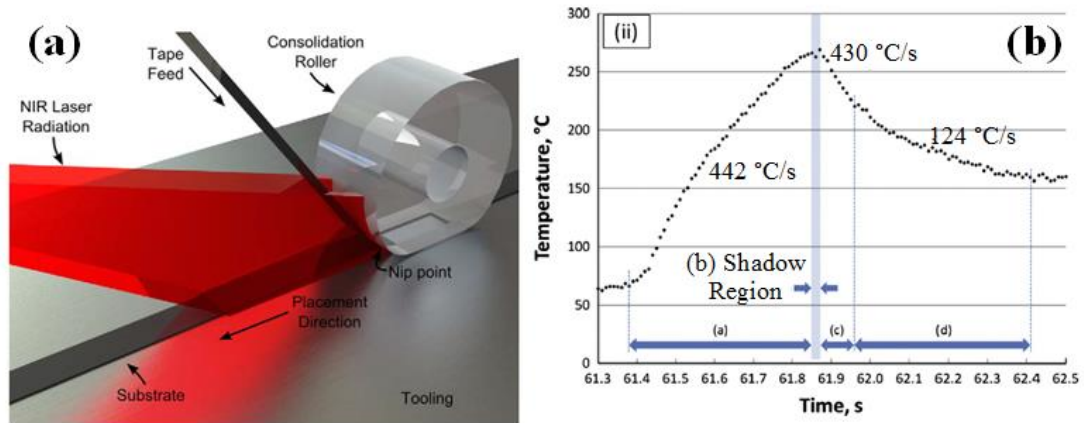


Figure 2.19. Overview of (a) the physical process and (b) the steps in the laser assisted ATP process based on temperature [182, 183].

A number of processing variables affect the quality of parts made, including laser power, laser angle, roller pressure, tool temperature, lay-down speed and roller temperature [183, 184]. While some previous research in L-ATP forming methods has been conducted some decades ago [188, 189], a renewed emphasis on L-ATP methods has emerged in recent years with a focus on fracture testing of Suprem IM7 CF/PEEK composites [183, 184] and thermal process modelling [182, 189-192] at the forefront. The main barrier to L-ATP acceptance has been the relatively poor mechanical performance of the tape-laid materials when compared to autoclave samples. Many authors concede that improvements in pre-preg properties and processing parameters are needed to achieve similar mechanical properties to autoclave samples [183]. Specific differences in void content and crystallinity percentages are highlighted as the main factors governing the difference in L-ATP and autoclave characteristics, with a drive towards process optimization to achieve a better balance in L-ATP characteristics [183, 184].

# 3. Materials & Methods

## 3.1. Chapter Overview

This chapter gives an overview of the materials and experimental methods used. This includes the material selection process, along with the properties of the as-delivered materials. The characterisation methods used to analyse these materials for rotational moulding suitability are also described. The methods used to form all samples are also covered in detail with the differences in material properties for each forming method included. Finally, the testing methods used throughout this project, including permeability testing, cryogenic cycling and microscopy techniques, are explained with reference to the relevant standards.

## 3.2. Polymer Liner Material Characterisation

The material selection process followed a number of criteria for identifying polymers for a low permeability liner. Methods used to highlight prospective materials included published literature and recent industrial research projects, with a number of factors being considered in selecting materials for preliminary testing, including;

- Quoted permeability values
- Availability in powder form
- Operating temperature range
- Resistance to rapid temperature change
- Multilayer compatibility
- Overwrapping compatibility

All materials chosen as part of this study are thermoplastic materials which meet a number of these requirements as shown in Table 3.1 and Table 3.2. An overview of their properties and background is given in Section 3.3.

### 3.3. Polymer Materials Selected

*Table 3.1. Materials selected for low permeability characteristics.*

Material	Supplier	Identifier	Particle Size ( $\mu\text{m}$ )	Density ( $\text{g}/\text{cm}^3$ )
PEEK	Victrex	150P	700	1.30
PEEK	Victrex	150PF	50	1.30
PEEK	Evonik	1000P	500	1.30
PEEK	Evonik	2000P	500	1.30
PA11	Matrix Polymers	Roto 11	300	1.05
PA12	Matrix Polymers	950TLD	300	1.01
PVDF	Matrix Polymers	2850	300	1.71

*Table 3.2. Melt flow properties of polymer materials tested within this thesis.*

Material	Melt Volume Flow Rate ( $\text{cm}^3/10 \text{ min}$ )	Melt Viscosity (Pa.s)	Average $M_w$ (g/mol)
150P	N/A	130 (400 °C, ISO 11443 [193])	23000-30000 [194,195]
150PF	N/A	130 (400 °C, ISO 11443 [196])	N/A
1000P	140 (380 °C/5 kg, ISO 1133 [197])	100-3000 (400 °C/shear of $1 \text{ sec}^{-1}$ [198])	>30000 [199]
2000P	70 (380 °C/5 kg, ISO 1133 [200])	100-3000 (400 °C/shear of $1 \text{ sec}^{-1}$ [198])	>30000 [199]

*Note: Melt flow properties of PA11, PA12 and PVDF could not be found in the literature.*

### **3.3.1. Polyetheretherketone (PEEK)**

PEEK is a high performance thermoplastic polymer material from the polyaryletherketone family [201, 202]. It has a semi-crystalline structure and exhibits superior mechanical properties due to its benzene ring backbone [201, 202]. PEEK materials suit applications in high temperature environments with a melt temperature of approximately 340 °C [193-200] lending PEEK materials to applications in aerospace and automotive industries [201, 202]. Four different grades of PEEK have been analysed, 150P and 150PF from Victrex [193, 196], and 1000P and 2000P from Evonik [197, 200]. These materials were chosen on the basis that they provide a range of values of characteristic properties including melt flow index, quoted average particle size and differing mechanical properties. PEEK is not available commercially as a rotomoulding grade (as the market for rotomoulded PEEK products is quite small) and so the quoted materials were assessed for their viability as rotomoulding materials for a low permeability liner.

### **3.3.2. Polyamides (PA)**

Polyamides are materials that include the amide (-CONH-) in their repeating unit structure and are also referred to as Nylons [201, 202]. They are crystalline polymers characterised by their high strength, good impact properties and low abrasiveness [201, 202]. Different grades of Nylon are distinguished by the number of carbon atoms in their repeating unit structure. In the present study Nylon 11 and Nylon 12 (PA11 and PA12) have been selected as low permeability liner materials with specific rotomoulding grades supplied for each by Matrix Polymers [203, 204].

### **3.3.3. Fluoropolymers**

Fluoropolymers are a class of polymer which contain a fluorine element in their repeating unit structure. They are known for their high chemical resistance and low friction coefficients finding significant use as liner materials for chemical storage, corrosion resistant coatings in harsh environments and low friction linings in bearings experiencing excessive fretting [201]. The current project has tested the viability of polyvinylidene fluoride (PVDF) as a liner material as it was readily available in powder form and was the subject of previous research showing low permeability properties to helium diffusion. The PVDF material tested here has was

supplied by Matrix Polymers and is based on their rotomoulding grade of PVDF known as Explore PVDF 2850 [205].

### **3.3.4. Polyvinylchloride (PVC)**

Polyvinylchloride has not been chosen as a liner material but it has been used in calibration experiments between the two permeability test methods used in this project. Constructed from the repeating vinyl chloride unit,  $-(\text{CH}_2\text{-CHCl})_n-$ , PVC is an amorphous polymer material with low crystallinity percentage exhibiting good flame retardancy characteristics and suitability for applications in piping and cable shielding operations [201]. The PVC used here has been supplied by ENSIGNER and is classified as TECAVINYL PVC [206]. It was purchased in sheet form with a nominal thickness of 1 mm and was cut to size for each permeability test method.

## **3.4. Composite Materials Tested**

### **3.4.1. Suprem IM7**

Suprem IM7 is a unidirectional composite with a single tow of impregnated fibres. The composite consists of a PEEK matrix (Victrex 150UF10) with a carbon fibre reinforcement (Hexcel HS-CP-5000-IM7). The matrix/reinforcement ratio is 40/60% respectively by volume and 33/67% respectively by weight. The tape has a nominal thickness of 0.12-0.18 mm and is usually supplied in spools up to 150 mm in width [207]. The tape is cut to produce parts to the required size and angular cuts can be introduced to produce laminates of varying layup directions and mechanical properties. The tape has also been supplied in thinner widths of 13-14 mm for laser assisted automated tape placement. While the material properties for both the spool and the LATP tape are similar, the autoclave and LATP forming process produces significant part variance as explained in Chapter 2 and so both methods are tested for completeness and reproducibility.

## **3.5. Specimen Manufacture**

A number of manufacturing methods have been used throughout this project for specimen manufacturing. The majority of manufacturing has taken place in ÉireComposites using their hot plate, rotomoulding and autoclave facilities with subsequent tape placement work being carried out in the Irish Centre for Composites

Research (ICOMP) at the University of Limerick (UL). The following section describes these manufacturing processes and the reasons for their use along with their differences and intricacies.

### 3.5.1. Hot Plate Formation

Hot plate formation is a small scale manufacturing method for flat specimen production. As an alternative to manufacturing large rotomoulded parts, the hot plate produces smaller flat samples with properties similar to rotomoulding production methods [65, 71]. The hot plate consists of a flat metal surface which has a heating system embedded beneath the plate. Fig. 3.1 shows the powder polymer placed on the surface of the plate within a metal collar, with an aluminium sheath placed over the powder to protect the powder surface from contaminants.

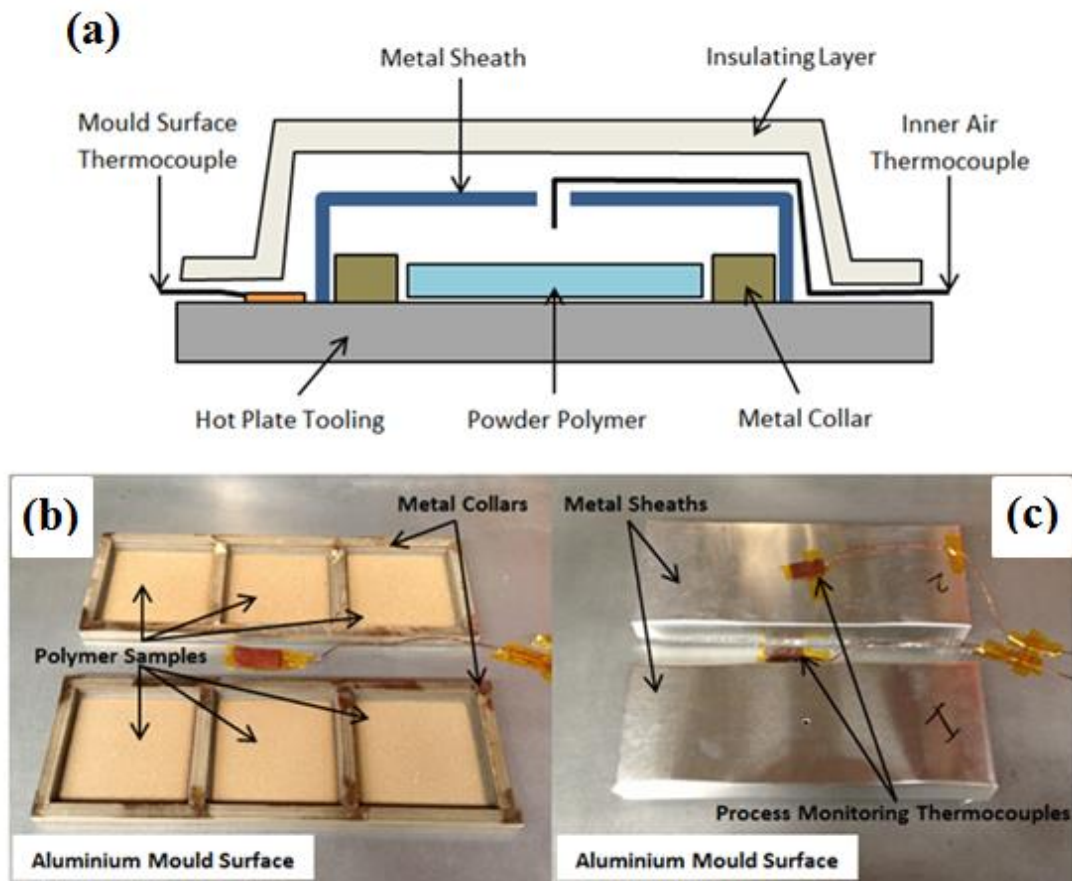
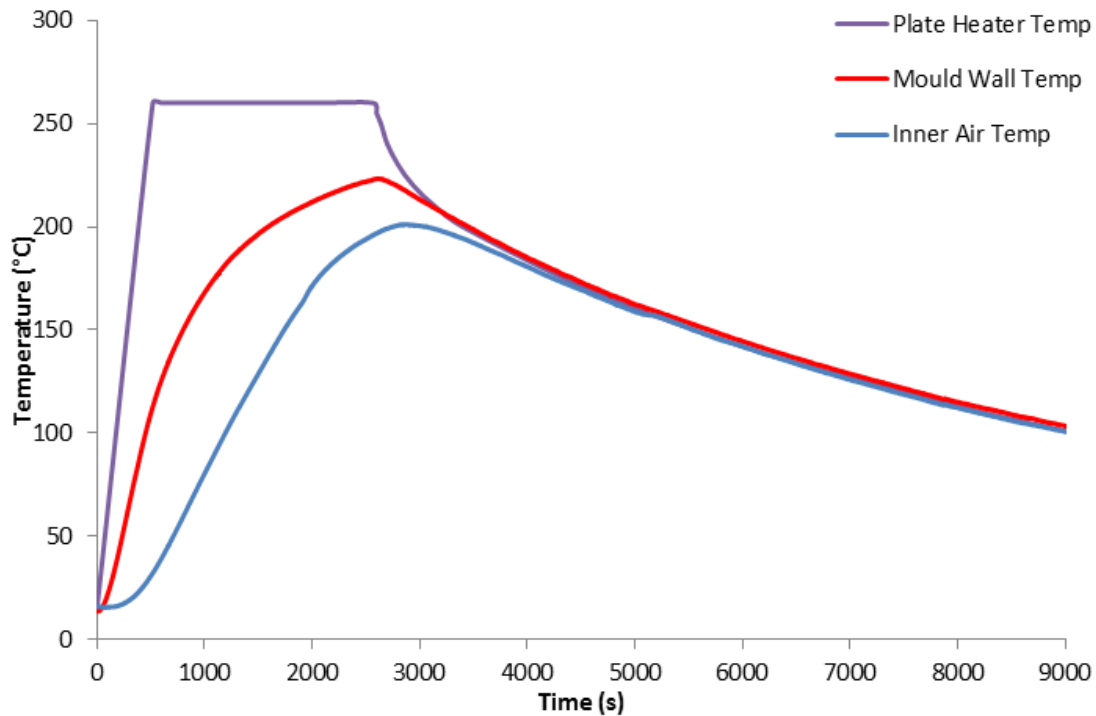


Figure 3.1. Hot plate apparatus for polymer sheet formation consisting of (a) an overview of the manufacturing layout, (b) and an image of the metal collar sample makers and (c) the aluminium sheaths surrounding them.

The heating system melts the powder where it is in contact with the mould surface. This melting polymer at the mould wall contact point creates a moving front which propagates slowly up through the powder, melting the powder particles and causing them to coalesce together forming a molten melt. A typical thermal heating cycle is shown in Fig. 3.2 where the temperature of the plate is held above the melting temperature of the polymer for a set period of time and then disengaged to allow the molten melt to cool and solidify. This processing method creates air voids within the part due to the lack of applied pressure on the powder particles. This by-product of hot plate formation was used to generate different void distributions in the part wall to analyse the effects of void dispersions on permeability, as the forming parameters directly affect void contents [64, 70].



*Figure 3.2. Typical thermal heating cycle for the hot plate apparatus showing the set temperature, the mould wall temperature and inner circulating air temperature for a PA11 Sample.*

### 3.5.2. Rotomoulding

Two different rotomoulding moulds were used throughout this project for part formation. The first was a rotomoulding tool fabricated by ÉireComposites for a previous project using an integrally heated mould tool and a resin based hold system.

This tooling created box shaped parts with flat sides for sample extraction and testing in a myriad of test programmes, specifically those tests in Chapter 5. The second tool used for part production was fabricated for this research project and produced a varied shape consisting of flat, cylindrical and dome regions for part analysis. The tooling utilised segregated heating lines so that the temperature distribution across the tool could be controlled giving equal heating throughout the part. This tooling will be described in detail in Chapter 6, with an analysis of the tooling using thermal imaging and demonstrator part production included.

### 3.5.3. Autoclave Manufacture

Flat panel composite samples were formed using an autoclave process under the application of heat and pressure. The composite sheets were laid up in the desired pattern with sheets being cut from the Suprem IM7 material and tacked together using a welding gun. The welding gun melts the plastic in the composite layer and ensures the laminates remain in the defined configuration and orientation during consolidation.

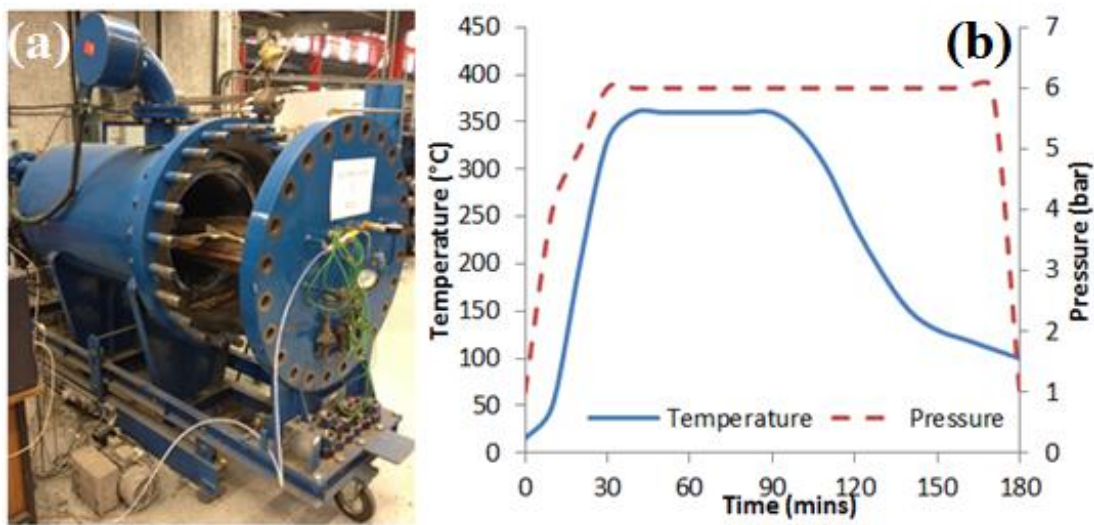


Figure 3.3. (a) ÉireComposites' autoclave along with (b) the typical temperature and pressure trace experienced by the laminate during the manufacturing process.

Once the laminate is laid up it is transferred to the forming plate. A release film is placed on the bottom of the laminate and then sealant tape is placed along the laminates edge to ensure leakage of the polymer matrix does not occur due to the applied pressure and heating of the autoclave process. A second release film is then

placed on top of the laminate followed by a rubber caul sheet and breather layer. Then a vacuum bag is placed over the entire plate and the vacuum is applied to consolidate the laminate. The caul sheet creates a smooth surface finish on the top of the laminate as the applied vacuum and pressure hold the caul sheet against the laminate surface. The breather layer ensures the vacuum can travel throughout the part as its thin fibrous structure allows gas to pass through it with ease. The final bagging allows for the entire part to be placed under a vacuum and helps consolidation of the part.

The consolidated part is then transferred to the autoclave where the composite plate is heated and subject to pressure to form a consolidated laminate [208, 209]. The heat melts the polymer matrix while the pressure consolidates the part forming a strong composite structure. A typical trace for the applied pressure and heating is shown in Fig 3.3 along with the autoclave used in ÉireComposites, which consists of a 0.6 m diameter by 1.2 m deep experimental autoclave with the ability to apply a pressure of up to 20 bar and temperatures close to 450°C. The process usually lasts three hours and includes a 30 minute ramp to the hold temperature, a 60 minute hold at the set forming temperature and then a 90 minute cool down to atmospheric conditions.

### **3.5.4. Laser Assisted Tape Placement Formation**

Laser assisted automated tape placement uses a robotic arm, a laser welding head and a wheel-fed strip of thin composite tape. Unlike the larger Suprem IM7 sheets, this process uses a thin 13-14 mm wide tape that is built up in multiple passes and layers to create a finished part of the desired shape, size and orientation. Fig. 3.4 shows some of the part geometries achievable using the LATP process with flat parts manufactured directly on to a mould tooling surface or cylindrical parts manufactured in a filament winding process.

The LATP unit used for the production of parts here consisted of a robotic arm (KUKA KR 180 R2900) with six axes of motion. Two additional axes of motion can be supplied by a winding spindle and a rotary table for holding the mandrel of the desired part shape. The tape heating is assisted through the use of a laser-line diode laser module (LDM) 3000 W system (supplied by Advanced Fibre Placement Technology (AFTP) GmbH). The required design parameters for the part are pre-

recorded and the software is used to produce the part of the required size, orientation and thickness.

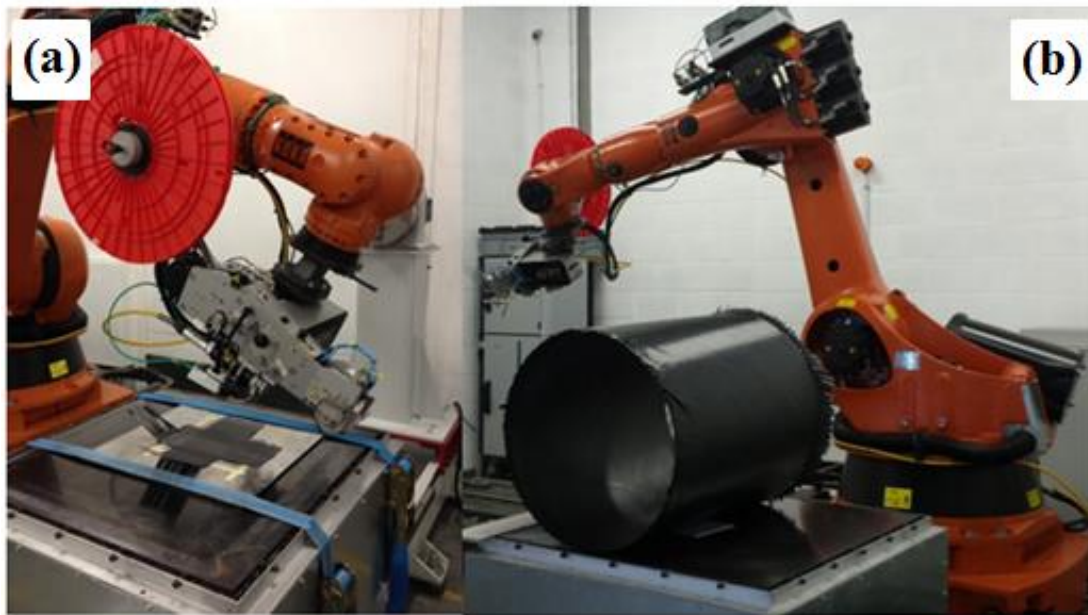


*Figure 3.4. Laser assisted automated tape placement of (a) flat and (b) cylindrical components with tooling in the ICOMP centre in UL.*

*Table 3.3. Parameters for Laser-Assisted ATP for composite tape-placement.*

Parameter	Consolidation Tests	Cryogenic Tests
Lay-up	[0]	[0/90/0/90] <sub>s</sub>
Lay-down speed (m/min)	12	12
Material Temperature (°C)	380	380
Tool Temperature (°C)	Unheated	Unheated
Roller Material	Silicone	Silicone
Roller Cooler Pressure (Bar)	6	6
Roller Pressure (Bar)	2.5 - 4.5	4.5

Layers are built up over time with repeated tape placement using the laser head to form a single layer of the given orientation and then altering the orientation to create the next layer on top of the pre-existing layer. In this way lay ups of differing

## Materials & Methods

orientations can be produced and so different properties can be imparted on the composite layup. Part consistency is heavily dependent upon parameter setting and so Table 3.3 has outlined the standard parameters used for part production in this thesis.

For tape-placement on polymer liner materials, a mild steel plate was used to accommodate the run in and run off of the LATP process as it takes a nominal length of 150 mm of tape for the processing conditions to reach equilibrium conditions before the process becomes uniform. The steel plate, 500 mm  $\times$  500 mm  $\times$  5 mm and pictured in Fig. 3.5, acts as a picture frame for the polymer sheet (nominal dimensions of 140 mm  $\times$  140 mm  $\times$  5 mm) and allows for uniform tape-placement over the polymer sample, without introducing unnecessary height variance between the 140 mm  $\times$  140 mm samples and the laser welder/consolidation roller, to mitigate the subsequent formation of defects.

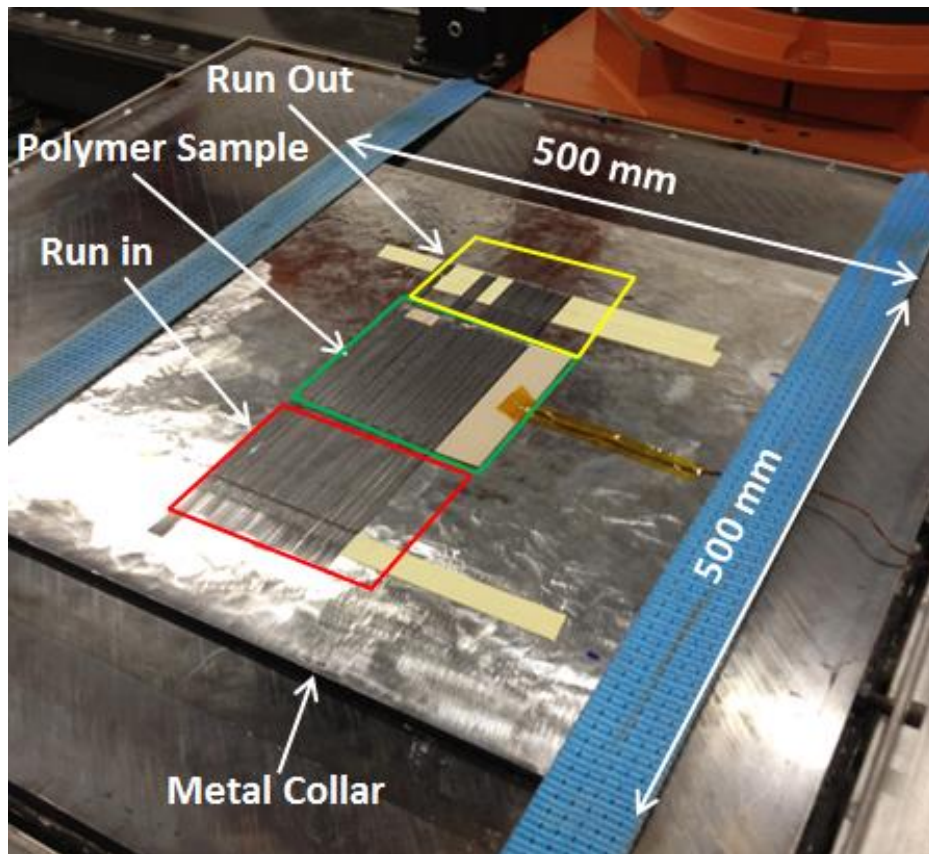


*Figure 3.5 Metal collar for the LATP process to account for run in and run off over the polymer sample.*

## **3.6. Test Methods**

A number of test methods have been employed to characterise materials throughout this thesis. These characterisation tests have been completed in conjunction with permeability tests, cryogenic cycling tests, X-ray CT scanning operations and nano-indentation tests. The differences between the permeability test methods used have also been outlined along with the methods used to calculate permeability results.

### **3.6.1. Powder Characterisation Techniques**

#### ***3.6.1.1. Sieve Testing***

Sieve testing was used to analyse the particle size distribution of the powder polymer materials tested and to determine the average particle size. Sieve testing involves the use of increasingly finer sieves and a shaker table to determine a powder's size distribution. Following ASTM D1921-12 [210], each sieve is weighed prior to testing to determine its initial (unloaded) weight. The sieves are then stacked as shown in Fig. 3.6 with the coarsest mesh on top and the collection pan on the bottom below the finest sieve. The sieves used here, in order of descending size, were 3.35 mm, 2.00 mm, 1.18 mm, 0.60 mm, 0.425 mm, 0.30 mm, 0.212 mm, 0.15 mm, 0.063 mm and, finally, the collection pan for anything below 0.063 mm in size.

An amount of powder (approximately 100 g) is then weighed, recorded, and fed into the top sieve which is closed when all of the powder has been fed into the top of the stack. The entire stack is then placed on a rotary shaking table which imparts a rotational tapping motion to the sieves and causes the powder particles to filter through the sieves. When the sieve size becomes so small that the particles can no longer pass through, they are retained in that sieve until the end of the test. The shaker table is engaged for 10 minutes and upon completion, the pans are removed and individually weighed again.

The net weight of material retained on each sieve is determined by subtracting the initial sieve weight from the final sieve weight. The particle size distribution is calculated by dividing the net weight of material retained on each sieve by the initial amount of powder placed in the sieve. This gives a percentage of powder material passing for each sieve used in the test and can be used to output a graph such as that

in Fig. 3.6 to demonstrate the particle size distribution. The mean particle size  $D_m$  is then determined as follows:

$$D_m = \sum (P_i \times D_i) \quad (3.1)$$

where  $P_i$  is the percentage of material retained on the sieve and  $D_i$  is the average particle size of material retained on the sieve.  $D_i$  is calculated by adding the nominal opening size of the current sieve to the nominal opening size of the sieve above it and dividing by two. Hence the mean particle size can be calculated by summing the product of the percentage of material retained by each sieve by its corresponding nominal opening size. This information can then be used to gauge the suitability of a polymer powder for rotational moulding operations [211] and the probability of it successfully producing consistent parts.

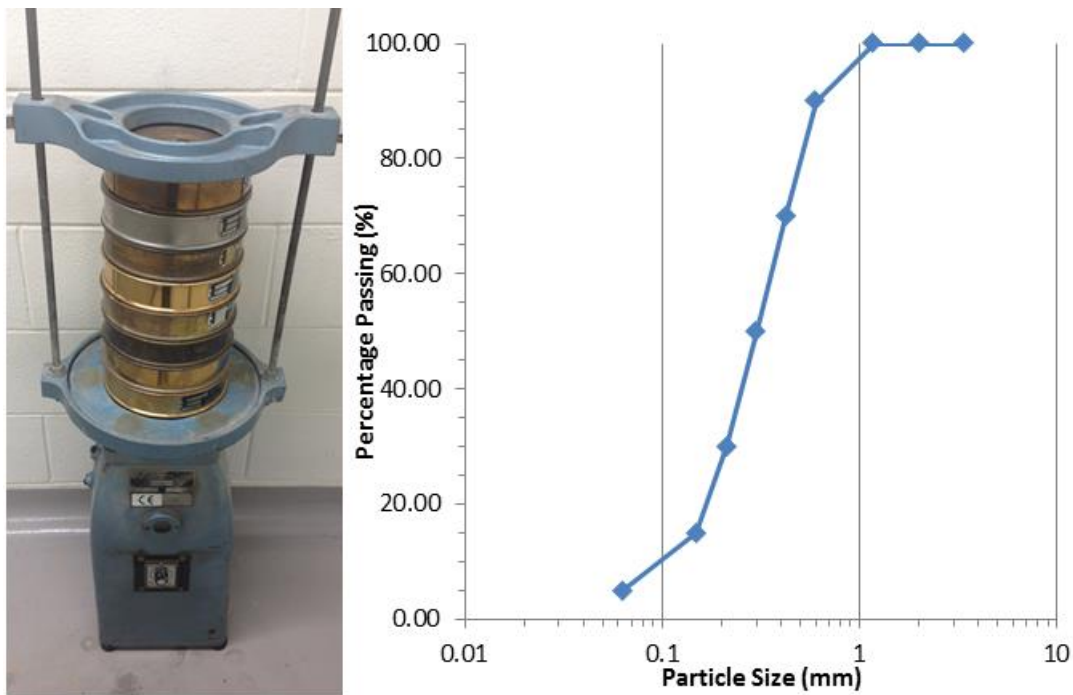


*Figure 3.6. Test apparatus for the sieve testing along with the standard graph output showing the percentage powder passing based on sieve size.*

### **3.6.1.2. Optical Microscopy**

Optical microscopy was performed using an OLYMPUS BX51M table-top microscope in conjunction with OLYMPUS Stream image analysis software. Microscopy was used for two separate characterisation operations; powder particle

## Materials & Methods

analysis and void content analysis. As has already been discussed, the powder shape is an important parameter for rotomoulding powders as the presence of tails or fibrils and the overall consistency of particles determines their suitability to the rotomoulding process. Optical microscopy has been used to characterise the powder materials tested and to identify which materials are the best candidates for further trials. Fig. 3.7 shows a typical microscopic image of powder particles.

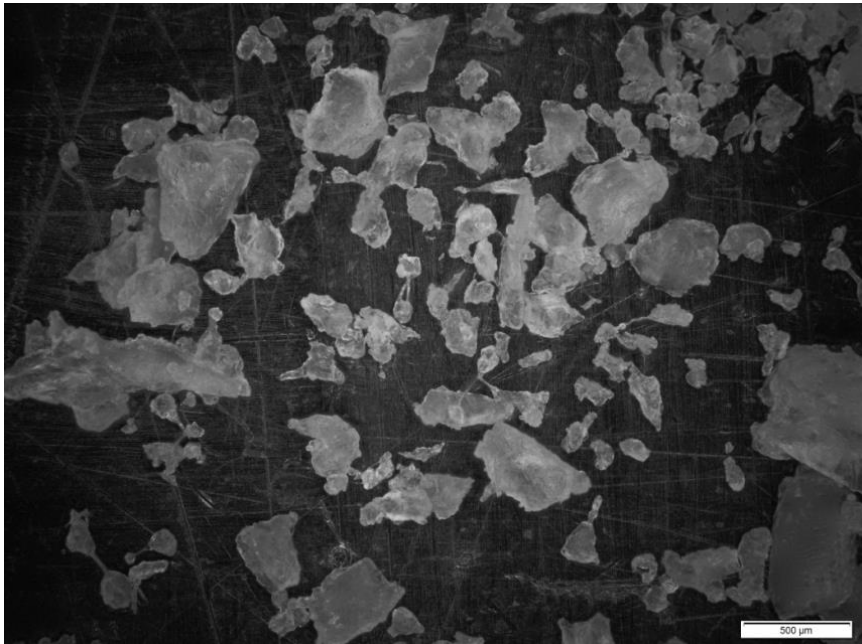


*Figure 3.7. Microscopic image of a PVDF powder material displaying the particle shape and size.*

Microscopy has also been used to determine void volume contents in polymer materials through the use of binary imaging techniques. Samples were cut from original materials for void volume fraction and void radius measurements. Fig. 3.8 shows how the OLYPMUS image analysis software differentiates pixel colours within the microscopy image and allows the user to set two colour bands into which the different pixel colours will fall. The void volume fraction can be obtained by calculating the relative area in each of the two colour bands set in the binary image.

The average radius of voids contained within the image can also be obtained using the image analysis software which identifies pixels in the same band which are connected together. The maximum straight line length between two such connected pixels can then be obtained with an output of average void radii being achieved. The

correlated data is then available for analysis giving important information such as void volume fraction and the radius of individual voids.

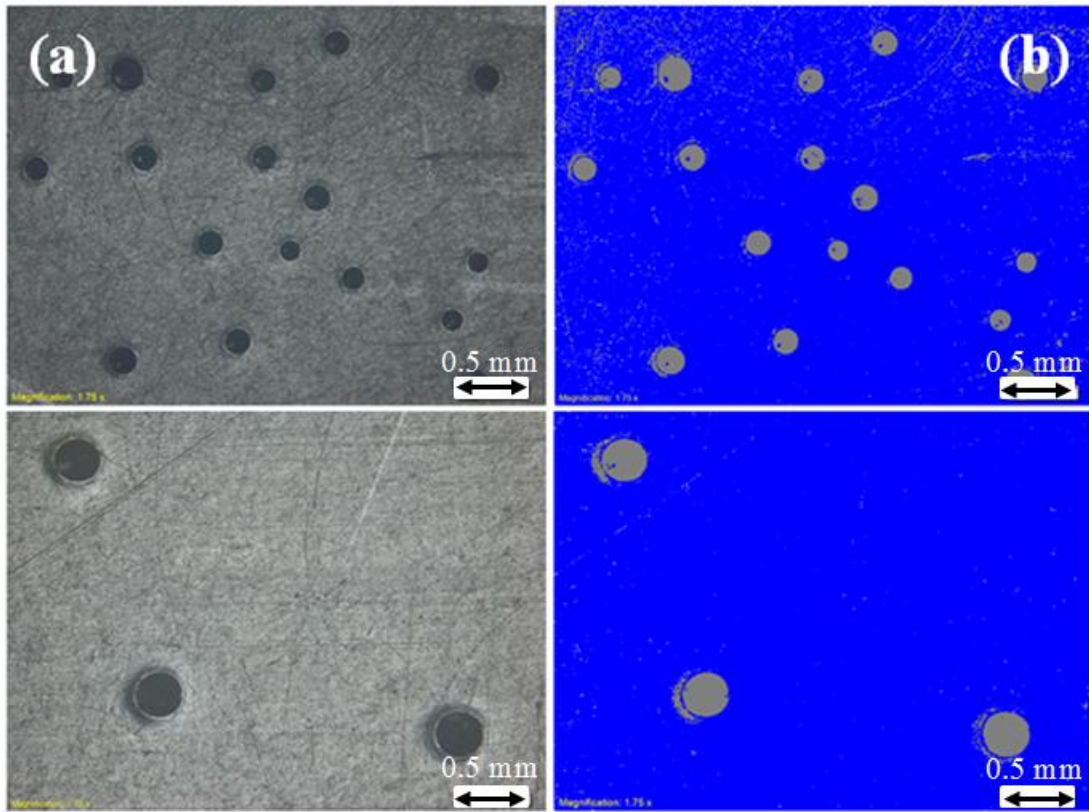


Figure 3.8. Void volume content analysis showing (a) the microscopic image on the left and (b) the corresponding binary image on the right [64].

### 3.6.1.3. Differential Scanning Calorimetry

Differential scanning calorimetry (DSC) is a thermal analysis technique that determines the melting temperature and crystallinity percentage of polymer materials by measuring the heat required to increase the temperature of a small sample of the material. Information about the exact melting point of the material is needed to set processing conditions for sample manufacturing and to ensure against degradation of the plastic due to prolonged hold times at elevated temperatures.

DSC testing was conducted in NUI Galway with a Shimadzu DSC-60 based on the heat-flux method. A small amount of powder (< 5g) is placed in an aluminium pan and is crimped with a lid in a press to enclose the sample. A second pan is also crimped with no powder inside it to act as a control sample. The control sample and test sample are placed in the same DSC furnace and a predetermined heating pattern

runs through the melting point of the material. The DSC monitors the temperature difference between the two samples as the furnace heats up and uses this to determine the difference in heat of fusion between both samples. The DSC-60 has a measurement range of 0 – 600 °C making it compatible with all materials tested here. Testing was conducted using five samples of each material and Shimadzu aluminium crimp pans (SH201-52943) following ISO 11357-1 [212], ASTM D3418-12 [213] and a heating rate of 20 °C/min.

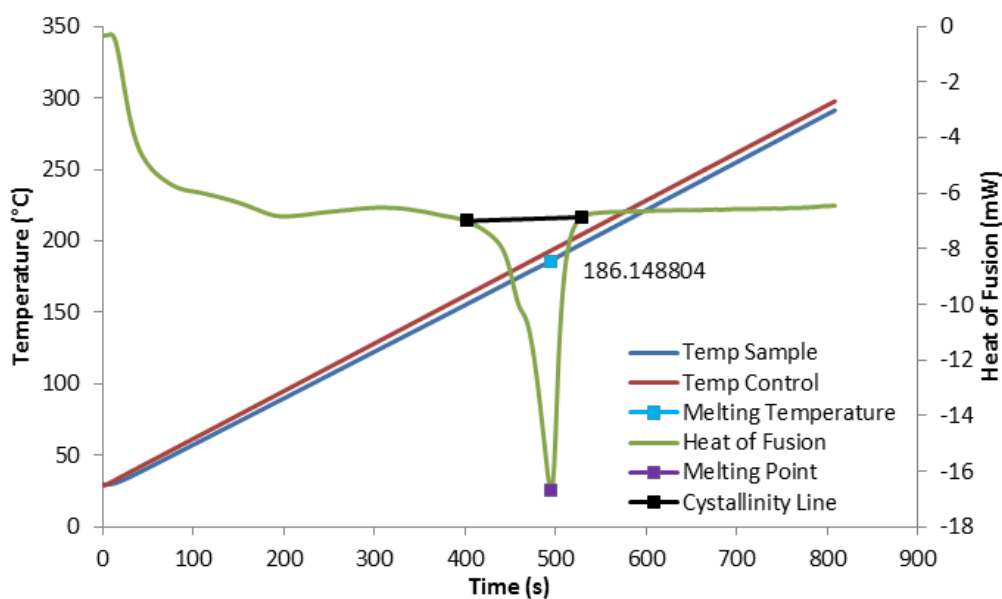


*Figure 3.9. Graphical output of DSC testing showing the sample melt temperatures and heat of fusion for calculating crystallinity.*

A typical DSC output graph is shown in Fig. 3.9. The melting point of the material is determined as the peak of the melting endotherm, on the heat of fusion output, as the solid material takes in energy to undergo a change of state. This peak is then linked back to the sample temperature, at that time, and is taken as the melting point of the material. The crystallinity % of the material is determined by calculating the area under the crystallinity line in mJ and dividing it by the initial sample weight. This gives a value in mJ/g and then this is divided by the heat of fusion of a 100% crystalline sample to determine the test samples crystallinity percentage. The value for heat of fusion for a 100% crystalline material is taken from published data which are readily available for most polymer materials [214]. In this way, the melting point and crystallinity of the materials tested can be determined for various processing conditions.

There are however distinct differences between hot plate formed samples and rotationally moulded samples. The very nature of rotational moulding adds a rotational motion which imparts flow and movement of powder particles within the mould which is not present in hot plate formed parts. This movement causes a clear mixing of particles, but also allows the smallest particles to be melted first (due to the lower amount of thermal energy needed to melt their solid structure) which causes these particles to stick to the wall first, a phenomenon which is not mirrored in hot plate formed parts as the lack of powder movement causes particles trapped at the bottom of the part to be melted first. The heating and cooling behaviour of rotomoulded parts is also quite different in comparison to hot plate formed parts. In rotational moulding, the part touching the mould wall cools faster than the free side on the internal surface of the part. This causes lower crystallinity in the outer skin and higher crystallinity in the interior structure due to the differences in cooling rates. In comparison, hot plate formed parts have the opposite effect, as the internal surface cools quicker than the surface in contact with the mould as it is free to air. This causes the free surface side to have lower crystallinity than the surface in contact with the mould plate and so has an opposite crystallinity structure to that of rotomoulded parts.

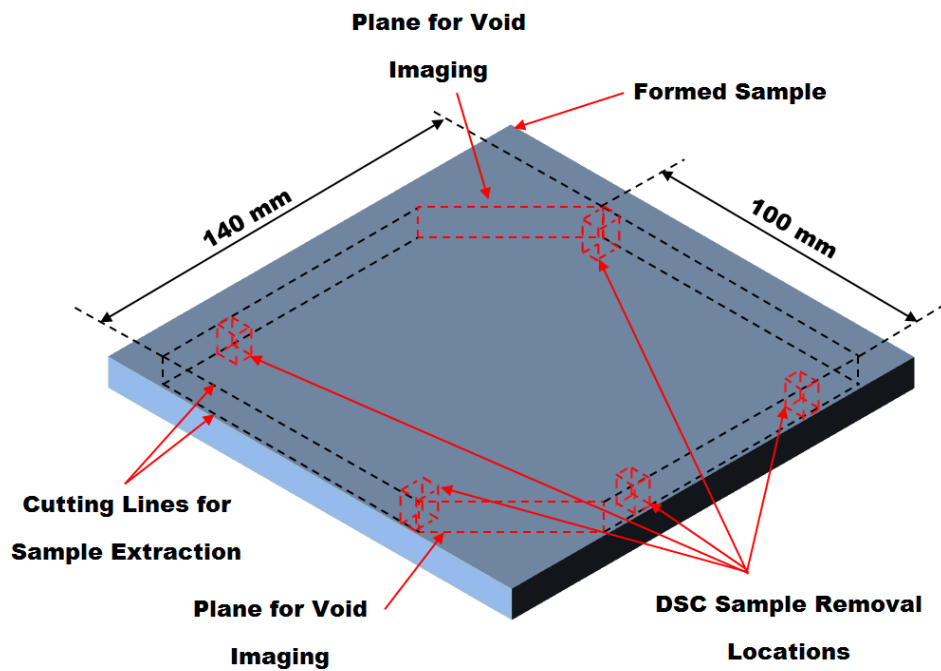


Figure 3.10. Diagram highlighting the cutting lines used for samples including the locations of void imaging planes the extraction regions for DSC samples.

A standard overview of the sample extraction plan for the permeability samples is included in Fig. 3.10. This overview also highlights the regions where void imaging has taken place while also showing the region where DSC samples were removed for testing. The samples were taken from different locations around the part, to avoid targeting a single area. However, as already described, the samples will have differing crystallinity percentages through the thickness of the sample due to the different cooling regimes applied. While the DSC samples should be representative of the entire part (i.e. they should encompass the entire part thickness to avoid targeting a certain layer of the through thickness), it cannot be confirmed with certainty that the DSC samples tested here were representative of the through thickness, due to discrepancies in the sample extraction and polishing procedures used to obtain samples small enough for DSC testing. This has added to the standard deviation of results and is one reason why scatter is observed.

### **3.6.2. Permeability Testing**

Two different permeability test methods were used for the analysis of helium leak rates through polymer materials. The first was built in NUI Galway specifically for this project and uses a variation of the volumetric method and a change in pressure to determine permeability. The second uses a mass spectrometer to determine the leakage of helium through a polymer sample over time and was provided by ÉireComposites Teo.

#### ***3.6.2.1. NUI Galway Pressure Increase Permeability Test Apparatus***

The NUI Galway permeability test apparatus used in this study is a modified method following ASTM D1434 [215] and designs based on work by Choi [156, 216, 217]. It must be noted that the ASTM D1434 standard, prior to being updated in the year 2015, had an error in its calculations which lead to the prediction of leak rates with a lower permeability by six orders of magnitude due to the improper cancelation of units. This induces significant scatter in published permeability results and was highlighted to the publishers of ASTM standards by the author in the year 2013. The updated standard does not acknowledge this significant error in the calculations but has updated the equations to their proper form.

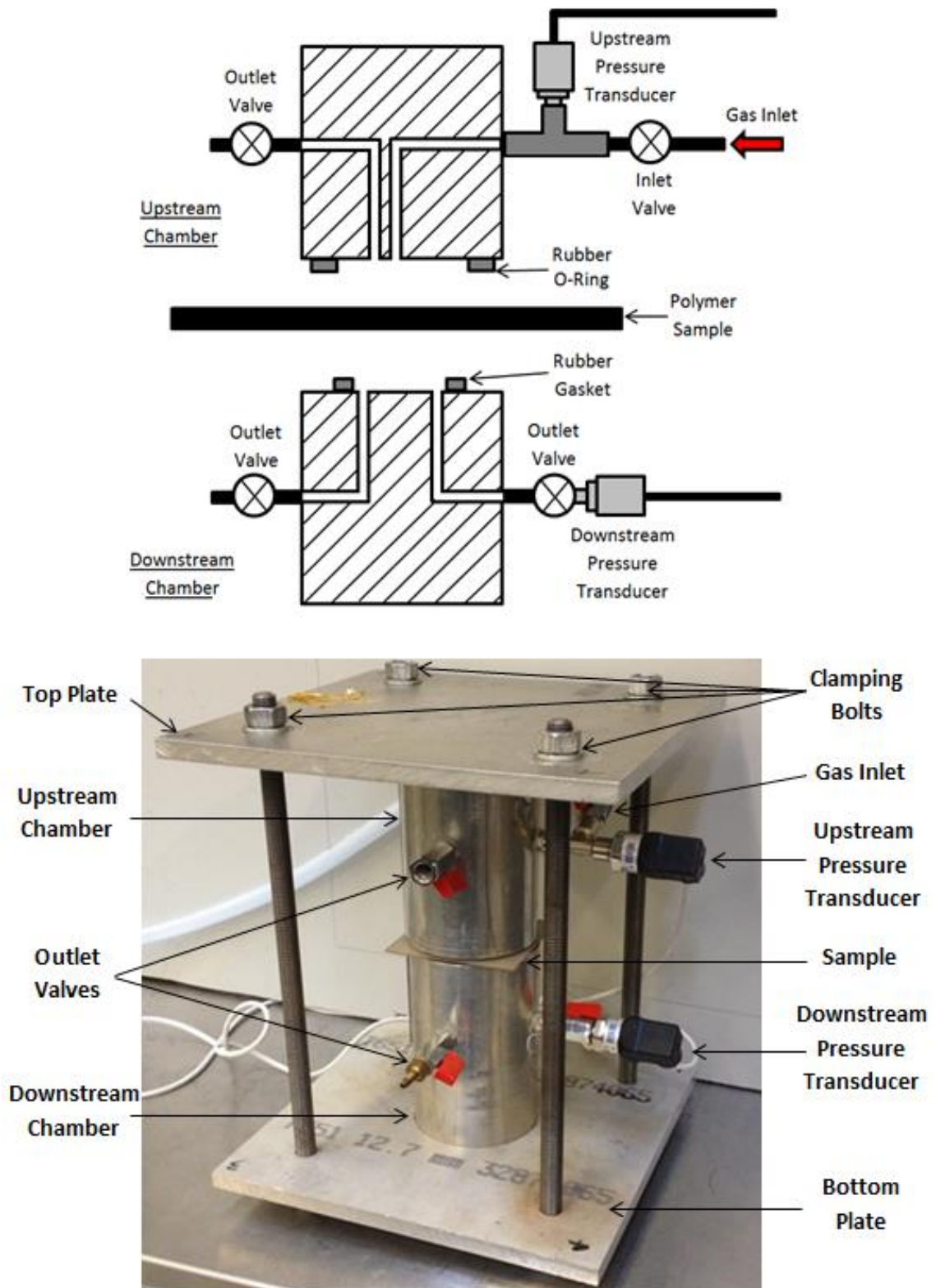


Figure 3.11. A schematic diagram of the volumetric permeability apparatus along with a photograph of the test apparatus itself.

## Materials & Methods

This apparatus follows the same principles as the standard but instead of using a liquid slug indicator, as in the volumetric method, a second pressure transducer has been placed in the downstream chamber to gauge the pressure increase over time. As shown in the schematic diagram of Fig. 3.11, the permeability test apparatus consists of two chambers, one upstream and one downstream of the flow, with a sample placed in between the chambers and clamped in place with a constant force. Helium gas, grade N5.0 at 99.999% purity [218], is supplied to the upstream chamber at a constant pressure and the downstream chamber is connected to a second pressure transducer to make experimental calculations. The permeating gas diffuses through the sample and the increase in gas pressure in the downstream chamber is used to calculate the rate of permeation for the given material. At the start of the test a barometer (a TEMPCON S-BPA-CM10 Smart Barometric Pressure Sensor) is used to calibrate the pressure transducer in the downstream chamber with ambient pressure. The ambient pressure and temperature are recorded simultaneously by a HOBO H21-002 Micro Station throughout the duration of the test.

The upstream and downstream chambers have been machined from 100 mm thick cylindrical aluminium columns with a height of 150 mm each. These dimensions limit permeability rates through the chamber walls and ensure the predominant direction of the flow is from the upstream chamber, through the sample, towards the downstream chamber collection area [216]. The gas enters the upstream chamber at a constant pressure and permeates through the sample into the downstream chamber. The pressure was held constant using a BOC 8500 series precision pressure regulator and was measured in both chambers using a WIKI A-10 pressure transducer (0-10 bar upstream, 0-1.6 bar downstream) connected to a NI USB-6008 data logger coupled with LABVIEW Signal Express software.

The sample is held in place using a clamping force which was provided by the two steel plates which envelop the apparatus. This removes the need for using a tensile testing machine to supply a compressive force. Before the test commenced the inlet gas hole coverage was also tested. If the applied clamping force is too high the sample can bend causing gas inlet hole coverage and an artificial reduction in the test area as indicated in Fig. 3.12. To mitigate the chances of this occurring before the test commences, the upstream chamber is filled with gas at the desired pressure and then all valves are closed (on the permeability test apparatus and the helium supply).

The pressure reading in the upstream chamber is monitored and then the outlet valve on the upstream chamber is opened. If the depressurisation of the upstream chamber is not instantaneous, then the applied clamping force is covering the gas inlet hole. This pre-test procedure ensures consistency of results and keeps the sample from covering the gas inlet hole and thereby artificially reducing the permeating test area.

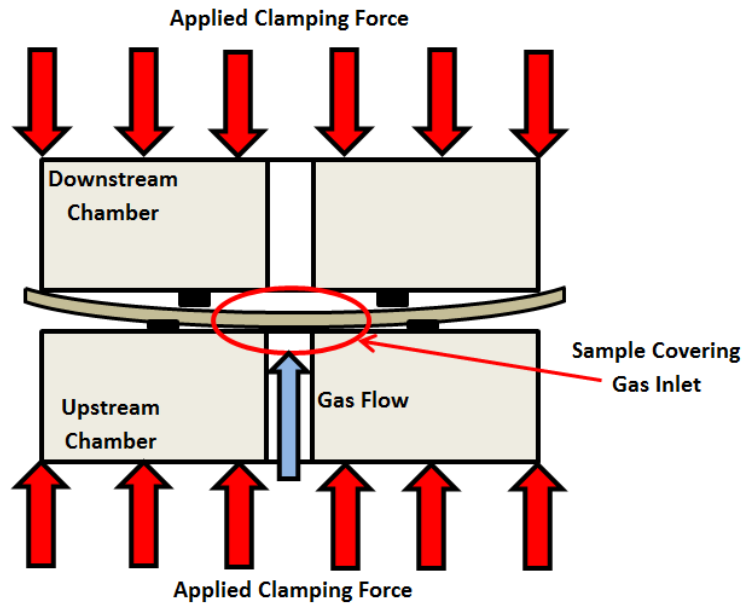


*Figure 3.12. Applied clamping force causing gas inlet coverage due to sample bending.*

Permeation and leakage of the gas at the contact points of the two chambers with the sample is limited through the use of a dual barrier in the form of a rubber O-ring and rubber gasket encompassing the test area for permeation. These rubber points act as sealants for the test apparatus and promote permeation of the gas to the downstream chamber, limiting leakage of the gas to the free surfaces. The gasket is of larger diameter than that of the O-ring as this ensures that the mass flow rate within the collection area is constant across the sample and leads to more accurate results without significant edge losses [219].

The ASTM standard [215] utilises a variation of the ideal gas law to determine the amount of gas which has permeated through the sample. The ideal gas law:

$$pV = nRT \quad (3.2)$$

## Materials & Methods

relates the gas pressure  $p$  (Pa) and volume  $V$  (L) to the number of moles  $n$  (mol), the gas constant  $R$  (L.Pa/mol.K) and the gas temperature  $T$  (K). The standard replaces the volume with a volume flow rate  $V_F$ . In the standard, the volume flow rate is calculated using a glass capillary tube, a moving liquid slug and the passage of time to quantify the change in volume in the downstream chamber as gas permeates through the sample. This value is then used to achieve a gas transmission rate  $GTR$  through the sample via Eq. 3.3:

$$GTR = \frac{pV_F}{ART} \quad (3.3)$$

By multiplying by the ambient pressure  $p$  and dividing by the collection area in the downstream permeation cell  $A$ , the gas constant  $R$  and the ambient temperature  $T$ , the number of standard cubic centimetres of gas (scc) which will permeate a metre square area can be calculated to arrive at units of scc/m<sup>2</sup>.s. The permeability coefficient  $P$  can then be calculated by dividing the gas transmission rate by the applied pressure difference ( $p_{upstream} - p_{downstream}$ ) and then multiplying by the sample thickness  $x$  to arrive at units of scc.m/m<sup>2</sup>sbar as indicated by Eq. 3.4:

$$P = \frac{GTR}{p_{upstream} - p_{downstream}} \cdot x \quad (3.4)$$

In the present study, a similar relationship is used to determine the mass flow rate and permeability coefficient. Two stages are analysed within the test set up, the first is the onset of steady state mass flow and the second is at some future time where the flow is still at steady state conditions. At stage one the ideal gas law relationship is used to equate the volume of gas in the chamber to an equivalent volume at standard temperature and pressure via Eq. 3.5:

$$\frac{p_1 V_1}{T_1} = \frac{p_2 V_2}{T_2} \quad (3.5)$$

For the permeability calculation, using the modified test method, two points (1 and 2) are defined in the test where steady state conditions have been achieved, Fig. 3.13. The values for pressure,  $p_1$  and  $p_2$ , and temperature,  $T_1$  and  $T_2$ , are taken from the pressure transducer in the downstream chamber and temperature recording data at that time step, with the volume of the internal chamber area being used for  $V$  (18.8

cm<sup>3</sup>). Standard temperature and pressure (STP) values for  $P_{STP}$  (100 kPa) and  $T_{STP}$  (273.15 K) are used to determine an equivalent volume for  $V_l$  at STP via Eq. 3.6:

$$V_1 = \frac{P_1 V T_{STP}}{P_{STP} T_1} \quad (3.6)$$

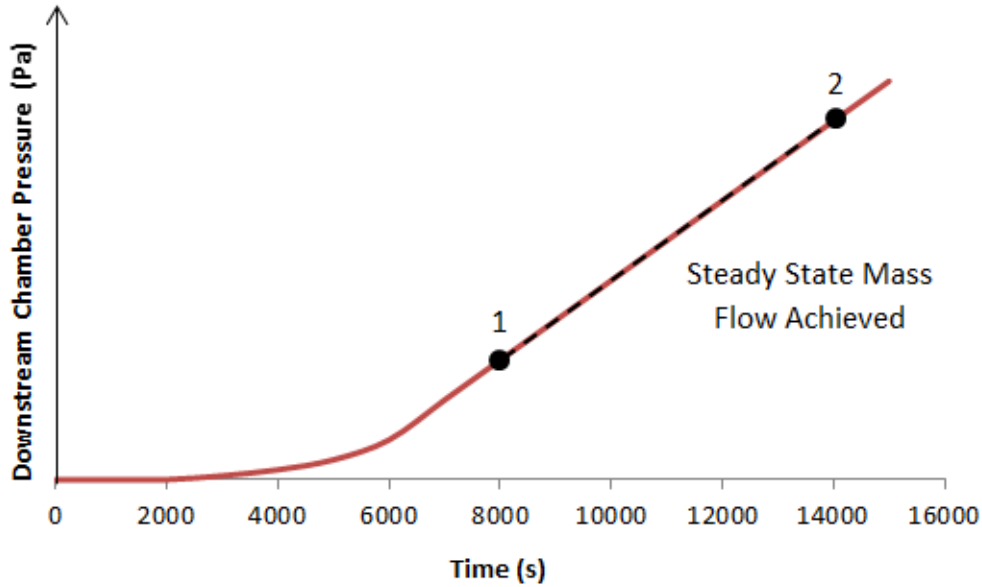


Figure 3.13. Permeability calculation explanation graph.

This is the assumed starting point for the mass flow rate calculation and indicates the zero set point for permeation. The process is then repeated at point 2 where steady state conditions are still observed and the increase in pressure is used to equate a second value  $V_2$  via Eq. 3.7 where the pressure and temperature for point 2 have replaced those in Eq. 3.6:

$$V_2 = \frac{P_2 V T_{STP}}{P_{STP} T_2} \quad (3.7)$$

The value of  $V_l$  for point 1 is taken away from the second value of  $V_2$  for point 2 and the remainder is defined as the volumetric increase  $V_{INC}$  via Eq. 3.8:

$$V_{INC} = V_2 - V_1 \quad (3.8)$$

The volumetric increase in standard cubic centimetres is then divided by the time  $t$  in between the two readings for points 1 and 2 and by the test collection area  $A$  so the final leak rate LR can be defined in units of scc/m<sup>2</sup>.s, Eq. 3.9:

$$LR = \frac{V_{INC}}{t \times A} \quad (3.9)$$

This leak rate is equivalent to the gas transmission rate calculated in Eq. 3.3 and so using ASTM D1434 the permeability coefficient can be calculated using a variation of Eq. 3.4:

$$P = \frac{LR}{p_{upstream} - p_{downstream}} \cdot x \quad (3.10)$$

where  $p_{upstream}$  is the applied pressure in the upstream chamber and  $p_{downstream}$  is the ambient pressure in the downstream chamber and  $x$  is the sample thickness to arrive at the permeability coefficient in units of  $\text{scc.m/m}^2 \cdot \text{s.bar}$ .

### 3.6.2.2. *Mass Spectrometer Permeability Test Apparatus*

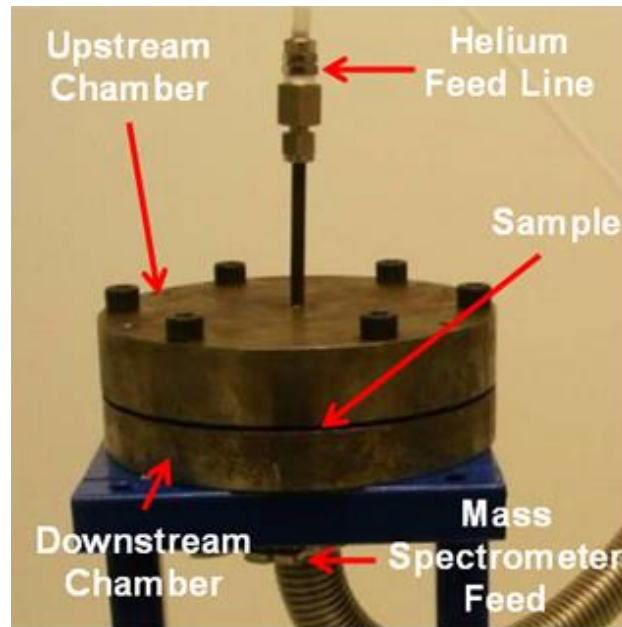


Figure 3.14. ÉireComposites mass spectrometer permeability test apparatus.

The ÉireComposites mass spectrometer apparatus used to test leak rates through polymer materials follows the standard test method as outlined in ASTM D1434 [215] and depicted in Fig. 3.14 and 3.15. The sample is clamped between two chambers and a vacuum is applied to both sides of the sample. The downstream side connected to the leak detector undergoes a two stage vacuum process whereby a TRIVAC D 2.5 E pump applies the initial vacuum while a TURBOVAC TMP 35 LS draws the chamber down to a lower vacuum so that mass spectrometer readings can take place [220]. Once a sufficiently low vacuum has been achieved ( $< 3$  mbar) in the downstream chamber the helium leak detector (UL 200 Leybold Leak Detector) is engaged and measures the leak rate through the sample via a mass spectrometer

[220]. Research grade helium gas supplied by BOC, grade N5.0 with a purity of 99.999% [218], is then introduced into the upstream chamber at 1 bar ( $\pm 20$  mbar) and allowed to permeate through the sample.

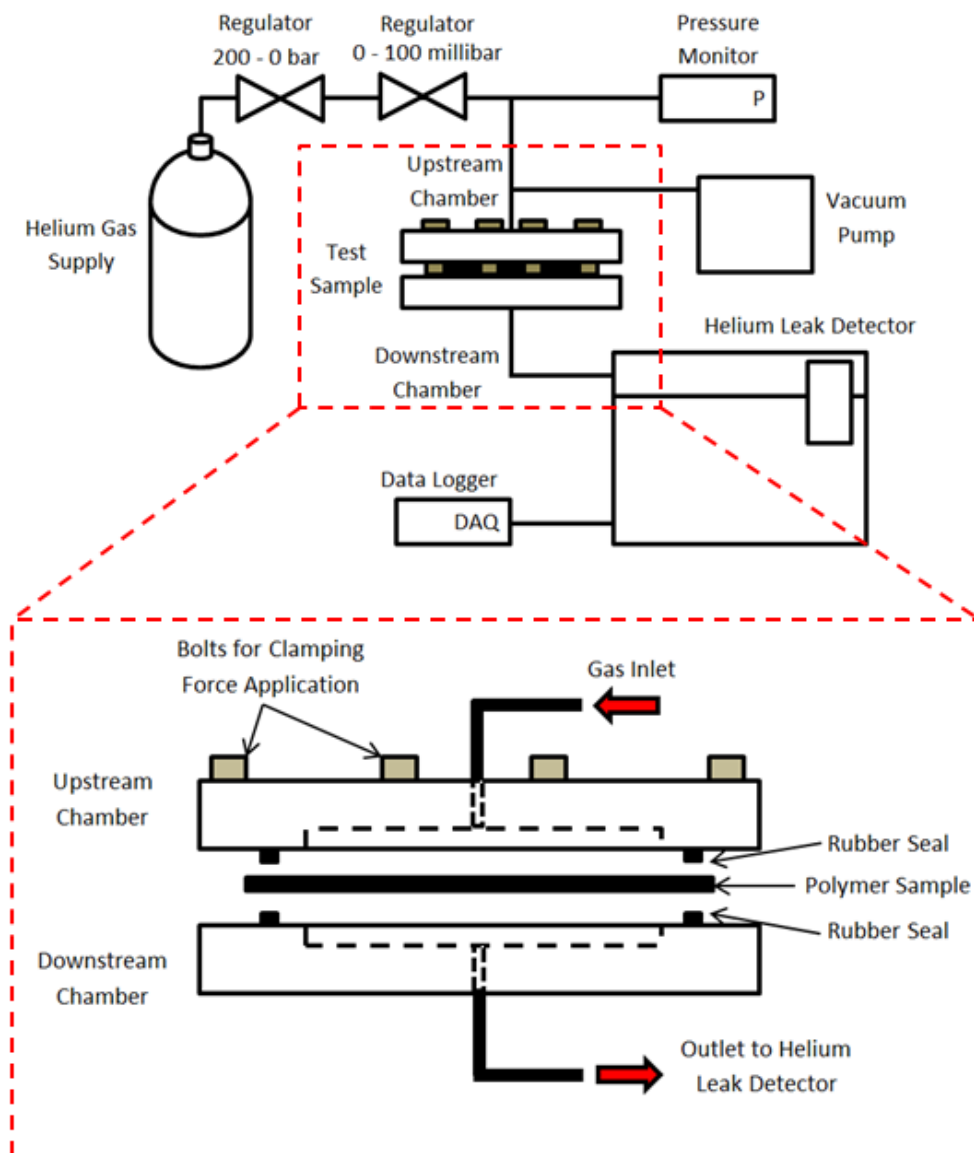


Figure 3.15. Schematic overview of ÉireComposites mass spectrometer permeability test apparatus.

The gas pressure is controlled with a multi-stage helium regulator (MUREX Saffire 10 Bar) and a fine pressure regulator (O Neill CG63-100B). The pressure is measured with a Digitron 2023p pressure gauge to ensure that the pressure difference across the sample is within test limits ( $\pm 10$  mbar). Once the gas permeates through the sample it is then collected by the mass spectrometer which outputs the leak rate

results to “Leakware” software which monitors the leak rate over the test duration. A typical test can last anywhere from 12 to 72 hours, depending on the polymer tested and the sample thickness, as steady state conditions must be reached before an average leak rate can be obtained.

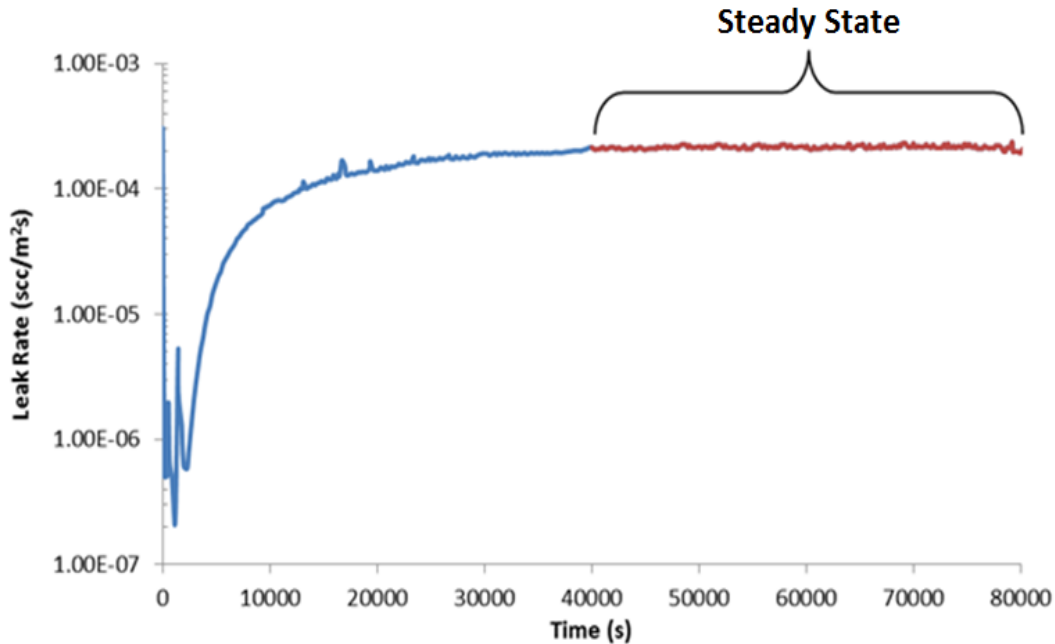


Figure 3.16. Standard leak rate output for mass flow rate against time.

A number of other factors can also be determined from the measured leak rate. Most notably permeability, diffusion and solubility coefficients can be calculated from the measured data. The helium leak detector outputs the leak rate in units of mbar.l/s. Standard units for the leakage of helium for an entire COPV structures are scc/s which are obtained by multiplying the mbar.l/s output by 0.987 [221]. Fig. 3.16 demonstrates that the calculation of the total leak rate per  $m^2$  area over the test duration can then be determined by dividing the leak rate by the sample area. This gives the standard leak rate through the sample at steady state conditions but does not give sufficient detail about the sample’s permeability coefficients.

To obtain values for permeability, diffusion and solubility coefficients, the leak rate must be changed to a graph mapping the increase in the volume of gas passing through the sample over time. By adding together the volume of gas which has escaped at each corresponding time step from  $t = 0$  onward the total volume of gas  $V$

that has passed through the sample at any time step can be calculated. Then by using the relationship [110, 171]:

$$V = PA\Delta p t/x \quad (3.11)$$

where  $A$  is the sample area ( $0.0095 \text{ m}^2$ ),  $\Delta p$  is the pressure difference across the sample (1 bar),  $t$  is the test time and  $x$  is the sample thickness. The permeability coefficient  $P$  can be obtained by rearranging the equation and plotting  $Vx/A\Delta p$  versus  $t$  to obtain  $P$  as the slope of the linear portion of the line at steady state conditions as demonstrated in Fig. 3.17.

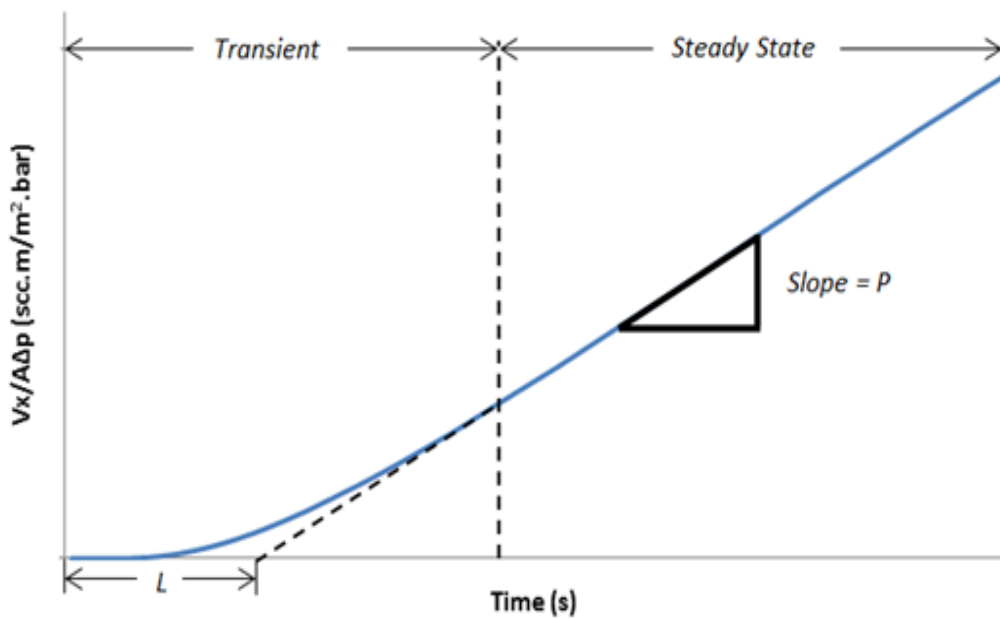


Figure 3.17. Graph to determine permeability, diffusion and solubility coefficients.

The diffusion coefficient  $D$  can also be obtained from this graph by defining the time lag  $L$  as the point where a straight line fitted to the linear steady state portion of the graph in Fig. 3.17 intercepts the time axis. This corresponds to the time taken for the diffusing gas to break through the sample and is governed by the relationship [110, 174]:

$$L = x^2/6D \quad (3.12)$$

From which the diffusion coefficient can be obtained. The solubility coefficient  $S$  is given by [174]:

$$S = P/D \quad (3.13)$$

where the coefficients are as previously defined and the value governs the relationship between the permeability coefficient and diffusion coefficient. While the leak rate has already been defined as the most important quantity for certifying COPVs these coefficients can be used in conjunction with Fick's law to make leak rate predictions for different COPVs based on applied pressure, liner thickness and temperature constraints for valuable information in regards to ranking prospective liner materials.

### **3.6.2.3. *Sealants Used During Testing to Improve Vacuums***

One of the drawbacks of using rotational moulding for manufacturing liners is the inherent production of air voids in the part cross section and mould surface. These voids act as leakage paths for the permeating gas and also make it difficult to seal samples properly for permeability testing. To this end, a number of sealants have been used to improve the vacuum to a level where permeation results could be taken. Sealants used included:

- DOW CORNING – High Vacuum Grease
- Epoxy Resin (PPG EC75 & ACT 65) – Two Part

In most cases the use of high vacuum grease was sufficient to seal to a level where an adequate vacuum could be drawn. In these instances, a thin layer of grease was applied to the sample at the point where the rubber O-ring was in contact with the sample. If the grease could not provide a sufficient seal then a thin layer of PPG EC75 epoxy (with ACT 65) was applied to the sample around the area where the rubber O-ring touches the sample. This fills any cracks or holes with a thin layer of epoxy and allows for thorough contact between the rubber O-ring and sample.

### **3.6.2.4. *External Influences on Permeability Readings***

As already discussed, the use of sealants around samples for permeability testing has been used to provide a sufficient seal for the applied vacuum during the testing of materials. The issues associated with this application of sealant are that the applied vacuum can sometimes pull helium gas through the seal from external locations causing the apparent leak rate to spike as shown in Fig. 3.18.

This causes the steady state leak rate to change momentarily and so increases the average leak rate. In instances where the leak rate has reached steady state conditions and intermittent spikes are present, the maximum leak rate quoted will be that of the steady state value and will not include intermittent increases. In cases where leakage spikes were the predominant value for the measured leak rate (greater than 10% of measured results), the test was repeated.

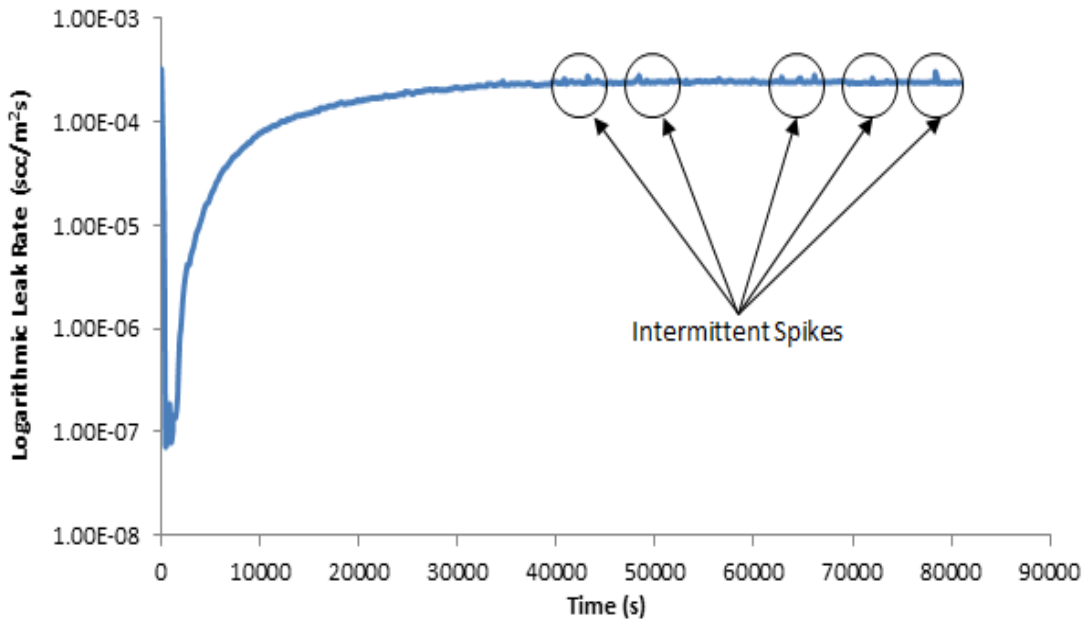


Figure 3.18. Intermittent spikes due to the use of a sealant during permeability testing.

### 3.6.2.5. Discrepancies between Permeability Test Methods

The pressure increase method has a number of benefits over the volumetric flow method on which the test is based. While the replacement of the liquid slug with a pressure transducer and data acquisition system removes the human error from the process, the issues associated with the sensitivity of the volumetric method are addressed.

Nettles [222] has conducted significant work relating to the use of the liquid slug method while also testing the effects of the glass capillary orientation, type and length of liquid slug used and the size of the glass capillary tube. Initial results showed that permeability testing was unaffected by the slug indicator type and length, as water and alcohol gave similar permeation results for different slug lengths

ranging from 60 – 400  $\mu\text{m}$ . However significant variations in permeability were found for different glass tube diameters with larger diameter tubes ( $\approx 3$  mm diameter) having more accurate results (and higher permeabilities) based on a reduction in the viscous force needed to move the liquid along the glass capillary tube [222].

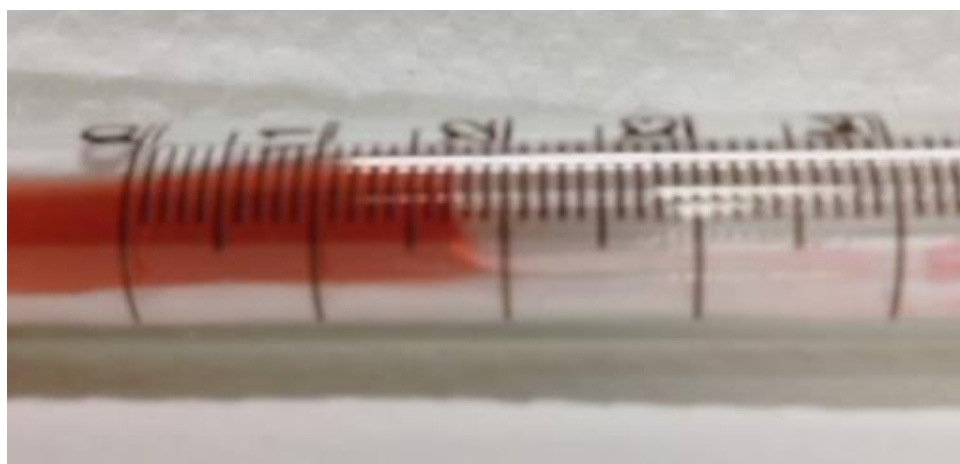
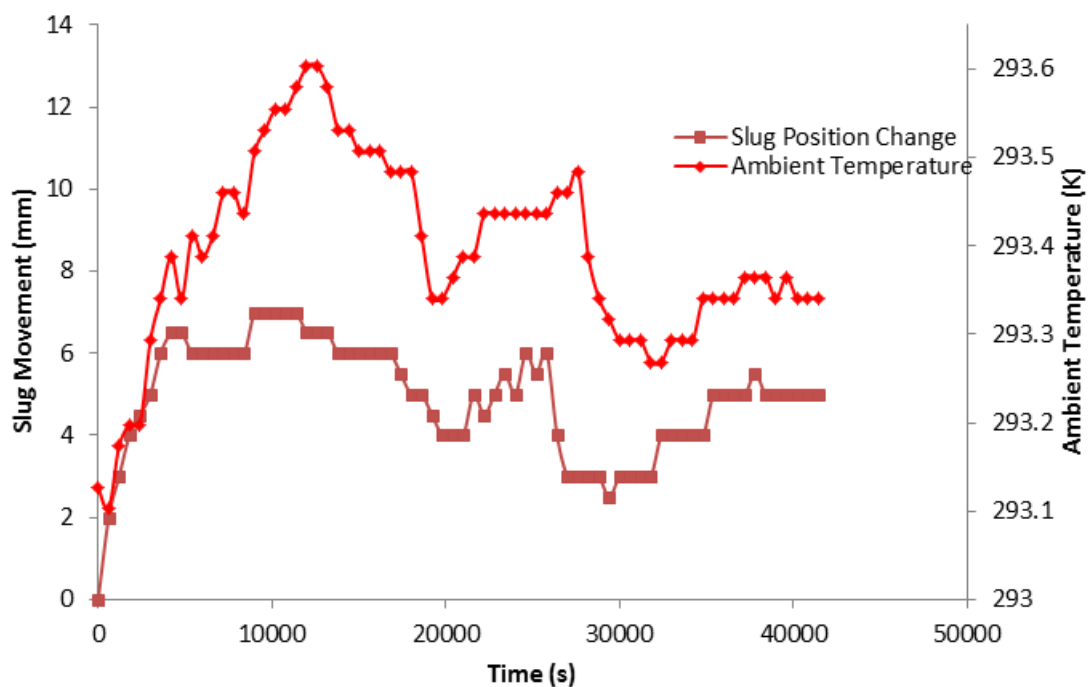


*Figure 3.19. Measured liquid slug movement for the testing of polyethylene using a 3 mm diameter glass capillary and phenol alcohol indicator against temperature along with an image of the liquid slug position measurement.*

Attempts were made to use the liquid slug method based on results by Choi [156, 216, 217] and Nettles [222] but issues related to anomalous results and large

## Materials & Methods

discrepancies in volume flow rates over time were observed. Due to the glass capillary tube and connecting plastic tubing being exposed to external sources of heat such as environmental lighting and changes in ambient pressure, the slug movement was very sensitive to these changes, and this made the recording of results almost impossible with positive and negative movement of the slug. Fig. 3.19 shows the typical output achieved with the liquid slug indicator along with the change in ambient temperature showing that the movement was directly affected by minimal changes in temperature.

The encapsulation of the test within the chambers by applying the pressure transducer directly to the chamber has removed the issues of ambient conditions significantly affecting the permeability test results. The thick metal cylinder and connections have minimised the rapid effects of changes in temperature and improved results while removing the human error associated with reading the capillary tube markings. The pressure transducers give a measured result based solely on the pressure increase and are more reliable for permeability readings.

The only drawback to this method of testing is the increase in pressure in the downstream chamber as the test progresses. The volumetric standard allows the liquid slug to be free to atmospheric pressure, while the present test method starts at ambient pressure and increases over time. This increase in pressure in the downstream chamber will decrease the permeation rate as the concentration of gas either side of the sample has a direct effect on the mass flow rate. While this is a concern for the accuracy of results obtained with this test method, the effects of this pressure increase have been quantified. An increase in pressure of less than 1% was observed in the downstream chamber for the entire test duration. The effects of this maximum increase are negligible and the results obtained show good consistency and accuracy.

The pressure increase method cannot be used to calculate the diffusion coefficient and the solubility coefficient from the time lag method, as the sensitivity of the apparatus is too low. The initial increase in leak rate is too fine to observe and so the time lag cannot be obtained as the sensitivity of the sensor is key for this initial test data. While the diffusion coefficient is a desirable value for measurements in permeability testing, the permeability coefficient is the product of the diffusion and

solubility coefficient and so still provides the key information needed for the current permeability study, along with the measured leak rate.

### 3.6.3. Cryogenic Cycling Testing

The temperature operating range for the COPV in this project is between 323 K (50 °C) to 50K (-250 °C), the boiling temperature of LH2, and so all materials used within this project must be able to withstand rapid cooling from ambient conditions to these cryogenic temperatures without failure, which would result in the loss of the contained gas or fuel. To this end cryogenic cycling has been used to simulate the rapid cooling experienced by materials in a COPV to determine the effect of the thermal gradients on the chosen materials.

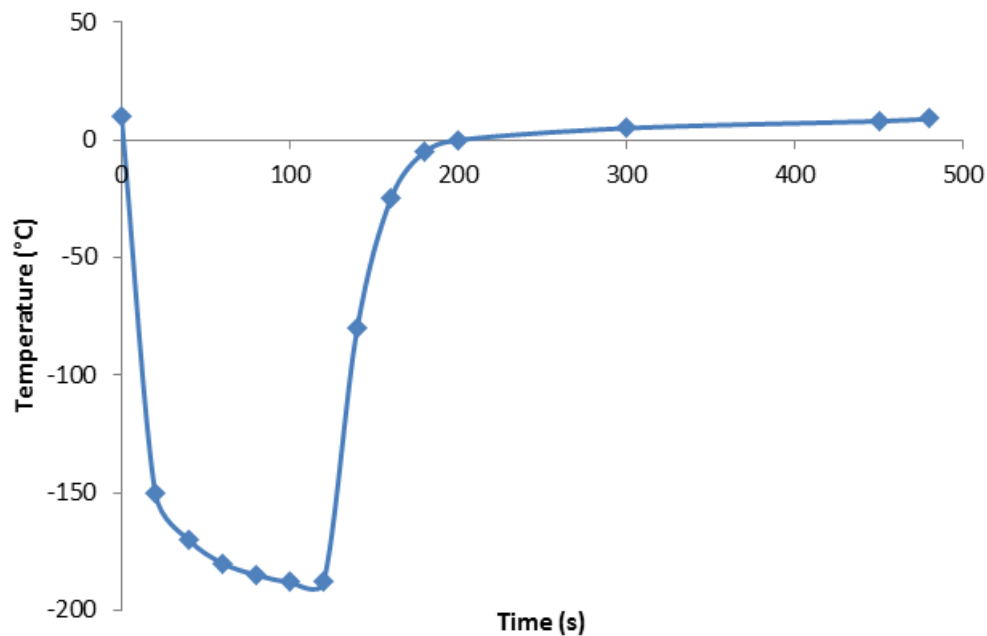


Figure 3.20. Typical cryogenic cycle experienced by samples dipped in liquid nitrogen.

Cryogenic cycling involves dipping samples in liquid nitrogen at approximately 77 K (-196 °C) for different numbers of cycles to determine if the materials change with respect to permeability, thermal stress cracking or material properties. A typical thermal cycle for the samples is shown in Fig. 3.20; the rapid cooling process involves holding the sample in liquid nitrogen for two minutes followed by the warming of the sample to ambient conditions over a further eight minute period, see Fig. 3.21, and is consistent with standard methods [156, 223-225].

## Materials & Methods

This equates to a ten minute cycle time and is repeated for the number of cycles as stated in the COPV standard operating requirements (50 cycles, for the current COPV design). Cryogenic cycling exposes the residual stress build-up in bonded materials of differing coefficients of thermal expansion and tests the susceptibility of the laminates to delamination and fracture over the rapid change in temperature.



*Figure 3.21. (a) Dipping of samples in a dewar of liquid nitrogen followed by (b) subsequent reheating to room temperature.*

### 3.6.4. X-ray Computed Tomography

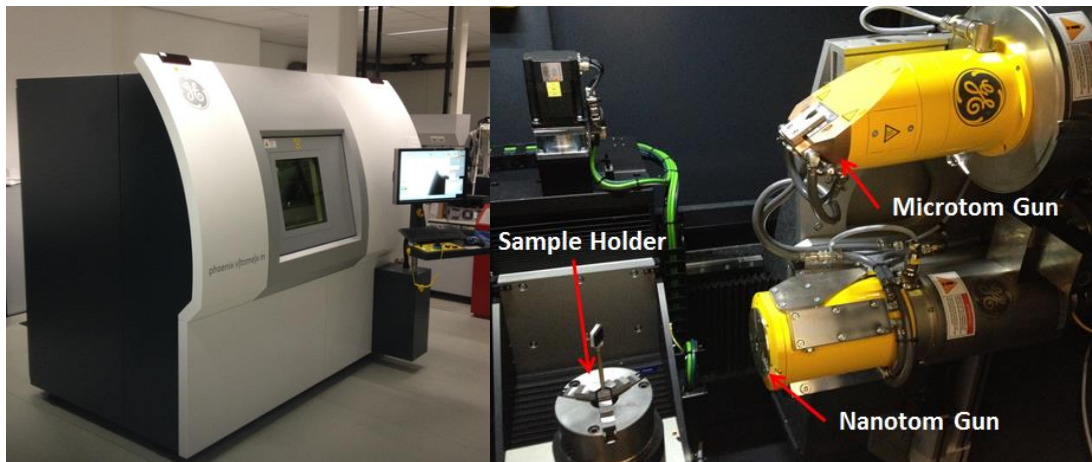


*Figure 3.22. X-ray CT machine used with an image of the Microtom and Nanotom gun included.*

X-ray CT scanning has been used to analyse the internal structure of polymer samples and LATP joints throughout this thesis, for evaluation of the internal void contents and consolidation properties of both materials respectively. X-ray CT

scanning uses an X-ray gun to take singular sequential images of a sample and then arranges and regenerates the collection of single images into a solid three dimensional structure with internal voids and defects highlighted. The X-ray CT machine used here, and housed in ESA's ESTEC facility in the Netherlands and pictured in Fig. 3.22, is a GE V/tome/X m300 with a Nanotom and Microtom gun operating at a voltage of up to 160 kV and 230 kV respectively. This machine gives a high resolution down to 1  $\mu\text{m}$  in size, depending on material properties, setting parameters and sample size. X-ray CT scanning has been used by a number of authors for analysing polymer composite materials, specifically in the area of void and microcrack mapping [180, 218].

*Table 3.4. X-ray CT settings used for the analysis of polymer materials.*

Parameter	Nanotom gun	Microtom Gun
Timing (ms)	1000	1000
Average	3	3
Skip	1	1
Binning	1	1
Sensitivity	2	2
V Sensor	1	1
Voltage (kV)	160	230
Current ( $\mu\text{A}$ )	28	60

The X-ray CT takes over 1000 images as the sample rotates on its internal mounting plate and uses these images to render a 3D image, which can be made transparent through the manipulation of the software. The rendering software used here is VG Studio Max 2.2 and this has been used in conjunction with the “defect analysis” tool to determine internal void structures in the tested polymer materials. The settings generally used throughout this analysis are shown in Table 3.4, with small deviations made to improve overall image quality. A number of extra features were also used to increase image clarity including the “shift” and “autoscan” features on the detector coupled with the “auto-optimisation” software tool which improves image clarity.

Filtering techniques have also been employed in the defect analysis to increase void definition and remove void bleeding, as shown in Fig. 3.23, which includes adjacent material surrounding a void in the analysis and leads to an inaccurate estimation of the void volume size.

The statistical analysis and wealth of data produced from the defect analysis tool has been used to study void structures in polymer materials with significant clarity at resolutions of less than 10  $\mu\text{m}$  (nominally based on sample size, position, and X-ray settings).

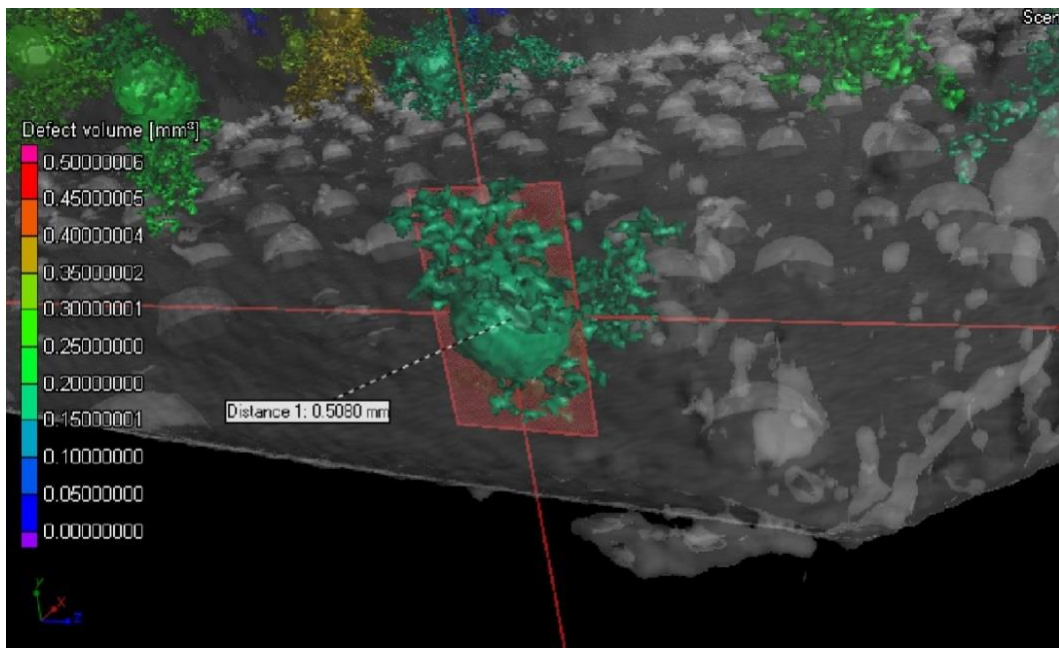


*Figure 3.23. Adjacent material wrongly included in the void volume calculation.*

### 3.6.5. Dynamic Mechanical Analysis

Dynamic mechanical analysis (DMA) is an experimental method that is used to measure the complex modulus of a material in different orientations. The storage and loss modulus can be assessed along with the determination of factors such as glass transition temperature, softening temperature, relaxation behaviour and crystallisation. These values are found experimentally by imparting a sinusoidal oscillating force to the sample and measuring the materials sinusoidal response to the force. The response can be measured across significant temperature ranges and gives insight into how the material will behave in different environments (varying temperatures, frequencies and forces).

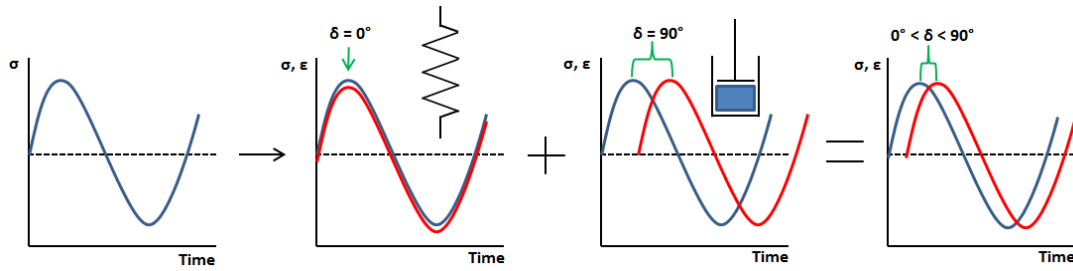


Figure 3.24. An overview of the DMA experimental theory showing (a) the sinusoidal forcing function resulting in (b) an elastic response modelled by a spring and (c) a viscous response modelled by a damper to give (d) a dynamic strain response with a phase shift between that of a perfectly elastic and perfectly viscous material (i.e.  $0^\circ < \delta < 90^\circ$ ).

Fig. 3.24 shows how an applied sinusoidal stress causes a sample to deform in a sinusoidal manner. The response can be characterised by both the elastic and viscous response of the material modelled as a spring and damper system respectively, Fig. 3.24 (b) and (c). In the elastic region the material behaves like a spring and the response of the material is in phase with that of the forcing function with the phase angle  $\delta = 0^\circ$ . The viscous response of the material is modelled as a dashpot and results in a phase lag of  $\delta = 90^\circ$  from the forcing stress.

The actual response of a material pulls on characteristics of both of these curves to form a phase response somewhere between  $0^\circ < \delta < 90^\circ$ , Fig. 3.24 (d). The elastic response can be broken down into the storage and loss modulus,  $E'$  and  $E''$  respectively, which are equal to the vector sum of their components which is the complex modulus  $E^*$  [226].

In the present study tensile and compressive tests have been performed on down selected materials to assess the changes in material properties of possible COPV liner materials over the operating range of the tank (-170 °C to 50 °C). A Mettler Toledo DMA/SDTA861e was used for the tensile testing while a Mettler Toledo DMA1 was used for the compression testing, both with nominal temperature ranges of -150/-190 °C to 600 °C, frequency ranges of 0.001 to 1000/300 Hz respectively and applied forces of 0.001 to 40/10 N respectively, Fig. 3.25.

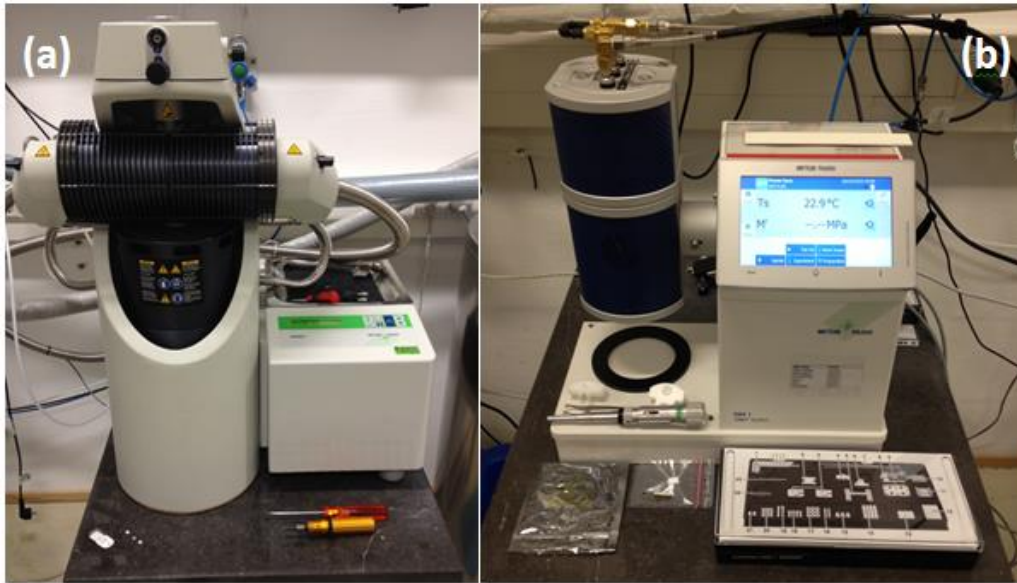


Figure 3.25. (a) The Mettler Toledo DMA/SDTA861e and (b) DMA1 used for DMA measurements in tension and compression respectively over a wide temperature range.

Five DMA tests were performed for each material tested (equating to ten tests per material; five in tension and five in compression) at a standard frequency of 1 Hz and an applied force range of approximately 10 N for the tension and an extension of 10  $\mu\text{m}$  for the compression tests, Fig. 3.26, following ASTM D5026-15 [227] and ASTM D5024-15 [228], respectively.

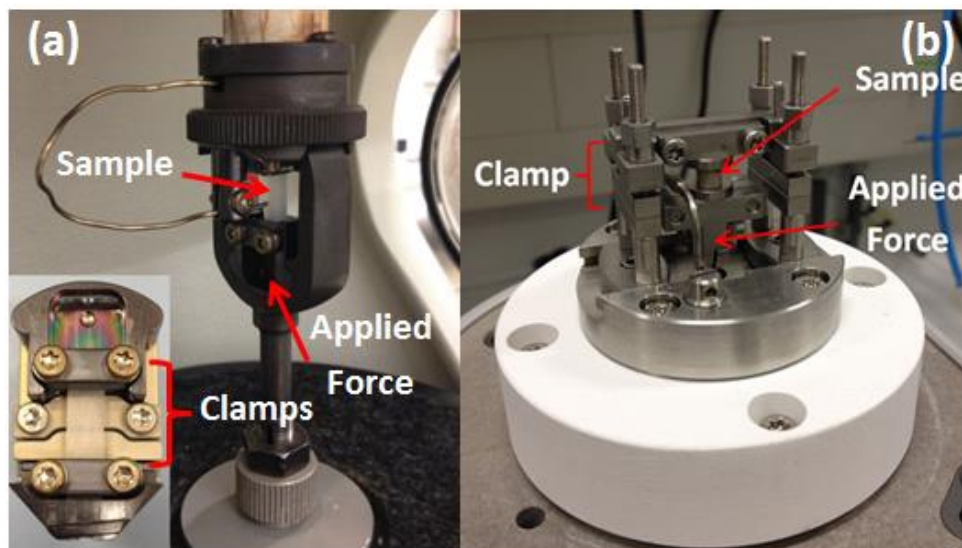


Figure 3.26. The test setup clamps for the DMA based on (a) tension, and (b) compression.

## Materials & Methods

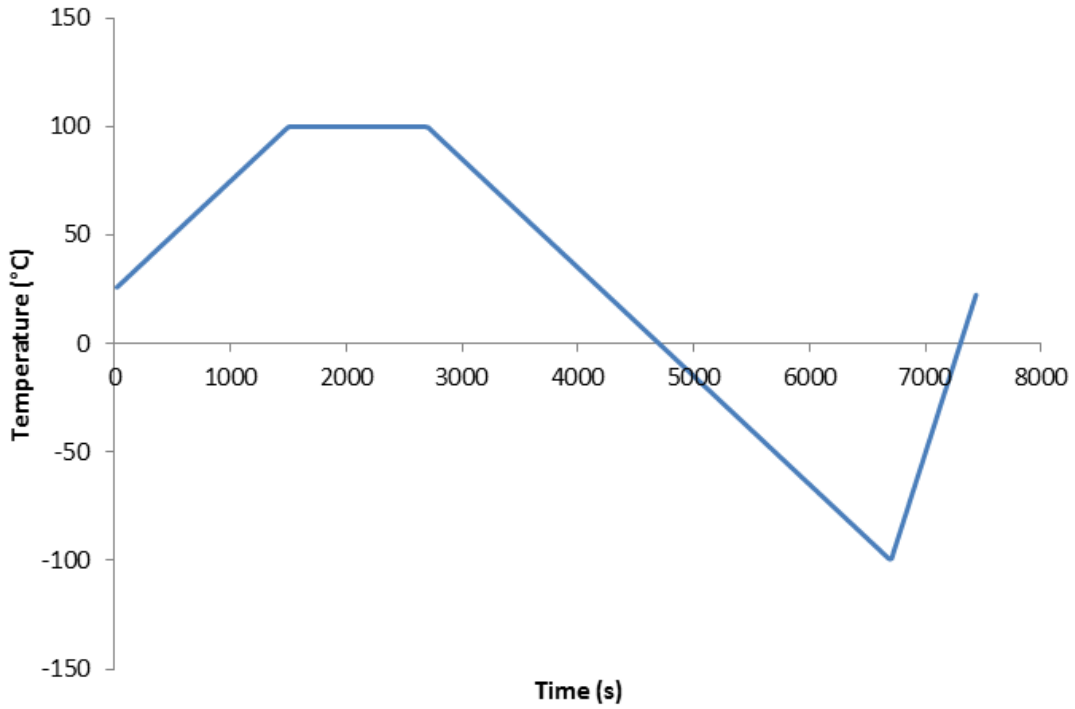


Figure 3.27. Temperature cycle used for DMA analysis of materials.

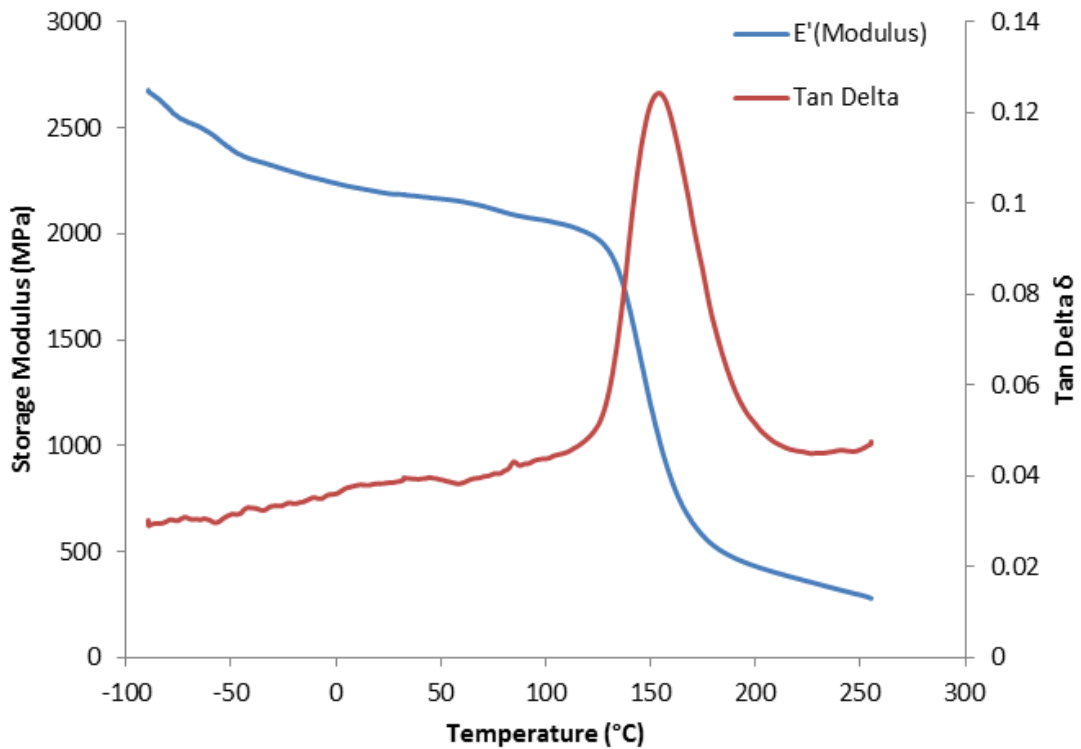
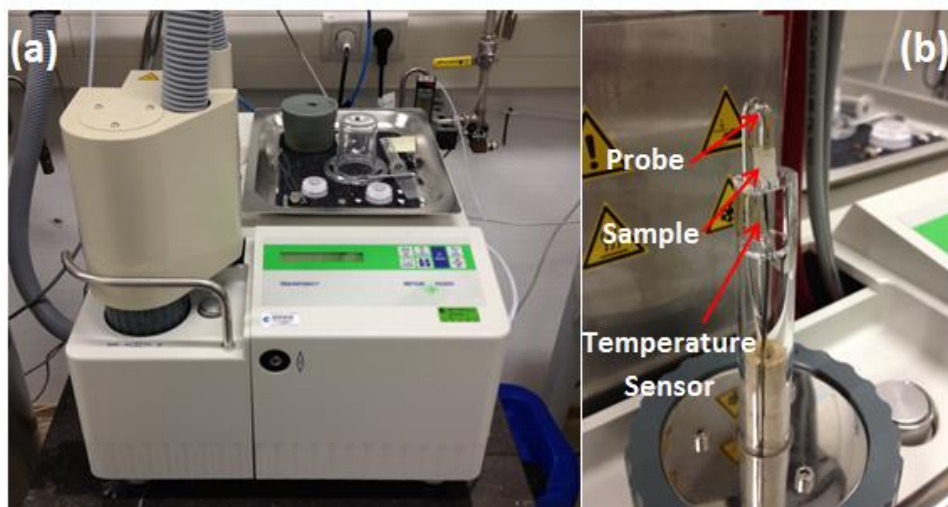


Figure 3.28. Typical DMA test result for a tensile test of a polymer sample highlighting the storage modulus and corresponding tan delta value over a wide temperature range.

The frequency was kept constant at 1 Hz across all test methods for consistency while the temperature was varied, as shown in Fig. 3.27, from 100 °C down to -100 °C. A standard DMA test output for a polymer sample is included in Fig. 3.28 with the storage modulus and tan delta values shown to vary across the measured temperature range.

### 3.6.6. Thermal Mechanical Analysis

Thermal mechanical analysis (TMA) is an experimental technique used to measure the coefficient of thermal expansion of a material over a wide temperature range. As already described in Chapter 2, the glass transition temperature of a material alters the rate of change of the specific volume of a material above and below its  $T_g$ . The TMA apparatus shown in Fig. 3.28 uses a 3 mm ball point probe and a cylindrical sample to (i) measure the change in size of the material over a wide temperature range, (ii) to define the CTE of the material above and below  $T_g$  and (iii) to determine the glass transition temperature where this change in rate occurs.



*Figure 3.29. (a) The Mettler Toledo TMA/SDTA841e apparatus including (b) the sample configuration for testing of parameters.*

TMA experiments in conjunction with ASTM E831 [229] have been performed on selected materials in ESA’s ESTEC facility to determine CTEs over the operating range of the COPV tank with these measurements being used to predict the shrinkage of the liner over this temperature range. The tests were performed using a Mettler Toledo TMA/SDTA841e apparatus with an operating range of -150°C to

## Materials & Methods

600°C with cooling provided by an external source of LN2 to reach the low temperatures needed for the analysis. Fig. 3.30 shows that the applied force of the probe directly affects the measured change in sample size and so an applied force of 0.05 N was used to mitigate indenting of the sample during testing and to increase the accuracy of results [230].

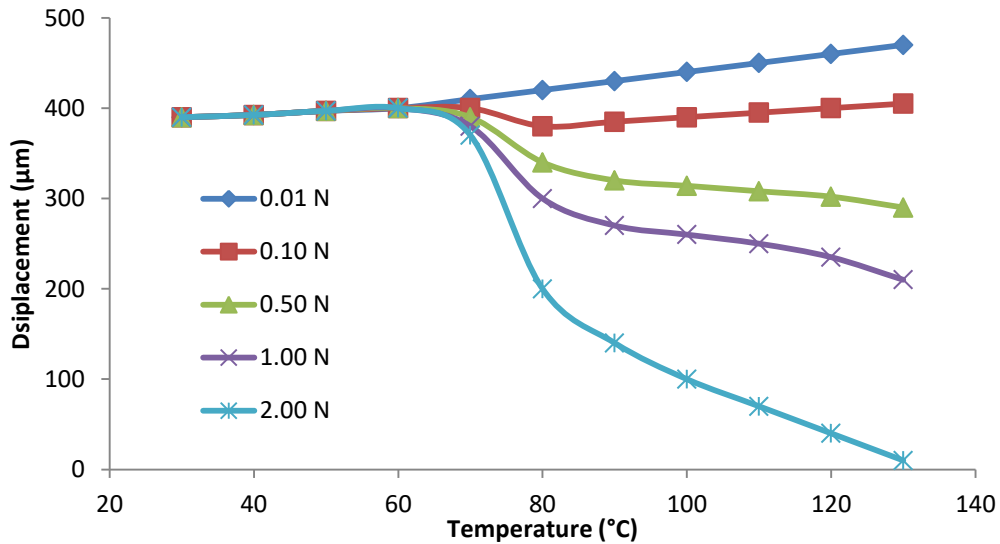


Figure 3.30. The effects of high applied force (above 0.10 N) during the TMA test procedure showing an improper calculation of CTE at higher temperatures (adapted from [230]).

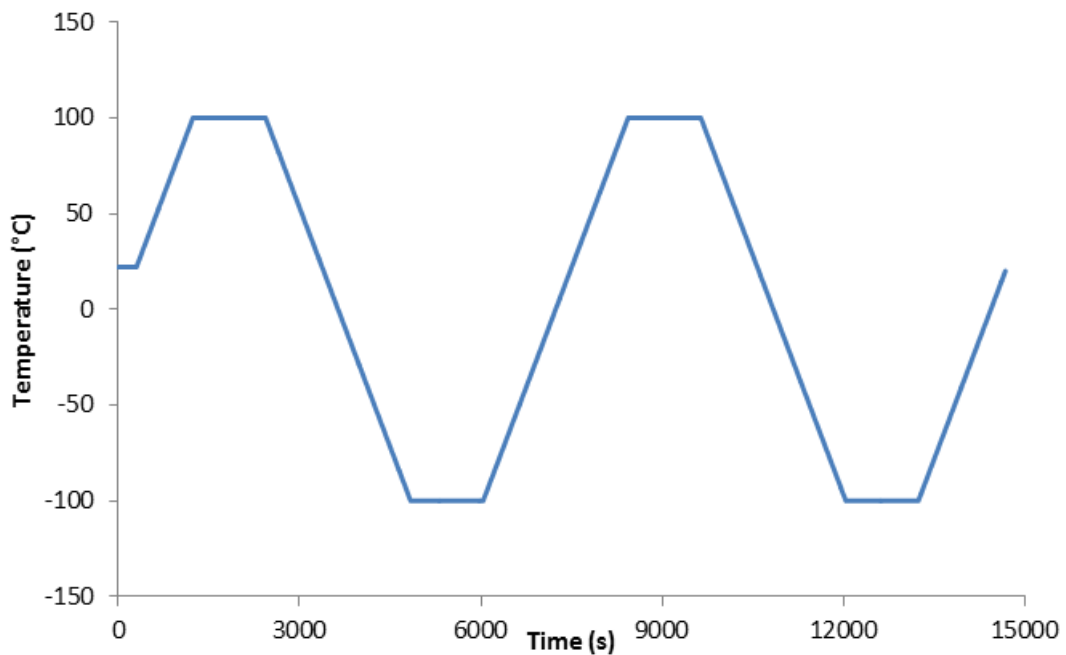


Figure 3.31. Temperature cycle used for CTE analysis of materials.

The temperature test scan followed a two cycle process whereby the sample was heated to 100 °C and cooled to -100 °C at a rate of 10 °C/min over two cycles to examine the effect of the thermal history on the value of the CTE as indicated in Fig. 3.31. In all cases, the sample followed the same curve for each cycle and so the first cycle has been used for the calculation of CTE values presented here above and below  $T_g$ , as this is the cycle which will be assessed for the COPV structure.

### 3.6.7. Nano-indentation Analysis

Nano-indentation is an analysis technique that characterises the mechanical properties of a material. It uses an indenter tip, with a known shape, to indent the sample while measuring the applied force and displacement during loading and unloading of the sample. These measurements allow for the calculation of a number of factors such as Young's Modulus and material hardness based on the sample indentation as shown in Fig. 3.32 [231-235].

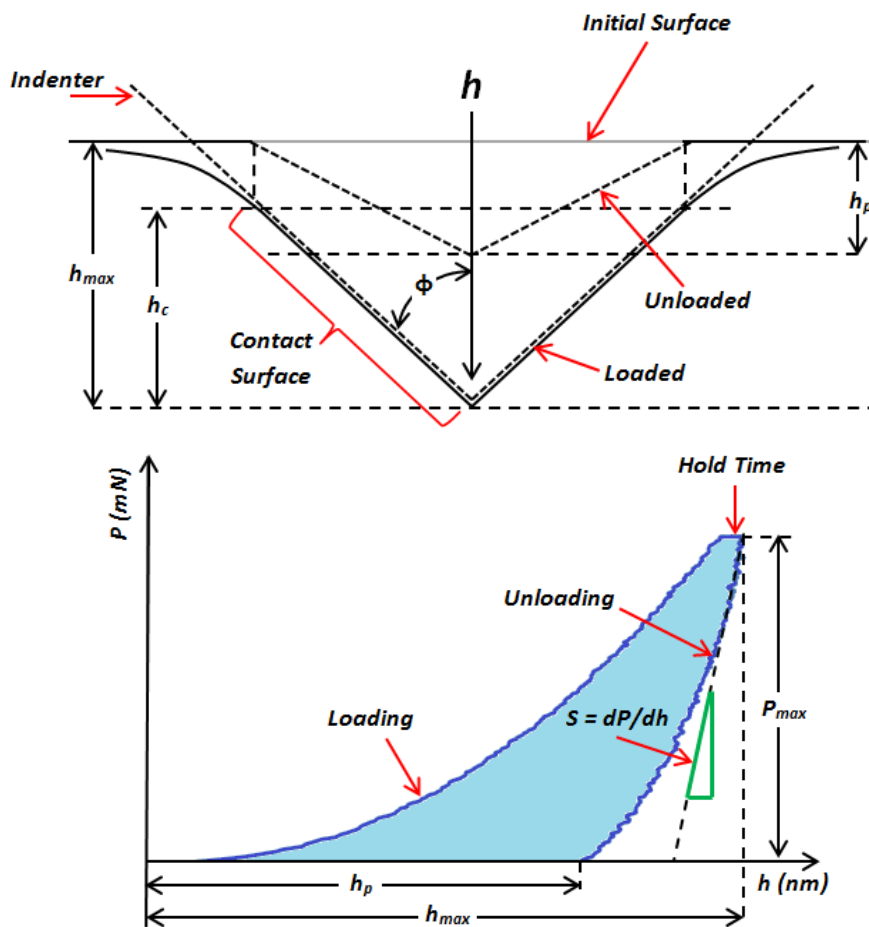


Figure 3.32. Overview of nano-indentation testing and the resulting force displacement graph [231-235].

The elastic modulus,  $E_{IT}$ , of the sample is calculated from the force displacement graph of the nano-indentation test by first assessing the unloading stiffness  $S$ . The unloading stiffness  $S$  was calculated from the derivative of the power law, in Eq. 3.14, which is fitted to the unloading curve (displayed in Fig. 3.32) to obtain the value of  $S$  via Eq. 3.15 [231-235]:

$$P = \alpha(h_{max} - h_p)^m \quad (3.14)$$

$$S = m\alpha(h_{max} - h_p)^{m-1} \quad (3.15)$$

where  $P$  is the applied load,  $\alpha$  is a geometric constant dependent on the indenter tip,  $h_{max}$  is the maximum displacement,  $h_p$  is the permanent displacement and  $m$  is the power law index ( $m = 2$  for a Berkovich tip [235]).

The contact area  $A(h_c)$  is then defined from the shape function [232, 233, 235]:

$$A(h_c) = C_0 h_c^2 + C_1 h_c + C_2 h_c^{1/2} + C_3 h_c^{1/4} \dots \quad (3.16)$$

where  $h_c$  is the contact depth defined earlier in Fig. 1, and  $C_0, C_1, C_2 \dots$  are constants determined by a curve fitting procedure. Once the stiffness and contact area have been calculated the reduced modulus  $E_r$  can then be found via [232, 233, 235]:

$$E_r = \frac{\sqrt{\pi}}{2\beta\sqrt{A(h_c)}} S \quad (3.17)$$

where  $\beta$  is an indenter dependent correction factor (equal to 1.034 for a Berkovich tip [232, 233, 235]:) and all other terms are as previously described. This then allows for the calculation of the elastic modulus  $E_{IT}$  via [231-235]:

$$E_{IT} = (1 - \nu_s^2) \left[ \frac{1}{E_r} - \frac{(1 - \nu_i^2)}{E_i} \right]^{-1} \quad (3.18)$$

where  $\nu_i$  and  $E_i$  are the Poisson's ratio and elastic modulus of the indenter tip (0.07 and 1141 GPa respectively [231-233]),  $\nu_s$  is the Poisson's ratio of the polymer (in this instance an assumed Poisson's value of 0.38 has been adopted for PEEK [236]), and  $E_r$  is the reduced elastic modulus as already described. Testing was performed with a nano-indenter (CSM Instruments SA, Switzerland) following ASTM E2546

[231] using a pyramidal Berkovich diamond indenter tip, in conjunction with the Oliver and Pharr method of material property analysis [235].

### **3.7. Conclusions**

The aforementioned test methods have been used throughout this thesis to determine important material properties and intrinsic characteristics of polymer materials and liner-overwrap designs while assessing the effects of large temperature changes and their effects on the internal structure of liner-overwrap configurations. Any changes from the stated standard practice given above have been highlighted in subsequent chapters with an every effort made to be as comprehensive as possible.

# 4. Material Characterisation and Permeability Testing

## 4.1. Chapter Overview

This chapter covers the results from all material characterisation testing and permeability analyses on prospective liner materials, including an analysis of forming temperature and crystallinity effects on permeability. The results presented are as follows:

- Material characterisation results including sieve testing, DSC testing and microscopic analysis of all powder materials tested
- Qualification of the NUI Galway permeability test apparatus and a review of the subsequent permeability tests conducted
- An assessment of the effects of forming temperature and air voids on permeability
- Permeability results from the ÉireComposites mass spectrometer permeability test apparatus
- X-ray CT scanning and DSC testing of the ÉireComposites tested samples with an analysis of the effects of void statistics, defects and crystallinity on permeability

Powder characterisation techniques were used to determine which materials exhibited the best properties for rotomoulding. The permeability testing was used to identify which materials exhibited the best barriers to helium permeation for further

testing as prospective liner materials. The effects of maximum temperature during the specimen forming process on crystallinity and void contents were also investigated with their effects on permeability quantified. A more intensive permeability analysis which utilised X-ray CT scanning to quantify void volume contents, average void radii and void position bias in polymer samples, was also conducted.

### **4.2. Material Characterisation**

The material characterisation includes an analysis of particle size distributions, the average particle size, the melting temperature of the materials tested and the crystallinity of the as-delivered powders along with a microscopic analysis of their respective particle shapes.

#### **4.2.1. Particle Size Distribution and Average Particle Size**

As already outlined in Chapter 2, powder quality is an important factor in the acceptability of a material for rotational moulding operations [50, 63, 66, 67] and so a sieve analysis based on ASTM D1921 [210] is used to determine the particle size distribution and average particle size of each powder material. The results are separated into Nylon and PVDF samples in Fig. 4.1 (specific rotomoulding grades) and PEEK samples in Fig. 4.2 (non-specific powder grades) to demonstrate the characteristics of a specific rotomoulding grade compared to non-specific grades. The Nylon and PVDF grades follow a similar sieve pattern and have comparable particle size distributions. The majority of particles for these materials are in the range of 100  $\mu\text{m}$  – 500  $\mu\text{m}$  which is the optimum range defined in Chapter 2. The Nylon and PVDF grades are specific rotomoulding grades and their near identical distribution pattern is taken here as the optimal result.

In contrast, the PEEK grades show different results, specifically the 150P and 150PF materials which deviate significantly from the optimal result at two different extremes. The 150P grade has a higher powder size distribution, from 500  $\mu\text{m}$  to 2000  $\mu\text{m}$ , which could lead to sub-optimal contact between particles during forming, creating larger void regions. The 150PF grade has a lower powder size distribution, from 60  $\mu\text{m}$  to 200  $\mu\text{m}$ , which could in turn lead to static build-up during rotation and clumping of particles, which could in turn reduce part consistency. Based on

sieve testing, the 1000P and 2000P PEEK polymers are the most suitable PEEK grades for rotational moulding, with only a slight deviation from the optimal particle size distribution. For both the 1000P and 2000P grades, the particle range is between 200  $\mu\text{m}$  and 1000  $\mu\text{m}$ . This is much closer to the optimal result, with a slight deviation towards a larger particle size.

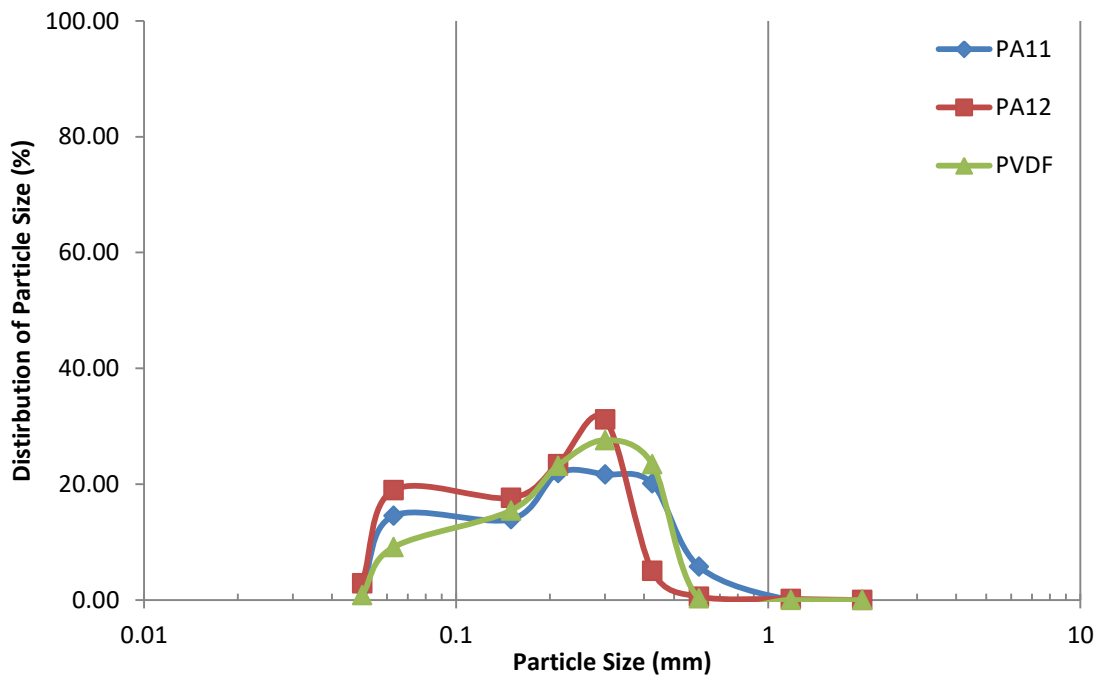


Figure 4.1. Particle distribution of PA11, PA12, PVDF and PE powders based on sieve test analyses.

The average particle size of each material is given in Table 4.1 with the PEEK grades showing significant differences in comparison to the Nylon and PVDF materials. The distribution of particles for each PEEK material has skewed their averages to regions which do not align properly with the optimal result, as demonstrated by the Nylon and PVDF grades which have average diameters around 300  $\mu\text{m}$ . The 1000P and 2000P PEEK grades have average particle diameters of 631  $\mu\text{m}$  and 542  $\mu\text{m}$  respectively, while the 150P and 150PF PEEK grades have diameters at 1830  $\mu\text{m}$  and 66  $\mu\text{m}$  respectively. Sieve testing only measures the size of particles; it gives limited information on the powder shape, which is just as important for rotomoulding operations.

## Material Characterisation and Permeability Testing

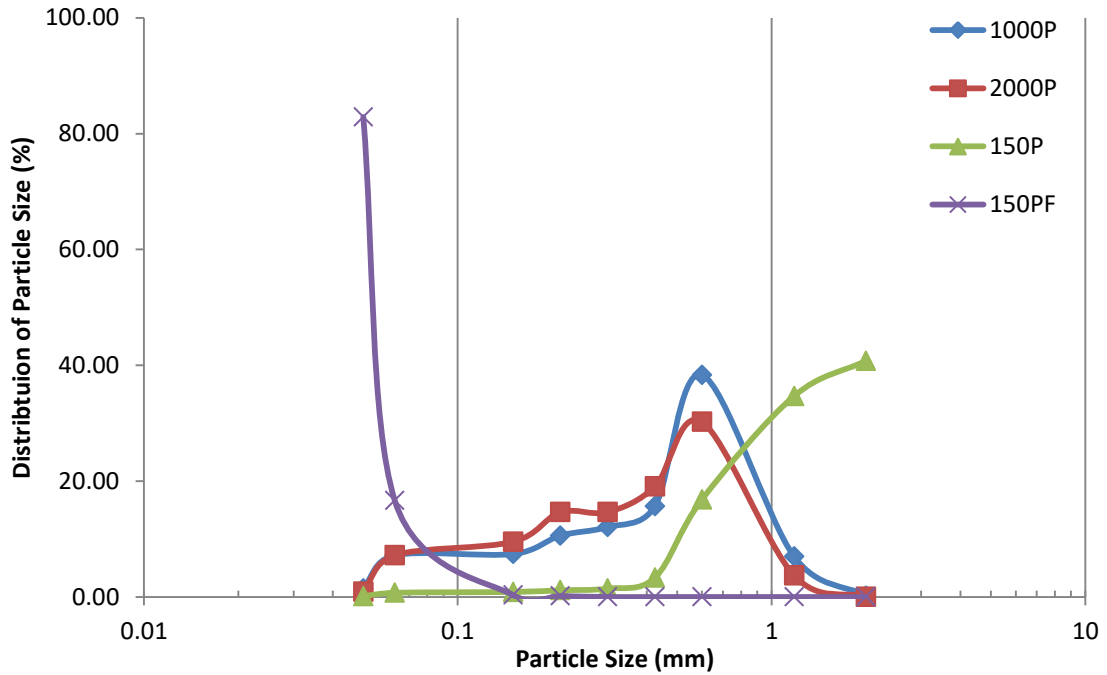


Figure 4.2. Particle distribution of PEEK 1000P, 2000P 150P and 150PF powders based on sieve test analyses.

Table 4.1. Material properties for powder materials from sieve testing and DSC testing.

Material	Particle Size ( $\mu\text{m}$ )	Melt Temperature ( $^{\circ}\text{C}$ )	Crystallinity (%)
1000P	631	346.19 ( $\pm 2.55$ )	41.60 ( $\pm 5.11$ )
2000P	542	344.18 ( $\pm 0.78$ )	45.97 ( $\pm 8.68$ )
150P	1830	343.08 ( $\pm 0.56$ )	48.39 ( $\pm 3.78$ )
150PF	66	340.86 ( $\pm 0.15$ )	45.75 ( $\pm 4.28$ )
PA11	331	186.5 ( $\pm 0.62$ )	22.37 ( $\pm 2.46$ )
PA12	261	176.16 ( $\pm 0.73$ )	23.94 ( $\pm 1.69$ )
PVDF	321	159.02 ( $\pm 1.62$ )	29.21 ( $\pm 2.26$ )

Note: All figures in brackets ( $\pm$ ) are a single deviation for the samples tested.

#### 4.2.2. Microscopy of Polymer Powders

Microscopic analysis has been used to determine the characteristic particle shape for each powder material. Small amounts of each material were placed under an optical microscope for analysis. A sample of the microscopy images obtained for each material is shown in Fig. 4.3.

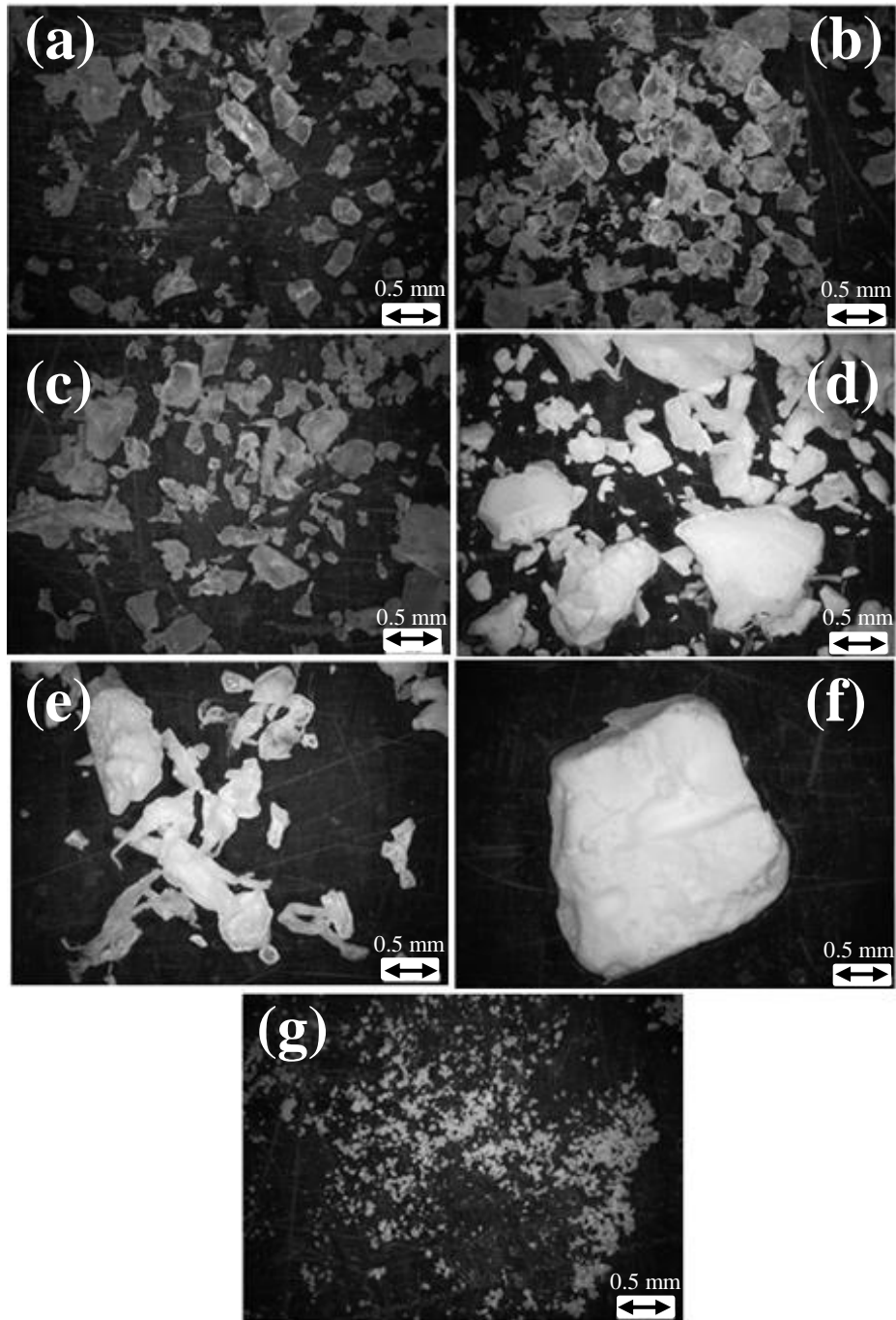


Figure 4.3. Microscopy images of the tested powders. (a) PA11, (b) PA12, (c) PVDF, (d) 1000P, (e) 2000P, (f) 150P, (g) 150PF.

The PA11 (Fig. 4.3 (a)), PA12 (Fig. 4.3 (b)) and PVDF (Fig. 4.3 (c)) powders are specific rotomoulding grades and so their microscopy images demonstrate the typical shapes of rotomoulding powder particles. Their particle sizes are also smaller showing a better consistency with the desired 300  $\mu\text{m}$  size goal. While the initial sieve testing results gave a favourable assessment for the 1000P and 2000P PEEK grades in regards to optimal powder size and distribution, further analysis of the powder using microscopy shows that their powder shape is not suited to rotomoulding. From Fig. 4.3 (d) and (e) it can be seen that the 1000P and 2000P grades have a complex shape consisting of a non-spherical particle with a long fibrils protruding from the main mass. This is a bi-product of the grinding process and is usually avoided for rotomoulding grades as the complex particle shape stops intimate contact with surrounding particles during melting, as this promotes void growth and hinders the consolidation of the melt as a whole [237]. The 150P and 150PF PEEK grades, in Fig 4.3 (f) and (g) respectively, have a superior spherical shape with no fibrils or complex shapes present and are more suitable for rotomoulding even if their average particle size falls well outside the optimal size distribution.

### 4.2.3. Melting Temperature

The melting temperature of each material is also important for identifying the forming parameters for specimen manufacturing. The melting temperature was obtained using DSC testing, as already outlined in Chapter 3, from the peak in the endothermic curve in the DSC graph. For the PEEK materials the melting temperature was between 340  $^{\circ}\text{C}$  to 347  $^{\circ}\text{C}$  with small deviations between individual materials. The PA11 and PA12 materials have average melting temperatures of 186.50  $^{\circ}\text{C}$  and 176.16  $^{\circ}\text{C}$  respectively whereas the PVDF material has the lowest average melting temperature of 159.02  $^{\circ}\text{C}$  as shown in Table 4.1. All materials fall above the operating range of the tank (50  $^{\circ}\text{C}$  to -190  $^{\circ}\text{C}$ ) as defined earlier and so all materials pass this requirement with a significant factor of safety. Obtaining the melting temperature also allows for the setting of more accurate forming parameters which will reduce the likelihood of degradation at unnecessarily higher processing temperatures. Examples of the typical DSC results obtained from each material are presented in Appendix B.

#### **4.2.4. Crystallinity**

The crystallinity of materials is also very important for permeability testing as it has been shown that higher crystallinity leads to lower permeabilities [91, 94, 238, 239]. From the results given in Table 4.1 it is clear for PEEK samples that the 150P sample has the lowest average crystallinity at approximately 42% while the 1000P has the highest average crystallinity at 48%. The 150P and 150PF samples have similar average crystallinities at around 46% but the standard deviation of the 150PF grade is quite significant. The PVDF powder has a crystallinity percentage of 29% while the Nylon materials have the lowest crystallinity at near 23%. The results are also only related to the as-delivered form of the material. The crystallinity properties are subject to change for all materials after they have been formed in any process, as the cooling rates imposed on each sample will inherently alter the crystalline structure.

### **4.3. Permeability Tests – NUI Galway**

#### **4.3.1. Qualification Testing PVC**

As already discussed, a permeability test apparatus was constructed in NUI Galway to provide an in-house test method for polymer permeability analysis. The apparatus was validated using PVC sheet material that had already been tested in ÉireComposites and this result was used for acceptance of the apparatus via repeatability and accuracy. The ÉireComposites PVC test was performed with a 1 bar pressure difference while the NUI Galway tests were performed with a 2 bar pressure difference (to decrease the time taken to reach steady state conditions). From the consistency of results in Fig. 4.4 between different test methods the NUI Galway apparatus is accurate and repeatable with little scatter present. The ten PVC samples tested are nominally uniform, as they were all taken from the same sheet of PVC. Hence the limited scatter exhibited by the results in Fig. 4.4 indicates an accuracy of  $\pm 10\%$  for permeability.

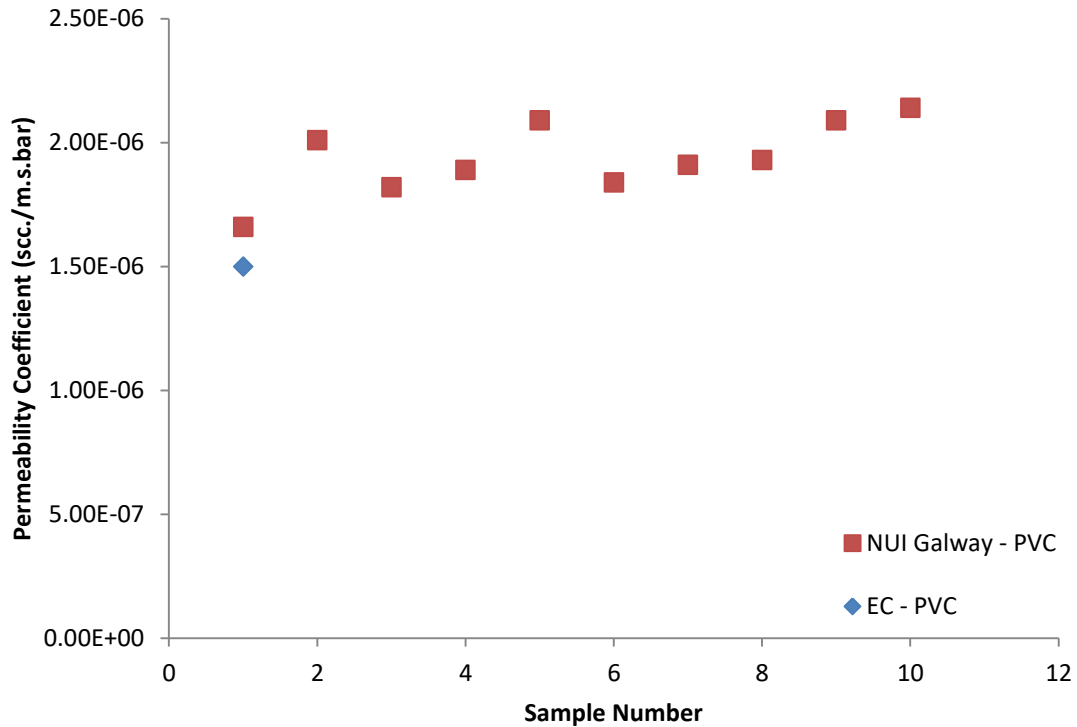


Figure 4.4. Measured permeability coefficients of PVC samples from the two different permeability apparatus.

### 4.3.2. Permeability Tests

The leak rates of prospective liner materials, formed on a hot plate surface at different maximum temperatures using the thermal cycles outlined in Fig 4.5 (PEEK), 4.6 (PA11 and PA12) and 4.7 (PVDF), were measured using the NUI Galway permeability test apparatus. Three samples of each material formed at three different temperatures, (i.e. nine tests per material) were tested at a pressure difference of 2 bar with results given in Table 4.2. From the permeability results in Table 4.2, the PVDF material has distinguished itself as the best barrier to permeation with a permeability coefficient of  $5.85 \times 10^{-7}$  scc/m.s.bar. It is followed by PA11, PA12, 1000P, 150P and 150PF materials with permeability coefficients ranging between  $6.00 \times 10^{-7}$  scc/m.s.bar to  $12.00 \times 10^{-7}$  scc/m.s.bar. The 2000P material has the highest permeability coefficient at a value above  $13.59 \times 10^{-7}$  scc/m.s.bar. This shows that the PVDF material is the best barrier to permeation and as such is the most promising candidate for future polymer liners based in the NUI Galway rig test results.

## Material Characterisation and Permeability Testing

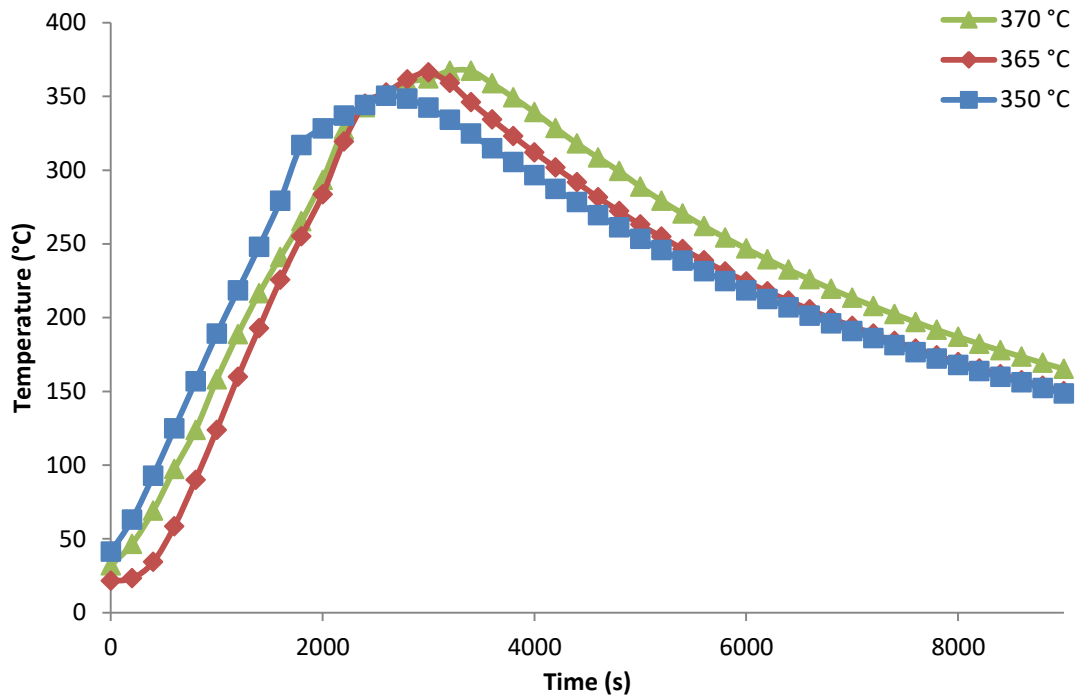


Figure 4.5. Heating cycles for hot plate formed PEEK samples tested using the NUI Galway permeability test apparatus.

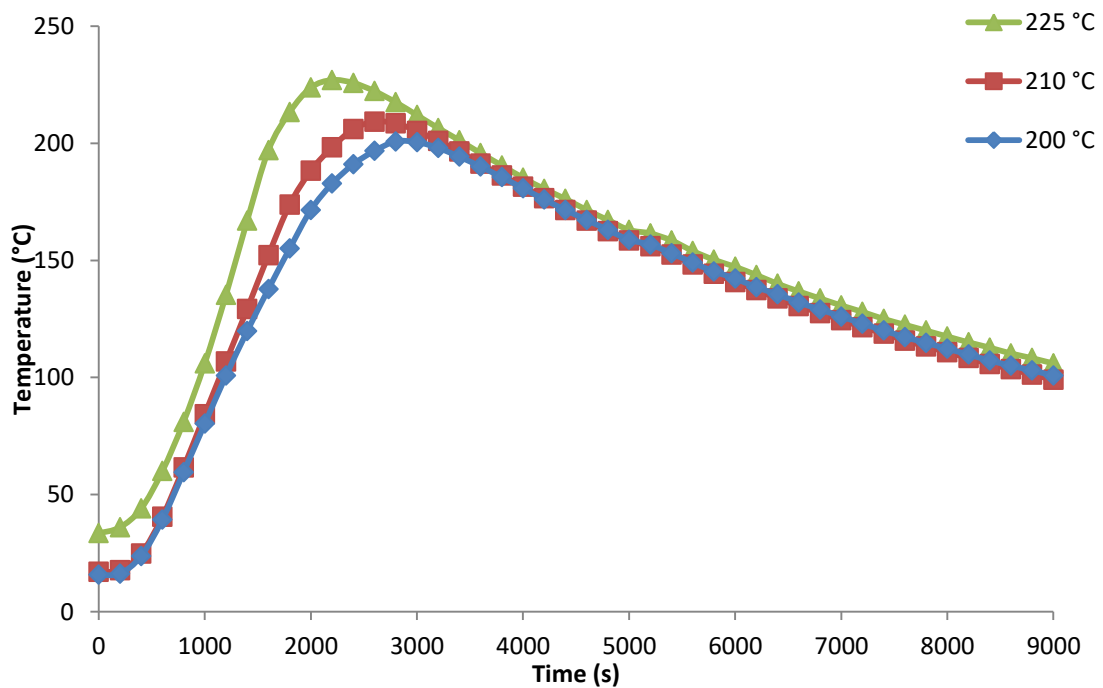


Figure 4.6. Heating cycles for hot plate formed Nylon samples tested using the NUI Galway permeability test apparatus.

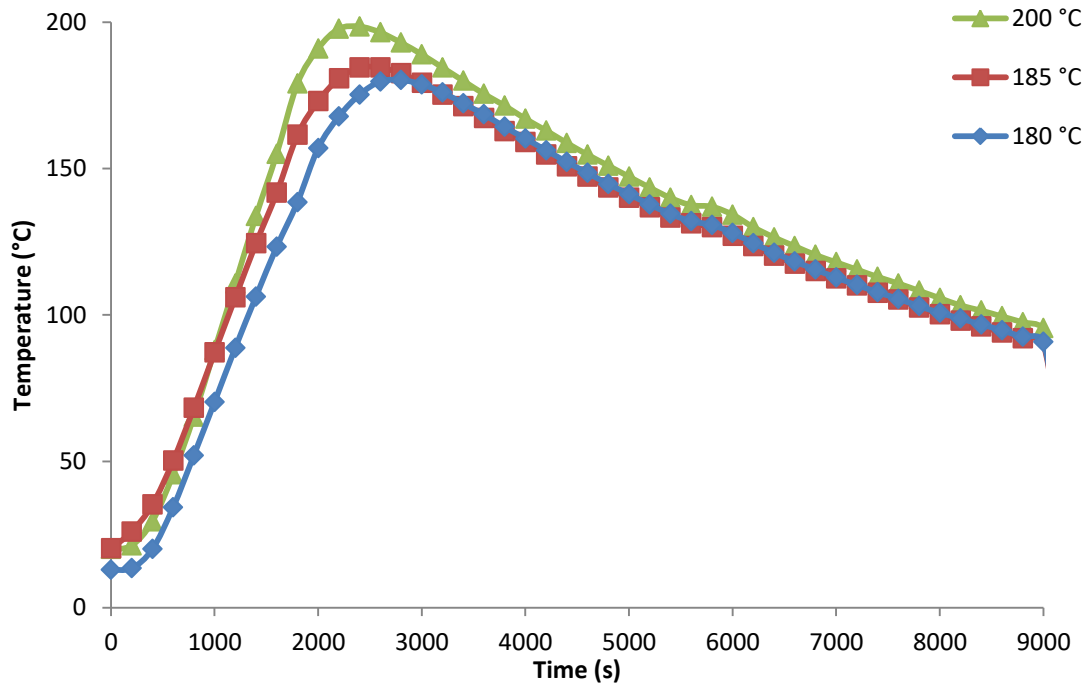


Figure 4.7. Heating cycles for hot plate formed PVDF samples tested using the NUI Galway permeability test apparatus.

An increasingly higher hold temperature has been used in each subsequent formation of samples to examine the effects of hold temperatures on permeability and void contents. The higher forming temperatures should theoretically reduce the void content [64], and hence the permeability, and so the expectation would be that the highest forming temperature would produce the best liner material (so long as polymer degradation was not present).

From the results in Table 4.2 for permeability coefficient measurements it can be seen that there is limited improvement in permeability based on increased forming temperatures, with the only significant change being seen in the 2000P material which has seen a reduction from  $16.78 \times 10^{-7}$  scc/m.s.bar to a minimum of  $13.59 \times 10^{-7}$  scc/m.s.bar. For all other materials, the increase in forming temperature has either caused degradation of the sample, which has led to an increased rate of permeability, or the void content has not been reduced to a level which has affected the permeability of the sample significantly. The differences in sample thickness will also impart a varied crystallinity percentage through the thickness of the sample due to the different cooling rates imposed on either side of the sample during the cooling phase of the hot plate forming process.

Table 4.2. Permeability coefficients for all liner materials tested using the NUI Galway permeability rig.

	Thickness (mm)	Permeability Coefficients ( $\times 10^{-7}$ scc/m.s.bar)		
Forming Temp ( $^{\circ}$ C)		350	365	370
1000P	2.31 ( $\pm 0.17$ )	11.64 ( $\pm 0.53$ )	11.68 ( $\pm 3.07$ )	11.46 ( $\pm 2.15$ )
2000P	2.29 ( $\pm 0.13$ )	16.78 ( $\pm 2.21$ )	13.59 ( $\pm 1.30$ )	14.25 ( $\pm 1.62$ )
150P	3.55 ( $\pm 0.26$ )	9.38 ( $\pm 0.39$ )	11.13 ( $\pm 2.45$ )	10.79 ( $\pm 0.78$ )
150PF	4.38 ( $\pm 0.20$ )	10.26 ( $\pm 0.79$ )	11.60 ( $\pm 1.73$ )	11.73 ( $\pm 0.23$ )
Forming Temp ( $^{\circ}$ C)		200	210	225
PA11	5.55 ( $\pm 0.18$ )	7.14 ( $\pm 1.01$ )	5.85 ( $\pm 2.48$ )	7.48 ( $\pm 0.34$ )
PA12	5.19 ( $\pm 0.20$ )	8.80 ( $\pm 1.51$ )	11.11 ( $\pm 1.13$ )	10.37 ( $\pm 1.24$ )
Forming Temp ( $^{\circ}$ C)		180	185	200
PVDF	4.96 ( $\pm 0.20$ )	5.17 ( $\pm 0.62$ )	5.25 ( $\pm 0.54$ )	6.04 ( $\pm 2.03$ )

Note: pressure difference = 2 bar, average test time of 70 -100 hours.

### 4.3.3. Void Volume Fraction and Average Void Radius

An assessment of the void volume fraction of all samples tested has been conducted to determine the change in void volume fraction and average void radius, based on changes in the maximum forming temperature. Two different locations have been assessed; the surface which was in contact with the hot plate mould surface and the cross section of the sample. Four images have been taken at each location for every sample tested (equating to 8 images per sample and 72 images for each material).

The mould surface results for void volume fraction and average void radius are presented in Table 4.3. The void volume fraction at the mould surface ranges from 0 to 20%. Increases in the maximum forming temperature have not resulted in a consistent reduction in the void volume fraction with no clear trend visible. The

## Material Characterisation and Permeability Testing

150PF material has the highest void volume fraction at the mould surface with 20% voids contained at this location. This is almost double that of any other PEEK material tested. The PVDF material has a much higher void volume fraction (at above 5%) than its PA11 counterpart (below 3%). This shows that there is room for improvement of the PVDF material's low permeability characteristics if a further removal of voids can be achieved. However the permeability coefficient has followed a relatively similar trend to the void volume fraction measurements, with higher void volume fractions giving higher permeability coefficients for samples of the same material.

*Table 4.3. Void volume fraction and average void radius results at the mould wall.*

Forming Temp (°C)	Mould Wall Void Volume Fraction (%)			Mould Wall Average Void Radius (µm)		
	350	365	370	350	365	370
1000P	3.13	9.02	0.70	156	197	111
2000P	8.49	0.24	6.38	171	46	276
150P	1.72	3.39	2.92	105	156	163
150PF	18.93	20.77	18.59	99	104	94
Forming Temp (°C)	200	210	225	200	210	225
PA11	2.41	0.77	0.44	169	167	123
PA12	0.00	0.00	0.00	0.00	0.00	0.00
Forming Temp (°C)	180	185	200	180	185	200
PVDF	7.08	5.72	8.85	93	96	121

The change in average void radius has not followed a linear trend either. The void data shows that the 1000P, 2000P and 150P materials have lower void fractions with larger voids at the mould surface, with average void radii above 150 µm. The data

## Material Characterisation and Permeability Testing

shows that the 150PF material has a higher void volume fraction of smaller voids with an average void radius below 100  $\mu\text{m}$ . The increase in temperature has decreased the size of voids in the PA11 samples but increased them in the PVDF samples. The average size of the voids at the surface of each material are quite small at between 100  $\mu\text{m}$  and 160  $\mu\text{m}$  which is consistent with those measured in the PEEK samples at the mould surface

*Table 4.4. Void volume fraction and average void radius results in the cross section.*

Forming Temp ( $^{\circ}\text{C}$ )	Cross Section Void Volume Fraction (%)			Cross Section Average Void Radius ( $\mu\text{m}$ )		
	350	365	370	350	365	370
1000P	0.13	0.02	0.26	72	30	101
2000P	0.00	0.00	0.00	0.00	0.00	0.00
150P	2.34	1.08	0.91	305	207	190
150PF	1.59	1.18	0.22	252	217	133
Forming Temp ( $^{\circ}\text{C}$ )	200	210	225	200	210	225
PA11	0.96	0.80	3.22	185	236	402
PA12	0.00	0.00	0.00	0.00	0.00	0.00
Forming Temp ( $^{\circ}\text{C}$ )	180	185	200	180	185	200
PVDF	3.10	2.93	2.70	115	126	134

Table 4.4 shows the cross sectional void statistics of the tested materials. The volume fractions are much lower than for the mould surface with volume fractions below 3.5% for all samples tested. The 2000P material shows no voids (above 5-10  $\mu\text{m}$  in diameter) in its cross section despite having the highest measured permeability of the PEEK materials tested. The lack of voids in the 2000P material is not due to having better flow properties as it has the highest viscosity and molecular weight of

all PEEK materials tested. It is more likely that there are voids in the 2000P samples but that they are thin and not spherical in nature and so they are difficult to image and identify using microscopy techniques. This is confirmed later by the use of X-ray CT imaging which highlights thin voids in the 2000P samples structure which have increased permeation rates through the 2000P samples.

The 150P and 150PF materials are seen to have dramatically higher void volume fractions and void radii than the 1000P and 2000P materials. The PA12 material has shown no voids present (above 5-10  $\mu\text{m}$  in diameter) at any forming temperature and so all results relating to PA12 have given a void volume fraction of 0%. As already outlined, the PA11 and PVDF are the best barriers to permeation with the lowest permeability coefficients measured, it is however much more difficult to compare void statistics between these materials as they are from different families of polymer materials. The void volume fraction is quite consistent for each material, except for the PA11 sample at the higher forming temperature which has increased by nearly 2%, which is indicative of the higher permeability coefficient measured for these samples. The measured average void radius in Table 4.4 is also quite similar to previous results, but again the higher forming temperature of the PA11 sample has a much higher average void size at over 300  $\mu\text{m}$  than all other materials tested which have average void radii between 100  $\mu\text{m}$  and 250  $\mu\text{m}$ .

From an assessment of the rheological properties of the PEEK materials, the 150P and 150PF grades have a lower molecular weight and a lower viscosity than their 1000P and 2000P counterparts. This should lead to a lower void volume fraction in the 150P and 150F materials (due to their superior flow properties) but this is not the case. Instead the 150P and 150PF samples have higher void volume fractions in nearly all test cases while exhibiting lower permeabilities. This is more likely due to the void shapes contained within the polymer cross sections as the 150P and 150PF materials contain spherical voids in their internal structure while the 1000P and 2000P materials have longer, thinner voids in their inner structure (as will be demonstrated later via X-Ray CT scanning), which is the contributing factor to their inferior permeability properties.

## 4.4. Permeability Tests – ÉireComposites

### 4.4.1. Permeability Tests

The leak rates of prospective liner materials formed on a hot plate surface at different maximum temperatures, using the thermal cycles outlined in Fig 4.8, were measured using the ÉireComposites permeability test apparatus. Three samples of each material were tested at a pressure difference of 1 bar. The test conditions and the permeability results are presented in Table 4.5 along with all void volume fraction measurements and crystallinity test data.

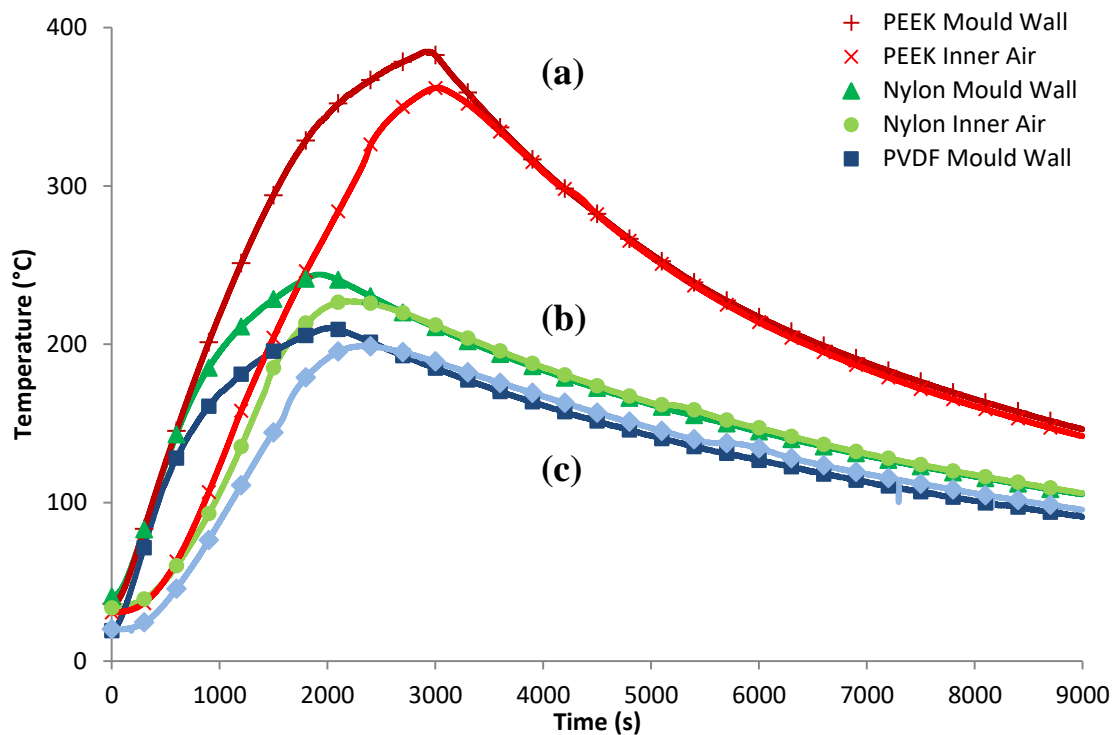


Figure 4.8. The heating cycle of (a) the PEEK samples, (b) the Nylon (PA11 and PA12) samples and (c) the PVDF sample.

From the results it is clear that the PA12, 1000P, 150P and 150PF materials have very similar permeability coefficients at around  $7.0 \times 10^{-7}$  scc/m.s.bar while the 2000P grade retains the highest permeability coefficient at a value of  $11.7 \times 10^{-7}$  scc/m.s.bar. PA11 and PVDF have the lowest permeability coefficients of  $3.36 \times 10^{-7}$  scc/m.s.bar and  $3.46 \times 10^{-7}$  scc/m.s.bar respectively. Hence, these tests indicate that they are the best candidates for low permeability liners.

Table 4.5. Permeability results based on the ÉireComposites measured helium leak rates at a 1 bar pressure difference including void statistics and crystallinity results.

Material Sample	Thickness (mm)	Test Time (hrs)	Leak Rate ( $10^{-5}$ scc/m <sup>2</sup> .s)	P ( $10^{-7}$ sec.m/m <sup>2</sup> .s.bar)	D ( $10^{-11}$ m <sup>2</sup> /s)	S ( $10^3$ scc/m <sup>3</sup> .bar)	V <sub>f</sub> (%)	R <sub>v</sub> (µm)	Crystallinity (%)
PEEK 1000P	2.40	9.00	35.23	8.25	18.27	4.54	1.72	149.91	31.6 (±5.6)
2000P	2.13	23.00	52.27	11.67	18.63	6.50	7.99	265.98	33.8 (±5.6)
150P	3.13	24.00	23.47	7.34	9.60	7.69	3.01	144.15	30.3 (±7.9)
150PF	4.42	27.00	16.00	6.52	12.12	5.44	6.98	103.50	32.6 (±7.1)
Nylon PA11	5.75	26.00	6.27	3.36	23.93	1.41	11.76	307.71	22.4 (±6.1)
PA12	5.23	26.00	12.75	6.59	38.43	1.80	0.00	0.00	21.0 (±6.1)
PVDF PVDF	5.09	36.00	7.55	3.46	8.47	4.11	3.62	128.13	41.4 (±3.2)

The diffusion coefficient has been calculated as part of the time lag method of calculating the permeability coefficient. This coupled with Eq. 3.3 allows for the calculation of the diffusion coefficient based on the relationship between the thickness and the time taken to reach the steady state leak rate.

The diffusion coefficient  $D$  is therefore a representation of the time taken to reach steady state conditions based on the sample thickness. Results showing that the Nylon materials are the quickest to reach steady state conditions based on their thickness with values above  $2.4 \times 10^{-10} \text{ m}^2/\text{s}$ , followed by the PEEK materials around  $1.5 \times 10^{-10} \text{ m}^2/\text{s}$  and finally PVDF at a value below  $1.0 \times 10^{-10} \text{ m}^2/\text{s}$ . This is useful in determining the length of time to reach steady state conditions as polymer liners for short term storage may be acceptable for short-use COPV tanks (less than 24hr hold times) if their diffusion coefficients are sufficiently low.

The results for solubility coefficient  $S$  are almost the opposite to those found with the diffusion coefficient as the Nylon materials exhibit the lowest solubility coefficients,. This shows why the Nylon materials still exhibit the lowest permeability coefficient (the product of diffusion and solubility coefficients) as they have a significantly lower solubility than all other materials tested at values below  $2.0 \times 10^3 \text{ scc/m}^3\text{bar}$ . The PEEK and PVDF materials have much higher values ranging from  $4.0 \times 10^3 \text{ scc/m}^3\text{bar}$  up to  $8.0 \times 10^3 \text{ scc/m}^3\text{bar}$ .

### 4.4.2. Crystallinity

The crystallinity of the as-formed materials has also been assessed with results again presented in Table 4.5. The PEEK materials have crystallinity percentages around 30% while the PA11 and PA12 materials have percentages of 22.37% and 21.00% respectively. The crystallinity of the PVDF has risen considerably from its initial powder measurement in Table 4.1 with a 41.43% crystalline structure. The consistency of the crystallinity percentages in the PEEK materials can be explained by the use of the same cooling rate in the forming of all samples, but it also highlights that differences in permeability between materials are not based on differing crystallinity percentages. The 150PF sample has the highest crystallinity of all PEEK samples tested at 33.79%, and also has the lowest permeability coefficient of all PEEK materials tested. Results for the 150P and 1000P materials are consistent with this as they have average crystallinity percentages of 31.65% and 30.31%

respectively, with correspondingly higher permeabilities. Although the 2000P material would then be expected to have the lowest crystallinity, due to having the highest permeability, this is not the case as the 2000P material has an average crystallinity of 32.63%. An explanation for this is given in the section below on the basis of measured internal voids and defects affecting the permeability of the 2000P material.

#### 4.4.3. Void Volume Fraction and Average Void Radius

A comprehensive analysis of void volume fractions,  $V_f$ , and average void radii,  $R_v$ , was also conducted on all of the samples tested. X-ray CT imaging was used to determine the void volume fraction and average void radius in each material along with an analysis of void location bias and void structure. Figs. 4.9 and 4.10 demonstrate the void analysis achieved in PVDF and PEEK 150PF materials respectively, with the defect analysis software highlighting internal voids of different volumes. The void volume fraction contained within each material is predicted to affect permeability with higher void percentages leading to higher permeabilities [64].

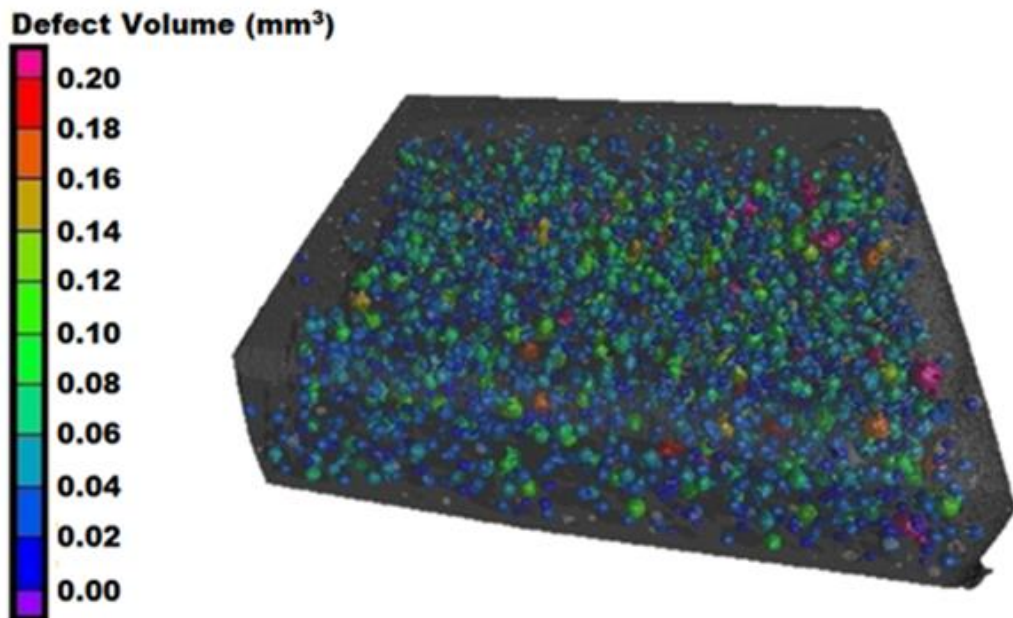
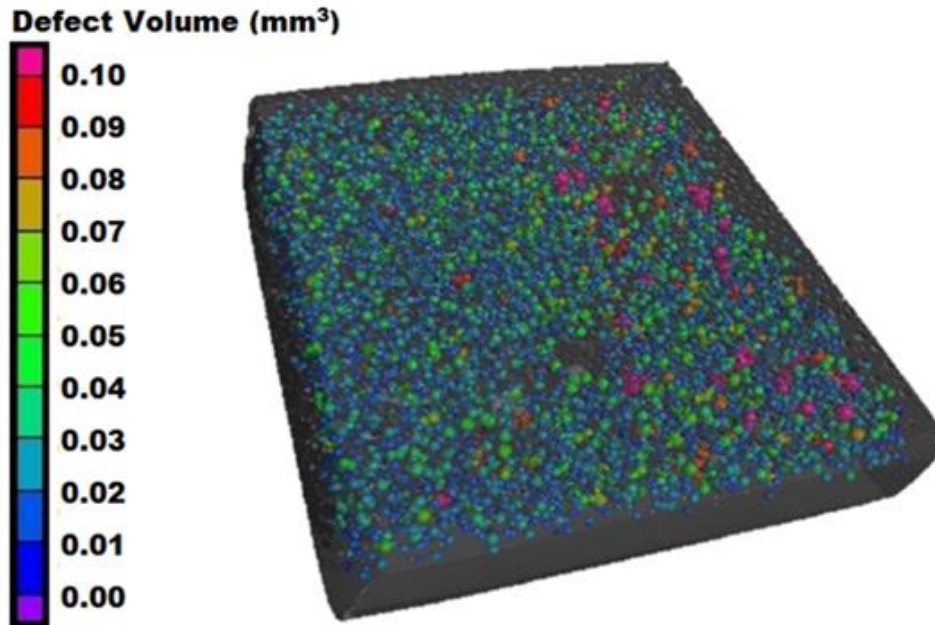


Figure 4.9. X-ray CT scan coupled with defect analysis software showcasing the internal voids in a PVDF sample.



*Figure 4.10. X-ray CT scan coupled with defect analysis software showcasing the internal voids in a PEEK 150PF sample.*

Table 4.5 gives an overview of the internal void volume fraction in each material as measured via the X-ray CT defect analysis tool. The PVDF, 150P and 150PF materials have the highest internal void percentages between 3.0 – 4.0% of their total volume. This is followed by PA11 at around 1% void volume fraction, the Evonik PEEK grades at < 1% and finally the PA12 grade with 0% voids detected. For the PVDF and Victrex materials, this void percentage will affect permeability with significant room for improvement via void removal techniques during processing. The PA12 material is the only one without any voids present and so represents the lowest permeation rate achievable for the material with the current production method. The average void radius has also been included in Table 4.5 with most voids falling in a range between 200  $\mu\text{m}$  and 300  $\mu\text{m}$  for the average void radius.

The PA11 and PA12 results for crystallinity and void volume fraction have resulted in counter-intuitive results for each materials respective permeability. PA12 has a higher permeability than PA11, but it also has a lower void volume fraction. However, PA11 has a lower permeability and a higher average crystallinity. It is assumed that the PA12 has a lower molecular weight and viscosity than PA11 as the low void volume fraction in PA12 samples indicates that it has better melt flow

properties. Therefore the result shows that the differences in crystallinity could be the deciding factor in the reduction in permeability for the PA11 samples.

This analysis of voids has also been coupled with studies of the void volume size in Fig. 4.11 where the volume of voids has usually ranged from  $0.40 \text{ mm}^3$  down to  $0.01 \text{ mm}^3$  for varying percentages of the total number of voids in each material. It can be seen here that the 1000P and 150PF materials have a higher percentage of smaller voids below  $0.10 \text{ mm}^3$  while PA11 has a collection of larger voids above the  $0.10 \text{ mm}^3$  mark.

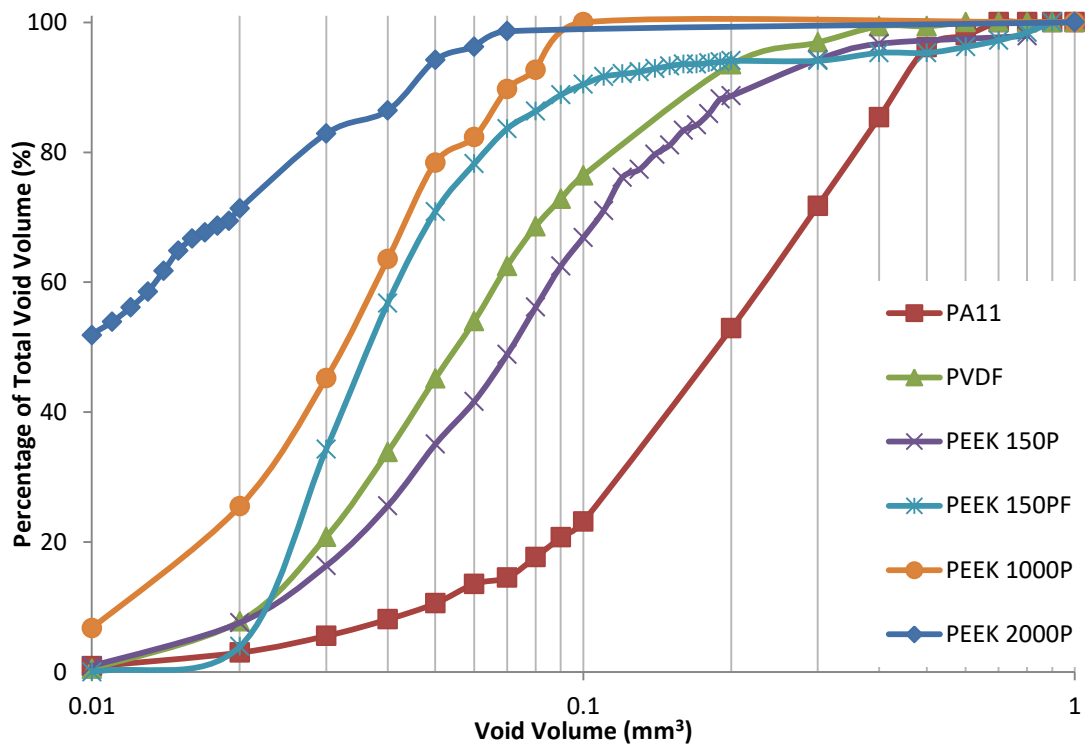


Figure 4.11. Graph displaying the percentage of void volume fraction of which the average void volume was made up from.

The void location bias has also been assessed with the defect analysis tool whereby Fig. 4.12 shows the percentage of voids located through the thickness of a material from the mould surface on the left of the graph to the free side of the sample on the right side of the graph. The void content in rotationally moulded parts is influenced by a number factors but it is controlled by the applied heating cycle [52, 178]. During the forming process, as the powder particles melt and coalesce together, the collapsing structure traps air beneath the surface in a pattern similar to that of the of the majority of materials tested here (PVDF, 1000P, 150P and 150PF) with a higher

distribution of voids located at the mould surface side of the sample. In these samples, the applied heating cycle has not allowed for sufficient time for voids to diffuse into the polymer melt and so they have become trapped in the sample cross section [63, 71]. Due to the viscosity of the polymer melt, the bubbles do not rise and so diffusion is the main method of void removal [63, 71]. For the samples with void bias at a location closer to the free surface and minimal voids throughout the rest of the cross section, such as in the PA11 and 2000P materials, the heating cycle has provided enough time for the voids in these specific materials to diffuse into the melt (starting at the mould surface side closest to the heat source) but has still trapped air voids at locations nearer the free surface side [50, 63].

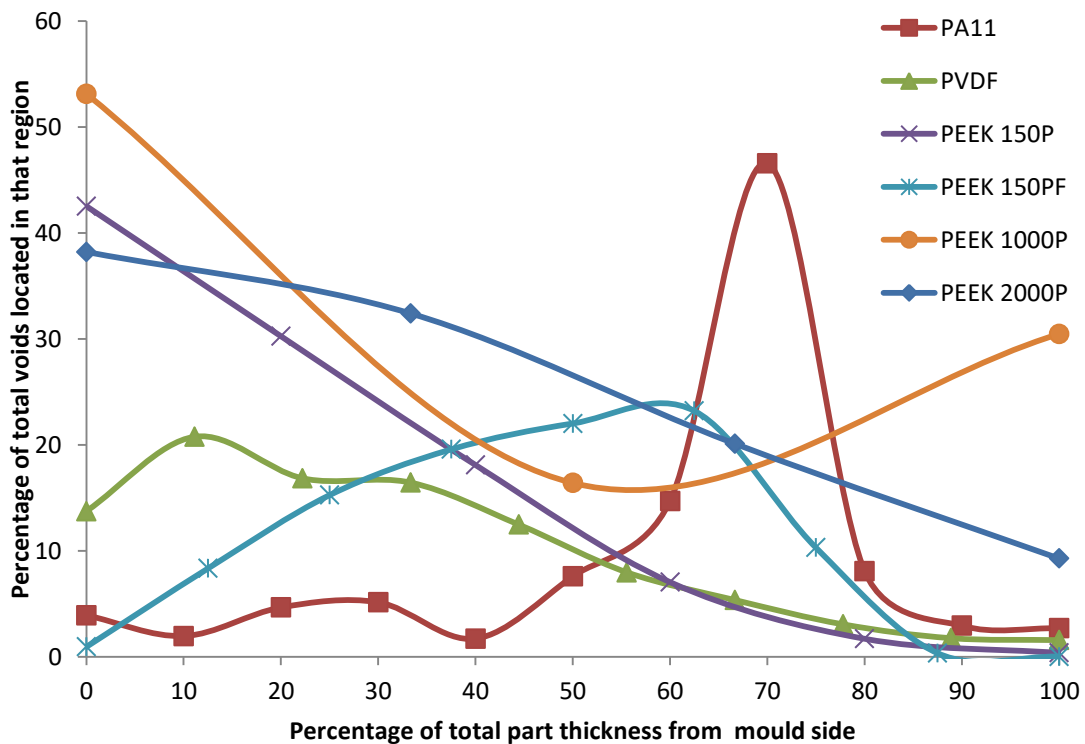
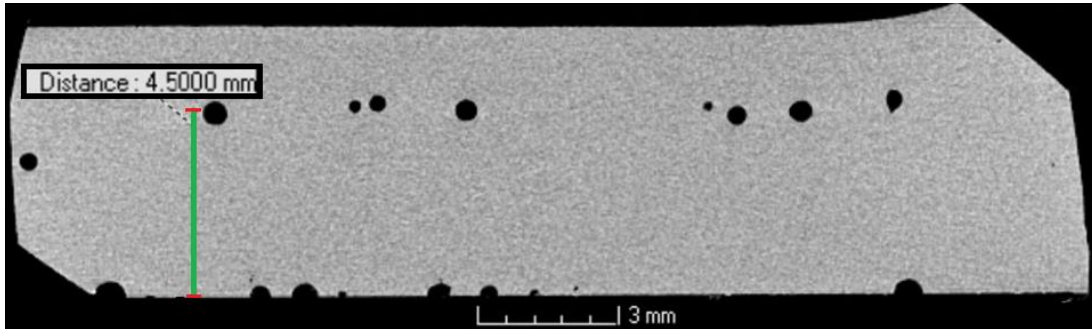


Figure 4.12. Void location as a percentage of the total number of voids in each sample.

An example of the bias of void locations is highlighted in Fig. 4.13 where voids in a PA11 sample can clearly be seen to be located mostly in a region 3.5 – 4.5 mm from the mould surface at the bottom of the image. For most other samples the voids are located towards the mould surface with the side free to the air having a lower void distribution. The main drawback to the X-ray CT scanning used here is that the defect analysis only includes internal defects in its analysis. This is because the

software needs to define the surface of the sample to distinguish between the solid material and surrounding air, which removes surface voids and defects from the analysis as shown in Fig. 4.14. This has led to lower predictions of void contents, specifically in the 1000P and 2000P materials, which are important for the permeability analyses, as will be shown.



*Figure 4.13. X-ray CT scan showing void location bias in a PA11 sample in a horizontal region around 4.0 mm away from the mould surface at the bottom of the image.*

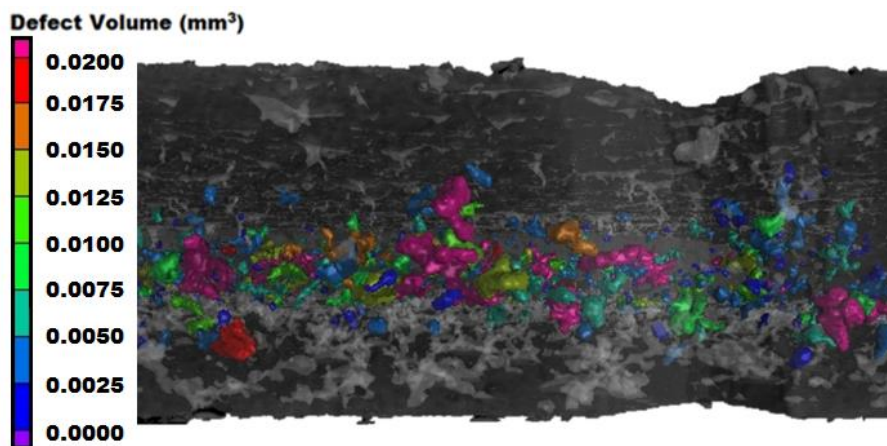


*Figure 4.14. Highlighted voids in a 2000P transparent X-ray CT view with the unused surface defects also visible having a lighter grey colour.*

While it is difficult to compare void statistics across different materials, as inherent rheological and particle shape properties are a major influence on void formation, certain conclusions can be drawn from a coupled analysis of the permeability results and void statistics. For the PVDF material, a reduction in the void content should lead to a further reduction in the permeability of the material, meaning that it has more room for improvement in regards to barrier properties. For the Nylon materials, PA11 is clearly the better permeation barrier as it maintains a lower permeation rate

## Material Characterisation and Permeability Testing

than PA12, even with 1% voids contained within its internal structure. A more comprehensive analysis of the effect of voids and internal defects can be carried out from an analysis of the PEEK materials tested. From the void statistic results it would suggest that the Evonik PEEK materials (1000P and 2000P) should have lower permeation rates due to their lower void contents, but this is not the case. In fact the Victrex PEEK grades (150P and 150PF) have a much lower permeability than the Evonik PEEK grades (1000P and 2000P), even with an almost 3% higher void content. .

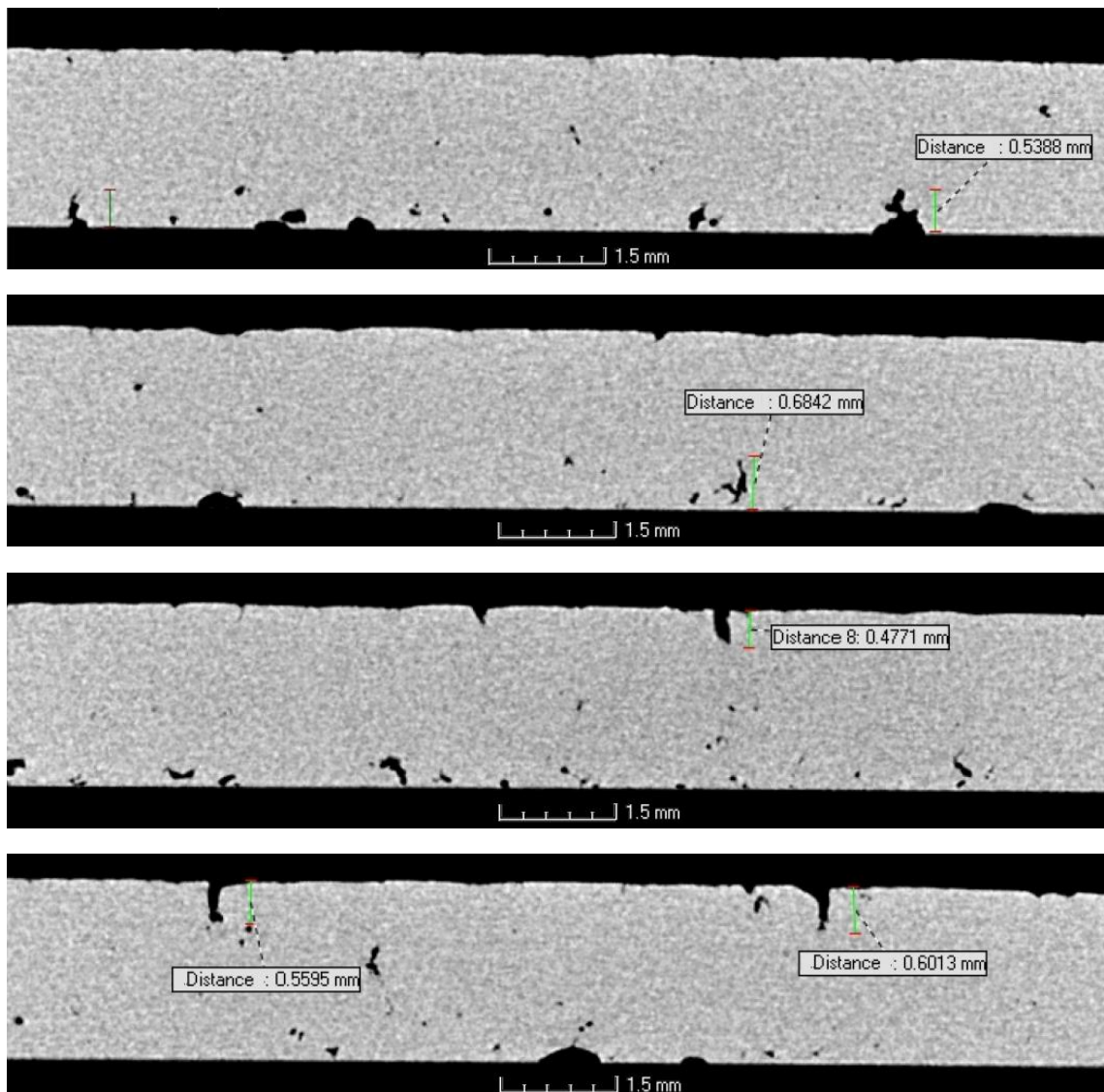


*Figure 4.15. X-ray CT images of the internal defects in a PEEK 2000P samples showing cracks through the part thickness at both surfaces.*

The 2000P material has a permeability coefficient at almost twice that of every other PEEK material tested. With an analysis of the X-ray CT images it can be seen

somewhat in the 1000P material, and almost entirely in the 2000P material, that there are significant surface defects throughout the specimen, with Fig. 4.15 highlighting a selection of these defects in a 2000P sample. These defects are 0.5 – 0.7 mm deep into both sides of the sample making up almost half of the specimen's overall thickness. These defects allow for higher rates of permeation by decreasing the effective thickness of the material and hence are the reason for the heightened rates of permeation. These surface defects have a substantial presence in the 2000P material and are the reason why the Evonik PEEK materials have significantly higher permeabilities than the Victrex PEEK materials.

These defects are a direct result of poor powder consolidation during melting due to poor melt flow rheology and powder shape effects, with Fig. 4.3 (e) showing the presence of tail sections in the 2000P powder particles prior to specimen formation. These long fibrils and tails create larger air gaps throughout the sample during specimen formation which prevent proper consolidation of the powder during melting and hence increase permeability. This, coupled with the high viscosity of the 2000P material also mitigates flow of the polymer sample during melting and as such resists collapsing of the powder particles during sintering and coalescence leading to poor consolidation of the melt and a more permeable liner sample. These defects allow for higher rates of permeation by decreasing the effective thickness of the material and hence are the reason for the heightened rates of permeation which are present in the 2000P material (and to a much smaller extent in the 1000P material) and are the reason why the 1000P and 2000P materials have significantly higher permeabilities than the 150P and 150PF materials in the current analysis.

### **4.5. Predicted Leak Rates for Demonstrator Tank**

While it has already been shown that the leak rate is thickness dependent and thus the permeability coefficient is a better measure for ranking materials for permeability, the leak rate is still used to qualify COPV tanks and so it is the usual value quoted in COPV liner studies [161, 162]. To this end, Fick's law, in conjunction with the permeability coefficients calculated in both the NUI Galway and ÉireComposites apparatus have been used to predict the final leak rate of a liner material at a given pressure and thickness for a prospective COPV tank. For the current project the envisaged use of the polymer materials studied here is for a

standard 90L cylindrical COPV tank with domed ends and a maximum allowable leak rate of  $1 \times 10^{-3}$  scc/s of helium at an operating pressure of 5 bar. If the tank has an internal surface area of around  $1.0 \text{ m}^2$  then the maximum allowable leak rate can be assumed to be  $1 \times 10^{-3}$  scc/m<sup>2</sup>s. Fig. 4.16 and Fig. 4.17 outline the effectiveness of each material at achieving this limit for a 5 bar pressure difference.

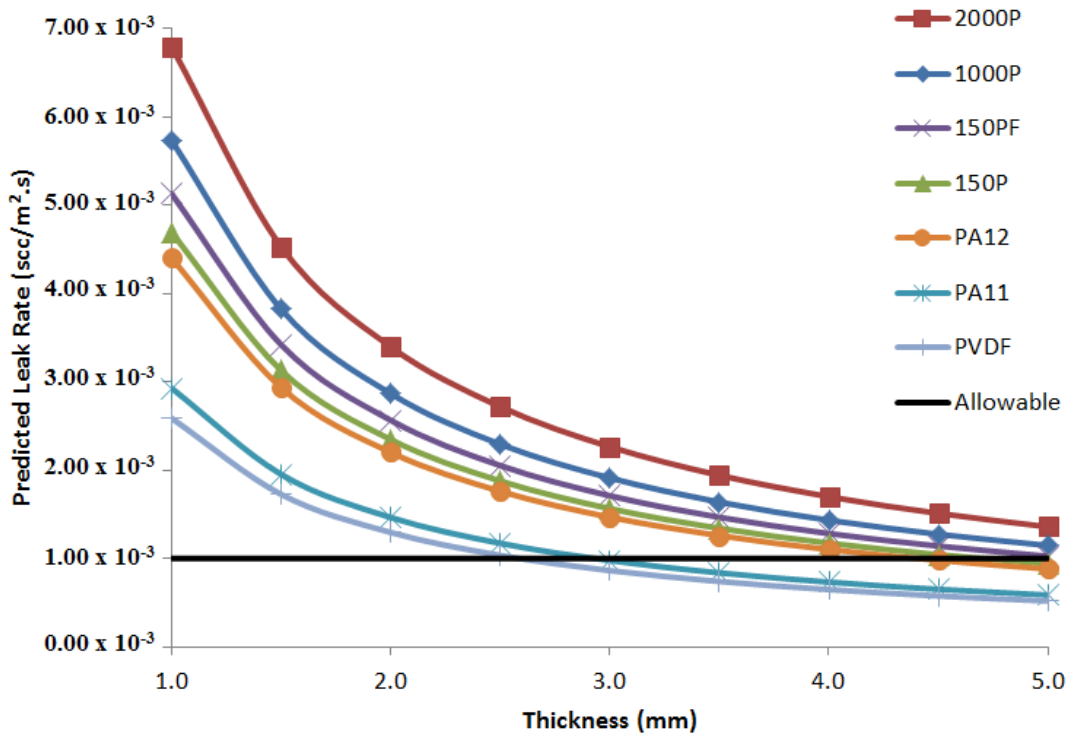


Figure 4.16. Predicted leak rate for varying liner thicknesses based on measured coefficients from the NUI Galway permeability test apparatus.

Fig. 4.16 shows the predicted results based on the NUI Galway permeability test results, while Fig. 4.17 shows the predicted results for materials measured with the ÉireComposites permeability apparatus. The NUI Galway results use the lowest measured permeability coefficient for each material tested and so have shown a lower leak rate for the PEEK 150P material then the PEEK 150PF material, which is the opposite to that of the results obtained with the ÉireComposites apparatus. The PVDF material also shows a lower leak rate than the corresponding PA11 material in the NUI Galway apparatus which is not reciprocated in the ÉireComposites results. The other main difference between these graphs is that the NUI Galway results give higher leak rates then the corresponding ÉireComposites results. This is reflected in the increased thickness needed for every material to achieve a leak rate below that of

the allowable leak rate in Fig 4.16, for the NUI Galway test results, in comparison to the ÉireComposites test results.

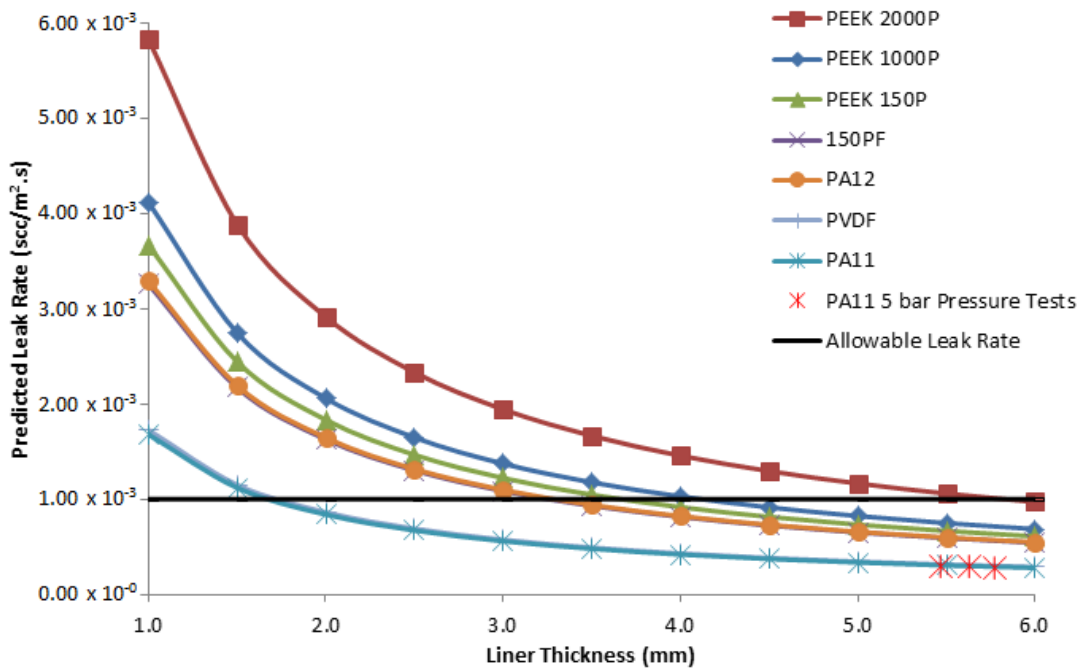
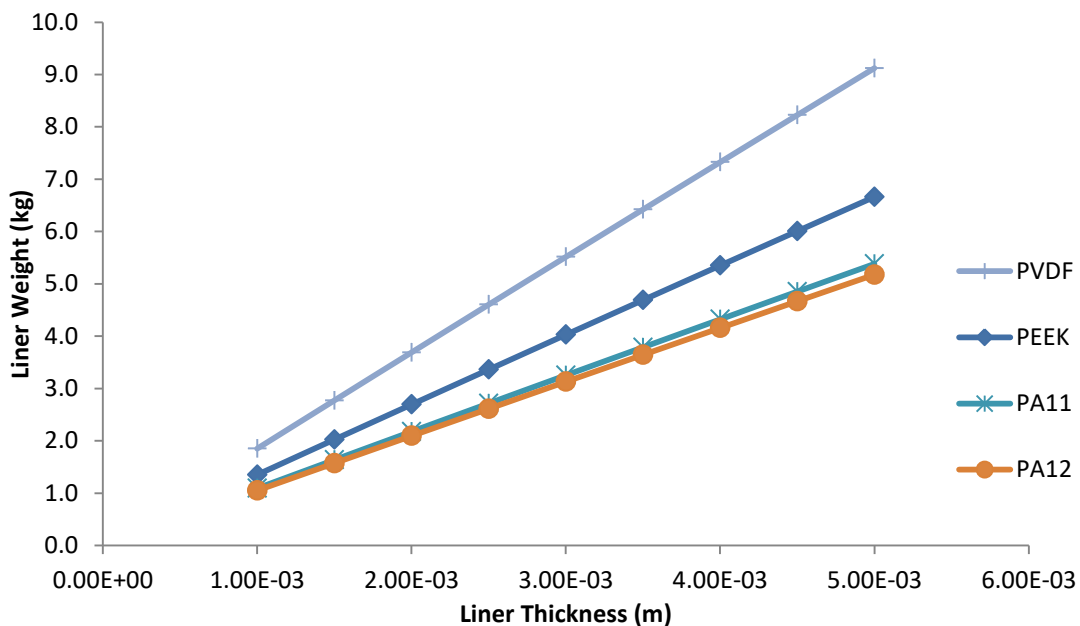


Figure 4.17. Predicted leak rate for varying liner thicknesses based on measured coefficients from the ÉireComposites permeability test apparatus.

Given the subtle differences between test methods, the predicted leak rates for all materials are quite consistent overall. The ÉireComposites test results will be discussed further (Fig. 4.17) as this test method is a more stringent method of permeability analysis. The overall results from these graphs clearly show that PA11 and PVDF outperform all other polymers tested, displaying leak rates below that of the maximum allowable for a liner with a minimum thickness of 2.0 mm. A liner of twice this thickness (at 4.0 mm) is needed for the PEEK 150PF and PA12 materials to reach a sufficiently low leak rate to be acceptable as a liner material. At a 4.0 mm thickness the PA11 and PVDF materials have reduced the leak rate further to less than half that of the allowable leak rate (at an average of  $4.25 \times 10^{-4}$  scc/m<sup>2</sup>.s), providing a significant factor of safety for the integrity of a prospective COPV tank. The 1000P, 2000P and 150P PEEK grades eventually reach the maximum allowable limit at the 5.0 mm thickness mark, but at this point their reduced performance lags behind that of the PA11 and PVDF.

## Material Characterisation and Permeability Testing

These results has been confirmed experimentally by further testing of three PA11 samples (with an average thickness of 5.6 mm) at a pressure difference of 5 bar (the expected operating pressure of the COPV designed here), the results for which have been included in Figs. 4.17 and 4.19. The leak rate from these samples had an average value of  $2.91 \times 10^{-4}$  scc/m<sup>2</sup>s which is accurate to within 3% of the predicted value of  $3.00 \times 10^{-4}$  scc/m<sup>2</sup>s. This proves the accuracy of the permeability testing conducted here at a 1 bar pressure difference and further verifies that the PA11 material is the best barrier to permeation. The second effect of liner thickness which must be considered is the overall liner weight which is linked to the density of the specific polymer material tested. The cost of sending materials to space has been estimated to be almost €10,000 kg<sup>-1</sup> to €17,000 kg<sup>-1</sup> (cost significantly affected by launch type and final orbital position of payload) and so reducing the weight of inherent systems is a main priority of future launch designs [171, 240, 241].



*Figure 4.18. Liner thickness versus approximate liner weight for given tank dimensions.*

When analysing the density of each material the Nylon materials are almost half as dense as PVDF which further separates the PA11 material from PVDF as the better material for low permeability liner applications. Fig. 4.18 shows the estimated liner weight versus liner thickness for the proposed COPV dimensions where the Nylon materials are significantly lighter than PEEK and PVDF.

This means that for tanks of the same weight a 4 mm Nylon liner can be used instead of a 2 mm PVDF liner which would effectively halve the permeability for the same liner weight. For a polymer lined COPV to be approved for test flights it must meet all of the requirements of a metallic lined COPV, but to surpass it as the standard in all future launches it must also reduce the tanks weight for the same level of permeation resistance and so minimising weight is a major concern.

With the liner weight in mind, Fig. 4.17 has been updated to show the predicted leak rate versus the calculated liner weight in Fig. 4.19. This further solidifies the Nylon materials as the best barriers to permeation while showing that the PVDF liner will be significantly heavier for similar permeation resistances.

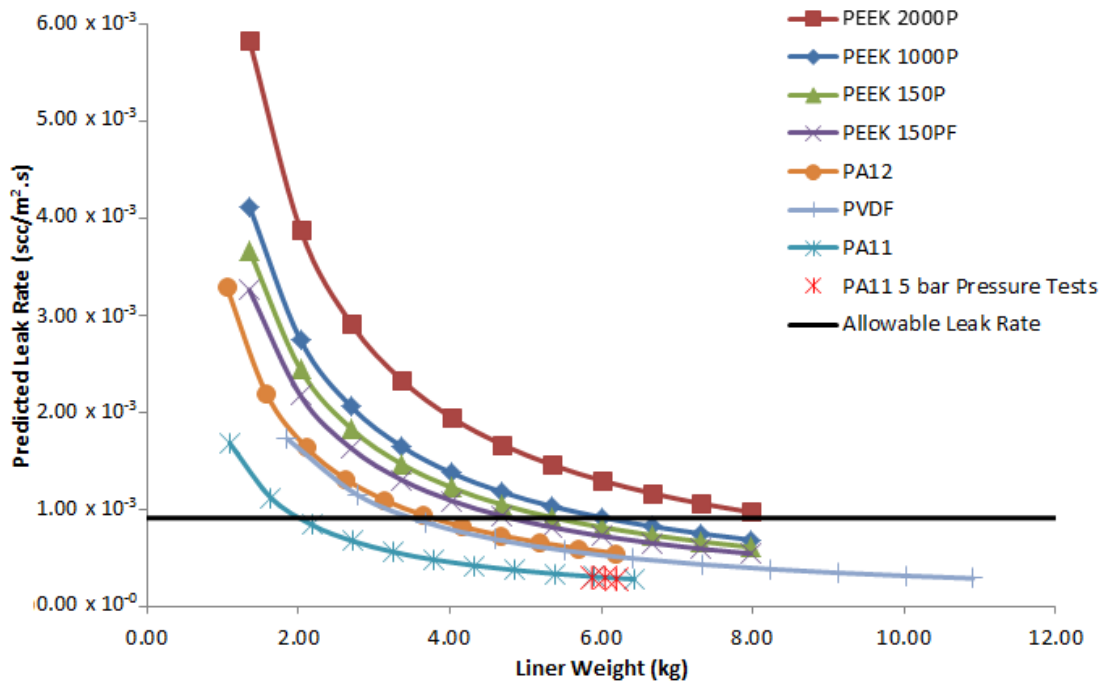


Figure 4.19. Predicted leak rate for varying liner weights based on measured coefficients.

## 4.6. Conclusions

A number of conclusions can be drawn from the results obtained here. Firstly, material characterisation techniques to assess powder materials before sample formation can be used to identify which materials are the best candidates for rotational moulding operations, specifically in the area of air void reduction in

## Material Characterisation and Permeability Testing

formed parts. The NUI Galway and ÉireComposites permeability apparatus have shown similar results for permeability measurements giving consistent and repeatable measurements. The NUI Galway apparatus has been successful at ranking polymer materials in regards to permeability, with an analysis of void effects also achieved.

The importance of defect analysis in liner cross sections has been highlighted, specifically in the case of PEEK 1000P and 2000P materials, where the inclusion of crack like surface voids which penetrate deep into the sample thickness can significantly increase the permeability of the aforementioned materials. X-ray CT scanning has been instrumental in highlighting these differences, as the microscopy analysis conducted, while helpful in showing general trends, could not achieve the same level of detail as a three dimensional image.

PA11 and PVDF have been identified as the best materials for low permeability operations with the Nylon materials of PA11 and PA12 further separating themselves from the other materials tested due to their comparably lower density. The permeability coefficients could be reduced further with the usage of optimum processing conditions for the removal of voids and the maximisation of crystallinity percentages. The use of a greater number of test samples (i.e. more than the three standard samples used here) would also increase the accuracy of the test results and reduce the standard deviation of results. Three samples were used here as each test took approximately one week to complete and so more samples would equate to a large investment of time to expand the test matrix (for the NUI Galway test rig). The predicted results for the demonstrator tank liner have shown that polymer materials are capable of containing fuels at permeation rates which are below that of the set allowable leak rate with a significant factor of safety achievable. These are all positive outcomes for the future of polymers as liner materials and signify a first step towards the realisation of a rotationally moulded polymer lined COPV.

# 5. Heterogeneous Modelling

## 5.1. Chapter Overview

This chapter covers a combined experimental and computational study of void distributions in rotationally moulded polyethylene. The effects of key variables such as maximum process temperature and nominal wall thickness (via powder mass) are studied. Analytical models and finite element mass diffusion models for the permeability of heterogeneous polymers with air voids are presented and comparatively assessed. The FE method allows modelling of realistic (measured) void distributions. A preliminary estimation method for void volume fraction and mean void radius is presented. The method, based on hot plate measurements, is shown to give good correlation with rotationally moulded materials for different processing temperatures.

## 5.2. Polyethylene Void Analysis

### 5.2.1. Test Program for Void Analysis

A programme of tests for void volume fraction and average void size was undertaken for hot plate moulded and rotomoulded polyethylene samples. Three different moulding temperatures (150 °C, 170 °C and 190 °C) were used to produce three samples on the hot plate for each temperature. These samples were analysed for void volume fraction,  $V_f$ , and average void radius,  $R_v$ , as shown in Fig. 5.1. All samples had a nominal thickness of 3.0 mm. Subsequently, three box components were rotomoulded at three similar temperatures (160 °C, 170 °C and 180 °C), again with

## Heterogeneous Modelling

nominal thicknesses of 4.0 mm. These samples were analysed for void volume fraction and average void size, with a comparison drawn with earlier hot plate moulded samples. Two additional boxes of increased thickness were rotomoulded at the higher temperature of 180 °C to determine the effect of nominal thickness on void distributions. This was achieved by using larger powder masses for each case. Four images from each of three different samples for one moulding temperature were taken and analysed for void volume fraction measurements in the hot plate moulded parts.

*Table 5.1. Material Properties of Borealis Low Density Polyethylene Powder*

Material	Borealis LDPE
Average Particle Size	300 – 400 $\mu\text{m}$
Melt Temperature	123 °C
Melt Flow Index	7.6 g/10min
Crystallinity	62%
Density ( $\rho$ )	0.94 g/cm <sup>3</sup>

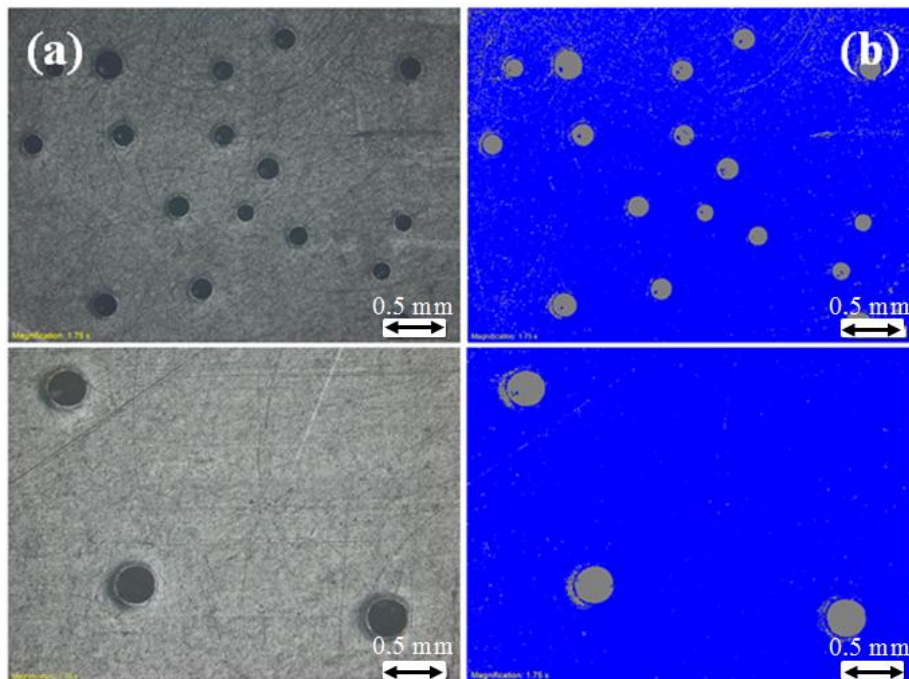


*Figure 5.1. (a) Collection of microscopy images for void volume fraction analysis in hot plate moulded parts with (b) their respective binary images beside them.*

## Heterogeneous Modelling

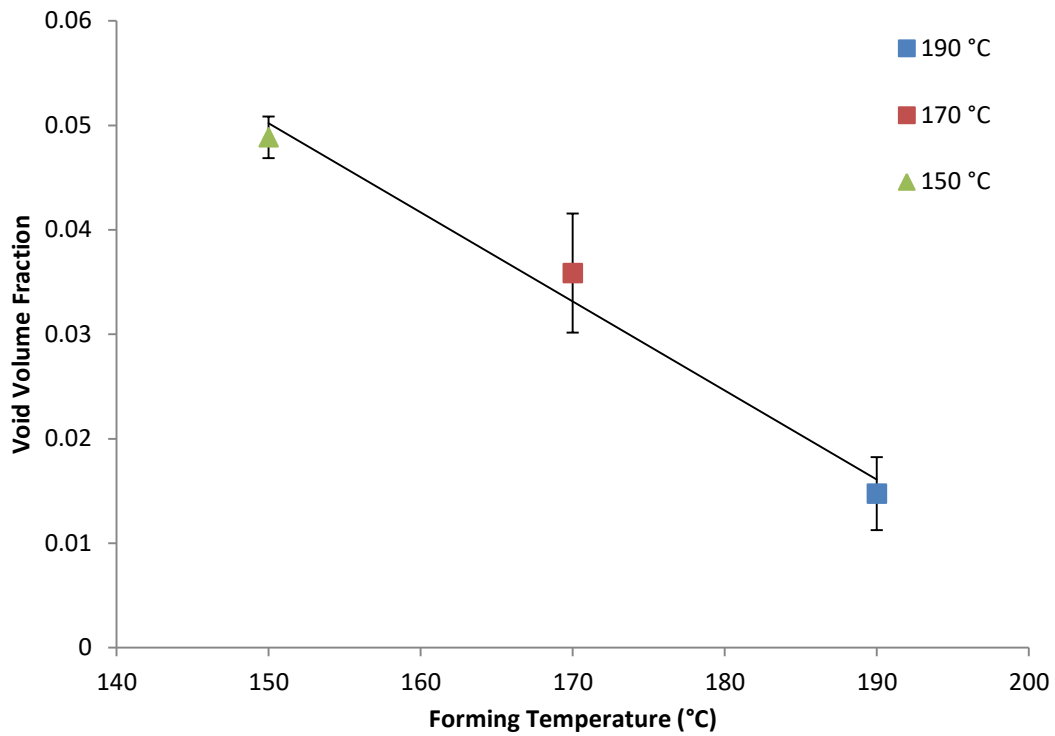


Figure 5.2. Measured effect of hot plate moulding temperature on void volume fraction in polyethylene samples.

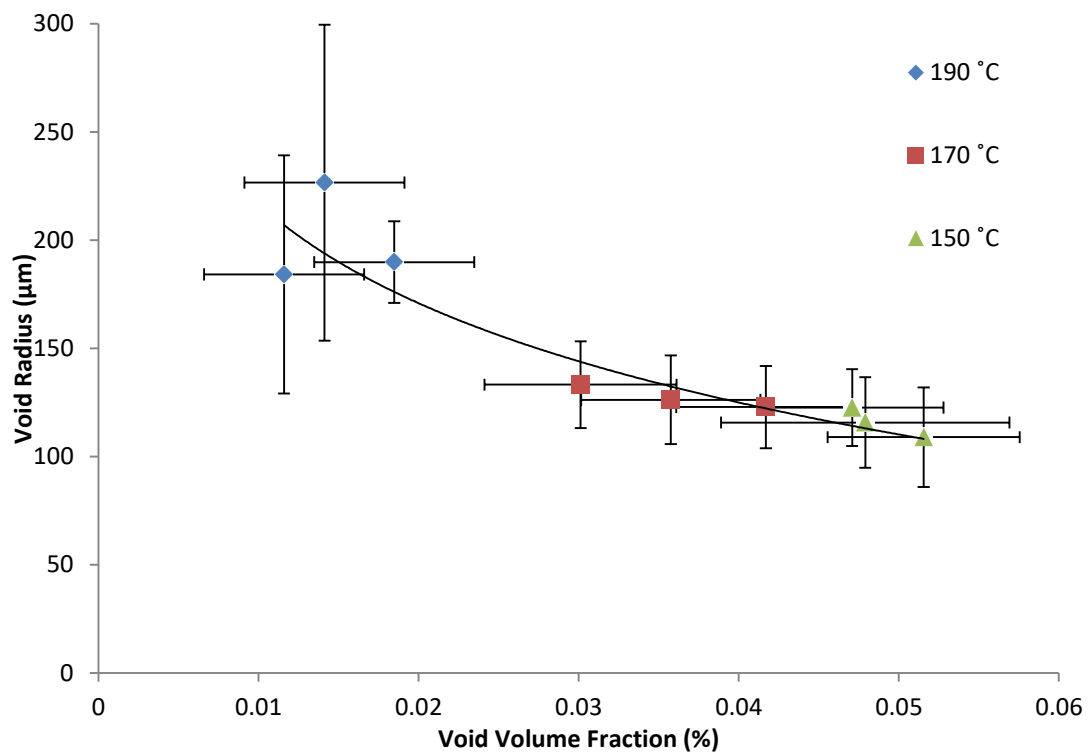


Figure 5.3. The effect of moulding temperature on void size and volume fraction for hot plate polyethylene samples.

Fig. 5.2 shows the measured relationship between average void volume fraction and the corresponding moulding temperature. Each data point consists of results taken from four microscopy images of each sample at the specified mould temperature to give an average void volume fraction. A linear trend is observed, with increased forming temperatures leading to a decrease in the void volume fraction. Fig. 5.3 shows the relationship between mean void radius and void volume fraction where the void volume fraction for each data point is the average void volume fraction of four microscopy images. The void radius is calculated from the average radius of every void contained within the four microscopy images. A relatively high volume fraction of smaller voids was formed at the lower moulding temperatures and a lower volume fraction of the relatively larger voids were formed at higher forming temperatures.

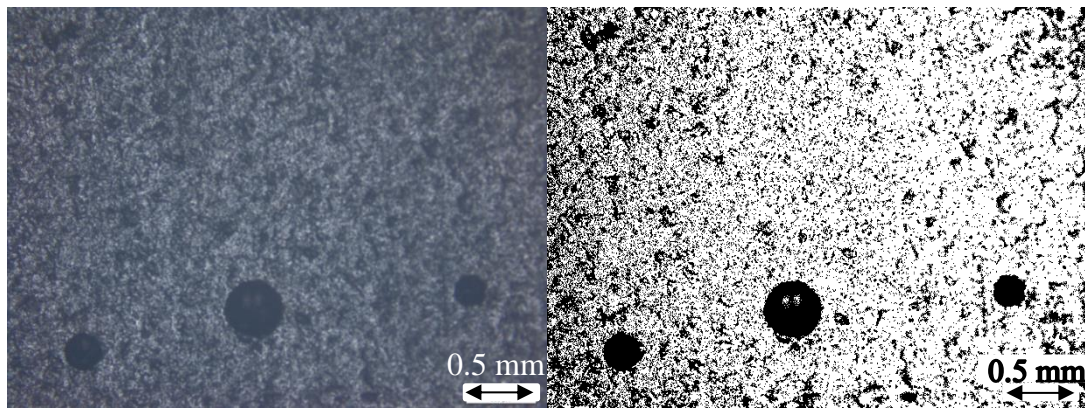


Figure 5.4. Microscopy image translated into a binary image for void volume fraction analysis of rotomoulded samples.

These results were then compared to the rotationally moulded samples. Eight images of polymer samples, Fig. 5.4, taken from each side (equating to 48 images) of the box component (Fig. 5.5) were taken and measurements for void volume fraction and void size was compiled. Fig. 5.6 shows a similar trend to the hot plate moulded samples, Fig. 5.2, with a decrease in void volume fraction observed for parts moulded at higher moulding temperatures. Fig. 5.7 shows that the average void radius was also found to increase (somewhat) with increased moulding temperature and reduced void volume fraction in a broadly similar trend to that of the hot plate moulded samples in Fig. 5.3. It should be noted that the hot plate results do not replicate the same trends as the rotomoulded results which is evident by the non-linear relationship between temperature and void volume fraction in Fig. 5.6 and the more linear relationship which is displayed in Fig. 5.7. A more accurate

## Heterogeneous Modelling

representation of these relationships would result in an enhanced predictive methodology and lower predictive errors for the following assessments in section 5.4.



Figure 5.5. Photograph of sample rotomoulded parts.

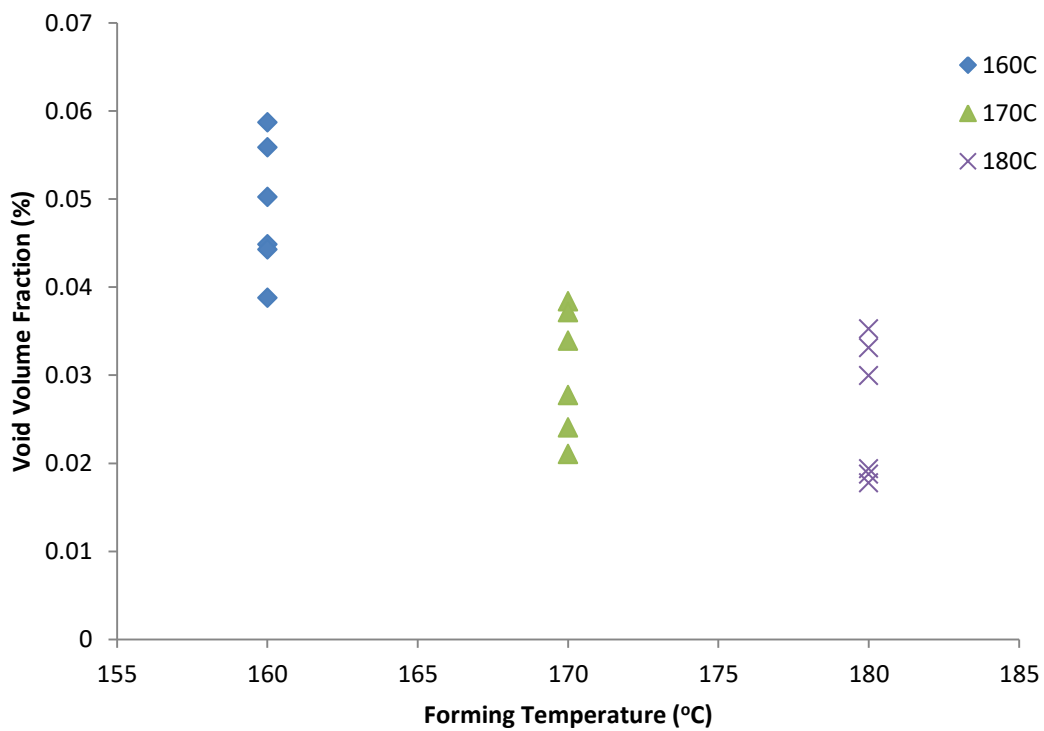


Figure 5.6. Measured effect of moulding temperatures on void volume fraction for rotomoulded samples.

## Heterogeneous Modelling

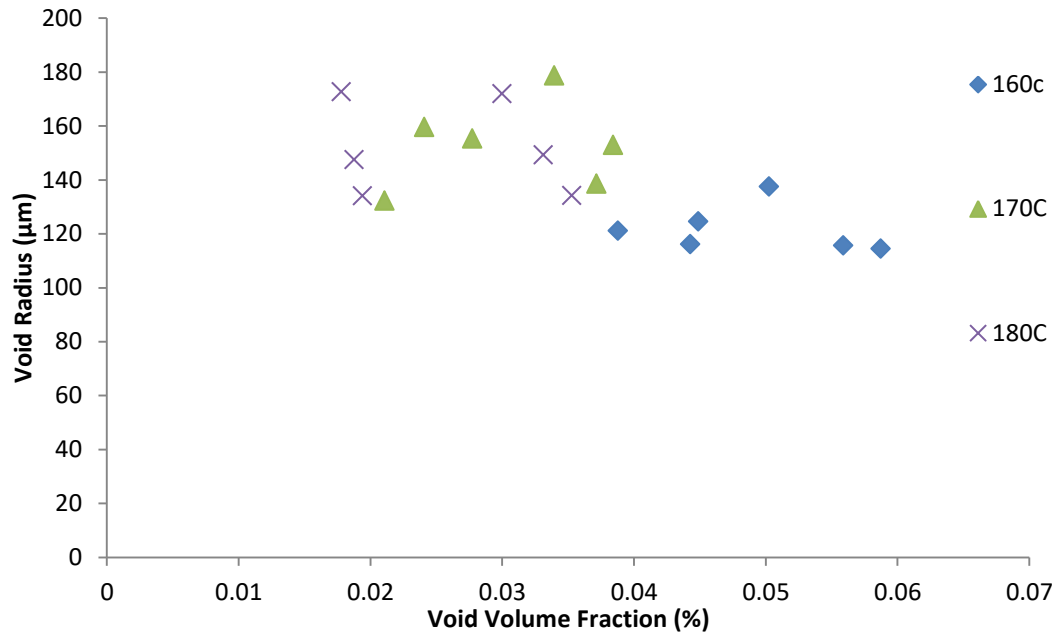


Figure 5.7. Measured relationship between void radius and void volume fraction for rotomoulded samples at different moulding temperatures.

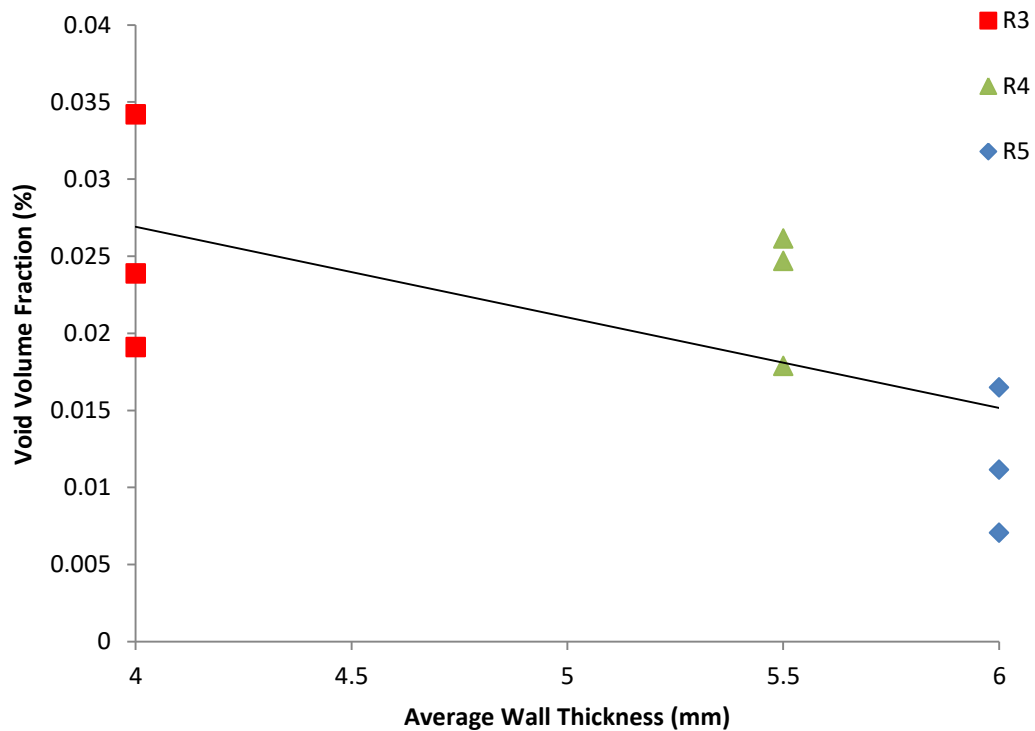


Figure 5.8. Relationship between void volume fraction and measured wall thickness for rotomoulded components at 180 °C as detailed in Table 5.2.

The final analysis undertaken for the rotomoulded parts was to analyse the void volume fraction trends in rotomoulded parts as a result of changes in the thickness of the wall cross section. Three boxes, one of which is shown in Fig. 5.5, were rotomoulded at 180 °C, with resulting average wall thicknesses of 4.0 mm (R3) 5.5 mm (R4) and 6.0 mm (R5). The thicker boxes exhibited a further reduction in void volume fraction, as shown in Fig. 5.8. This is attributed here primarily to the increased diffusion of voids at higher temperatures and is further accentuated by the longer time period required to reach the higher moulding temperature for higher powder masses. The average void size was found to be negligibly affected by wall thickness as average void radius measurements were consistent across all samples.

### 5.3. Finite Element Mass Diffusion Analysis

#### 5.3.1. Continuum Mechanics

As has already been outlined in Chapter 2, the diffusion of mass through a solid membrane is governed by Fick's law [108, 110, 111].

$$J = -DA \frac{\partial C}{\partial x} \quad (5.1)$$

This equation is very useful when dealing with the mass flow through a homogenous one dimensional membrane but becomes significantly more complicated with the addition of particles or discrepancies with different diffusion characteristics. Heterogeneous equations, also outlined as part of Chapter 2, can be used to overcome these shortcomings with idealised models of a single inclusion in a surrounding matrix being used to predict mass flow rates for an entire system [140-150]. Again this is an approximation that gives a single result for the mass flow rate in a system and is not always inclusive of multiple voids, shapes, or sizes. To this end, a continuum mechanics approach using a finite element model based on ABAQUS software has been used to approximate the mass flow rate through polymer materials containing randomly distributed voids in a three dimensional part.

Continuum mechanics is a method of kinematic analysis which models a solid material as a continuous mass occupying all the space contained within its defined region [242-244]. It is based on the laws of conservation (mass, energy, momentum) and has been readily incorporated in to analyses of complex geometries with the

advent of computer technology allowing for expedited calculations giving realistic and accurate predictions. The continuum mechanics approach breaks down problems into a series of complex differential equations with an infinite number of unknowns. Through the use of numerical methods and an idealization of the problem using simplified equations, a realistic analysis can be achieved with predicted results giving a close approximation to the behaviour of the real life system.

### 5.3.2. Finite Element Analysis of Mass Diffusion

Finite element analysis is a numerical tool that is used to make approximate solutions to continuum mechanics problems. It does so by breaking down the desired geometry into a number of smaller elements with a known shape (such as triangular or quadrilateral elements) connected to each other by a number of nodes in a finite element mesh, Fig. 5.9.

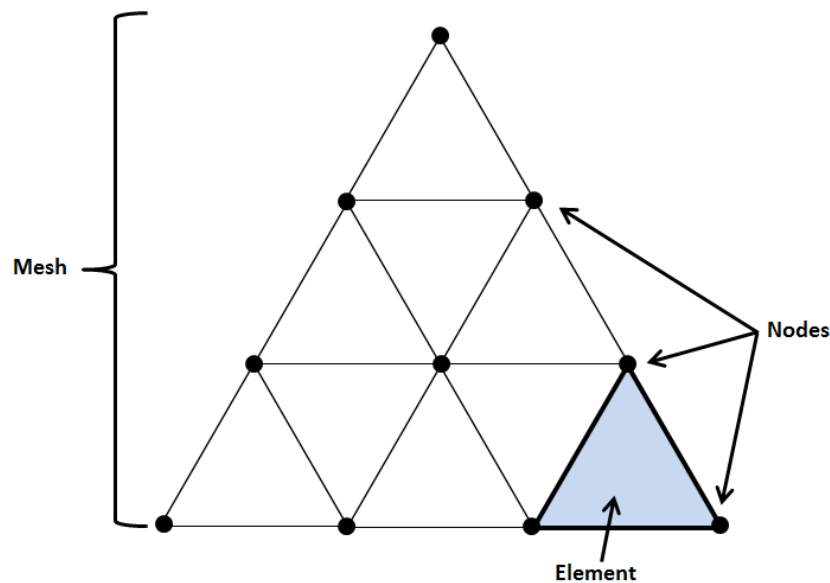


Figure 5.9. Description of a finite element mesh including elements and nodes.

The equations associated with each element must then be assembled by forming a diffusion matrix  $[K]_e$  and a mass flow rate vector  $\{f\}_e$  which express the properties of each element within the mesh along with the applied mass flow rates on the system as outlined in Eq. 5.1 [244]:

$$[K]_e = \frac{AD}{x} \begin{bmatrix} 1 & -1 \\ -1 & 1 \end{bmatrix} \quad (5.2)$$

$$\{f\}_e = \left\{ \begin{matrix} J_i \\ J_j \end{matrix} \right\} \quad (5.3)$$

where  $e$  is the element,  $J$  is the total mass flow,  $D$  is the diffusion coefficient,  $x$  is the thickness of a one dimensional (two node) linear element,  $A$  is the surface area and  $i$  and  $j$  are the respective nodes within the element.

The unknowns are the penetrant concentrations at each node. These individual elemental equations are then combined in a larger global matrix which incorporates all of the elements into a single set of simultaneous equations such that the resulting matrix represents the solution to the entire problem. The boundary conditions (or original concentrations) are then incorporated into this equation such that [244]:

$$[K]\{C\} = \{f\} \quad (5.4)$$

Where  $K$  is the global diffusion matrix,  $f$  is the global mass flow rate vector and  $C$  is the unknown global concentration vector. These equations are then solved to obtain the nodal values for concentration differences at each point. From an analysis of the concentrations at each node other values such as the mass flow rate can be obtained giving the desired quantity. To determine the impact of the factors such as distribution, position bias and the interaction between different voids, a randomised finite element analysis of the system would have to be undertaken. In the past this would have been quite difficult and cumbersome as slow computer speeds and long model simulation times would have made this operation quite time consuming. Computer advancements and increased processing speeds have made these calculations quite easy to undertake and so a finite element analysis is a viable tool for mass diffusion modelling. Finite element analyses will also create an envelope for permeability calculations, giving a permeability range instead of a single value for the permeability of a heterogeneous material.

### **5.3.3. Three Dimensional Finite Element Mass Diffusion Model**

An FE based implementation of Fick's law is employed to study the steady-state mass diffusion behaviour of the polymer with random distributions of voids [245]. An idealised three dimensional model with cross sectional dimensions of 3 mm × 1 mm × 1 mm was developed as shown in Fig. 5.11. A Python scripting code,

Appendix C, was developed to define the random distribution of three-dimensional spherical voids (of uniform size), corresponding to a given void volume fraction.

In the analyses presented below, and based on measured void sizes, void radii of between 100  $\mu\text{m}$  and 200  $\mu\text{m}$  are modelled, Fig. 5.12. For a given set of processing conditions, the measured range of void radii was found to be quite small, so that the assumption of uniform void size is considered reasonable. This assumption also makes the mesh generation process more straightforward. The analyses were based on the use of helium as the diffusing gas based on a standard permeability test for plastic sheeting [215].

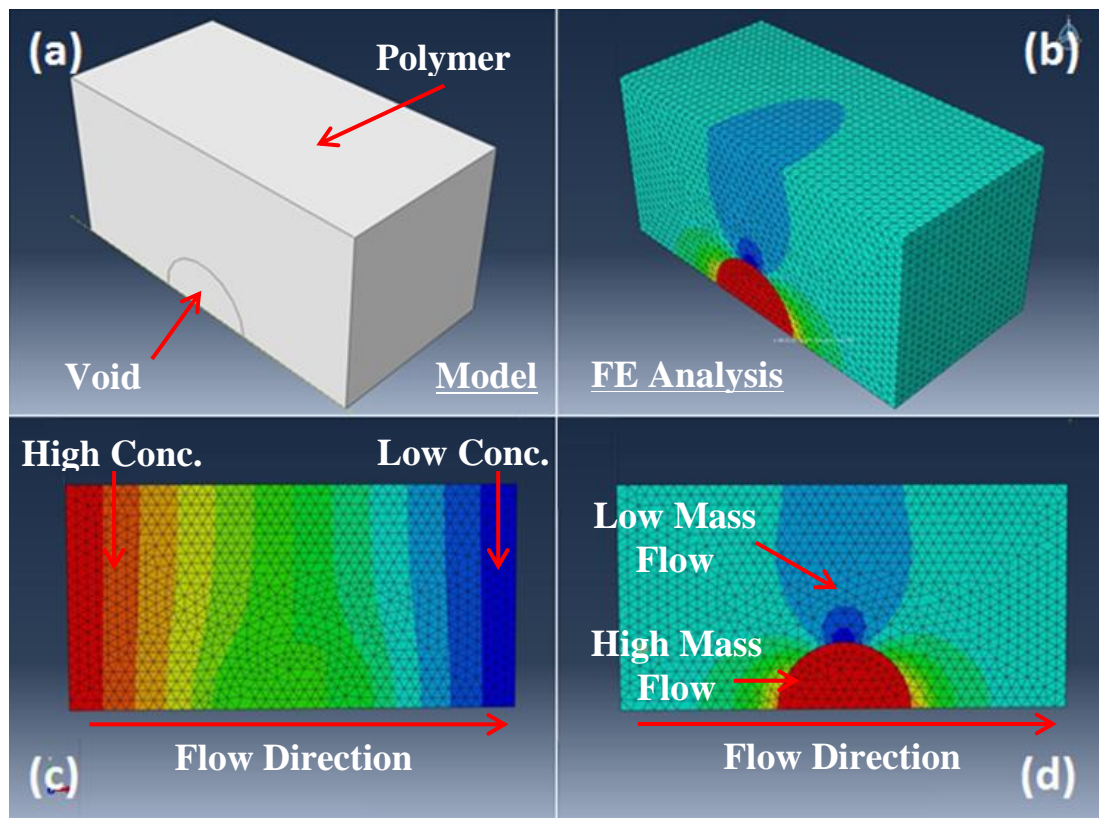


Figure 5.10. Development of a (a & b) single void model with (c) concentration gradients and (d) mass flow rates highlighted showing dominant mass flow through the void inclusion from the higher concentration on the left to the lower concentration on the right.

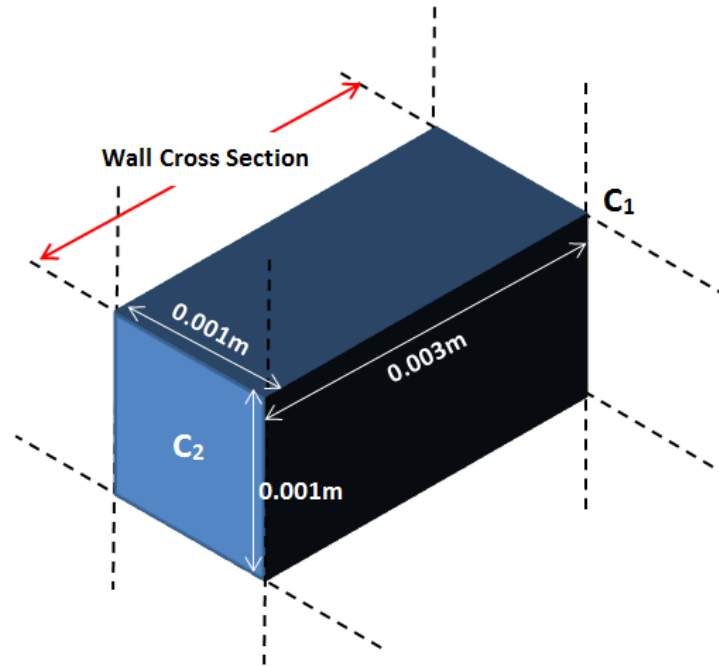


Figure 5.11. Schematic of the finite element model employed for the analysis of void contents in rotomoulded parts.

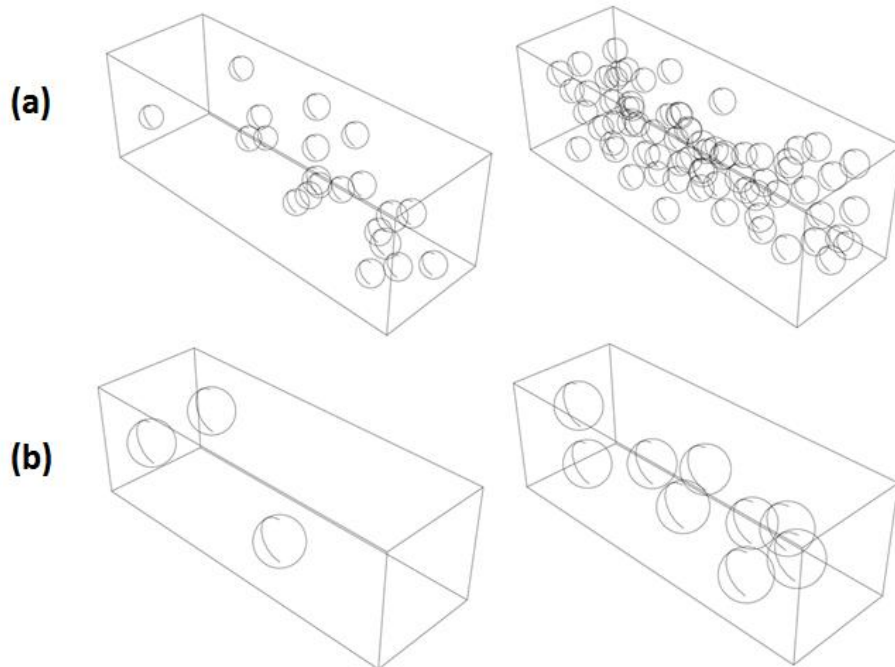


Figure 5.12. Random distributions of voids in the finite element model for (a) 100 μm voids and (b) 200 μm voids with different void volume fractions.

## Heterogeneous Modelling

*Table 5.2. Experimental data for the parts formed throughout this analysis.*

I.D.	Hold Temperature (°C)	Manufacturing Method	Thickness (mm)	Heating Rate (°C/min)
H1	150	Hot Plate	3.0 – 4.0	10 – 15
H2	170	Hot Plate	3.0 – 4.0	10 – 15
H3	190	Hot Plate	3.0 – 4.0	10 – 15
R1	160	Rotomoulded	3.0 – 4.0	10 – 13
R2	170	Rotomoulded	3.0 – 4.0	10 – 13
R3	180	Rotomoulded	3.0 – 4.0	10 – 13
R4	180	Rotomoulded	5.0 – 5.5	10 – 13
R5	180	Rotomoulded	5.5 – 6.0	10 – 13

The FE model was used to study the effect of void volume fraction using ten different random distributions of voids for each value of volume fraction. These results are compared to the results from the theoretical permeability models, which cannot include the effect of random distributions. The FE model was also used to study the effect of wall thickness on permeability. This study consisted of (i) a generic study of the effect of wall thickness for three different void volume fractions of 0%, 5% and 10%, all using a uniform void radius of 150  $\mu\text{m}$  and (ii) three separate analyses corresponding to three different powder mass cases (R3, R4 and R5), all at 180 °C, of Table 5.2. The analyses of (i) are intended to demonstrate the effect of wall thickness for different void volume fractions. In contrast, the analyses of (ii) incorporate the combined effects of wall thickness variation and the associated measured void volume fractions (with a void radius of 150  $\mu\text{m}$ ). The analyses here used linear four node tetrahedral elements for the steady-state analyses. Other details used in the FE analysis are given in Table 5.3. A convergence study was carried out to establish convergence of the predicted mass flow rates with respect to element size. The finite element analyses conducted here utilise a 25  $\mu\text{m}$  mesh size.

## Heterogeneous Modelling

*Table 5.3. Overview of values used for the finite element analysis [173, 247].*

Parameter	Finite Element Model
Model Dimensions	3 mm × 1 mm × 1 mm
Void Sizes (Radius)	100 – 200 μm
Diffusion Coefficient of Air	$7.2 \times 10^{-5}$ m <sup>2</sup> /s
Diffusion Coefficient (ρ=0.92 g/cm <sup>3</sup> )	$1.4 \times 10^{-9}$ m <sup>2</sup> /s
Concentration	0.54 mol/m <sup>3</sup>
Volume Fraction Analysed	0 - 10%

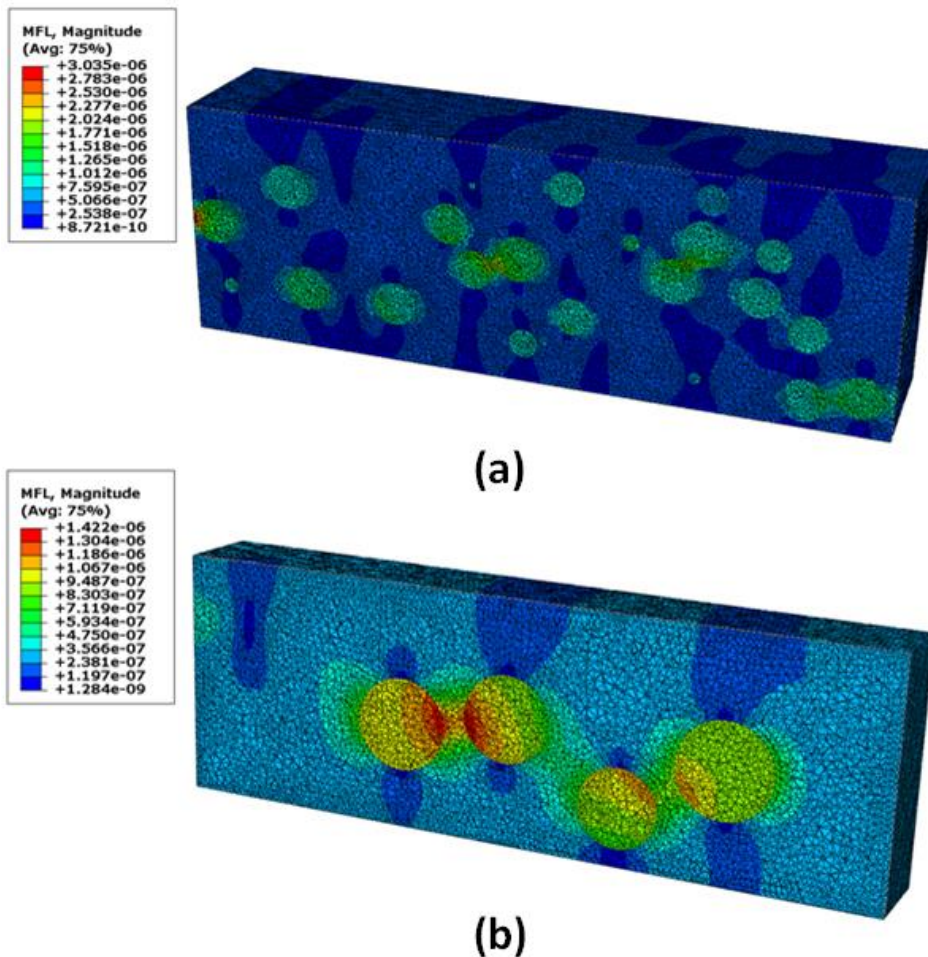


*Figure 5.13. Finite element predictions of steady state helium mass flow with diffusion models of typical liner cross-sections. Random void distributions for (a) 100 μm void radii and (b) 200 μm void radii.*

Fig. 5.13 shows the FE models developed using mean void radii of between 100  $\mu\text{m}$  and 200  $\mu\text{m}$ . A range of void volume fractions were used to study the effect of void morphology on permeability. In the FE results of Fig. 5.13, the lighter regions indicate significantly higher mass flow rates and darker regions indicate regions of reduced mass flow rate. It can be seen that the diffusion path tends to follow the void pattern, as this results in the path of least resistance for the mass flow, as discussed earlier. The lower diffusion coefficient of the air voids contained within the liner increases the mass flow, which will increase fuel leakage and will be detrimental in cryogenic fuel storage applications. It is clear that the voids significantly affect the mass flow pattern, leading to a concentration of the flow through the void and allowing for an easier path for mass flow to occur.

### 5.3.4. Finite Element Mass Diffusion Results

The predicted permeability results for the random void distribution models are shown in Fig. 5.14. An increase in void volume fraction is predicted to significantly increase permeability, with multiple data points (corresponding to different random distributions of voids) from the FE model displaying this trend. The smaller (100  $\mu\text{m}$ ) voids are predicted to have a higher permeability than the larger (200  $\mu\text{m}$ ) voids for similar volume fractions. The blue and red lines follow a best fit of the FE results for the 100  $\mu\text{m}$  and 200  $\mu\text{m}$  void analyses respectively. The smaller voids can distribute more uniformly throughout the model, thus creating a more continuous path which increases permeability. These FE results are compared to the heterogeneous diffusion models described in Chapter 2. The FE model trend follows that of the predictive equations. The latter only give one data point for each volume fraction and this lies within the FE predicted range, due to the random distributions analysed. The FE trend agrees more closely with the Maxwell and Lewis-Nielsen models than the Bruggeman model. The FE model accounts for void morphology statistics and thus provides a statistical range for permeability.

From Fig. 5.14, the FE predicted permeabilities for the higher moulding temperature void volume fraction of 1.5% with 200  $\mu\text{m}$  voids and the lower moulding temperature void volume fraction of 5.5% with a void size of 100  $\mu\text{m}$  are  $2.55 \times 10^{-7}$   $\text{mol/m}^2\text{s}$  and  $2.9 \times 10^{-7}$   $\text{mol/m}^2\text{s}$  respectively. This indicates that higher moulding temperature is beneficial for reducing the predicted permeability. Another factor

which can significantly affect permeability is part thickness. In order for designers to assess the implications of increased part size and weight vis-à-vis reduced permeability, it is important to understand the effect of thickness on permeability for realistic void morphologies.

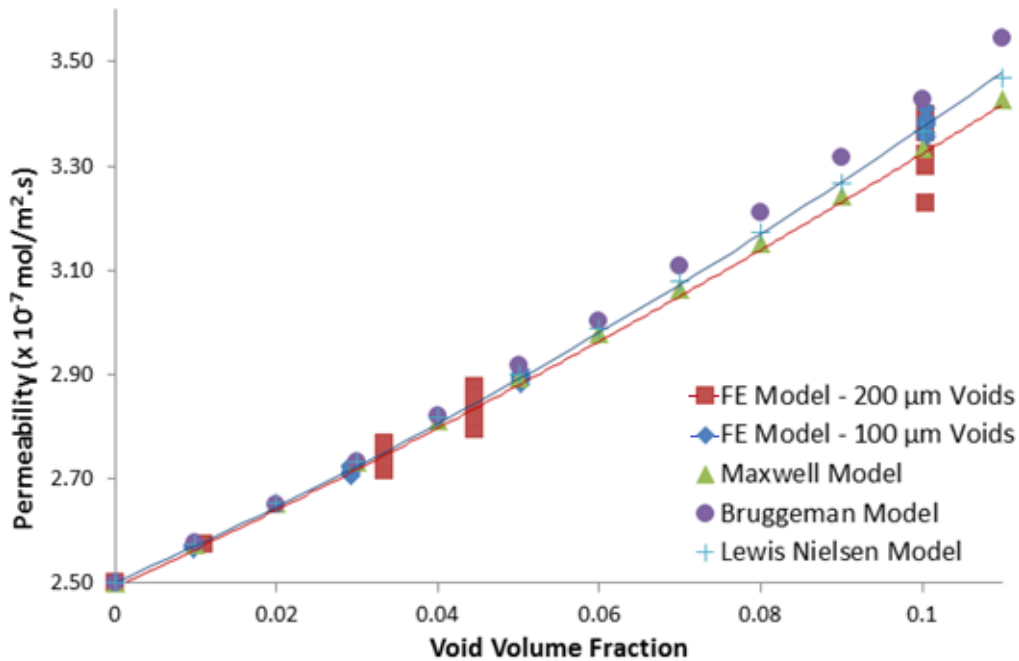


Figure 5.14. Comparison of finite element predicted and theoretically predicted mass flow rates for different void sizes as a function of the void volume fraction.

In Fig. 5.15 a study of the effect of thickness on permeability in rotomoulded samples has been conducted for polyethylene components formed at 180 °C, by using different total powder weights. The  $V_f = 0\%$  trend line is effectively a Fick's Law prediction of thickness effects. The 5% and 10%  $V_f$  trend lines, which show multiple data points, correspond to different random distributions of voids for each thickness value, showing that:

1. Even with realistic void morphologies, a Fick's law trend is predicted to persist for each  $V_f$  shown
2. The effect of random void distributions is relatively small for a given  $V_f$  and thickness

Fig. 5.15 also shows that for the zero void volume fraction, the permeability is less than the quoted target value of  $2.23 \times 10^{-7} \text{ mol/m}^2\text{s}$  (mentioned earlier for COPV

applications) for thicknesses greater than 3.5 mm. Also shown in Fig. 5.15 are separate predictions for the R3, R4 and R5 cases from Table 5.2. These specific predictions use the measured values of  $V_f$  for their corresponding thickness. In all three cases the predicted permeability is seen to be below the target maximum permissible permeability. This shows how a combination of increased moulding temperatures and increased wall thickness can be used to control permeability.

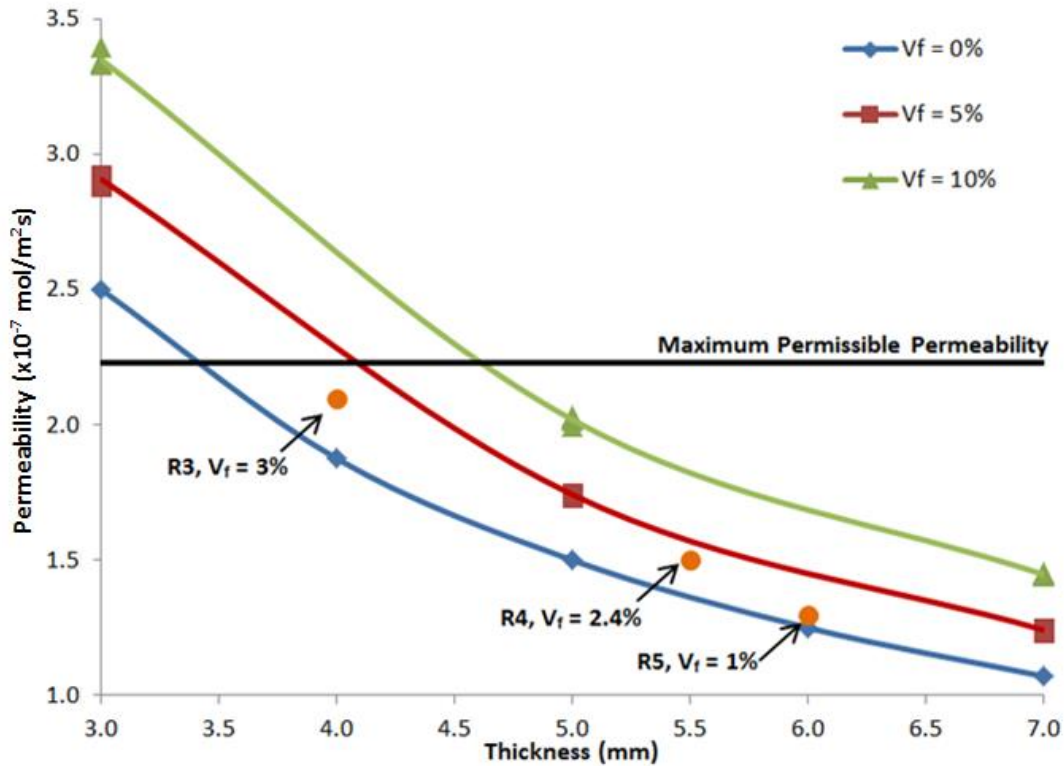


Figure 5.15. Finite element predicted effect of thickness on permeability for different void volume fractions.

## 5.4. Permeability Prediction Model

As has been shown by the previous hot plate and rotomoulding results, good correlation has been found between void volume fractions and void sizes in both manufacturing methods. This suggests that hot plate results can be used to estimate void volume fraction parameters for rotomoulded polyethylene components. The relationship between moulding temperature and void volume fraction follows a linear trend for the hot plate samples, where the void volume fractions,  $V_f$ , can be related to hold temperature,  $T$ , as follows:

$$V_f = aT + b \quad (5.5)$$

where  $a$  and  $b$  are constants with values of  $-8.25 \times 10^{-4}/^{\circ}\text{C}$  and  $0.17358$ , respectively. The measured relationship between void volume fraction,  $V_f$ , and average void radius,  $R_v$ , for a range of moulding temperatures can also be interpreted for the hot plate samples. It is clear that increased processing temperatures lead to an increase in average void size and a decrease in average void volume fraction, as one would expect [74]. The reduced void volume fraction at increased temperatures can be attributed to the diffusion of voids due to thermal diffusion effects [80]. The relationship between average void radius,  $R_v$ , and void volume fraction,  $V_f$ , can be represented by the following equation:

$$R_v = \alpha(\ln(V_f) + \beta) \quad (5.6)$$

where  $\alpha$  and  $\beta$  are constants with values of  $-66.225 \mu\text{m}$  and  $1.33$ , respectively, for the polymer and processing conditions investigated here. This suggests the possibility of predicting void volume fraction and size in rotomoulded parts based on the measured (hot-plate) relationships between moulding temperature, void volume fraction and average void size.

These predictive equations are applied here to the rotational moulding process presented above, as follows (see Fig. 5.16):

1. A part (Fig. 5.5) is rotationally moulded and material samples are extracted from selected locations for void analysis. The void analyses are conducted to characterise the void sizes and volume fractions for the selected locations
2. The maximum temperatures during the moulding cycles for the locations corresponding to those at which void analyses were conducted in step 1 are identified
3. Eq. 5.5 is applied to predict the void volume fraction, based on this temperature
4. Eq. 5.6 is applied to predict the mean void radius, based on the void volume fraction from Step 3
5. Mass diffusion models are created for the defined parameters and, using Eq. 5.1, the rotomoulded liner's permeability is predicted using FE analyses

## Heterogeneous Modelling

This methodology is applied here to rotomoulded samples formed at three different temperatures. Table 5.4 shows the comparison of predicted (from hot plate data) and measured (rotationally moulded) values for the three temperatures. This predictive approach shows particularly good accuracy at the higher moulding temperatures. The derived predictive equations have slightly over and under predicted the value of  $V_f$  at 170 °C and 180 °C respectively but are still accurate to within 10%. The predictive equations have also under-predicted the value of  $V_f$  for the 160 °C samples but are accurate to within approximately 15%.  $R_v$  predictions are slightly over-predicted at 160 °C and 180 °C but are within 5% of measured values. The predicted  $R_v$  value for the 170 °C samples was also under-predicted by roughly 8%.

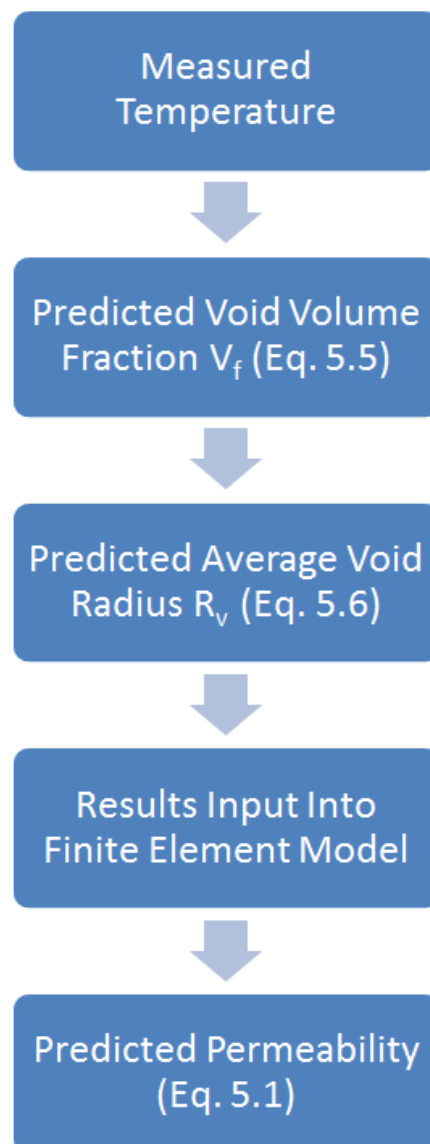


Figure 5.16. Flow chart for permeability estimation method.

Table 5.4. Comparison of measured and predicted mean of void distributions for rotomoulded samples at varying temperatures.

Temperature (°C)	Measured				Predicted		Error	
	Vf (%)	STDV (%)	Rv (µm)	STDV (µm)	Vf (%)	Rv (µm)	Vf (%)	Rv (%)
180	2.7	1.0	150	39.2	2.5	156	-7.1	+3.9
170	3.0	1.0	149	36.6	3.3	137	+9.8	-7.6
160	4.9	1.0	120	32.2	4.2	123	+14.8	+1.8

Note: the table above also shows the standard deviations (STDV) of the measured values.

The specific forms of Eq. 5.5 and 5.6, although giving a reasonably good fit over the full temperature range, do not necessarily capture the detailed variations of  $R_v$  and  $V_f$  with temperature. In particular the predicted equations over-predict the change in  $R_v$  between 170 °C and 180 °C and, vis-à-vis the measured change, under-predict the change in  $R_v$  between 160 °C and 170 °C relative to the measured increase.

However, in the present work, the effect of temperature is first captured via the effect on  $V_f$  which is linked to  $R_v$  through Eq. 5.6. The latter over and under predictions in  $R_v$  with respect to temperature changes can be traced back to imperfections in the linear fit of  $V_f$  to temperature in Eq. 5.5.

Hence a more complex equation (e.g. non-linear) between  $V_f$  and temperature would help to achieve an even better accuracy of predictions for  $V_f$  and  $R_v$  with respect to changes in temperature. Nonetheless, the errors of the predictions are less than 8% for average void radius and less than 15% for void volume fraction predictions. This methodology will facilitate identification of optimum processing temperatures for the production of polymer liners with acceptable void morphologies for predicted permeability.

## 5.5. Conclusions

Moulding temperature for rotomoulded components has been shown to have a significant effect on void volume fraction, with higher temperatures giving lower void volume fractions and hence lower predicted permeabilities. Nominal wall

## Heterogeneous Modelling

thickness has also been shown to have a significant effect on void volume fraction for rotomoulded components, with larger thicknesses giving a lower predicted leak rate. A simplified predictive methodology, based on hot plate measurements, for void volume fraction and void radius depending on temperature, has been shown to give reasonably good correlation with rotomoulded components. FE mass diffusion models predict permeability results which are consistent with theoretical models. The FE method presented provides a statistical range for permeability based on measured void morphology statistics. The present work represents an important step towards a combined experimental and modelling methodology for development of inexpensive, low permeability polymer liners.

# **6. Integrally Heated Rotomoulding Tooling Development**

## **6.1. Chapter Overview**

This chapter describes the design, fabrication and testing of an integrally-heated rotomoulding tool constructed for the production of rotationally moulded polymer demonstrator liners for testing and proof of concept. The chapter begins with a description of the rotational moulding machine, an analysis of the initial design considerations and the required functionality for the mould tooling. The physical design of the tooling, including detailed CAD drawings, is presented with a description of the tooling fabrication and heating system also included. Finally, the calibration of the tooling along with the manufacture of demonstrator components and an analysis of the effectiveness of the process for liner production is presented. The parts manufactured are used in subsequent chapters for analysis of the process and qualification of the production method for liner manufacturing.

## **6.2. Modified Rotational Moulding Process**

The modified rotational moulding process employed here utilises the original principles of rotational moulding outlined in Chapter 2, but replaces the heating oven with an integrally-heated mould tool contained within the rotating axes themselves [64, 65]. This allows for better control of mould heating parameters while also reducing the cost of running this process by localising the heating around the mould tooling and reducing the energy losses that occur when using a large oven. Two

## Integrally Heated Rotomoulding Tooling Development

biaxially rotating arms are used with separate speed controls so that the rotation ratio can be adjusted for improved control in part production. The free standing structure in Fig. 6.1 has an inner rotating area of nearly 2 m<sup>2</sup> allowing for the moulding of large parts contained within the rotating arm diameter.

Fig. 6.2 displays the modified rotational moulding machine used in this process with a box shaped mould mounted in the centre of the rotating axis. This mould was used for proof of concept tests and the analyses undertaken in Chapter 5 and has provided valuable information in the design and development of the demonstrator tooling described below. The box shaped mould and rotomoulding machine were fabricated by ÉireComposites Teo [65] prior to the start of this project but the entire rotational moulding machine had to be reconstructed for the work conducted in this thesis.

The mould tooling is electrically powered via slip ring connections in the joints at the main rotating axes, which transfer power through the rotating arms. The integrally-heated tooling does not significantly affect the temperature of the surrounding area within the turning radius of the rotomoulding machine and so thermal analysis and control systems can be located directly outside the tool without the risk of thermal degradation. The thermal control systems can be implemented through the slip ring connections or via wireless controls, due to the removal of the surrounding heating oven. The mould itself is constructed with heating coils uniformly distributed around the mould to allow for direct heating and improved thermal control.

Traditional rotational moulding processes utilising ovens have a tendency to produce hot spots within the mould, as burner locations and variations in mould wall thickness can affect the temperature distribution across the tool. It is almost impossible in traditional processes to control or quantify these effects during the rotomoulding cycle. The modified tooling allows for multiple temperature readings at critical locations around the mould tooling during processing, while the placement of the heating coils around the tool allows for increased control of temperature distributions. This gives a significant improvement in the dimensional accuracy of the part with temperature distributions and energy consumption being reduced [65].

# Integrally Heated Rotomoulding Tooling Development

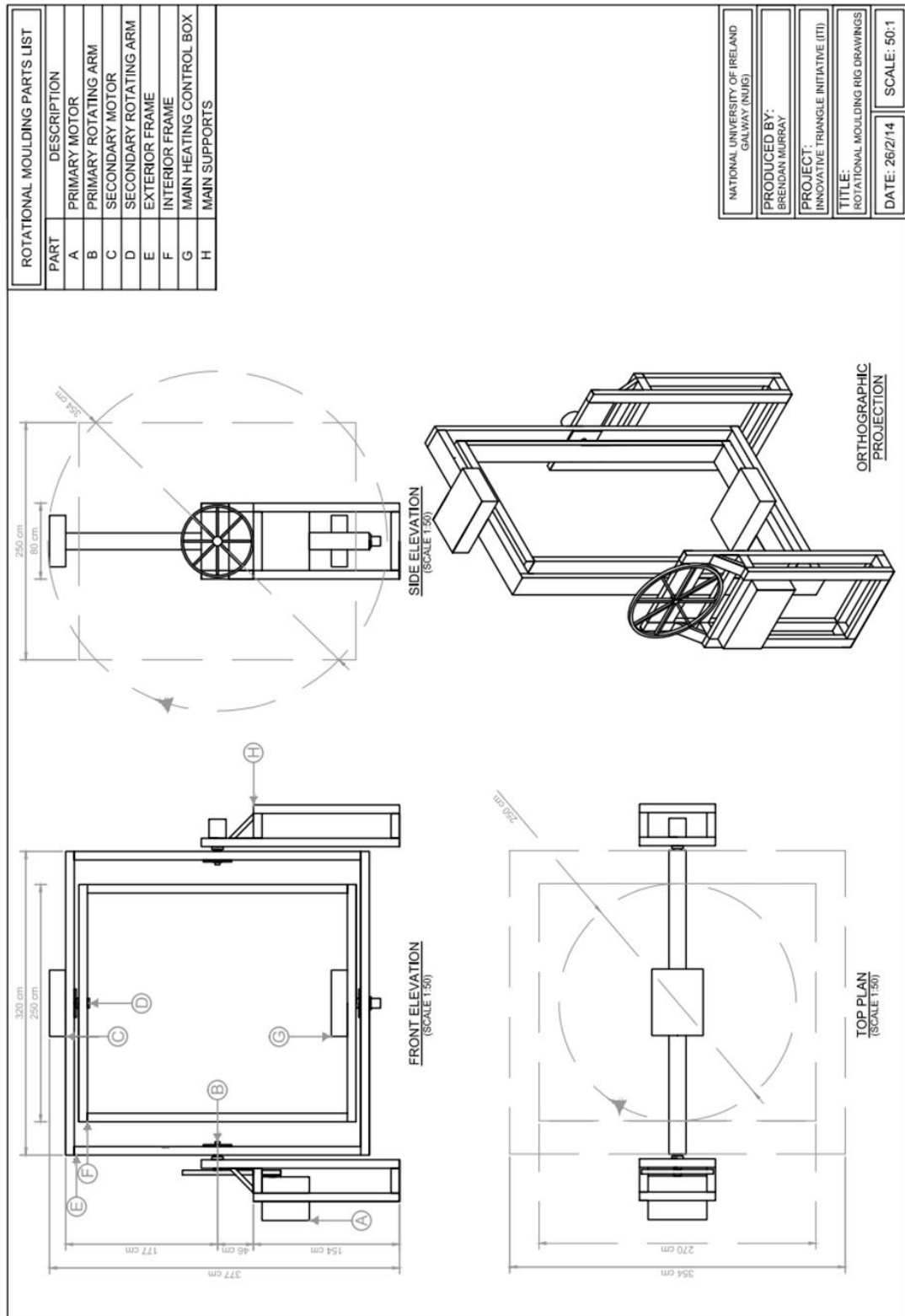
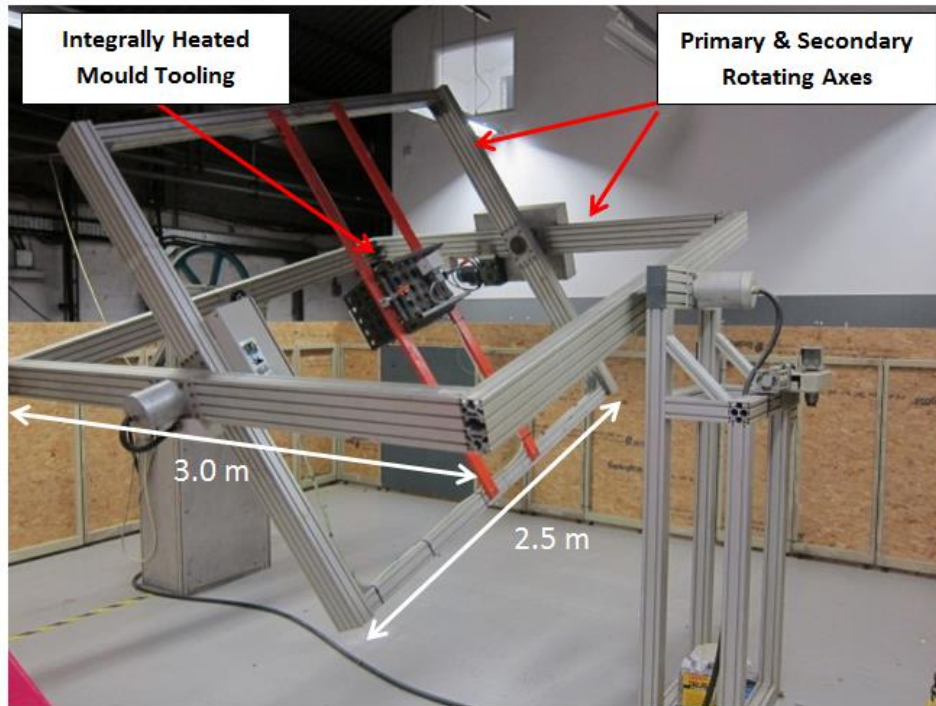
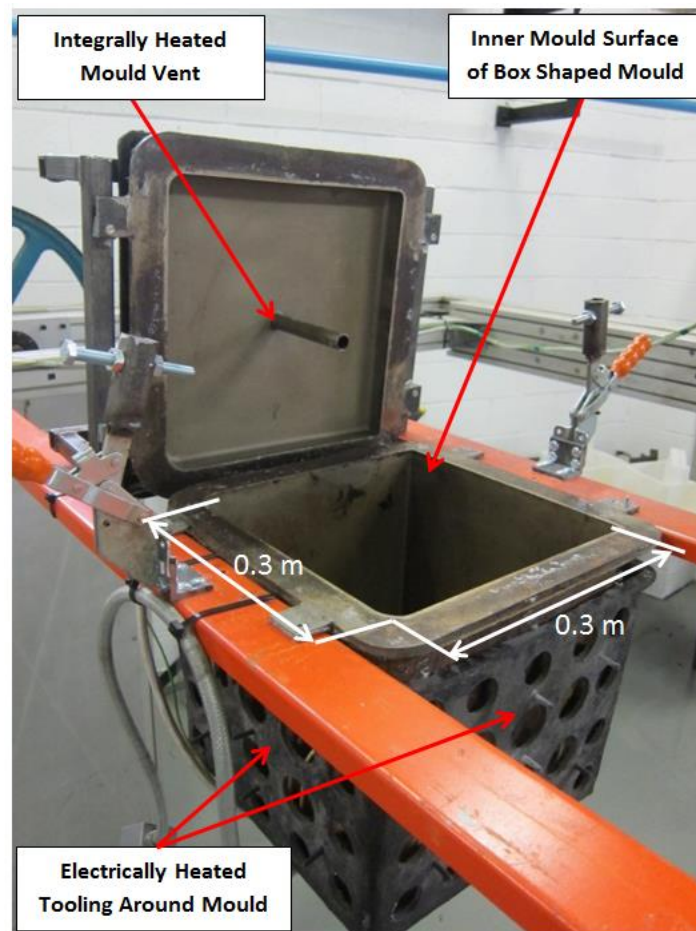


Figure 6.1. CAD drawings of the modified rotational moulding machine.

## Integrally Heated Rotomoulding Tooling Development



(a)



(b)

Figure 6.2. Photographs of (a) the rotational moulding machine and (b) the current modified rotomoulding tool used for proof of concept [64].

### **6.3. Initial Design Considerations**

The initial design considerations for the demonstrator tool centred on the testing of a number of critical features while also providing samples for permeability and mechanical tests. The designs of the specified COPV structure were analysed to determine which features were most important to analyse before upscaling to the full demonstrator scale tooling. The inclusion of all of the required functionality in a demonstrator mould was difficult in the sense of maximising the use of the tooling while also fitting all of the required components together. Due to these requirements, a number of desired features were highlighted for inclusion in the initial demonstrator mould functionality: A flat section capable of producing panels of at least 200 mm × 200 mm was needed to manufacture flat coupons for permeability and fracture testing. The permeability test apparatus has a standard circular test diameter of approximately 100 mm while fracture specimens require a minimum length of approximately 120 mm. Hence, a flat area was needed to provide specimens for both of these tests.

The wall thickness of the final component is affected by temperature distributions within the tool and so uniform heating is extremely important [50, 63]. By segregating the heating system at specific points, such as at the parting line where temperatures tend to lag behind the rest of the tool, an improvement in thermal control can be achieved to create a uniform temperature distribution across the tool surface. A cylindrical section was needed for the analysis of heating line orientation and placement around the tool for part formation and wall thickness variations. A semi-elliptical dome end was also included as the current COPV designs have a semi-elliptical dome at both ends. The dome was of sufficient diameter such that a consistent elliptical curvature was achieved, as any alteration to the curvature could change the mechanics of the vessel and redistribute stresses in an unknown and potentially dangerous manner.

### **6.4. Detailed Tooling Design and Fabrication**

#### **6.4.1. Initial Tooling Design**

The final demonstrator tooling designs are outlined in Fig. 6.3 with detailed schematics of the entire structure included in Appendix A.2. The design consisted of

## Integrally Heated Rotomoulding Tooling Development

a half hexagonal-half cylinder design whereby cylindrical and flat samples could be produced from the same tooling over a single production run. This was coupled with a semi-elliptical dome end which has been shaped to match the hexagonal-cylinder structure to investigate the effects of the manufacturing process on the polymer dome formation.

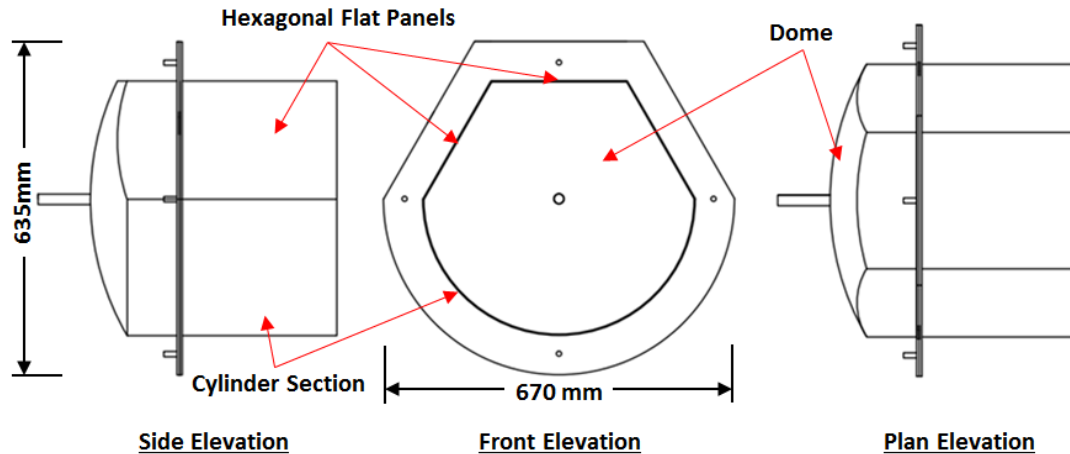


*Figure 6.3. Designs for the integrally-heated hexagonal-cylindrical mould tooling.*

The central image in Fig. 6.3, showing the front elevation, best demonstrates the use of the hexagonal-cylindrical design. Here the hexagonal section has three flat sides which can produce three flat samples for each production run, maximising the effectiveness of the tooling by producing flat samples for testing. Opposite to the flat sides is the cylindrical section which can produce half cylinder sections for testing the effects of curved surfaces on the integrally-heated tooling and also acting as a closer mock-up of the final demonstrator design.

The side and top elevations display the dome end which has been incorporated into the tooling due to the dual dome structure used in the original COPV designs given. To accommodate the hexagonal-cylinder structure, the dome has been altered on one side with three flat panels with curved ends, which join with the dome structure. This removes the need for high angle corners where the dome meets the flat section while also keeping the part consistent. A number of designs were considered which incorporated a moulded-in insert to the dome section, Fig. 6.4, which would have allowed the introduction of the metallic inserts, Appendix A.1, which are used for filling and emptying of the COPV. But due to time constraints, the availability of

inserts and the general difficulty in incorporating the insert into the tooling design, this feature was removed.

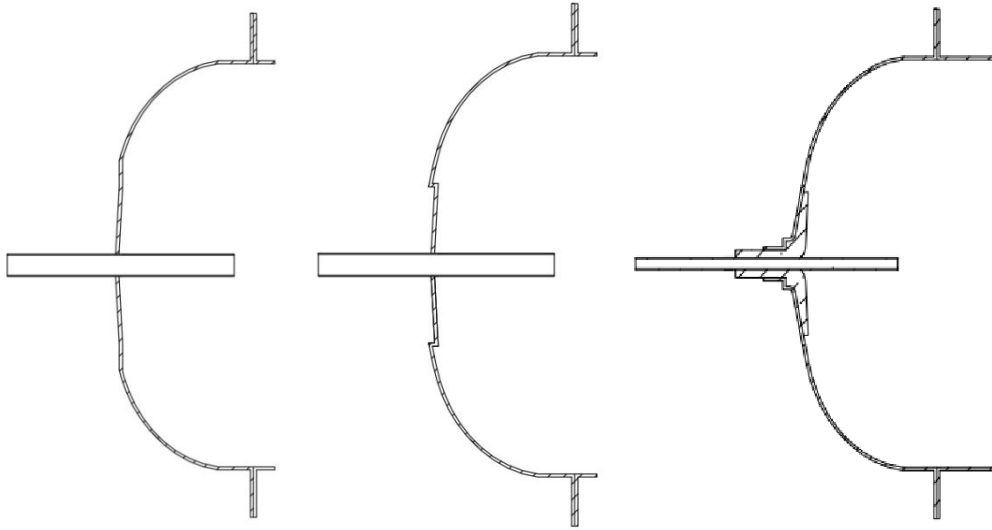


*Figure 6.4. Designs considered for incorporating a moulded in insert to the dome section.*

### **6.4.2. Mould Tooling Fabrication**

The mould tooling has been fabricated from a number of parts and components with mild steel chosen as the preferred mould tooling construction material. Due to the scarcity of elliptical domes of the appropriate size and thickness the tooling had to be redesigned around the availability of dome sizes. In rotational moulding, and specifically for an integrally-heated mould tool, a thinner mould wall thickness leads to a quicker and more efficient heating process [63]. Hence a 2 mm wall thickness was chosen for the entire tooling structure. The availability of mild steel semi-elliptical dome sections with 2 mm wall thicknesses was limited to a semi-elliptical dome with a 520 mm outer diameter (Fig. 6.5) and so the tooling design was scaled to fit these dimensions as outlined in Appendix A.2.

Once the dome size was known, the other sections of the tooling could be designed. The three flat panel sides were formed by bending a flat plate of 300 mm × 900 mm with two 60° bends at 300 mm intervals. This eliminated the need for subsequent welding of the flat sections together and reduced the amount of work needed to

## Integrally Heated Rotomoulding Tooling Development

fabricate the tooling. The cylindrical section was formed by rolling a flat 300 mm × 1630 mm panel into a half cylinder with a 520 mm diameter.



*Figure 6.5. Mild steel dome section with a 2 mm wall thickness and a 520 mm diameter.*

The three individual flat panels for the dome section and the back panel connecting the hexagon and cylinder together were formed using a laser cutter. The flange sections were fabricated using a thicker 5 mm mild steel plate, as the mounting of the tooling to the rotomoulding frame and the tool clamping mounts were contained on the flange. The welding of all parts together was performed using a TIG welder with the two finished pieces shown in Fig. 6.6 to 6.8. The dowels and their mating holes along with the pry points and the final polishing operations were completed to allow the direct application of the mounting and heating system to the tooling.



*Figure 6.6. Images of the inner mould surface of the dome section of the tooling.*

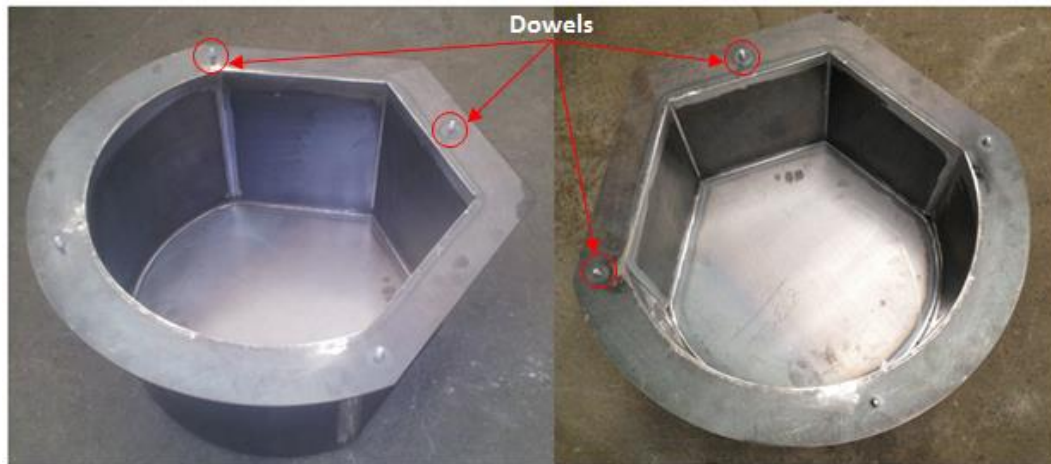


*Figure 6.7. Images of the bottom section of the tooling with dowels attached to the flange.*



*Figure 6.8. External images of the mould tooling in its closed configuration.*

### **6.4.3. Mould Tooling Fabrication**

The heating system application process consisted of building a layered configuration of fibre-glass and heating lines around the mould tooling. The first step in this process, Fig. 6.9, was covering the outside of the entire mould tool with a non-stick release film, Airtech Flashbreaker Tape, to ensure the heating system did not bond directly to the tool. Instead the mould tooling and heating system are free to expand at different rates due to their differences in thermal expansion coefficients with the lack of bonding reducing the risk of cracking in the heating system. The tape is applied in a thin layer with care taken to remove bubbles from beneath the tape. This

## Integrally Heated Rotomoulding Tooling Development

ensures that the heating system has the same shape as the metal mould tooling surface giving good contact without air gaps.

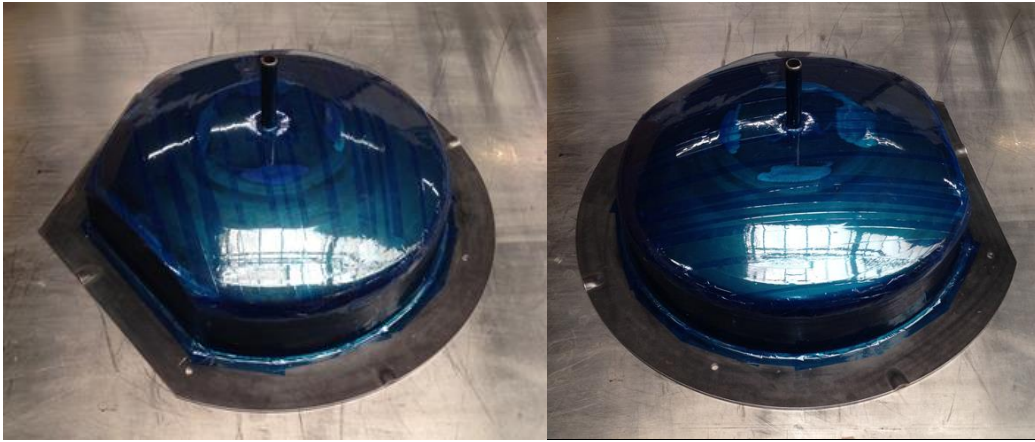


*Figure 6.9. Sealant tape application to mould tooling.*

Once the mould tooling has been completely covered the heating lines are prepared and cut to consistent lengths. The heating lines used are HTS/Amptek Standard Insulated Bulk Monotape with a maximum temperature of 760 °C and a resistance of approximately 65  $\Omega$ , equating to an average length of 200 cm. The consistency of heating line resistances is important as the entire heating system configuration is based on resistors in a parallel array which ensures an equal current across heating lines in the same zone and an equal heating rate across individual heating lines.

*Table 6.1. Materials list for ceramic mould tooling composition.*

Product Code	Material	Supplier
AFL13	Calcined Alumina	Almatis
CA470	Calcium Aluminate	Almatis
Alphabond	Alphabond	Almatis
ADS3	Dispersing Alumina	Almatis
ADW1	Dispersing Alumina	Almatis
PS	Potassium Silicate Solution	Mistral

The final step involves cutting fibre glass sheets to fit the design of the mould tooling and preparing the resin for the ceramic structure which is outlined in Fig

## Integrally Heated Rotomoulding Tooling Development

6.10. For this tooling a fibre glass sheet, Formax, with a pattern of  $-45^{\circ}/+45^{\circ}$ , was cut to shape for covering the mould tooling due to its drapability and usefulness in providing structural integrity. The resin is a combination of materials and follows the guidelines outlined in Table 6.1. The composition consists mostly of a calcined alumina and calcium aluminate cement mixture with the addition of a potassium silicate solution and water in an 80:20 powder to liquid ratio. The inclusion of Alphabond powder reduces the creation of low melting point silicates in the resin which can reduce the structural integrity of the casting at high temperatures. Choice amounts of ADS3 and ADW1 were used to reduce the amount of water needed in the mixture while also adjusting the flow properties of the resin and increasing the setting time to allow for specific placement of the resin. For this tooling, almost 18 kg of resin was used for the dome and hexagonal-cylinder sections.

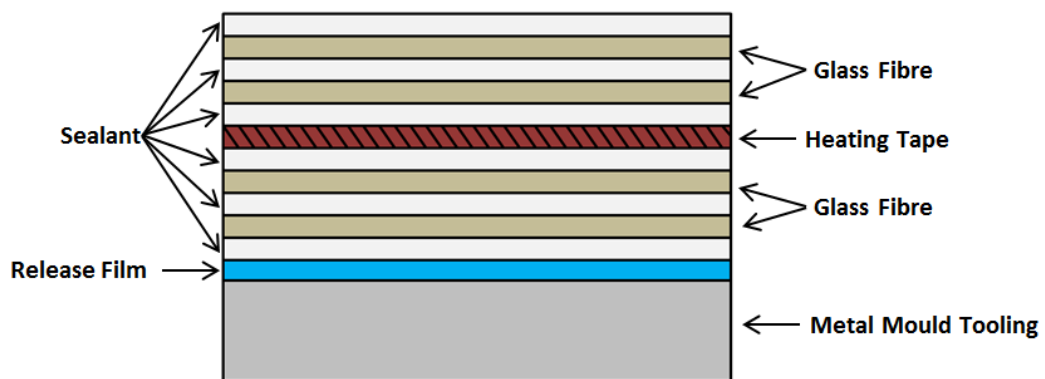


Figure 6.10. Ceramic mould tooling layup configuration.

The first step in applying the heating system was coating the prewrapped tooling with a single layer of resin. Then a glass fibre layer was placed over the tooling and pressed into the underlying layer of resin. Excess glass fibre was removed from the tooling so that a single layer surrounded the structure with minimisation of overlapping glass fibre layers. Another layer of resin was then applied until the gaps between the glass fibres were filled. Fig. 6.11 (a) shows the tooling after a second glass fibre layer and resin coating were applied, whereby this two layer system forms the underlying heating system layer.

The second stage involved placing the heating tape on the mould tooling with significant care given to positioning, Fig. 6.11 (b). Two lines (each 25 mm wide) were placed on both flanges to form their own heating zone on the tooling while the cylinder and hexagonal flat plate sections had the tape wound around the frame in a

## Integrally Heated Rotomoulding Tooling Development

simple circumferential pattern. The heating tape had to be altered for the dome end and its opposing flat section due to the angular nature of the surface. This involved cutting the tape casing to wind the tape around and along difficult edges. Once the tape had been applied, another coating layer of resin is applied to hold the tape in place with care taken to ensure the heating tape connections were free standing and uncovered.

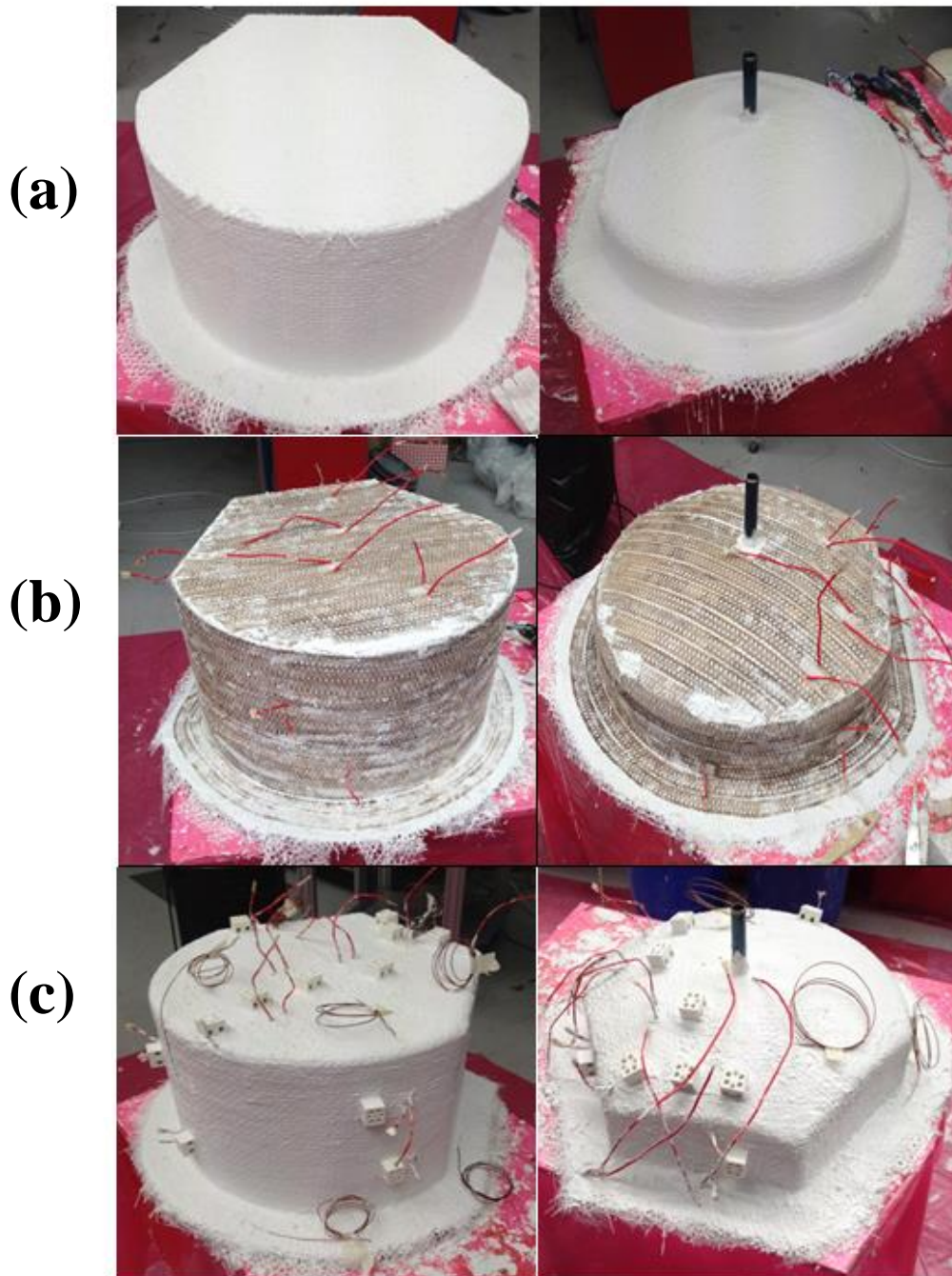


*Figure 6.11. Images showing (a) the initial glass fibre and resin application, (b) the heating tape application and (c) the finished mould tooling.*

## Integrally Heated Rotomoulding Tooling Development

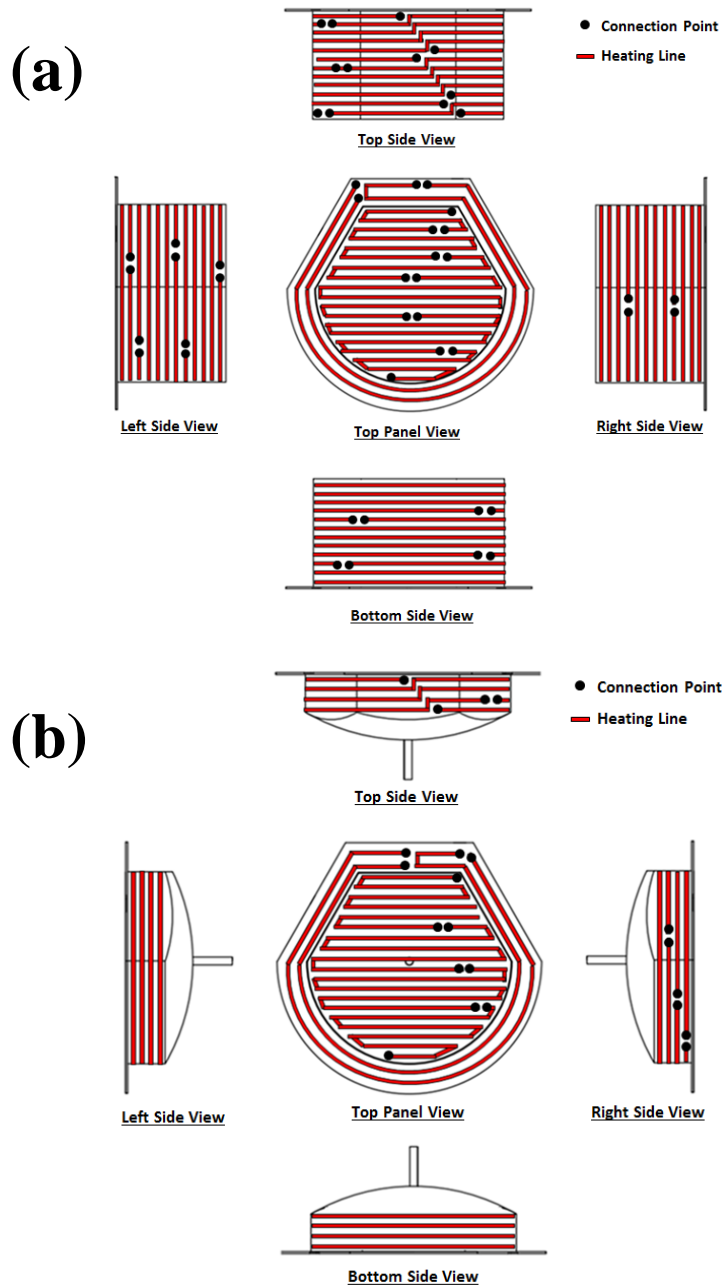


Figure 6.12. Heating line placement around the integrally-heated tooling for the (a) hexagonal-cylinder section and (b) the opposing dome section.

The third step in the heating system application process involved applying another two layers of glass fibre and resin coatings over the heating tape. Thermocouples were added before the final glass fibre layer to monitor the temperature of the tooling during processing. Fig 6.11 (c) shows the placement of Connectwell terminal blocks around the tooling after the final resin layer placement. This provides connection points for all of the different heating lines in the tooling, with Fig. 6.12 showing the layout heating lines on the tooling.

### 6.4.4. Wiring and Temperature Control

The connection ends are then crimped together using high temperature crimps to place each heating tape line in parallel with each other such that the voltage drop across them is equal as indicated by the schematic output in Fig. 6.13. Each line is then tested with a multimeter to ensure it is working properly before placing the entire structure in an oven for 12 hours at 60-70°C so the entire system is given time to solidify and set. The terminal blocks are then wired back to the control box using a combination of wire consisting of MG14-5107 and MG16-5107, both manufactured by Allied Wire and Cable Company. K type thermocouples were embedded within the mould during the application of the final layer of glass fibre and these are used in conjunction with CAL 9500 Temperature Controllers to regulate heating within the tooling. Two heating zones have been defined for this tooling; the flange and the body. As indicated in Fig. 6.13, the flange sections consist of two heating lines on each flange (equating to four lines) while the body section consists of twenty one heating lines on three individual loops, where seven are located on the dome and fourteen are on the hexagonal-cylinder section. This layout was designed to ensure uniform heating within the tool while also giving significant control in individual sections.

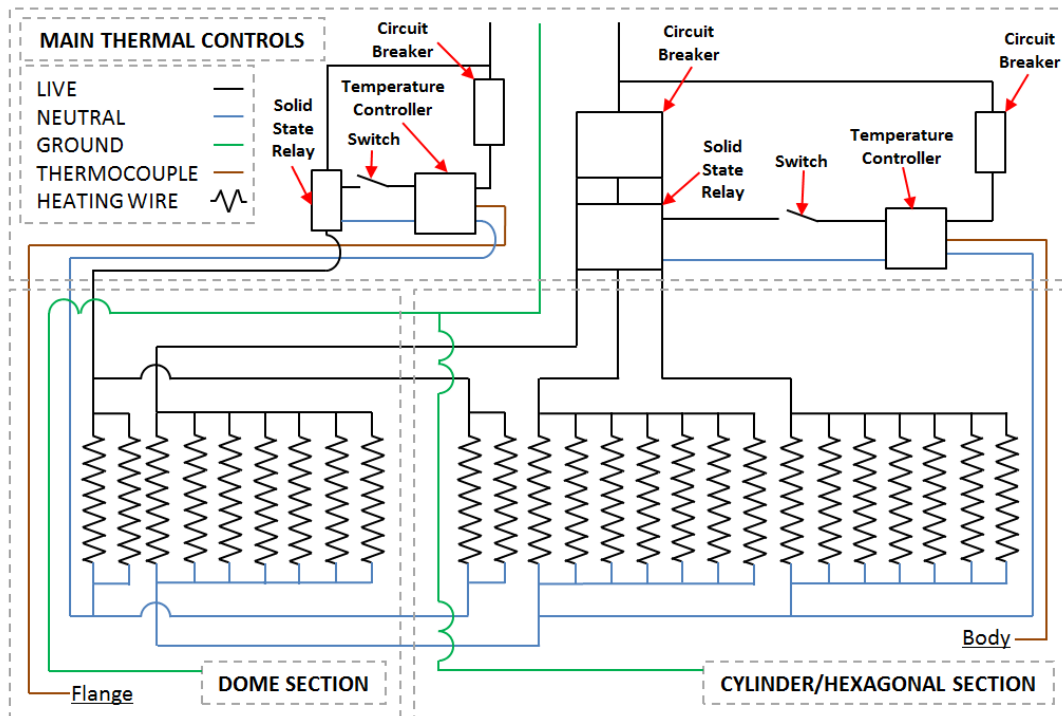


Figure 6.13. Schematic layout of the electrical system on the mould tooling.

## 6.5. Process Optimisation and Demonstrator Part Production

A Testo 881-2 thermal imaging camera in conjunction with TESTO IRSoft software has been used to map the temperature distribution across the tooling. Trial runs using polyethylene powders demonstrated the effects of varying processing conditions on part formation. The effects of flange heating have been highlighted with thermal images and moulded parts demonstrating the effects of temperature control on part consistency.

### 6.5.1. Heating Trials

Two different temperature cycles were applied to the tooling to highlight the difference in flange heating control optimisation. The first trial run for the integrally-heated tooling shows the effects of heating the flange and main body at the same rate for the entire tooling. The heating trace mapping the temperature change of the inner air and mould tooling is given in Fig. 6.14 with heating taking place at the same rate over all sections.

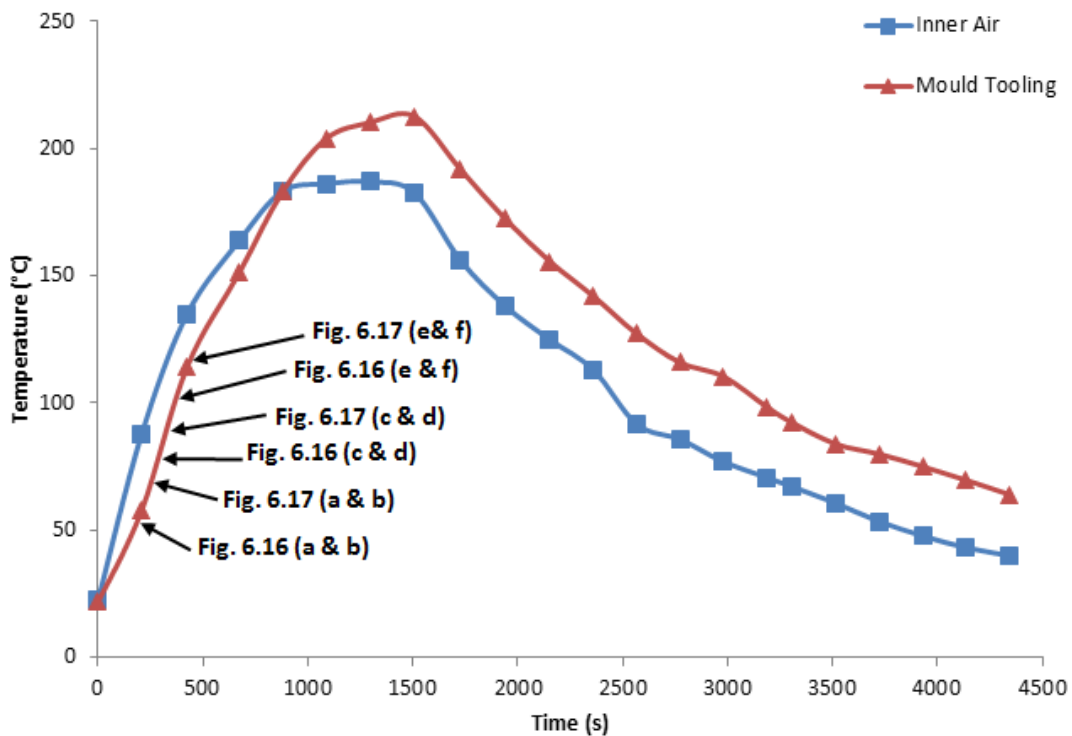
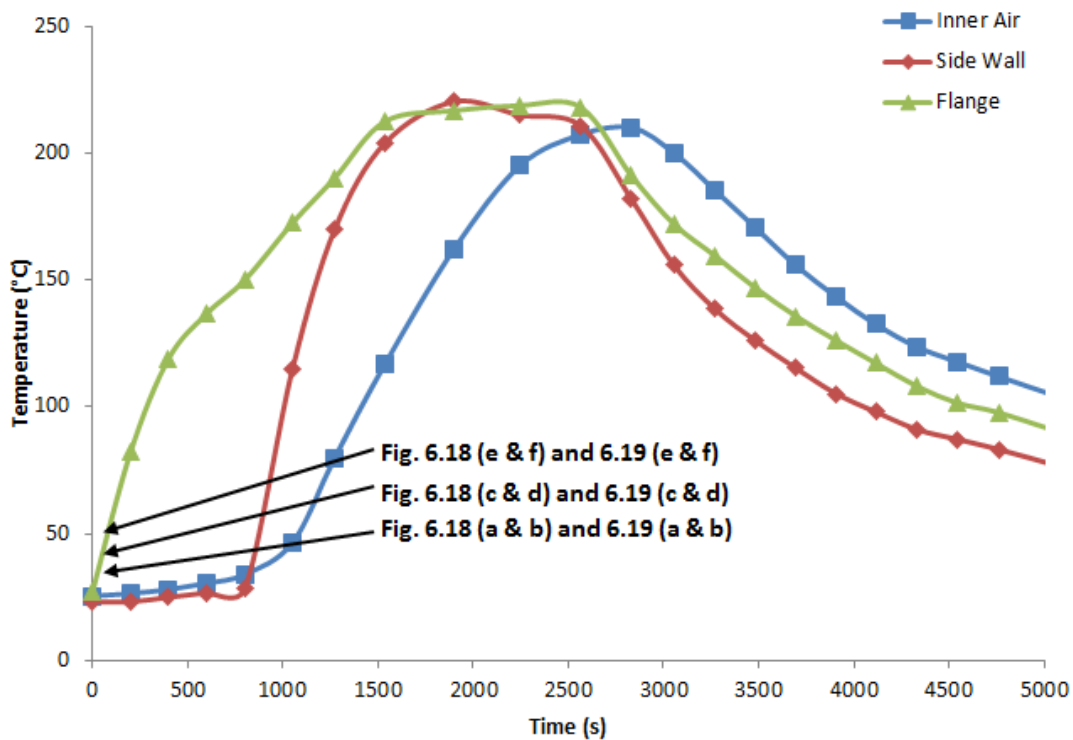


Figure 6.14. Measured heating trace for the integrally-heated tooling using the same heating rate across the tooling.

The second trial run utilises an optimised flange heating approach. The designation of the flange as a single zone allows for heating of the flange to occur at a faster rate, or earlier in the heating phase, promoting wall thickness build up around the parting line and keeping the temperature distribution uniform across the wall section of the tool during the forming process. This is exhibited by the heating trace in Fig. 6.15 where the flange is heated to the melting point of polyethylene over a 10 to 15 minute period prior to engaging the sidewall heating.



*Figure 6.15. Measured heating trace for the integrally-heated tooling where the flange zone has been engaged before the rest of the tooling to promote wall thickness build up near the parting line.*

In this way, the flange region near the parting line will start to melt polymer powder particles at an earlier stage in the process than the main body of the tool and so the wall thickness build up will be increased in this region to compensate for the heat loss experienced at the parting line. The heat loss at the parting line is due to the direct exposure to air at this gap in the tool and also due to the overlapping nature of the flange on the mould wall which hinders heating tape placement up to 5 mm away from the parting line on the hexagonal-cylinder region of the tool (reducing the heating in this region as will be shown via thermal imaging).

### 6.5.2. Thermal Imaging Analysis

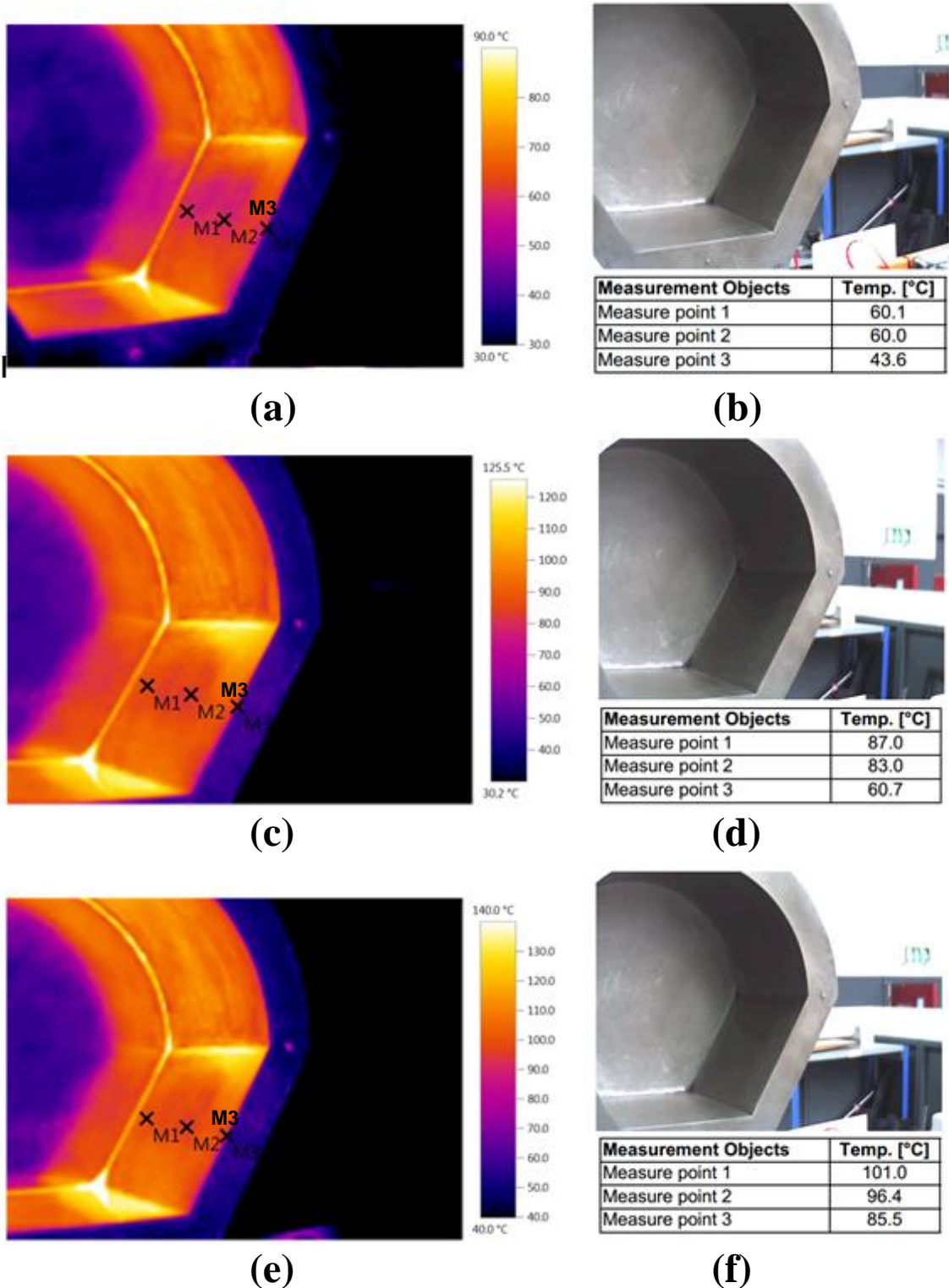


Figure 6.16. Thermal analysis of the hexagonal-cylinder section of the tool with a thermal image on the left and the temperature measurements on the right for (a & b) the initial heat up to (c & d) intermediate levels and finally (e & f) to elevated temperatures for Fig. 6.14.

## Integrally Heated Rotomoulding Tooling Development

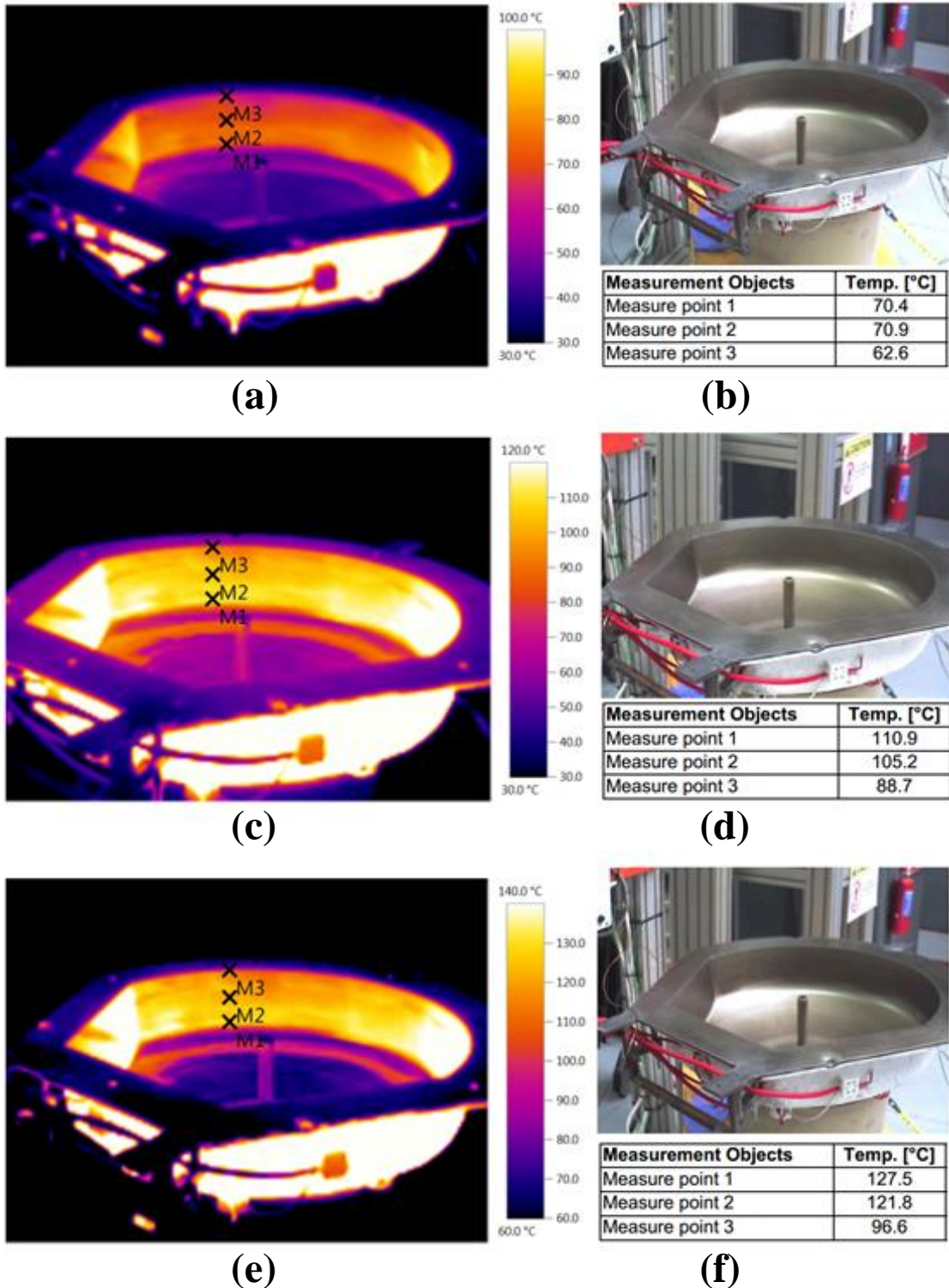
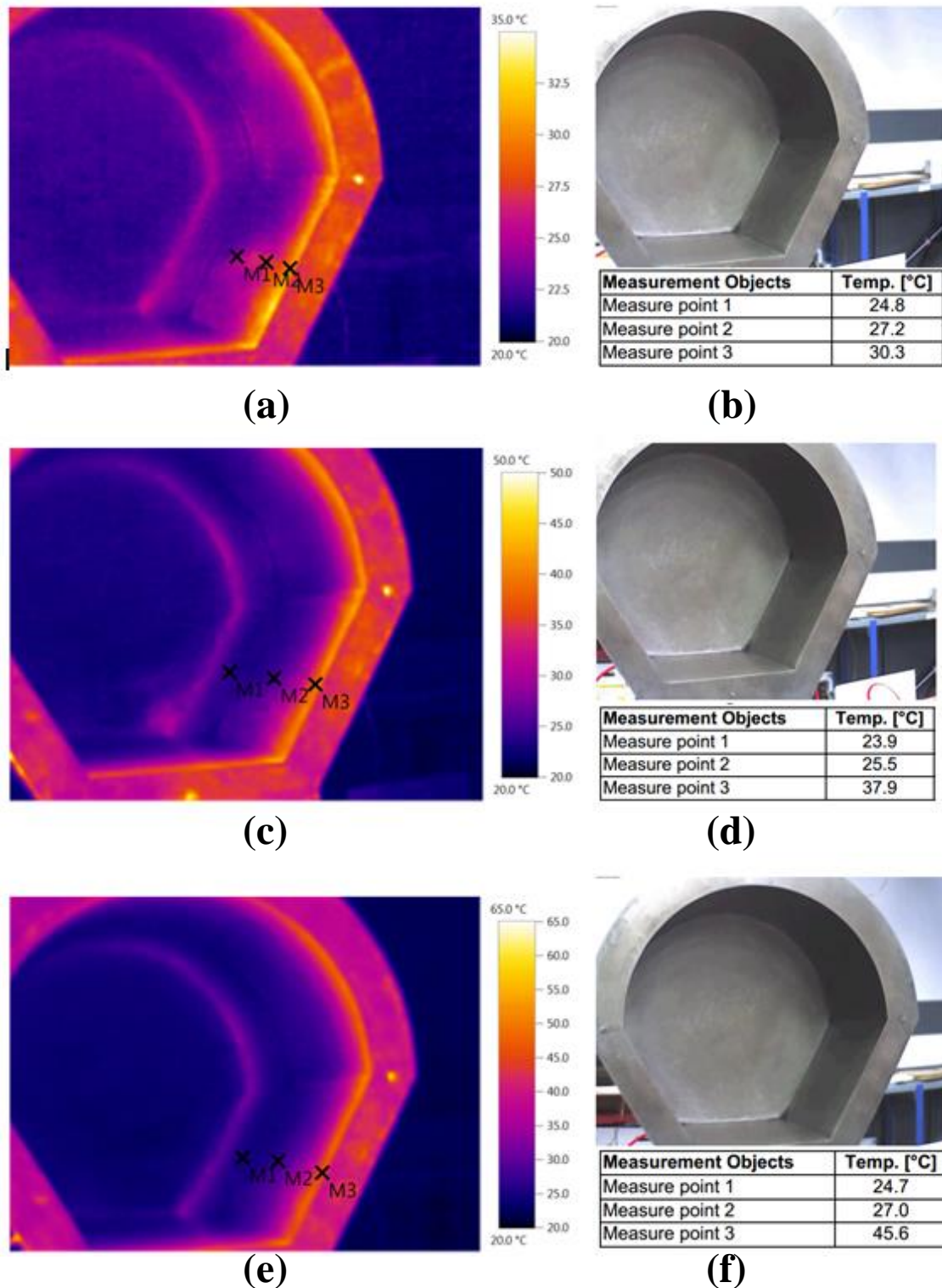


Figure 6.17. Thermal analysis of the dome section of the tool with a thermal image on the left and the temperature measurements on the right for (a & b) the initial heat up to (c & d) intermediate levels and finally (e & f) to elevated temperatures for Fig. 6.14.

## Integrally Heated Rotomoulding Tooling Development



*Figure 6.18. Thermal analysis of the hexagonal-cylinder section of the tool with a thermal image on the left and the temperature measurements on the right for (a & b) the initial heat up to (c & d) intermediate levels and finally (e & f) to elevated temperatures for Fig. 6.15.*

## Integrally Heated Rotomoulding Tooling Development

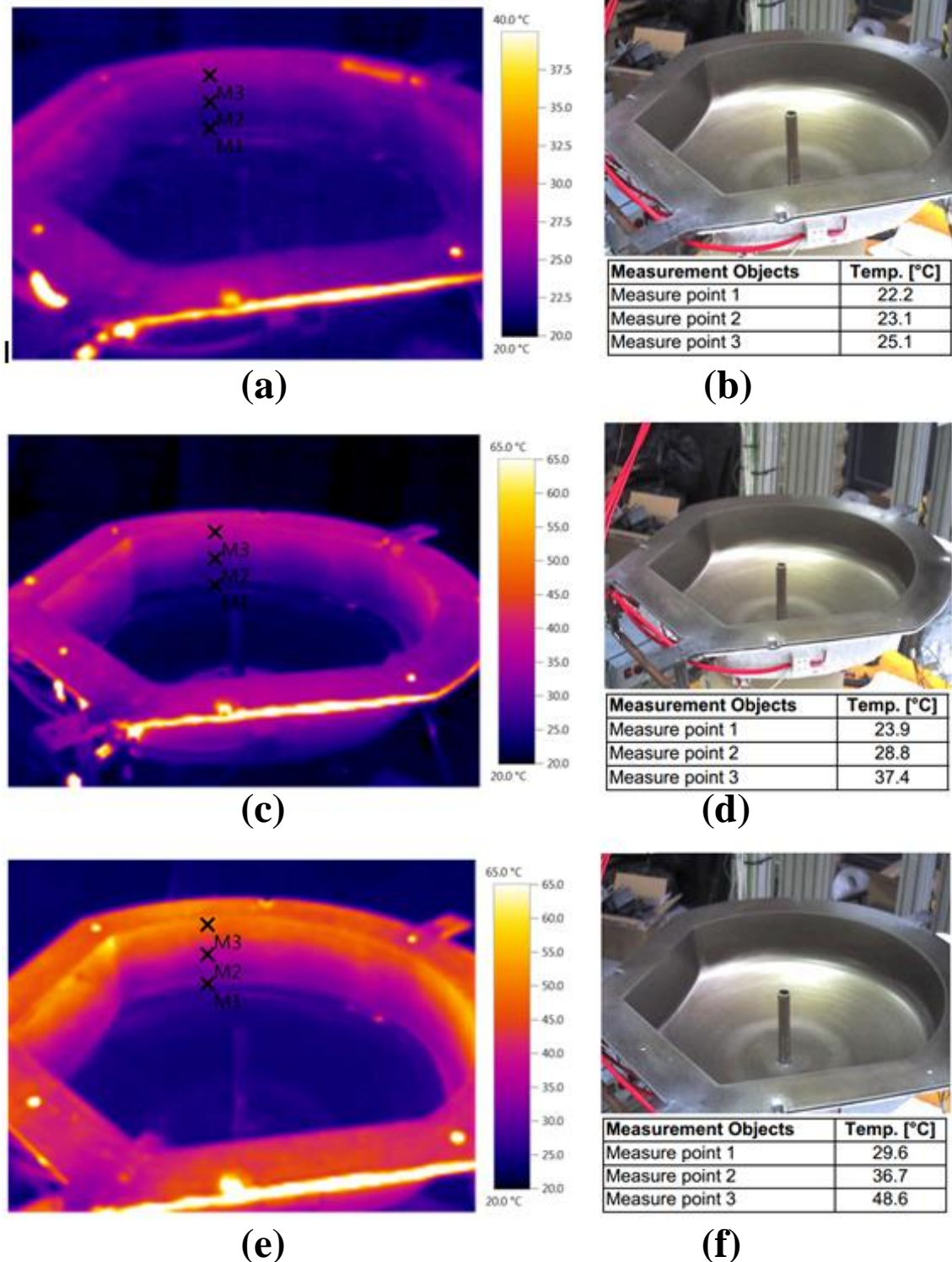


Figure 6.19. Thermal analysis of the dome section of the tool with a thermal image on the left and the temperature measurements on the right for (a & b) the initial heat up to (c & d) intermediate levels and finally (e & f) to elevated temperatures for Fig. 6.15.

A thermal imaging camera was used to characterise the two heating cycles individually in a separate analysis to examine the temperature distribution inside the tool during the heating cycle. Figs. 6.16 and 6.17 show the thermal images of the hexagonal-cylinder section and dome section for the first cycle in Fig. 6.14, involving the uniform heating rate across the entire mould tooling. Here the area near the flange for both parts of the tooling (measurement point 3 in all images of Figs. 6.16 and 6.17) is lower than the surrounding mould area from the start of the heating cycle right through to the end with 20 °C temperature differences achieved. The three images in Fig 6.16 and Fig. 6.17 (from (a) to (e)) are noted in the initial heating cycle graph, Fig. 6.14, to demonstrate their position in the heating cycle and to show that the thermal analysis conducted was indicative of the manufacturing process described.

In contrast the second heating cycle has the opposite effect. Figs 6.18 and 6.19 show that the area near the flange heats at a faster rate than the rest of the tool and so the flange region nearest to the parting line is now the hottest part of the tool. This will continue throughout the cycle and allows the parting line region to be at a higher temperature than the side regions for the duration of the forming process. Again the images in Figs. 6.18 and 6.19 have been highlighted at their corresponding points on the heating cycle graph in Fig. 6.15 to demonstrate their location in the heating cycle. As can be seen in the images, the flange region heats at an elevated rate, as demonstrated by the rise in temperature in measurement point 3 in all images in Fig 6.18 and Fig. 6.19.

### **6.5.3. Demonstrator Part Analysis**

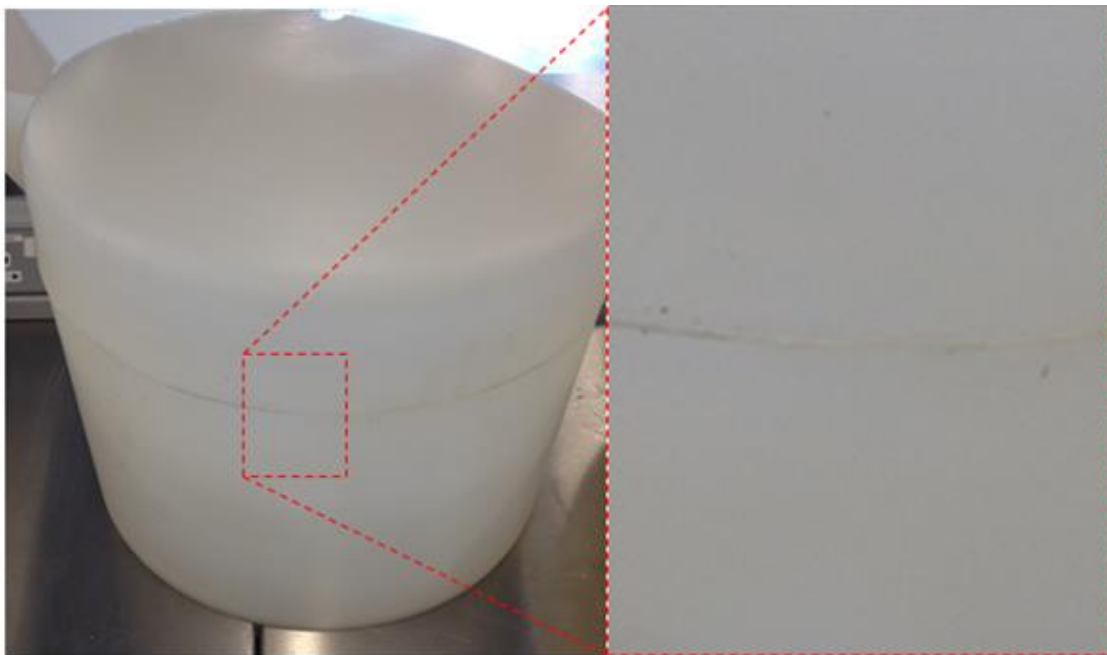
The demonstrator parts produced from these two heating cycles were then analysed to demonstrate the improvements achieved with flange heating optimisation. The first heating cycle utilising uniform heating is the general trace that most rotational moulding processes follow. The presence of blow holes is apparent in Fig 6.20 (b) due to the significant heat loss at the mould parting line. An assessment of the demonstrator part produced with the second heating cycle, incorporating flange optimisation, shows a vast improvement over its counterpart. Fig. 6.21 (a) shows the resulting rotomoulded polyethylene part which does not exhibit blow holes or other defects as shown by the smooth surface finish in Fig. 6.21 (b).



**(a)**

**(b)**

*Figure 6.20. (a) Rotomoulded polyethylene part using equal heating rates throughout with (b) a sample blow hole shown at the parting line (2 kg).*



**(a)**

**(b)**

*Figure 6.21. (a) Rotomoulded polyethylene part using the heated flange method to support parting line wall thickness consistency with (b) no defects visible at the parting line (3 kg).*

Fig. 6.22 shows the average wall thickness distribution of each demonstrator formed, with the first cycle using uniform heating showing a sporadic distribution with a

significant decrease in thickness at the parting line. The second cycle shows a clear and consistent linear distribution which is superior to the first heating cycle. The flange heating at the parting line (300 mm mark in Fig 6.22) is clearly beneficial for part consistency and highlights the level of control achievable.

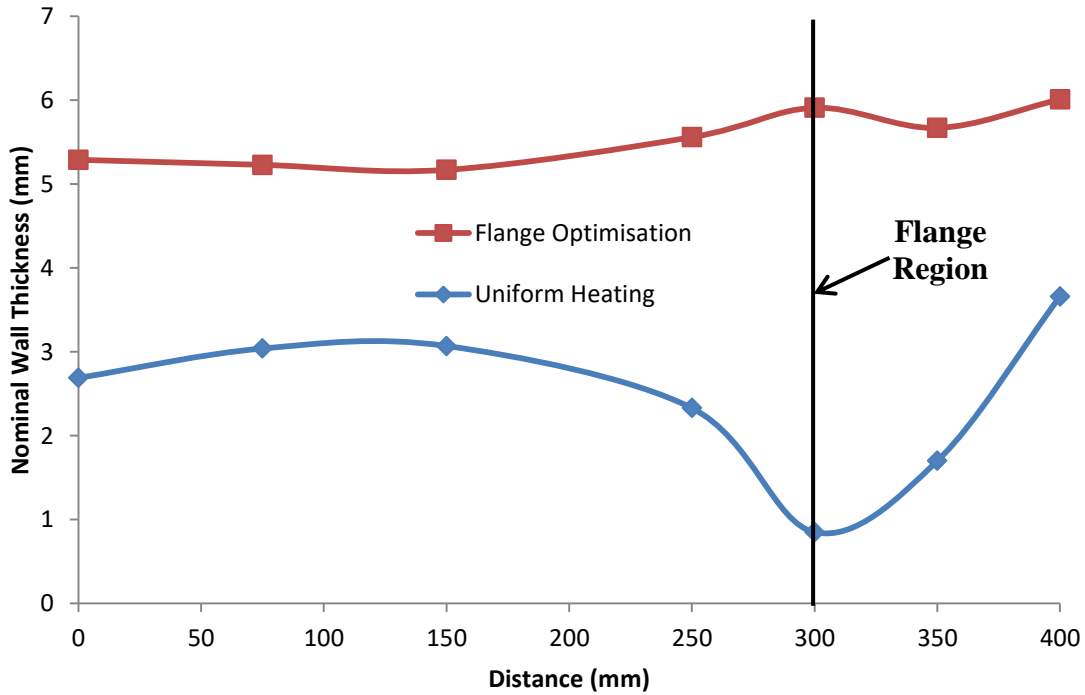
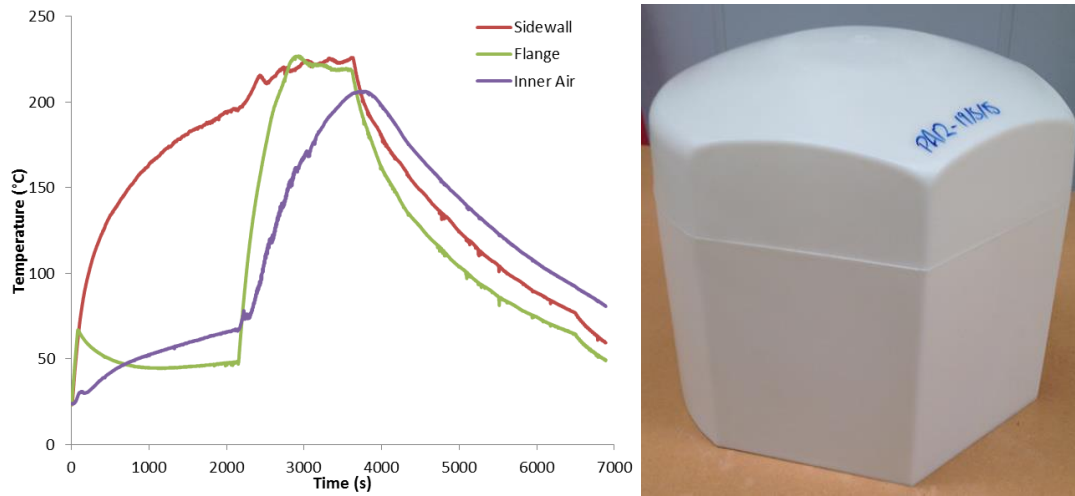


Figure 6.22. Wall thickness distribution for both rotomoulding cycles tested.

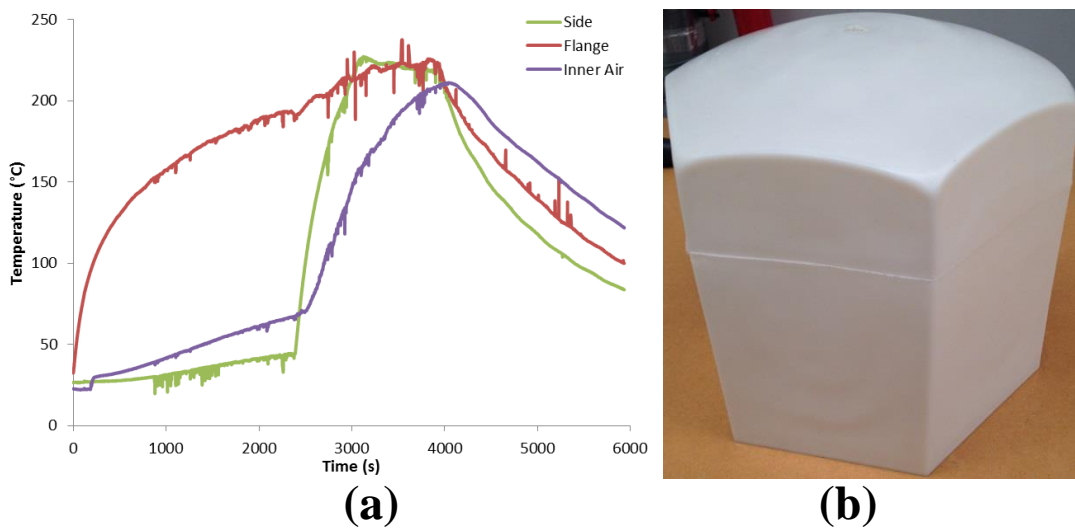
#### 6.5.4. Demonstrator Part Production

The final part of this chapter discusses the manufacture of demonstrator parts using the fabricated mould tooling and viable liner materials, as highlighted by the permeability testing conducted in Chapter 4. PA11, PA12 and PEEK (a powder mixture of 150P and 150PF at a 1:1 ratio) tanks have been fabricated using the tooling. Good part consistency was observed, demonstrating that the tooling is capable of producing liners from the required low permeability materials. This is a key step in the realisation of a manufacturing process for rotationally moulded polymer liner production.

## Integrally Heated Rotomoulding Tooling Development



**(a)** *Figure 6.23. (a) Heating trace for the rotational moulding of a PA12 demonstrator part using the heated flange method with (b) an image of the final part included (3.0 kg).*



**(a)** *Figure 6.24. (a) Heating trace for the rotational moulding of a PA11 demonstrator part using the heated flange method with (b) an image of the final part included (2.66 kg).*

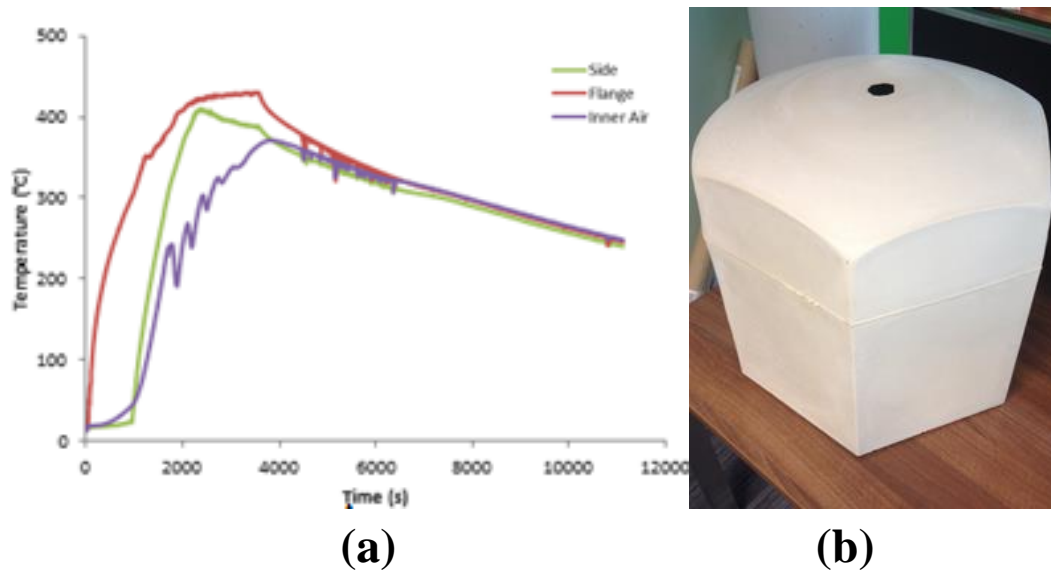


Figure 6.25. (a) Heating trace for the rotational moulding of a PEEK demonstrator part using the heated flange method with (b) an image of the final part included (6.88 kg).

### 6.6. Conclusions

The demonstrator mould tooling developed here for the integrally-heated rotational moulding process successfully produced demonstrator polymer liners for COPV applications. The ceramic heating system is capable of manufacturing polymer liners at various temperatures and the use of segregated heating zones has significantly increased the dimensional accuracy of the parts with respect to wall thickness consistency. The use of a heated flange has been shown to increase the temperature of the mould tooling along the parting line, which in turn has equalised the temperature distribution across the entire mould surface for the duration of the moulding process thus reducing the risk of defective formations. This is a significant improvement for part consistency and exemplifies the level of control achievable in integrally-heated rotomoulding tooling operations.

# 7. Liner and Overwrap Cryogenic Testing

## 7.1. Chapter Overview

This chapter presents the results from liner and overwrap testing across the operating temperature range of the COPV structure (-190 °C to 50°C). The effects of cryogenic environments on the bonding between the liner and external overwrap are investigated along with an analysis of the effects of cryogenic temperatures on the mechanical properties of the polymer liner materials as follows:

- Cryogenic cycling of polymer-composite welds to determine the effects of cryogenic cycling on the bond strength between the liner-overwrap configurations
- DMA of prospective liner samples including tensile and compression tests to measure the polymer storage modulus, tan delta and glass transition temperatures
- TMA of prospective liner materials to determine the coefficient of thermal expansion over the operating temperature range of the COPV
- X-ray CT analysis of the fracture joints before and after cryogenic cycling to determine the fracture characteristics of the welded joints

## 7.2. Cryogenic Cycling of Polymer Composite Welds

Down-selection of prospective liner materials has resulted in the selection of 150PF PEEK, PA11, PA12 and PVDF for testing of the bonding properties of these materials with CF/PEEK laminates. Bonding of polymer powders to composite

## Liner and Overwrap Cryogenic Testing

materials was achieved using a hot plate to form samples, melting the powder on to the upper surface of a preformed autoclave CF/PEEK composite laminate in the layup shown in Fig. 7.1. The composite laminates used here were manufactured in an autoclave, as outlined in Chapter 3, and were made from CF/PEEK Suprem IM7 with a layup consisting of a [45/135/0<sub>4</sub>/135/45] construction. Grit blasting has been used on the composite laminates, in certain cases, prior to bonding to roughen the laminate surface and enhance bonding while also removing any residual mould release agent from the composite surface.

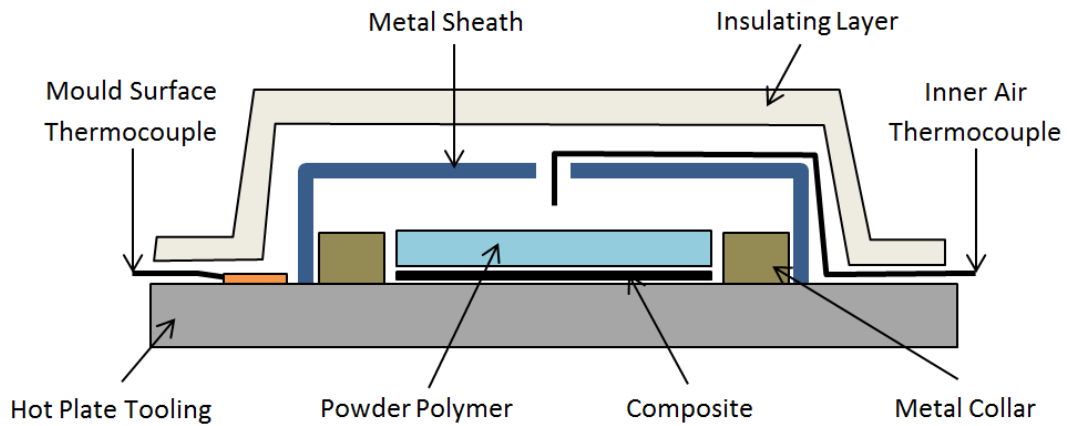


*Figure 7.1. Layup used for single layer polymer liner deposition on a composite laminate.*

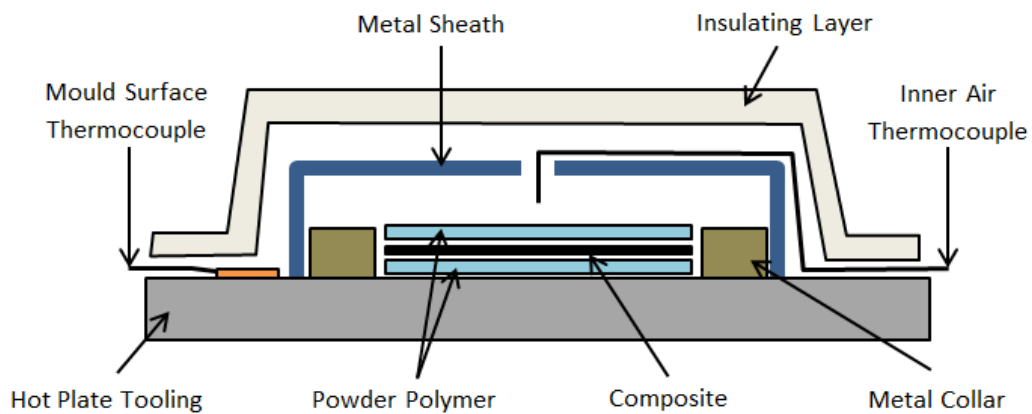


*Figure 7.2. Layup design for dual layer polymer liner deposition on a composite laminate.*

## Liner and Overwrap Cryogenic Testing

This layup, while effective at bonding the liner to the composite sheet, caused significant warpage due to the unbalanced nature of the layup and the mismatch in coefficients of thermal expansion between the two layers. To counteract this, and to produce flat sheets for testing, the composite plate is embedded between two powder layers of equal size to produce a flat sample as shown in Figs. 7.2 and 7.3.

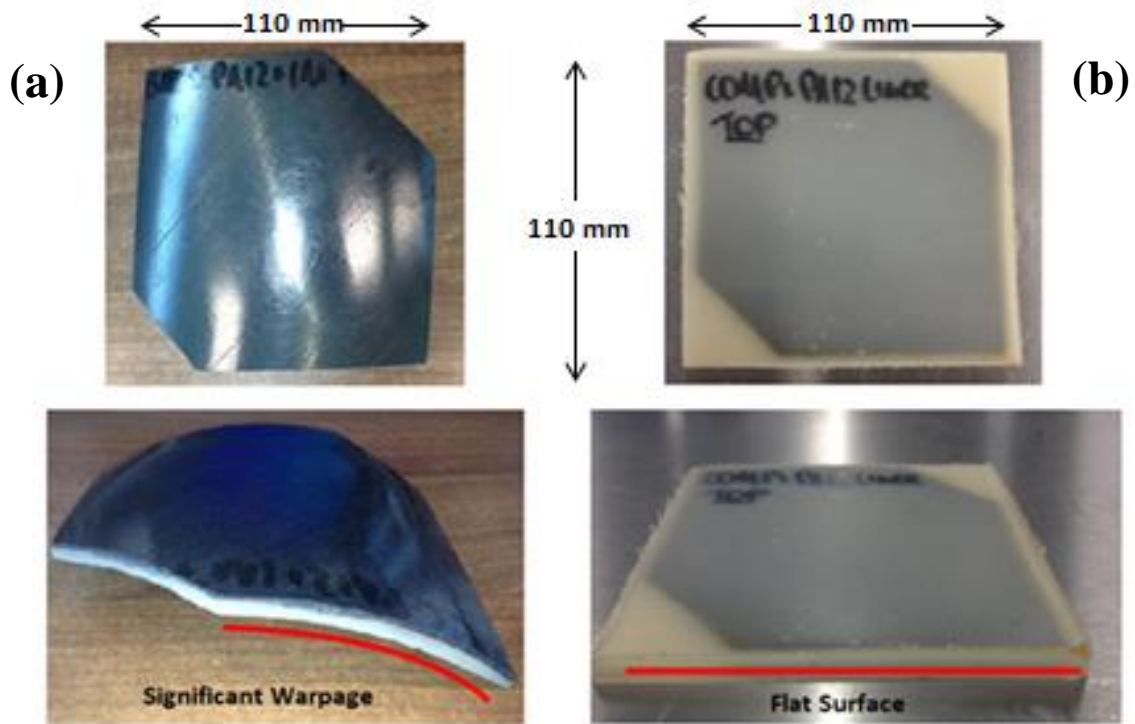


*Figure 7.3. (a) Warped laminate due to unbalanced design and (b) a dual layer laminate with even thicknesses of PA12 either side of the composite to balance the structure.*

### 7.2.1. Permeability Testing Flat Laminate Specimens

This allowed for permeability tests to be conducted with flat samples, specifically an 8 layer  $[0/45/135/90]_s$ , 1.3 mm thick Suprem IM7 CF/PEEK composite laminate, embedded within 2.2 mm of PA12 either side of the composite (equating to a 5.7 mm thick sample). The permeability results for an individual 5.25 mm thick PA12 laminate and for a Suprem IM7 CF/PEEK composite laminate of 1.3 mm thickness are shown in Fig. 7.4 for comparison. The results show a significant reduction in leak rates for the PA12-CF/PEEK-PA12 laminate. This indicates that the polymer lined samples are effective at reducing leak rates in prospective COPV layups. However, due to the operating conditions of the tank, the COPV layup must be able

to withstand a temperature range of 50 °C to -190 °C (323 K to 83 K) and so bond strength testing and cryogenic cycling of these laminates also needs to be investigated.

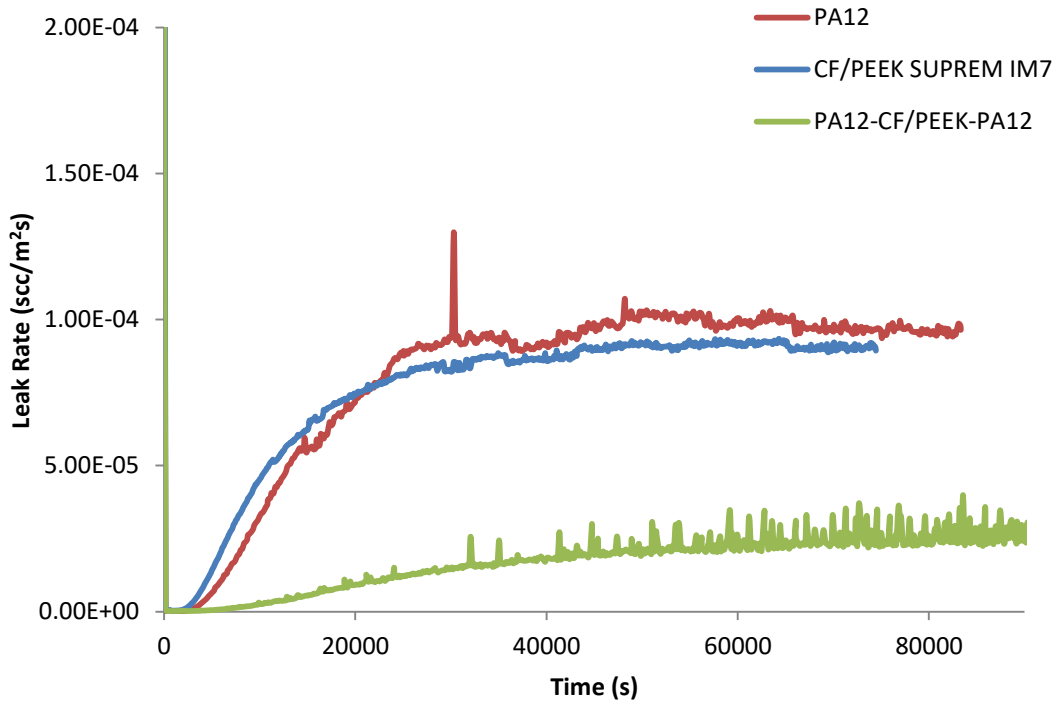


Figure 7.4. Leak rate results for individual PA12 and composite samples compared to that of the dual layer PA12 composite sample, showing a significant reduction in leak rate.

### 7.2.2. Bond Strength Testing

The bond strength between multilayer laminates of PEEK to PA12 and PA11 was initially investigated using a flatwise tensile test, based on testing sandwich structures as set out in ASTM C297 [2448]. This test is used to define the bond strength between core and facing materials and uses the fixture shown in Fig. 7.5. The samples (50 mm × 50 mm) are bonded to two aluminium load blocks using a suitable adhesive and a tensile force is applied to the sample to test the bond strength. The ultimate flatwise tensile strength in MPa is defined as the ultimate force prior to failure (of the bond between the polymer faces) divided by the specimen cross sectional area.

The samples tested included PEEK-PA12-PEEK and PEEK-PA11-PEEK sandwiches. Initial tests carried out in NUI Galway resulted in failure of the bonding

## Liner and Overwrap Cryogenic Testing

adhesive rather than fracture of the sample. This was initially attributed to inadequate curing of the bonding adhesive but subsequent tests in Composites Testing Laboratory (CTL) of the PEEK-PA12-PEEK sandwiches also lead to failure of the adhesive before fracture of the samples. It was not possible to find an adhesive of greater strength than bond strength between the laminates. Hence, it is only possible to report a minimum bond strength here.

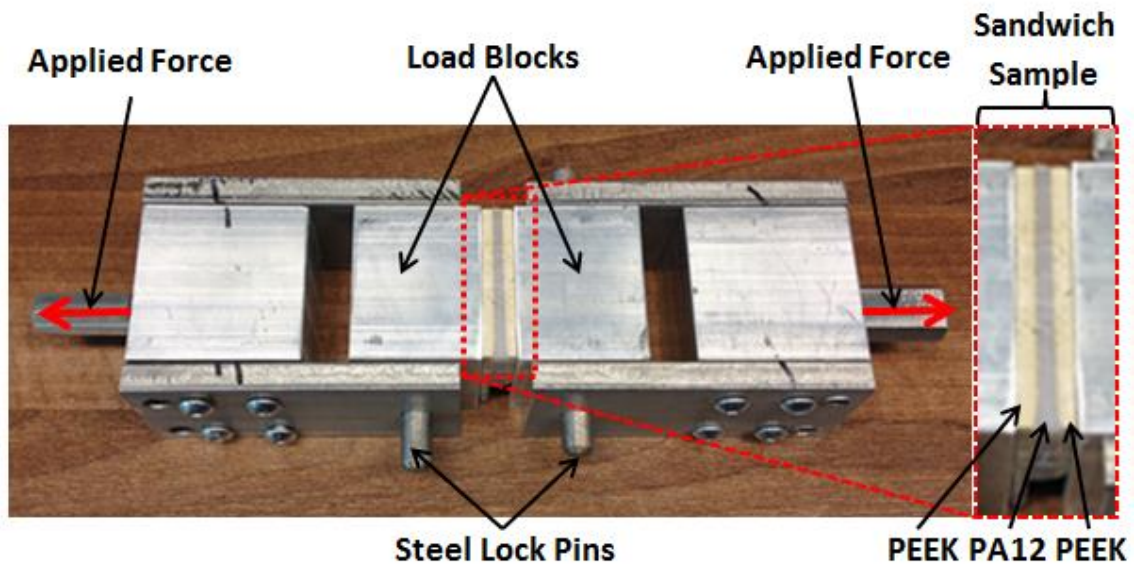


Figure 7.5. Flatwise tensile strength test apparatus for sandwich core materials.

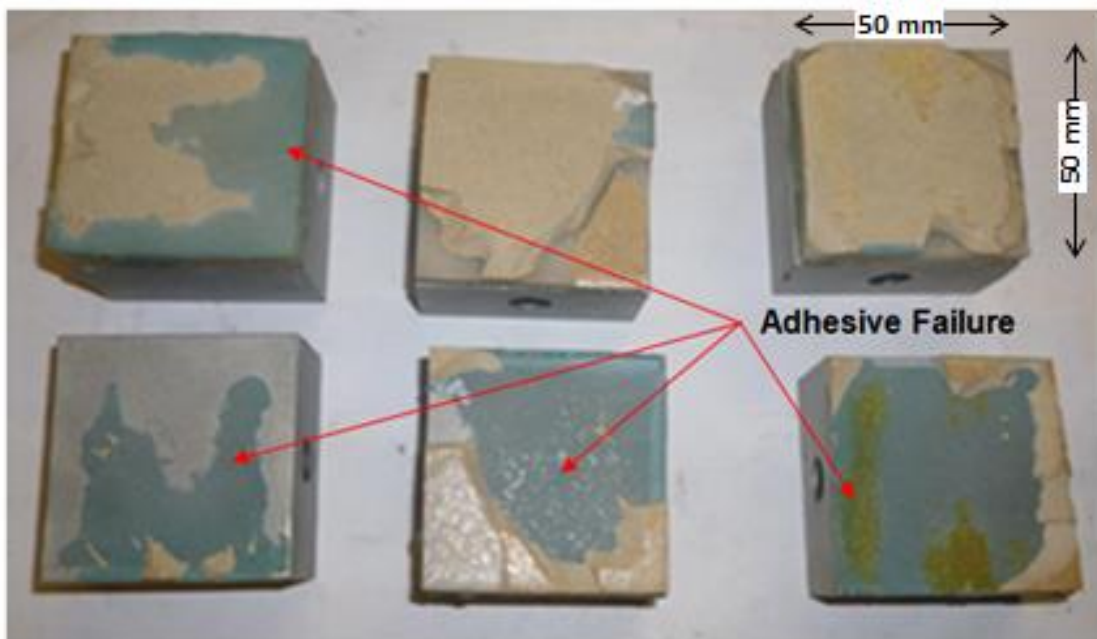


Figure 7.6. Fracture surfaces of failed sandwich samples of PEEK-PA12-PEEK tested by Composites Testing Laboratory Teo.

## Liner and Overwrap Cryogenic Testing

Images of the tested PEEK-PA12-PEEK samples are included in Fig. 7.6 with the adhesive failure highlighted by its distinct blue colour. The measured force displacement responses and the resulting minimum ultimate flatwise tensile strengths are shown in Fig. 7.7 and Table 7.1.

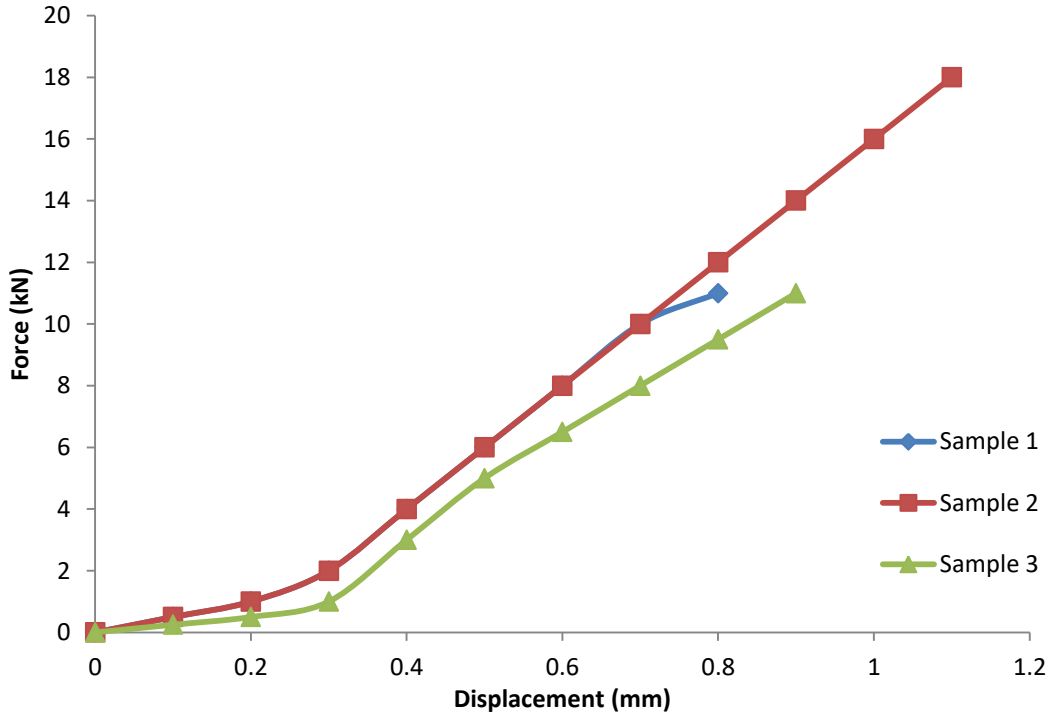


Figure 7.7. Force versus displacement graph for PEEK-PA12-PEEK sandwich samples.

Table 7.1. Flatwise tensile strength (FWT) test results for PEEK-PA12-PEEK samples with adhesive failure.

Specimen	$F_{\max}$ (kN)	FWT Strength (MPa)	Failure Mode
FWT1	10.97	>4.5	Adhesive Failure
FWT2	17.91	>7.4	Adhesive Failure
FWT3	10.87	>4.5	Adhesive Failure

The bonding properties of PVDF were also investigated but due to the fluorine content in PVDF, it was difficult to form a satisfactory bond between PVDF and any other material. All samples formed could be peeled off by hand and so the bond

strength was deemed unsatisfactory, with delamination occurring before the parts had cooled to room temperature. This lack of bond strength precludes PVDF from all subsequent cryogenic cycling testing.

### 7.2.3. Cryogenic Cycling of Bonded Laminates

Temperature changes were simulated via cryogenic cycling of laminates in liquid nitrogen (LN<sub>2</sub>) to simulate the effects of the rapid temperature drop in a thermal process. The laminates were submerged in LN<sub>2</sub> for 2 minutes and then allowed to cool to room temperature over a further 8 minute period. This process was used to test the bonding properties of PA12 and PA11 liners, with PEEK and CF/PEEK materials. As mentioned above, all samples were formed using the hot plate to melt the polymer powder into the CF/PEEK sheet which had been previously grit blasted. Cryogenic testing of bonded joints of three different types was conducted: Nylon to PEEK, Nylon to CF/PEEK, and PEEK to CF/PEEK. The results from all of these tests are included in Table 7.2 with a description of sample failure mechanisms included.

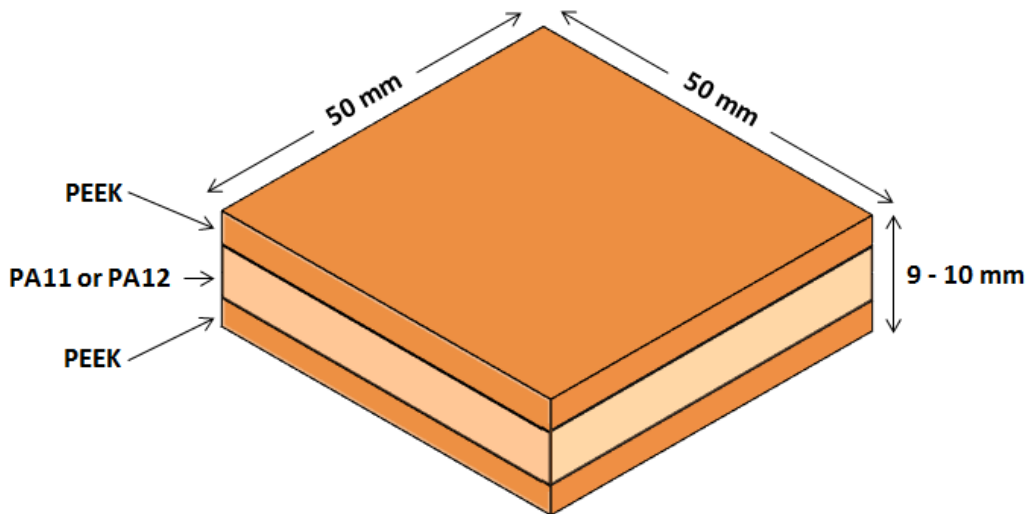


*Figure 7.8. Configurations for PEEK-PA11-PEEK and PEEK-PA12-PEEK samples.*

PEEK-PA11-PEEK and PEEK-PA12-PEEK sandwich samples formed the basis of polymer bond testing conducted here. These samples were used to test the basis of a dual layer liner configuration with an outer skin of PEEK material. The samples dimensions were 50 mm × 50 mm wide with three individual layers; each having a nominal thickness of 3 to 4 mm, giving an overall sample thickness of 9 to 10 mm, Fig. 7.8.

Table 7.2. Bond testing results from sample formation testing and cryogenic cycling.

Sample	Grit Blasting	Annealing	Cryogenic Cycles	Comments	Reason For Failure
<u>Polymer Bonding</u>					
PEEK-PA11-PEEK	No	No	1	Debonding after a single cryogenic cycle, no cracking in any samples	Inadequate bond strength between PEEK and PA11
PEEK-PA12-PEEK	No	No	1	Debonding after a single cryogenic cycle, no cracking in any samples	Inadequate bond strength between PEEK and PA12
<u>Composite Bonding</u>					
PA12-CF/PEEK	No	No	0	Debonding at room temperature, no cracking	Improper bonding due to lack of grit blasting
PA12-CF/PEEK-PA12	Yes	No	1	Cracking after a single cryogenic cycle	Sample shape influenced cracking
PA12-CF/PEEK-PA12	Yes	Yes	1	Cracking after a single cryogenic cycle	Sample shape influenced cracking
PA12-CF/PEEK	Yes	No	1	Debonding after a single cryogenic cycle, one single crack formed	Sample shape influenced cracking
PA12-CF/PEEK	Yes	No	1	Debonding after a single cryogenic cycle, no cracking	Inadequate bond strength between PA12 and CF/PEEK
PEEK-CF/PEEK-PEEK	Yes	No	0	Cracking at room temperature	Residual stress induced cracking during cooling to room temperature
PEEK-CF/PEEK-PEEK	Yes	Yes	0	Cracking at room temperature	Residual stress induced cracking during cooling to room temperature
PEEK-CF/PEEK	Yes	No	1	Cracking after a single cryogenic cycle	Residual stress induced cracking during cooling to cryogenic temperature



*Figure 7.9. Sample debonding of PA11 from PEEK specimens after a single cryogenic cycle.*

Samples were immersed in LN2 for two minutes and then removed for heating back to room temperature for 8 minutes. Upon immersion of the PEEK-PA11-PEEK and PEEK-PA12-PEEK samples into LN2, debonding occurred almost simultaneously. These test results demonstrate that delamination is prevalent in PEEK to PA11 bonds and PEEK to PA12 bonds, with no visible cracking occurring in any layer under cryogenic cycling conditions. Fig. 7.9 shows an example of the debonding which occurs within these samples. While polymer materials should exhibit similar CTEs, leading to lower residual stress build up, the differences between CTE values for Nylon (at 80 to 230  $\mu\text{m}/\mu\text{m}^\circ\text{C}$  [91]) and PEEK (at 48  $\mu\text{m}/\mu\text{m}^\circ\text{C}$  [51]), are sufficient such that thermal stress build up, during cooling to cryogenic temperatures, causes significant delamination.

## Liner and Overwrap Cryogenic Testing

These failures have effectively eliminated the possibility of a dual layer bonded liner, as improving the bond strength between samples is quite difficult. Grit blasting was not used to improve the bonding as it is impossible to perform grit blasting on the inner liner surfaces during rotational moulding and so utilising grit blasting would not be representative of the final manufacturing process.

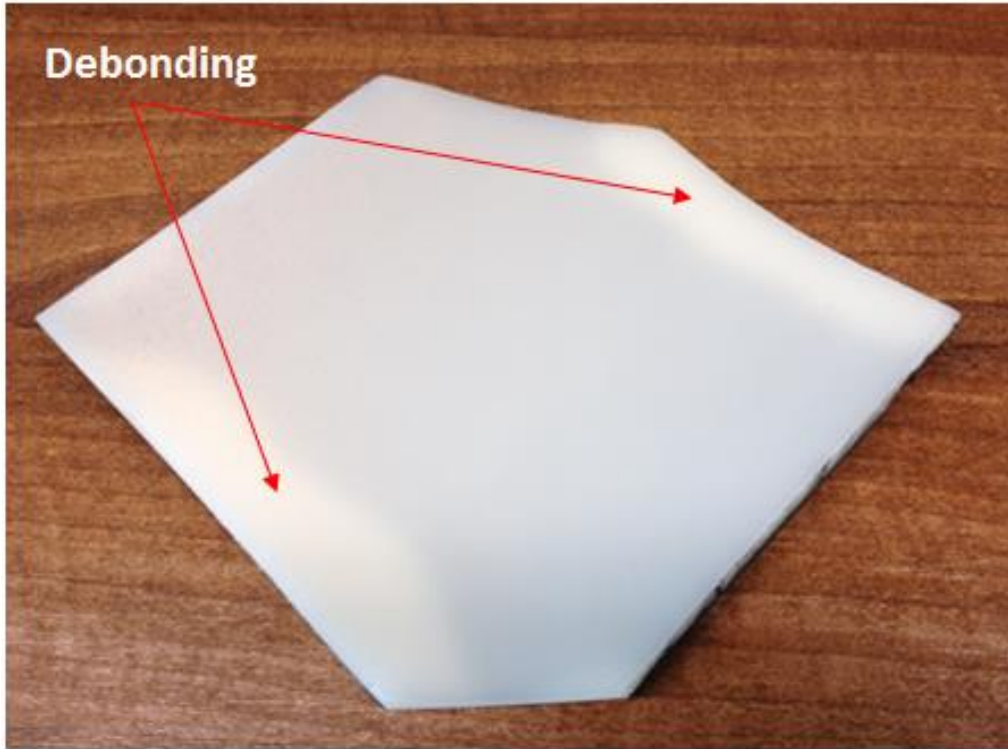


*Figure 7.10. Debonding at room temperature between PA12 and CF/PEEK Suprem IM7.*

The composite bonding conducted here involved the testing of PA12-CF/PEEK and PEEK-CF/PEEK samples. The samples dimension were again 50 mm × 50 mm with thicknesses ranging from 6 to 10 mm. Dual layer and single layer samples were tested throughout this analysis. Initial bonding tests for single PA12-CF/PEEK laminates resulted in debonding of the plastic from the composite at room temperature, Fig. 7.10. To increase the bond strength and to remove any residual mould release agent from the CF/PEEK laminates, the composite sheets were grit blasted with alumina particles to roughen the surface, increasing the surface area and hence the bond strength. Further testing with PA12-CF/PEEK samples which had been grit blasted prior to bonding gave no delamination at room temperature.

## Liner and Overwrap Cryogenic Testing

Subsequent testing of PA12-CF/PEEK involved the use of dual layer PA12 sandwich laminates encompassing a Suprem IM7 sample, similar to that described in section 7.2.1. The samples had dimensions of a 110 mm × 110 mm. The same cryogenic cycling as described above was used with significant cracking and debonding occurring during the first cycle, as indicated in Fig. 7.11. This was again attributed to the build-up of thermal residual stress, due to the CTE difference between the polymer and composite material, exacerbated by the significant change in temperature down to cryogenic temperatures.

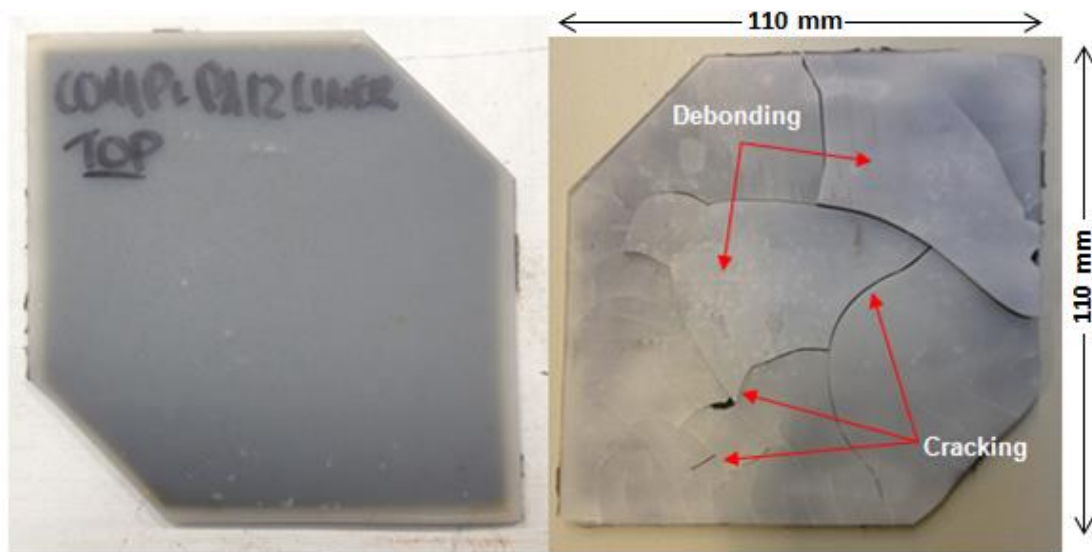


*Figure 7.11. Debonding and cracking in PA12-CF/PEEK-PA12 samples after cryogenic cycling.*

The main issue causing cracking in the laminates is considered to be thermal residual stress build-up, caused by the change in temperature from the stress-free temperature of each material down to the cryogenic temperatures of the LN<sub>2</sub>. For the Nylon materials, this is equivalent to approximately 250 °C to 300 °C, with movement of the liner constrained by the bonding to the CF/PEEK material. This causes a stress build-up in the material as the temperature decreases below the glass transition temperature and the polymer begins to behave as a glassy material.

Thermal stresses can be alleviated (but not removed completely) through a number of processing changes. Lower crystallinity materials exhibit lower residual stresses as the inclusion of more amorphous regions reduces the stress build-up. Holding the laminate at its stress-free temperature for prolonged periods of time and slowly cooling it to room temperature can also alleviate stress build-up in the laminate

[249]. Attempts were made to alleviate the build-up of residual stress in the Nylon-CF/PEEK laminates through the use of higher cooling rates (lower crystallinity) and through holding the laminates at their stress-free temperatures for longer periods of time and slowly cooling to room temperature. The crystallinity was reduced from 23% to 19% (Fig. 7.12).

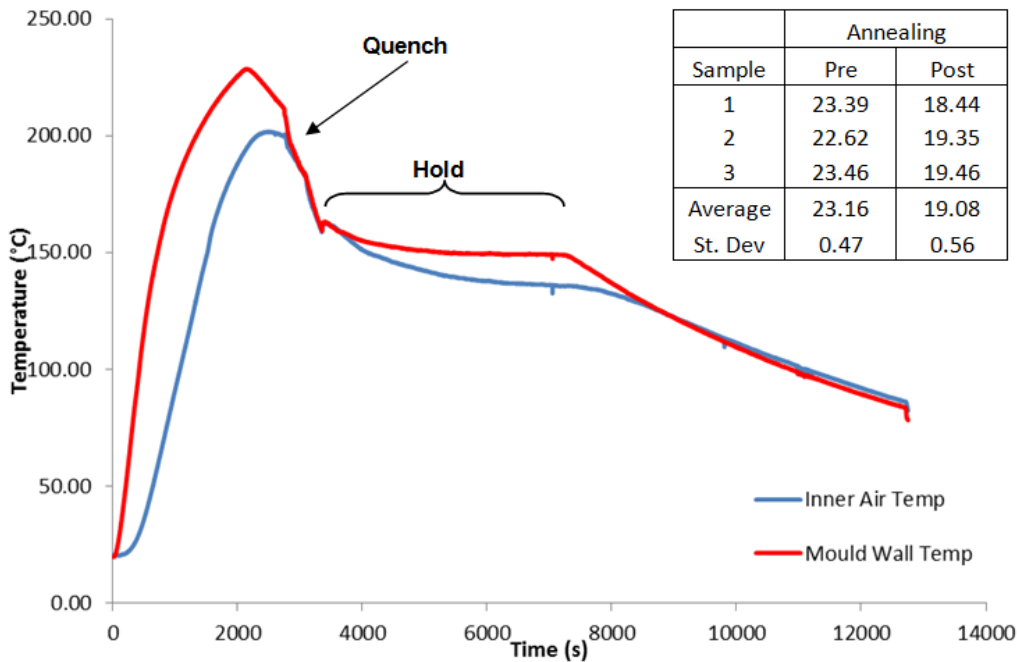
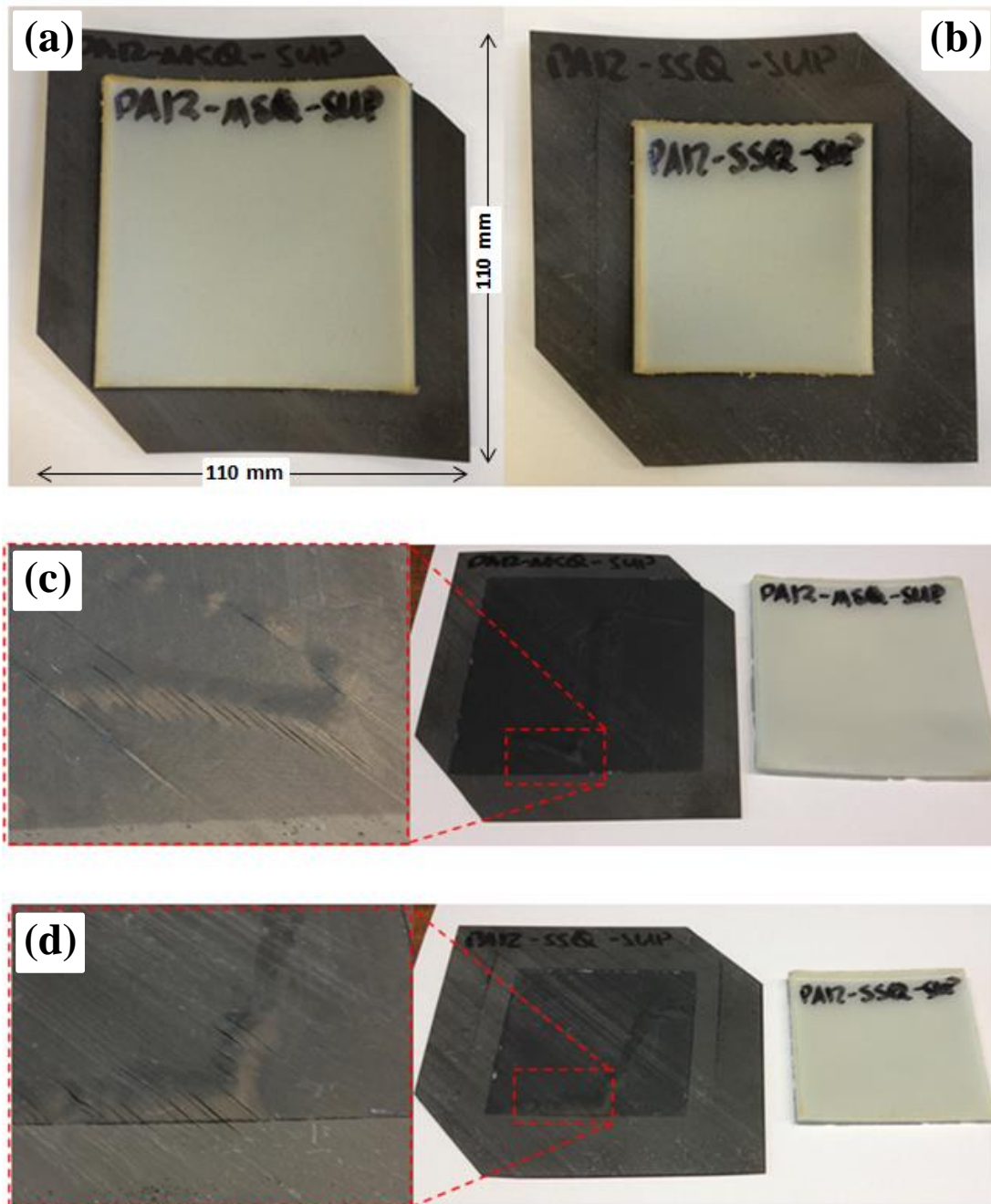


Figure 7.12. Heating trace for PA12 hot plate formed parts with an increased cooling rate to reduce the part's crystallinity (from 23% to 19%) and a prolonged hold around its stress free temperature.

After annealing, the sample was then cryogenically cycled in LN2. However, this again resulted in extensive cracking and debonding from the laminate. The annealing did not alleviate residual stress to a sufficient level to prevent cracking and delamination at cryogenic temperatures. Finally, a single thicker layer of PA12 on a CF/PEEK plate was tested. The first PA12-CF/PEEK sample suffered significant warpage and resulted in debonding and the production of a single crack in the Nylon laminate after cryogenic cycling. It was hypothesised that cracking was caused by the equal sided laminae of Nylon and PEEK with collinear edges inducing cracking. Therefore, further tests using smaller PA12 lamina bonded to CF/PEEK laminates were conducted as shown in Fig. 7.13.



*Figure 7.13. Single layers of PA12 bonded to CF/PEEK Suprem IM7 with a (a) 100 mm square and (b) a 60 mm square area resulting in (c and d) debonding of the polymer layers from the composite sheets after a single cryogenic cycle in liquid nitrogen.*

Cryogenic testing of these laminates resulted in debonding of the polymer with no cracking. This was significant in determining that the cryogenic environment would not induce cracking in the PA12 laminates but would result in debonding of the layers from each other. Fig. 7.13 also shows a large amount of damage at the composite-polymer bond interface with delamination occurring in the composite

## Liner and Overwrap Cryogenic Testing

layer. This shows that the bond strength between the PA12 and CF/PEEK is quite high, but not sufficient enough to resist debonding during cryogenic cycling.

PEEK-CF/PEEK composite bonding trials were conducted using Victrex PEEK 150PF and were performed using the described hot plate process, with dual and single polymer layers deposited on the Suprem IM7 composite substrate to assess the effects of cryogenic temperatures on the laminates. This Victrex polymer was chosen as the PEEK material because Suprem IM7 also uses a Victrex brand of PEEK in their CF/PEEK composite structure and so it was assumed that 150PF would have the best compatibility for bonding. Dual layer bonding of 150PF to CF/PEEK Suprem IM7 led to cracking of the laminates when cooled to room temperature conditions. There was no debonding but the cracking was significant, as shown in Fig. 7.14.

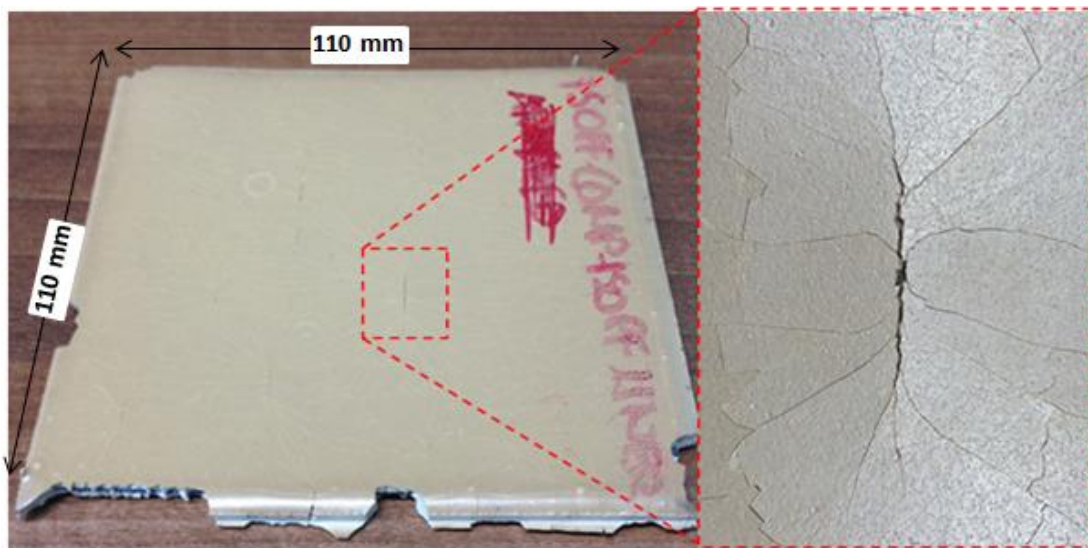


*Figure 7.14. Cracking at room temperature in a PEEK-CF/PEEK-PEEK sample with a close up of the cracking included.*

The change in temperature for PEEK from its stress-free state to cryogenic conditions is in the range of 400 °C. Annealing was applied to reduce the thermal residual stress. The temperature trace for the PEEK sample is shown in Fig. 7.15, with the increased cooling rate reducing the crystallinity from 32.7% to 30.8%. The resulting dual layer PEEK-CF/PEEK-PEEK sample again cracked at room temperature. The cracking in the laminate was on a smaller scale but the PEEK liner remained bonded to the composite plate. Tests were also conducted using a single thicker layer of PEEK with the CF/PEEK composite sheet. Initial results were

promising, as a single thicker layer did not result in cracking at room temperature. However, upon cryogenic cycling of the laminate, cracking occurred again in the sample. The pre and post-test images of the sample are shown in Fig. 7.16 with a close up of the cracking included and no debonding present.

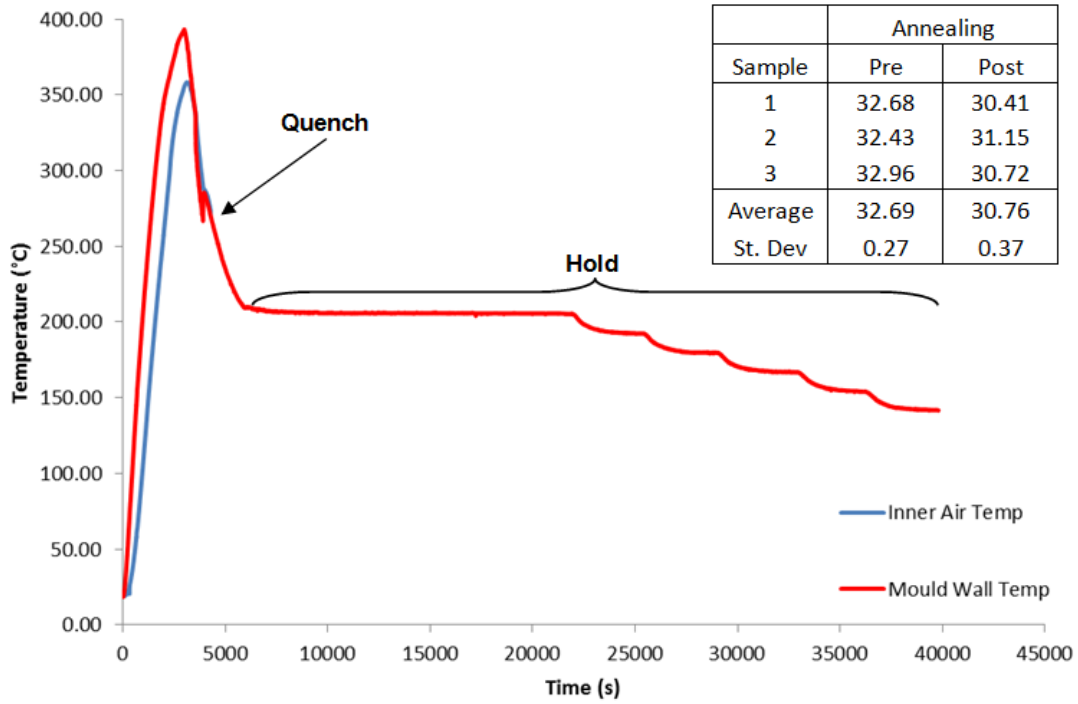


Figure 7.15. Annealing heating trace for PEEK hot plate formed parts with an increased cooling rate to reduce the part's crystallinity (from 32.7% to 30.8%) and a prolonged hold around its stress free temperature.

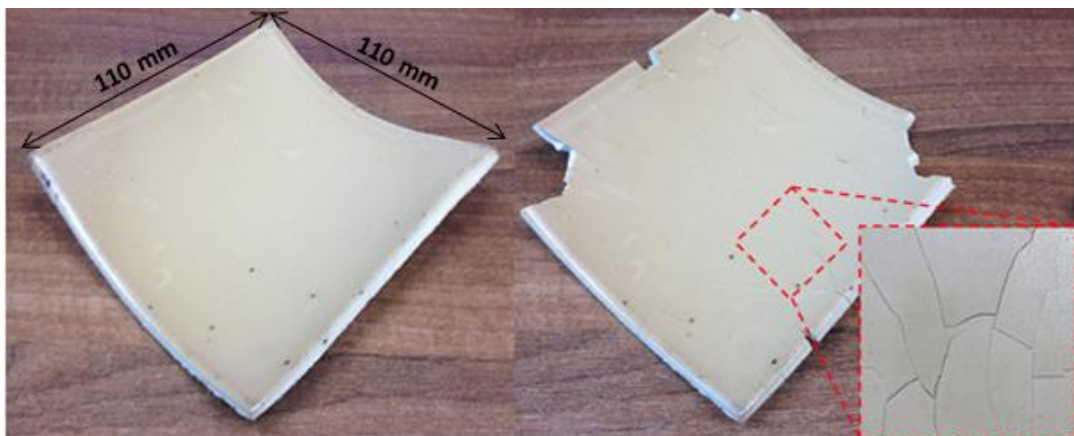


Figure 7.16. Results from cryogenic cycling of a single layer of PEEK deposited on a CF/PEEK Suprem IM7 sheet with a close up of the cracking in the laminate after cycling shown.

### 7.3. Dynamic Mechanical Analysis (DMA)

Dynamic mechanical analysis, described in Chapter 3, has been used within this study to determine the glass transition temperature from the tan delta peak and to assess the changes in material properties which occur across the COPV operating temperature range for the polymer liner materials investigated here. Fig. 7.17 shows the typical output for measurements of storage modulus, for a standard DMA test, with specific areas of interest highlighted [228]. The changes in the storage modulus, versus temperature, can be linked to specific changes in the physical properties of the polymer material, with a decrease in volume from local chain bending and side group motion being the predominant factors in the increase in storage modulus as the temperature is reduced to cryogenic conditions.

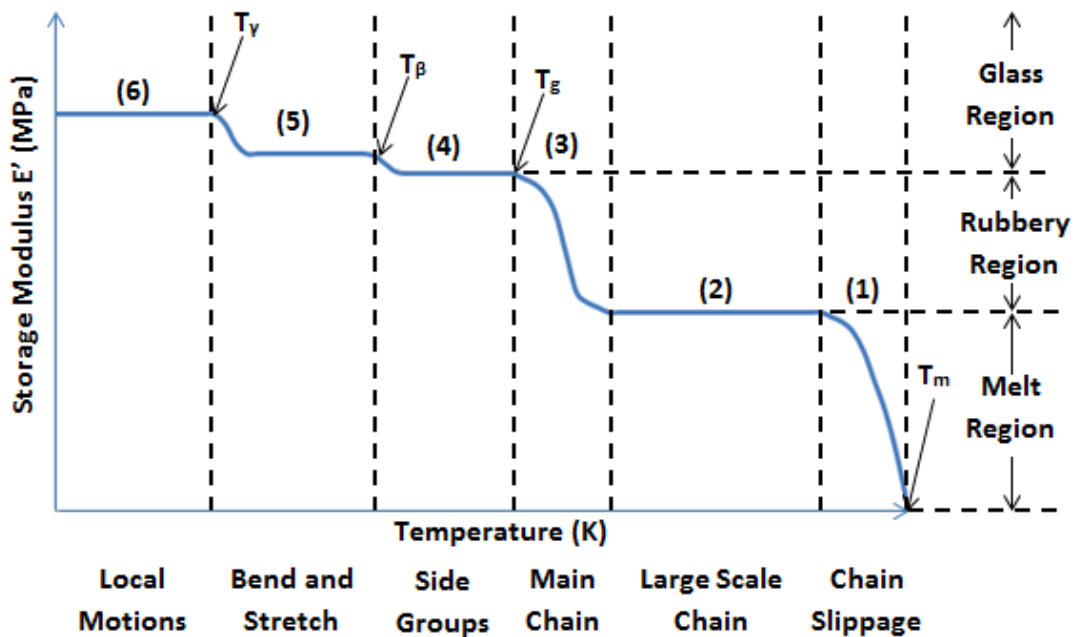


Figure 7.17. Characteristics of a temperature scan of a polymer material with the changes in storage modulus shown against the physical polymer changes (adapted from [228]).

Four materials have been tested in both tension and compression modes as these are the failure modes that the materials are most likely to experience in the COPV design, due to the combined loading of cryogenic temperature and an internal pressure of 5 bar. Five individual tests (for statistical purposes) were conducted for each material, with samples cut directly from the permeability test samples in

Chapter 4. Graphs covering the measured storage modulus and tan delta peaks are included for each material at a frequency of 1 Hz and over a temperature range of 100 °C to -100 °C (except for PEEK 150PF whose temperature range was extended to 250 °C to -100 °C to include glass transition temperature and hence the tan delta peak). All tensile and compressive test data curves are included in Appendix D.1 with an overview of all properties included in Table 7.3.

### **7.3.1. Tensile DMA Test Results**

For the PEEK 150PF material, an initial analysis of the results in Table 7.3 shows that, over the operating temperature range of the tank, the tensile storage modulus will remain quite consistent with a value ranging from 1700 MPa to 2200 MPa approximately. There is a general increase in modulus as the temperature decreases but there are no major changes in material properties which is beneficial for the material's consistency. The tan delta peak for PEEK 150PF is situated around 155.3 °C and this has been defined as its glass transition temperature. It should be noted that there are large differences in storage modulus among the 5 samples tested, with almost a 1000 MPa difference in the storage modulus of samples at -100 °C. This is most likely due to the testing variance of the TMA measurement system and operator error, leading to significant differences in storage modulus measurements. Nevertheless, the measured results are consistent with published data for PEEK materials [250, 251].

The tensile DMA results for PVDF are quite different to that of the PEEK material, due to what appears to be a gradual linear increase in storage modulus over the tested temperature range of 100 °C to -100 °C. In a similar manner to the PEEK material, the maximum storage modulus at -75 °C is 1964 MPa, but the storage modulus at 75 °C is much lower at a level of around 312 MPa. This shows a significant change in material properties over this temperature range. The constituent tan delta results for PVDF show multiple changes in properties over the tested range with multiple peaks. The tan delta peak relating to glass transition temperature has been measured at an average value of -38.68 °C, which is reflected in the storage modulus measurements in Table 7.3 by the change in properties in this region. Again these graphs are consistent with other published DMA tests of PVDF [252, 253].

Table 7.3. DMA Results for tensile and compression tests performed on all materials.

Test Method	Material	Storage Modulus E' (MPa)						Glass Transition Temperature °C	
		75 °C	50 °C	25 °C	0 °C	- 25 °C	- 50 °C		- 75 °C
Tension	PEEK	1773.65	1819.33	1864.41	1903.09	1967.63	2055.34	2174.56	155.30
	PVDF	312.71	464.30	647.57	928.67	1239.27	1671.47	1964.84	-38.68
	PA11	191.00	275.05	540.94	1022.96	1236.91	1325.49	1496.27	29.48
	PA12	379.92	515.52	943.58	1306.37	1419.81	1527.82	1715.38	33.48
Compression	PEEK	683.93	712.97	738.78	762.03	786.61	839.46	911.93	161.29
	PVDF	194.97	283.18	398.14	555.62	737.13	1004.51	1444.64	-48.86
	PA11	153.85	234.64	467.50	762.18	855.07	910.65	1334.28	31.65
	PA12	100.43	144.61	244.91	290.69	308.39	325.67	371.60	41.95

The results for the Nylon materials, PA11 and PA12, are similar with only subtle differences in the measured results. Both experience a maximum storage modulus of between 1500 MPa and 1700 MPa at a temperature of -75 °C with significant changes in the material properties over the tested range. Both materials reach their glass-like behaviour regions at 0 °C with the material properties becoming consistent below this temperature. An analysis of their tan delta peaks gives glass transition temperatures of approximately 29.48 °C and 33.48 °C respectively which is consistent with published data [254-260].

### **7.3.2. Compression DMA Test Results**

The compression testing followed a similar pattern to the tensile testing. The main difference was the larger amount of measured noise which is attributed to the differences in testing methods. The tensile specimens are clamped between two arms which grip samples tightly throughout the testing period, whereas the compression samples are held between two fixed plates without grips. The compression results are therefore dependent on the initial compressive force applied to the samples and therefore tend to introduce more noise at lower temperatures due to the natural shrinkage of the samples. Again, all DMA compression test results are included in Table 7.3. In all cases, significant noise is present in measurements below room temperature due to the shrinkage of materials as seen in the results in Appendix D.1.

The results are reasonably consistent with the tensile tests. The glass transition temperature of PEEK 150PF has held steady with a measured tan delta peak of 161.29 °C, only 6 °C higher than in the tensile tests. The elastic storage modulus results are also lower with a maximum value of 912 MPa at -75 °C. The PVDF compression results are also quite similar to the tensile results for storage modulus, with an apparently higher rate change at the lower temperatures. Its compressive storage modulus has exceeded that of the PEEK material with an average value of 1445 MPa. The glass transition temperature is again slightly higher than for tensile tests, with an approximate value of -43.86 °C, almost 6 °C higher than the tensile test results. Significant differences exist between the tensile and compressive results for the Nylon samples of PA11 and PA12. Here there is clearly a secondary change at the lower temperature of around -70 °C to -80 °C in both elastic storage modulus, and tan delta response. This is attributed to local chain motions and bond stretching,

as shown earlier in Fig. 7.17 [228], as the temperature is decreased further. However this is not contained in the tensile test results. The glass transition temperatures of PA11 and PA12 have been measured as 31.65 °C and 41.95 °C respectively, which is between 3 °C to 10 °C higher than their tensile test measurements.

#### 7.4. Thermal Mechanical Analysis (TMA)

The purpose of the thermal mechanical analyses undertaken here was to obtain the coefficients of thermal expansion (CTE) for all materials tested. Measurements were taken across a broad temperature range from -100 °C to 250 °C to assess the CTE above and below the glass transition temperature for each material. The glass transition temperature has also been approximated from the intersection of linear lines along both CTEs for every material. The measured CTEs, above and below  $T_g$ , have been included along with the approximate value for  $T_g$ , for every material tested in Table 7.4. The resulting graphs from the five test samples for each material have been included in Appendix D.2.

*Table 7.4. CTE results and glass transition temperatures for TMA testing.*

Material	Coefficient of Thermal Expansion ( $\mu\text{m}/\text{m}^\circ\text{C}$ )		Glass Transition Temperature
	Above $T_g$	Below $T_g$	$^\circ\text{C}$
PEEK	134.8	53.9	137.4
PVDF	210.3	58.9	-21.3
PA11	227.0	109.6	-0.5
PA12	184.6	100.6	-7.9

For every material tested, the CTE above  $T_g$  is significantly higher than that of its counterpart below  $T_g$  with results consistent with published data for similar materials [51, 91, 260-262]. The glass transition temperatures measured here are quite different than those measured from the tan delta peaks in the DMA tests conducted previously. This can be attributed to the more exact nature of the DMA results with the tan delta peaks in comparison to the curve fitting methods of the TMA test

results. In all cases, except for PVDF, the measured  $T_g$  is much lower than that of the DMA test results for PEEK, PA11 and PA12.

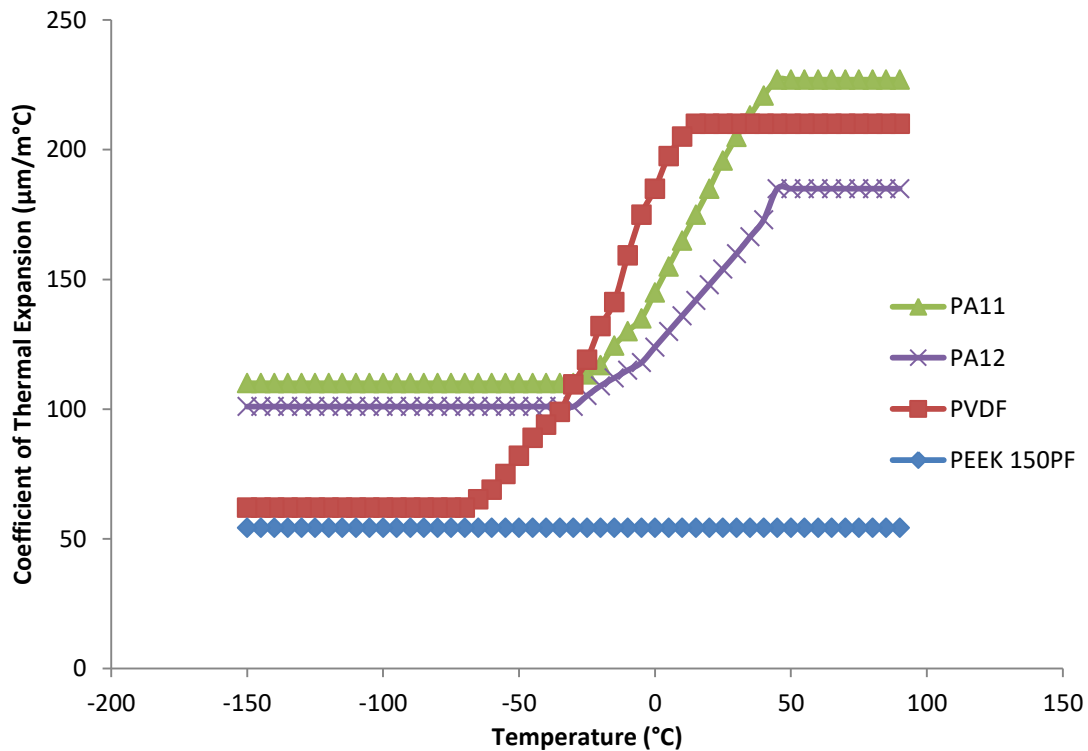
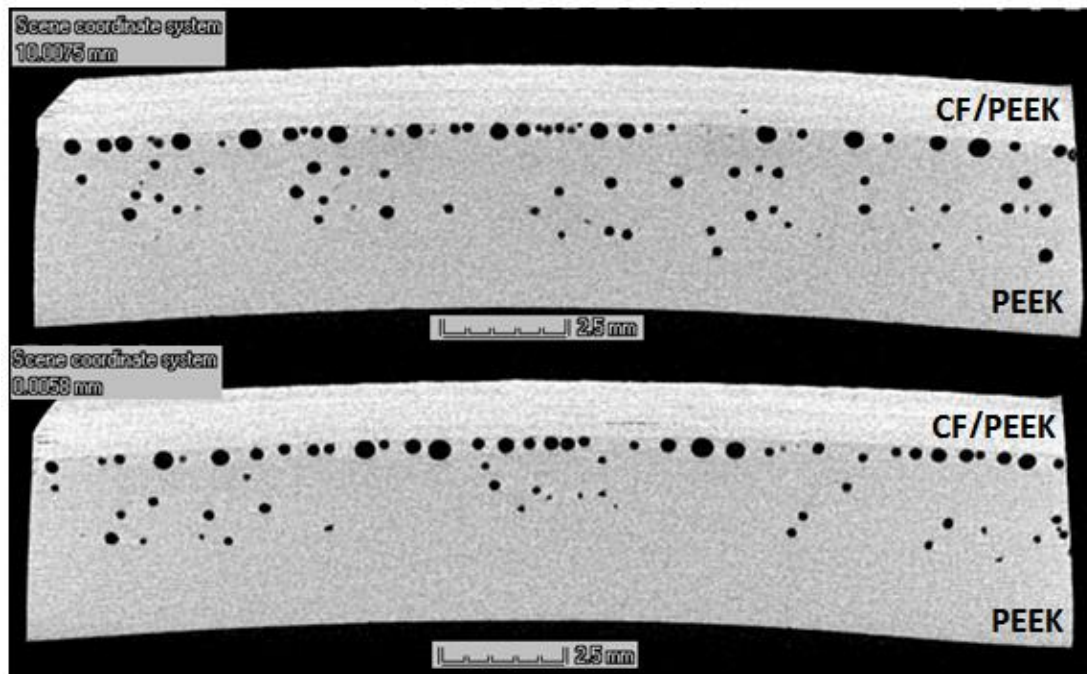


Figure 7.18. Variation in CTE for each material over the operating temperature range of the tank.

Fig. 7.18 shows the effect of temperature on CTE for the four materials tested here. Significant changes in CTE occur for all materials across the operating temperature range of the tank (except for PEEK, as its glass transition temperature is outside this range). This is important for thermal residual stress measurements, as the CTE directly controls the deformation of the liner when bonded to the composite overwrap. From Fig. 7.18, the change in CTE for the Nylon materials is almost 100  $\mu\text{m}/\text{m}^\circ\text{C}$  (from approximately 200  $\mu\text{m}/\text{m}^\circ\text{C}$  down to 100  $\mu\text{m}/\text{m}^\circ\text{C}$ ), which is a large change that is localised to the higher end of the COPV operating range from 50  $^\circ\text{C}$  down to -30  $^\circ\text{C}$ . The PVDF material undergoes a larger change in CTE from 210  $\mu\text{m}/\text{m}^\circ\text{C}$  down to 59  $\mu\text{m}/\text{m}^\circ\text{C}$ , which is much closer to that of PEEK, which has a CTE of 54  $\mu\text{m}/\text{m}^\circ\text{C}$  across the entire operating range of the tank as its  $T_g$  value is above the defined range. These significant changes in material properties within the operating range of the tank are not optimal, as they make the development of predictive structural models of the tank more difficult.

## 7.5. X-ray CT Analysis of Hot Plate Formed PEEK-CF/PEEK Joints

While the Nylon-CF/PEEK samples exhibited delaminations when cryogenically cycled, the PEEK-CF/PEEK samples exhibited significant cracking in the PEEK liner while still remaining bonded to the CF/PEEK laminate. These samples, which had been hot-plate formed via melting of PEEK powder on to a CF/PEEK laminate, are assessed here using X-ray CT imaging techniques before and after cryogenic cycling, to determine the extent of cracking and factors leading to the formation of these cracks.



*Figure 7.19. X-ray CT images of the cross section of a PEEK-CF/PEEK hot plate formed laminate prior to cryogenic cycling.*

A 20 mm × 20 mm × 5 mm PEEK-CF/PEEK sample was imaged, using the X-ray CT machine described in Chapter 3, as shown in Fig. 7.19. There is a large presence of voids (particularly around the PEEK-CF/PEEK interface) in the material, but no cracks are seen in the cross section. There is a characteristic bend in the sample, which is indicative of the residual stress build up in the sample due to the cooling of the PEEK down to room temperature.

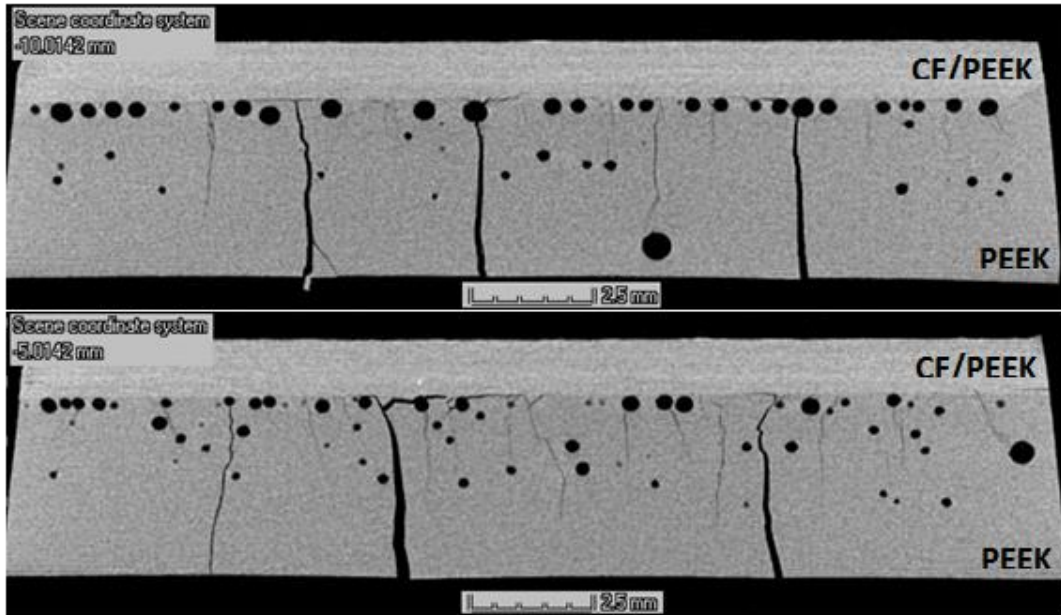


*Figure 7.20. X-ray CT images of the cross section of a PEEK-CF/PEEK hot plate formed laminate after cryogenic cycling with massive cracking visible.*

This sample was then cycled in LN2 over a ten minute cycle (a two minute hold in LN2 followed by an eight minute reheating to room temperature). Cracking was audible before the completion of the two minute LN2 hold. This sample was then rescanned using the X-ray CT machine and the X-ray images of the fractured sample are shown in Fig. 7.20. Extensive cracking can be seen throughout the sample with hundreds of smaller cracks at the PEEK-CF/PEEK, demonstrating the major damage caused by the large temperature change on the laminate. Some larger cracks have penetrated through the depth of the PEEK liner material itself, which would lead to significant leakage of gas from the COPV and possibly catastrophic failure of any vessel manufactured with these materials with these methods. A 3D reconstruction of the sample is shown in Fig. 7.21, to demonstrate the extent of the larger cracks seen within the previous image. Here the cracks are not isolated but have grown into a network which covers the PEEK liner material's entire volume. An X-ray image taken from a plane view of the PEEK-CF-PEEK bonding region also highlights the extent of cracking through the void regions at the bonding interface, Fig. 7.22. The smaller cracks which have not penetrated the entire thickness of the PEEK liner have created a more extensive network deep within the liner which seems to follow through void regions specifically as they act as crack initiation points.

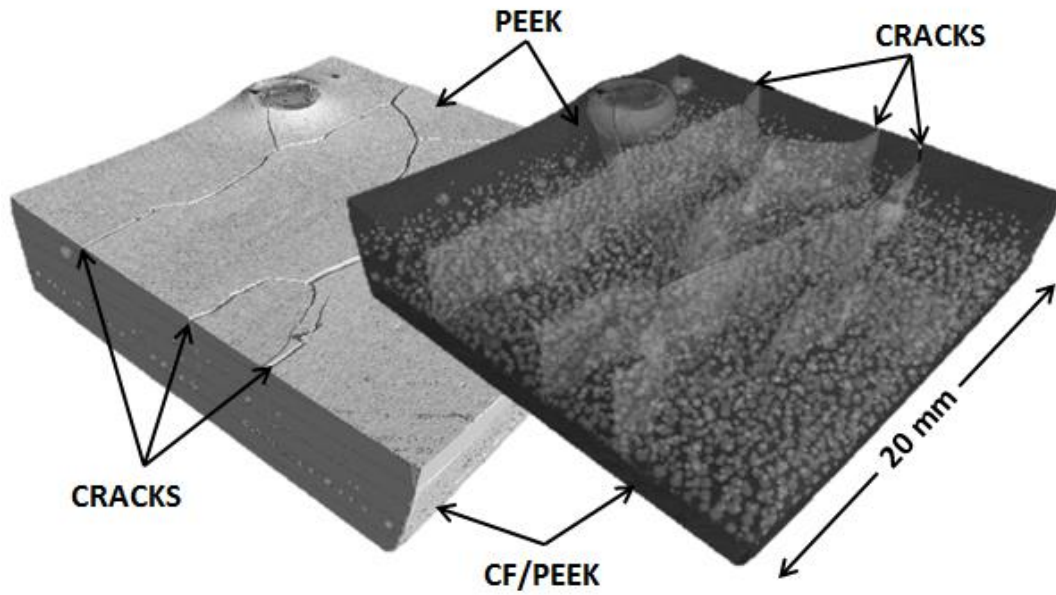


Figure 7.21. Three-dimensional rendering of a PEEK-CF/PEEK hot plate formed sample after cryogenic cycling with cracking visible in a solid and transparent view.

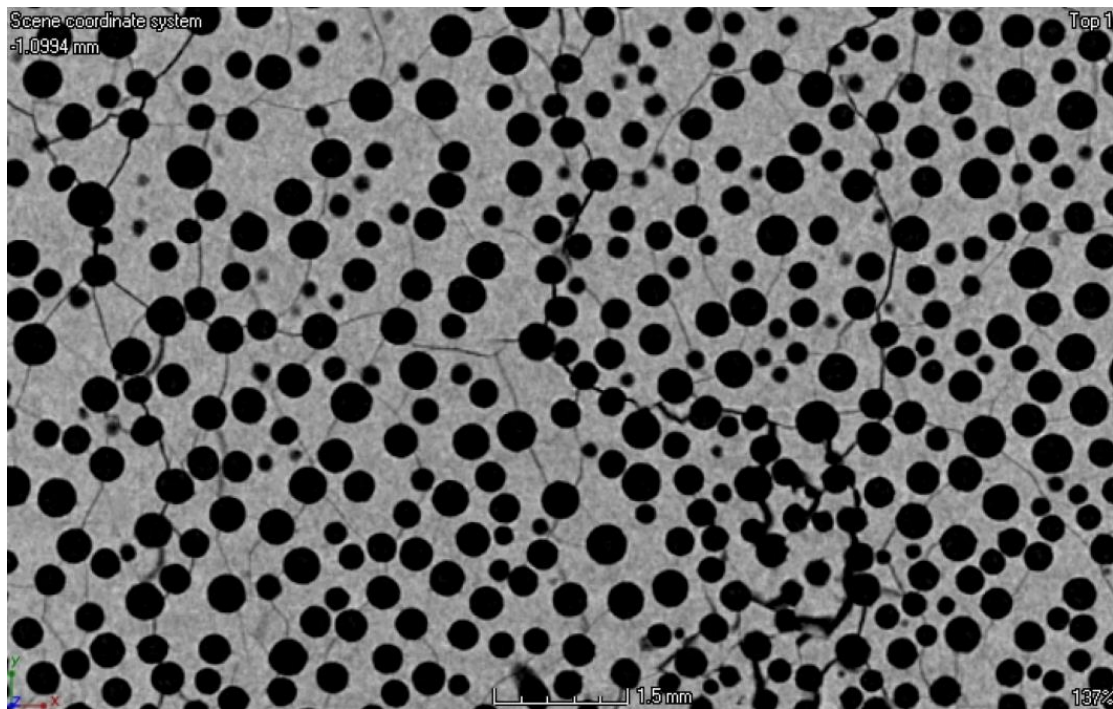


Figure 7.22. X-ray image of crack networks in the bonding region of a hot plate formed PEEK-CF/PEEK laminate with cracks running through void regions.

## 7.6. Conclusions

From an analysis of the results the following conclusions can be drawn:

## Liner and Overwrap Cryogenic Testing

- The addition of a polymer layer onto a composite surface decreases the permeability of the structure and so improves the low permeability properties of the laminate as a whole
- The bond strength between multilayer liners (PEEK to Nylon bonds) is quite strong as shown by the failure of the standard adhesive used in these tests prior to the fracture of the sandwich structures
- Cryogenic cycling of all hot plate formed laminate configurations resulted in failure of the laminates, with Nylon-CF/PEEK samples exhibiting debonding characteristics and PEEK-CF/PEEK samples exhibiting cracking characteristics
- These failures can be attributed to the mismatch in CTE values between materials causing significant residual stress build up
- Higher cooling rates, while lowering the crystallinity of liner materials, did not alleviate the cracking and delamination experienced by the liner materials
- Significant changes in material properties over the operating temperature range of the COPV have been shown via dynamic mechanical analysis of storage modulus and thermal mechanical analysis of CTEs
- X-ray CT scanning has shown widespread cracking networks in PEEK-CF/PEEK materials after cryogenic cycling with void regions at the liner-overwrap interface evidently acting as crack initiation points

From these results, the design of a bonded liner-overwrap configuration for the designated COPV structure would seem to exceed the ability of the present materials tested. The use of a bonded dual layer liner would also encounter difficulties in bonding Nylon materials to PEEK. The manufacturing methods used in these analyses, however, are not the same as the methods chosen for the final production of the COPV (rotational moulding for liner formation and laser assisted tape placement for overwrapping) and so it would be premature to exclude the possibility of using a bonded structure from the final design of the COPV. Furthermore, while the use of a bonded liner-overwrap was the intended design for this project, an unbonded liner-overwrap configuration is not unprecedented, as many manufacturers use an intermediary rubber layer between the liner and overwrap configuration to allow for easier shear stress distribution in an unbonded structure [263]. This could

## Liner and Overwrap Cryogenic Testing

be incorporated into the present design to alleviate the residual stress build up and possibly reduce failures at cryogenic conditions.

# 8. Cryogenic Cycling and Final Layup Testing

## 8.1. Chapter Overview

This chapter covers the results from the final layup testing for permeability and cryogenic cycling performance, vis-à-vis cracking resistance. Polymer liner samples were formed using rotational moulding techniques and then tape-laid with CF/PEEK thermoplastic tape in a laser assisted tape placement (LATP) process. These processing methods were used to provide a polymer lined COPV section which is representative of the final tank design. Testing conducted here includes:

- Polymer liner formation using the tooling constructed in Chapter 6 and laser assisted tape placement of CF/PEEK tape on flat square sections of the formed liners
- Permeability testing of the final layup design for assessment of low permeability properties which are consistent with previous test results
- Cryogenic cycling of the final layup designs to test their ability to perform in cryogenic environments
- X-ray CT scanning of LATP CF/PEEK-PEEK samples before and after cryogenic cycling to determine the effects of cryogenic temperatures on the inner structure
- Nano-indentation analysis of the layup cross section to test material changes due to the LATP process across the polymer liner sample depth

## 8.2. Polymer Liner Formation and LATP Tape-Placement

### 8.2.1. Liner Formation

Three separate liners were formed using the rotational moulding tooling developed in Chapter 6, using PA12, PA11 and PEEK 150P/150PF materials. The forming conditions for each liner are shown in Fig. 8.1 (PA12 with a maximum forming temperature of 250 °C), Fig. 8.2 (PA11 with a maximum forming temperature of 270 °C) and Fig. 8.3 (PEEK with a maximum forming temperature of 400 °C).

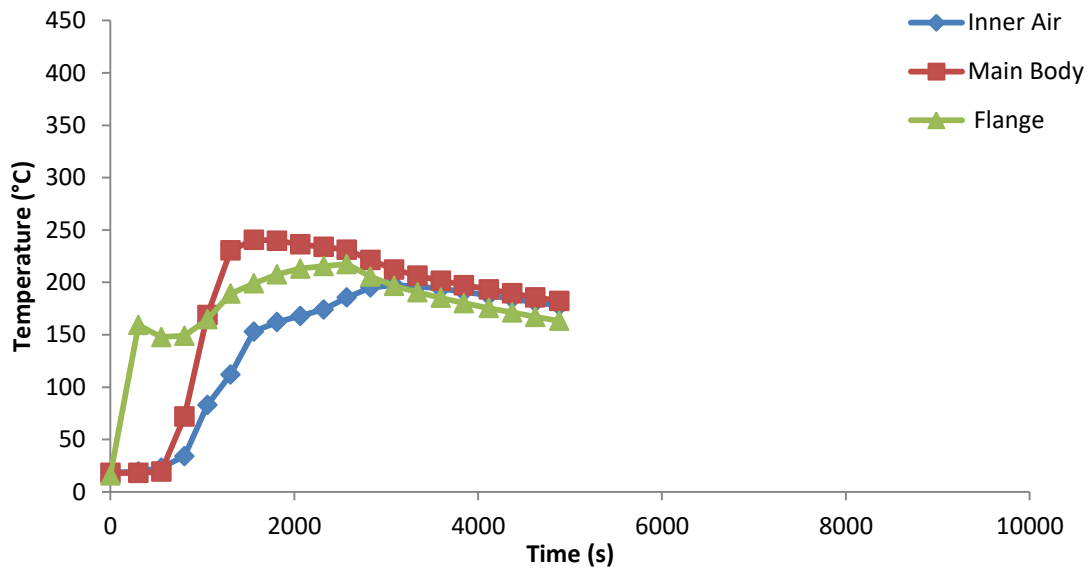


Figure 8.1. Temperature cycle graph for the PA12 liner.

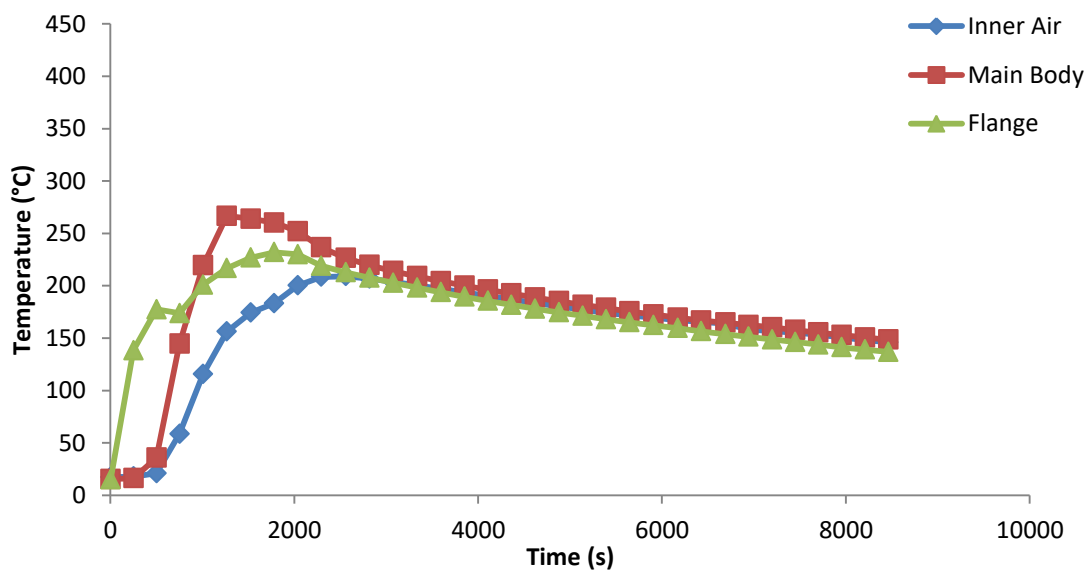


Figure 8.2. Temperature cycle graph for the PA11 liner.

## Cryogenic Cycling and Final Layup Testing

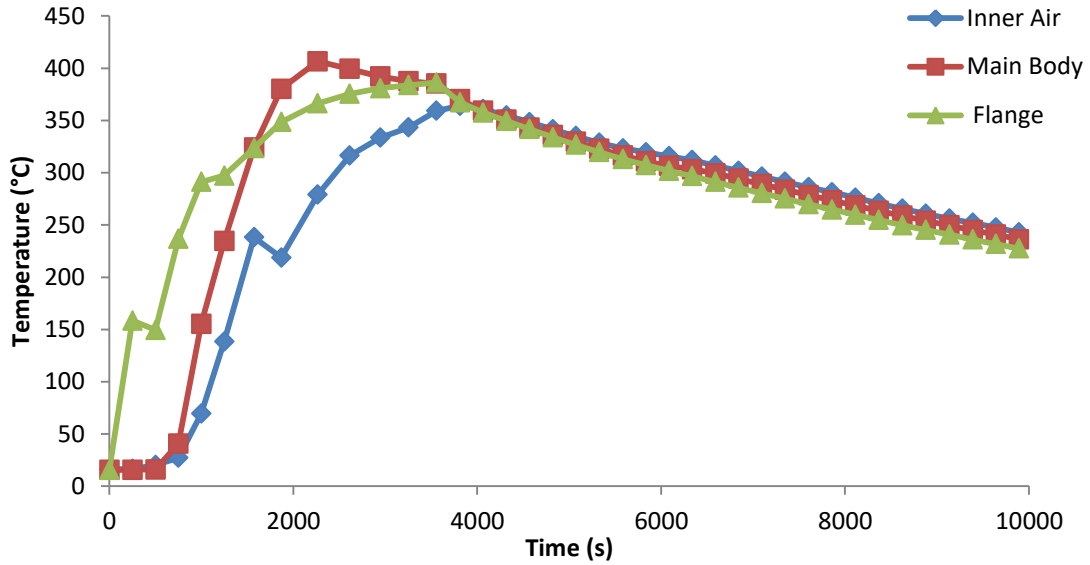


Figure 8.3. Temperature cycle graph for the PEEK150P/PEEK150PF liner.

### 8.2.2. Permeability of Rotomoulded Liner Samples

Three flat panel sections (each with dimensions of 140 mm × 140 mm) were removed from each of the liners for testing. These samples were permeability tested using the ÉireComposites permeability test apparatus (see Chapter 3 [208]). Helium gas was used at a pressure of 1.15 bar, to compare the permeability from hot plate samples and rotomoulded samples. Crystallinity tests [205, 206] were also conducted on the rotomoulded samples, again to compare hot plate samples to rotomoulded samples. The results are shown in Table 8.1.

From the results in Table 8.1, it is clear that PA11 still exhibits the lowest permeability of all materials tested with a permeability coefficient of  $3.29 \times 10^{-7}$  scc/m.s.bar, which is very close to the hot plate formed samples in Chapter 4 which had a coefficient of  $3.46 \times 10^{-7}$  scc/m.s.bar. The rotomoulded PA12 samples have permeability coefficients of  $6.98 \times 10^{-7}$  scc/m.s.bar which is also quite similar to the hot plate value of  $6.59 \times 10^{-7}$  scc/m.s.bar. The rotomoulded PEEK samples have a higher permeability coefficient of  $11.17 \times 10^{-7}$  scc/m.s.bar in comparison to the hot plate PEEK 150P value of  $7.76 \times 10^{-7}$  scc/m.s.bar, which can be directly related to the miss match of particle sizes in the 150P/150PF mixture which has created defects in the rotomoulded parts. The permeability coefficient is independent of pressure, and so it is the best measure of consistency across different sample forming methods.

## Cryogenic Cycling and Final Layup Testing

The diffusion coefficients for the rotomoulded samples are almost identical to the hot plate formed samples. Rotomoulded PA11 and PA12 materials have diffusion coefficients of  $3.86 \times 10^{-10} \text{ m}^2/\text{s}$  and  $2.32 \times 10^{-10} \text{ m}^2/\text{s}$  respectively which is comparable the hot plate values of  $3.84 \times 10^{-10} \text{ m}^2/\text{s}$  and  $2.39 \times 10^{-10} \text{ m}^2/\text{s}$  respectively.

The rotomoulded PEEK samples have a diffusion coefficient of  $1.56 \times 10^{-10} \text{ m}^2/\text{s}$  which is quite higher than the PEEK 150P hot plate value of  $9.49 \times 10^{-11} \text{ m}^2/\text{s}$ . Measured solubility coefficients are identical for PA11 and PA12, with rotomoulded and hot plate samples having solubility coefficients of  $1.41 \times 10^3 \text{ scc}/\text{m}^3\text{bar}$  and  $1.80 \times 10^3 \text{ scc}/\text{m}^3\text{bar}$  respectively. Rotomoulded PEEK has a solubility coefficient of  $7.69 \times 10^3 \text{ scc}/\text{m}^3\text{bar}$  which is also identical to the hot plate formed 150P sample.

The crystallinity of the rotomoulded samples has also been tested, showing consistency with the hot plate samples from Chapter 4. The PA12 crystallinity is quite similar with both hot plate and rotomoulded samples having a crystallinity of 21%. For the PA11 and PEEK samples however, the respective crystallinities of 26% and 39% are almost 5% higher than the hot plate values. This will affect permeability properties but overall the hot plate samples are a good representation of the rotomoulded samples.

*Table 8.1. Permeability results for the rotomoulded liner samples*

Material	Thickness (mm)	Leak Rate ( $10^{-5} \text{ scc}/\text{m}^2.\text{s}$ )	$P$ ( $10^{-7} \text{ scc.m}/\text{m}^2.\text{s}.\text{bar}$ )	$D$ ( $10^{-10} \text{ m}^2/\text{s}$ )	$S$ ( $10^3 \text{ scc}/\text{m}^3 \text{ .bar}$ )	$X_c$ (%)
PA12	3.17	26.1	6.89	3.86	1.80	20.94 ( $\pm 1.57$ )
PA11	3.88	9.82	3.29	2.32	1.41	25.93 ( $\pm 3.24$ )
PEEK	3.13	46.3	11.7	1.56	7.69	39.04 ( $\pm 4.23$ )

### 8.2.3. Tape-Laying of Flat Liner Samples Using LATP

The second stage of the final design process was to tape-lay these samples with a CF/PEEK thermoplastic composite tape. This was conducted at the University of Limerick (UL) with the Irish Centre for Composites Research (ICOMP) using the LATP process described in Chapter 3. The first step was to test the ability of each material to be tape-laid via the LATP process. Rotomoulded flat panel sections of PA11, PA12 and PEEK 150P/150PF were tape-laid with eight layers of CF/PEEK tape in a  $[0/90/0/90]_S$  layup.

Fig. 8.4 and 8.5 show the outcome of these trials on the Nylon samples, displaying poor adherence of the CF/PEEK tape on to the PA12 and PA11 surfaces. The PA12 sample showed the extent of the poor bonding, highlighted by the darker region of the PA12 sample in Fig. 8.4; peeling and debonding of the liner from the overwrap occurred in a similar pattern to the hot plate samples in Chapter 7. The PA11 sample had similar results, with the CF/PEEK overwrap detaching itself from the PA11 laminate almost immediately after formation. Grit blasting of the outer surface of the rotomoulded liners could improve the bonding, as it did in Chapter 7, but the surface alteration inflicted by the laser welding process could mitigate any benefits that grit blasting could contribute.

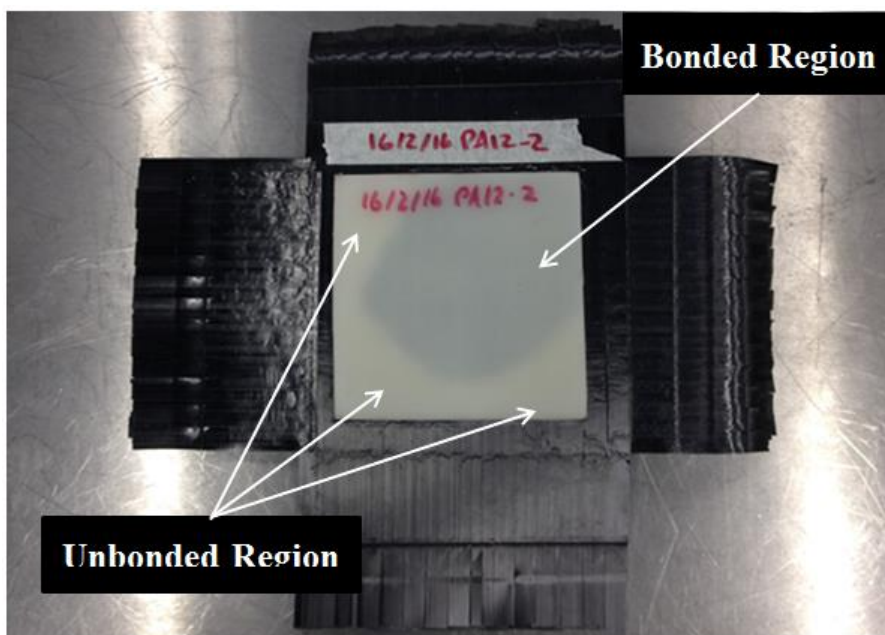
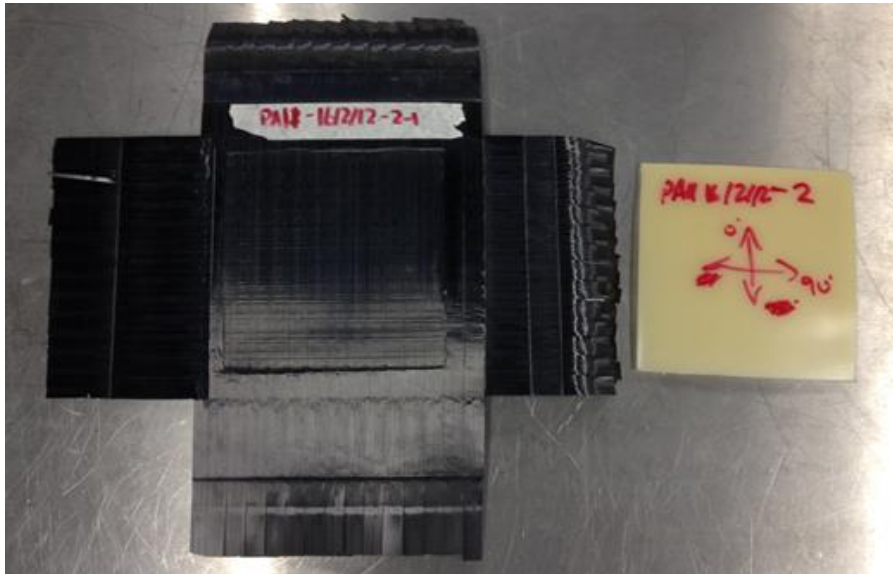
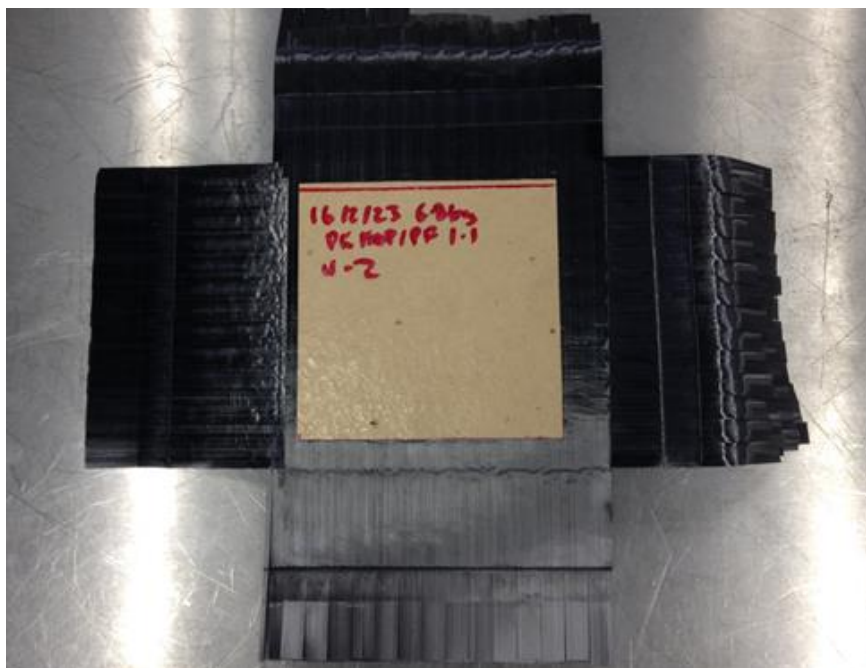


Figure 8.4. Poor quality bonding of CF/PEEK tape to a rotomoulded PA12 laminate.



*Figure 8.5. Absence of bonding of CF/PEEK tape to a rotomoulded PA11 laminate.*

As shown in Fig. 8.6 the tape-laying of PEEK specimens was successful. Fig 8.6 shows the tape-laid PEEK samples with good adherence between the liner and tape-laid configuration. This allowed for further testing of the CF/PEEK-PEEK samples and proved the viability of the LATP process as an overwrapping method for liner-overwrap configurations for PEEK liners.



*Figure 8.6. CF/PEEK-PEEK tape-laid liner sample using the LATP process.*

### 8.3. Permeability Testing with Cryogenic Cycling

The permeability testing conducted here centred on the testing of all materials in the LATP process. An 8 layer [0/90/0/90]<sub>s</sub> LATP CF/PEEK laminate and an 8 layer [45/135/0<sub>4</sub>/135/45] CF/PEEK autoclave sample were permeability tested and cryogenically cycled for comparisons between LATP and autoclave samples. This gives permeability coefficients for all of the individual materials in the liner-overwrap configuration and facilitates permeability predictions for the LATP CF/PEEK-PEEK samples and comparisons with the measured results. The permeability testing was carried out in the ÉireComposites permeability test apparatus using helium gas. The results are shown in Table 8.2.

*Table 8.2. Permeability results for autoclave and LATP samples.*

Specimen	Thickness (mm)	Leak Rate (10 <sup>-5</sup> scc /m <sup>2</sup> .s)	$P$ (10 <sup>-8</sup> scc.m/ m <sup>2</sup> .s.bar)	$D$ (10 <sup>-11</sup> m <sup>2</sup> /s)	$S$ (10 <sup>3</sup> scc/m <sup>3</sup> .bar)	$X_c$ (%)
Autoclave CF/PEEK	1.18	8.40	8.68	2.27	3.81	44.5 (±4.16)
LATP CF/PEEK	1.23	10.4	11.2	14.5	2.30	35.0 (±3.17)
Rotomoulded PEEK-LATP	(5.0 + 1.2) 6.20	9.42	50.5	16.1	3.10	39.0 (±4.23)

Table 8.2 shows good correlation of permeability coefficients for the autoclave and LATP samples, with values of  $8.68 \times 10^{-8}$  scc.m/m<sup>2</sup>.s.bar and  $1.12 \times 10^{-7}$  scc.m/m<sup>2</sup>.s.bar respectively, with increased permeability coefficients in the LATP samples due to the inconsistencies of this process (see X-ray CT scanning results below). The other difference between autoclave and LATP samples is crystallinity,  $X_c$ . This has been calculated using the following equation which takes account of the mass fraction  $\alpha$  of the composite fibres in each sample to provide a true measure of crystallinity [264-266]:

$$X_c = \frac{\Delta H}{\Delta H_f(1 - \alpha)} \quad (8.1)$$

where  $H$  is the heat of fusion measured from the DSC curve and  $H_f$  is the heat of fusion from a 100% crystalline PEEK material. The samples with higher crystallinity will have lower permeability coefficients [91-94], as mentioned earlier. In this case, the autoclave samples have a higher crystallinity of 44.47%, in comparison to the LATP samples which have a crystallinity of 35.00%. The autoclave samples go through a much slower cool down process and hence have higher crystallinity. The LATP samples are cooled in air instantly after the tape layer is applied and so they have a much lower crystallinity due to the rapid cooling of the samples.

The other positive outcome from these tests is the low leak rate of the rotomoulded PEEK liner material which has been tape-laid with the CF/PEEK tape. The permeability coefficient is higher for the rotomoulded sample than its composite counterparts, but this is a measurement of the effective permeability. If the individual permeability coefficients of the overwrap,  $P_{Overwrap}$ , and the liner,  $P_{Liner}$ , are used in the following equation [267]:

$$P_{effective} = \frac{1}{\frac{V_{Liner}}{P_{Liner}} + \frac{V_{Overwrap}}{P_{Overwrap}}} \quad (8.2)$$

with the volumes  $V_{Liner}$  and  $V_{Overwrap}$  based on the constituent materials relative thickness, the predicted effective permeability is  $4.04 \times 10^{-7}$  scc.m/m<sup>2</sup>.s.bar. This is very close to the measured value of  $5.05 \times 10^{-7}$  scc.m/m<sup>2</sup>.s.bar given the inconsistency of the LATP CF/PEEK samples. This gives an equivalent predicted leak rate of  $7.51 \times 10^{-5}$  scc/m<sup>2</sup>.s for the samples tested here which is also close to the measured value of  $9.42 \times 10^{-5}$  scc/m<sup>2</sup>.s.

The samples were immersed in LN2 following the cryogenic cycling procedure in Chapter 3. After cryogenic cycling, the composite samples were retested for permeability. The results show an increase in leak rate which is indicative of microcracking in the composite laminate. The rotomoulded PEEK samples tape-laid with the CF/PEEK tape which were also cryogenically cycled, showed visible cracking in the through thickness direction of the liner. This obviously compromises its effectiveness as a permeation barrier. The resultant leak rates for the composite

## Cryogenic Cycling and Final Layup Testing

samples are shown in Table 8.3. No leak rate results were obtained for the tape-laid PEEK samples due to the cracking which mitigated the effective sealing of the sample. The majority of cracking has occurred after the first cryogenic cycle in the composite samples, as the leak rate has not increased significantly after continued cryogenic cycling up to ten cycles, which is consistent with past research [225]. Fig. 8.7 shows a comparison of cracking in the hot plate samples (from Chapter 7) and the LATP tape-laid rotomoulded PEEK samples. It is clear that the rotomoulded samples show reduced cracking although the samples still fail as a low permeability barrier.

*Table 8.3. Leak rates for cryogenically cycled composite laminates.*

Material	Thickness (mm)	Pressure (bar)	Leak Rate ( $10^{-5}$ scc/m <sup>2</sup> .s)		
			0 Cycles	1 Cycle	10 Cycles
Autoclave CF/PEEK	1.18	1.15	8.4	12.2	12.3
LATP CF/PEEK	1.23	1.15	10.4	16.2	16.5

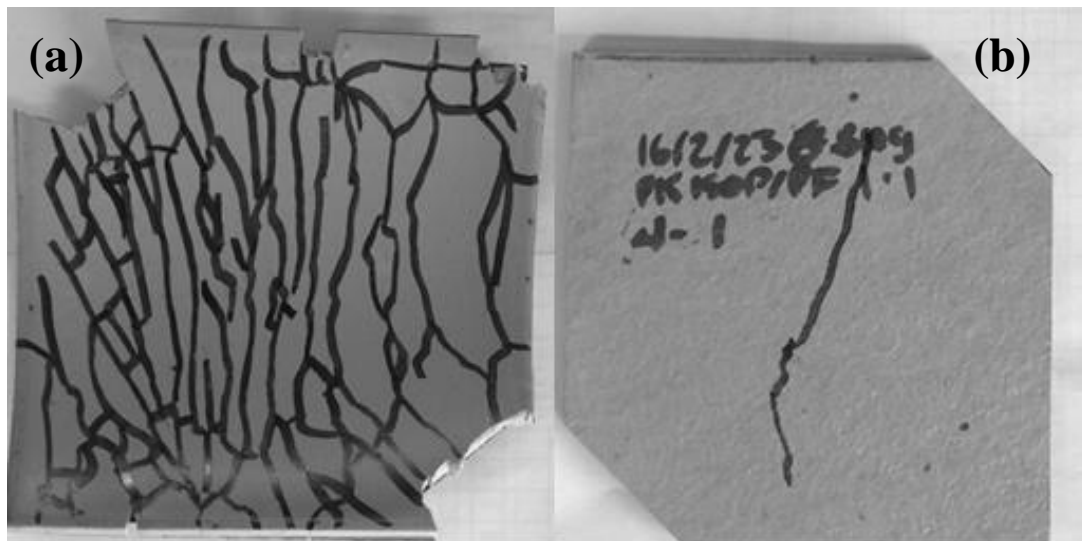


*Figure 8.7. Highlighted cracks in the liner region of (a) hot plate samples (extensive cracking) and (b) rotomoulded LATP samples (single crack) using a marker to show visible cracks.*

## **8.4. X-ray CT Scanning of CF/PEEK-PEEK Samples**

X-ray CT scans have been taken to assess a number of different aspects of the LATP process. These include a comparison of LATP and autoclave CF/PEEK samples, an assessment of the effects of roller pressure on tape consolidation for the LATP CF/PEEK tape-laid samples, and an assessment of the internal structure of the LATP liner-tape-laid samples before and after cryogenic cycling. All X-Ray CT scanning of tape laid LATP CF/PEEK tape on PEEK liners used a hot plate formed PEEK liner sample.

### **8.4.1. Comparison of LATP and Autoclave CF/PEEK**

The internal structure of the LATP CF/PEEK samples and autoclave CF/PEEK samples mentioned in Section 8.3 have been compared using X-ray CT scanning, a standard method of assessment for composite materials [183, 268-272]. The bulk of analyses conducted for COPV applications have centred on epoxy composites with graphite [273, 274] and carbon fibres [223, 275-278] with limited analyses of carbon fibre PEEK composites [170, 225, 279], and even less so for LATP CF/PEEK laminates [279]. 20 mm × 20 mm samples were removed from the formed laminates for analysis. An assessment of the bonding between all layers is undertaken with an overview of the direction of the X-ray image shown in Fig. 8.8. Fig. 8.9 shows X-ray images corresponding to the seven individual bonding layers viewed from a plan perspective moving down through the LATP laminate. They are labelled from (1) to (7), (1) being the first applied layer between the bottom 0° and 90° layers and (7) corresponding to the bonding region between the 90° and 0° layers on the top of the laminate.

A number of conclusions can be drawn from the images. Significant gaps between individual tape layers can be seen in bond regions (7) and (5) which are denoted by the large dark regions. This is due to the inconsistent width in the CF/PEEK tape used here which restricts the accuracy by which the tape layer can be applied, leading to such gaps, which creates an inhomogeneous structure within the laminate. The smaller shaded regions in (3) and (4) (the thin black lines contained within these specific X-ray images) are also indicative of unbonded regions which are not fully consolidated. A small fragment of foreign matter has also been picked up in layer (6)

## Cryogenic Cycling and Final Layup Testing

(highlighted by the red circle) which has caused a gap or crack in the sample. These issues affect the part quality while also affecting permeability, since the inclusion of cracks and air voids will increase the rate of permeation through the laminate.

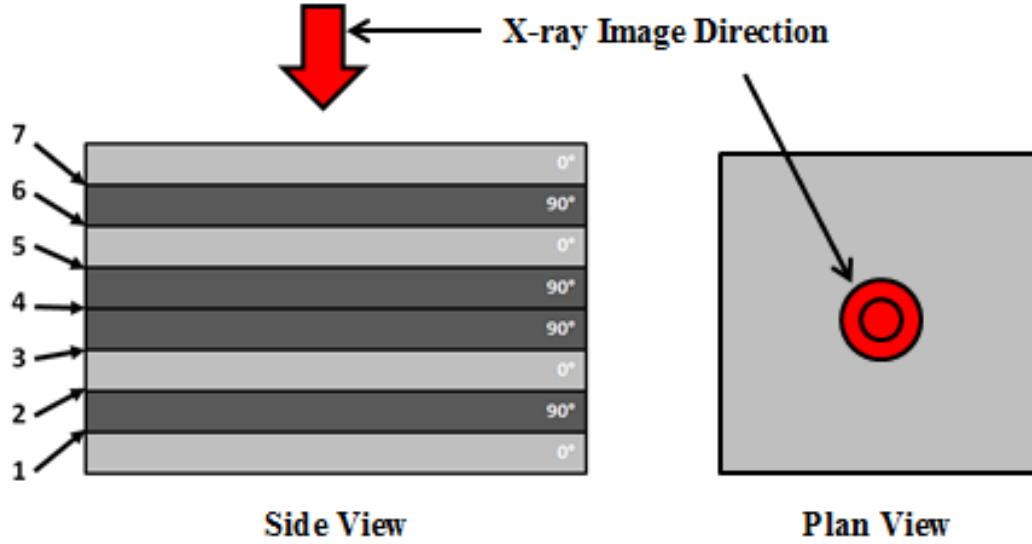


Figure 8.8. Image direction for the X-ray images of LATP CF/PEEK samples.

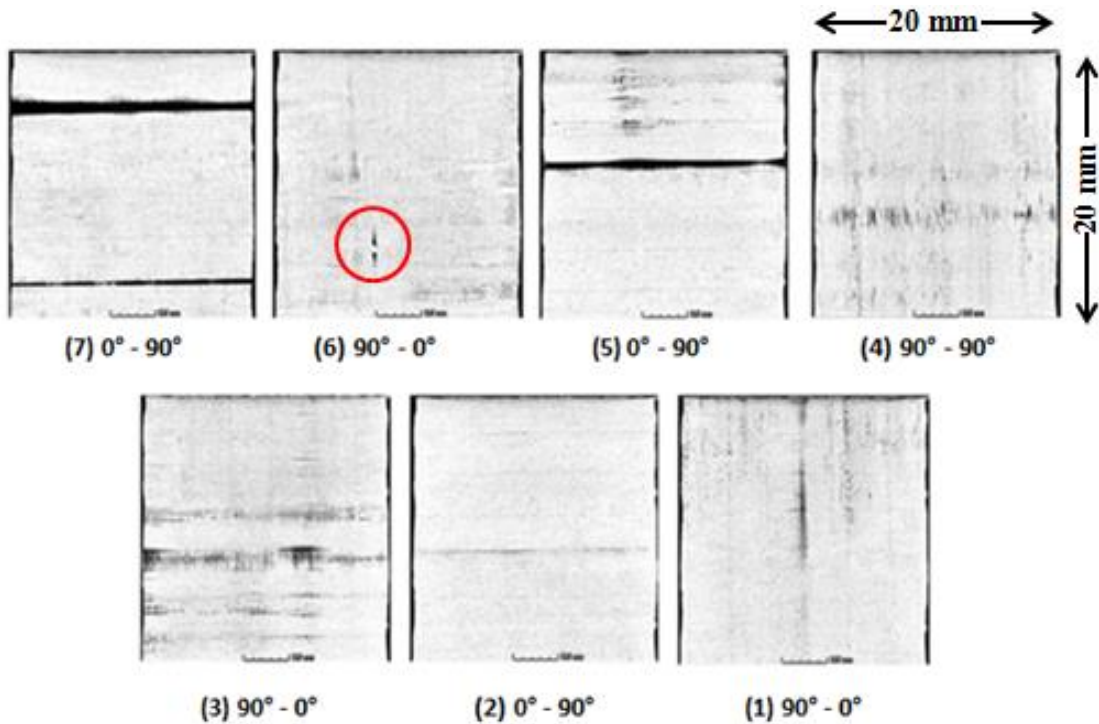


Figure 8.9. Plan view X-ray images of the bonding regions in a  $[0/90/0/90]_S$  CF/PEEK laminate formed using the LATP process.

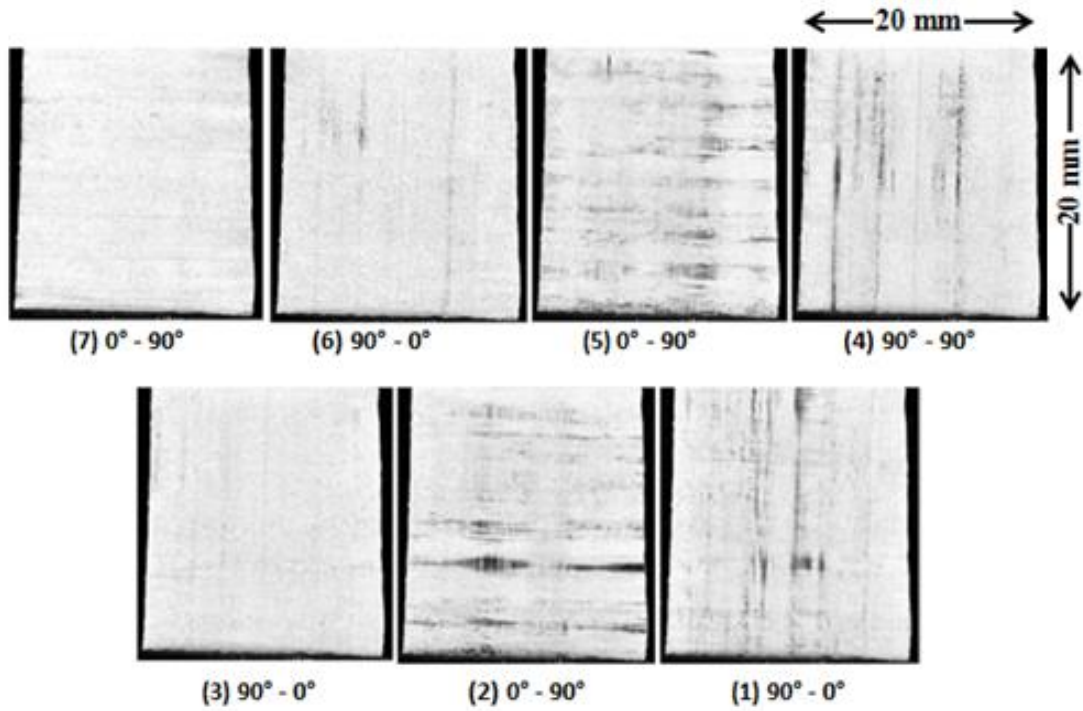


Figure 8.10. Further plan view X-ray images of the bonding regions in a  $[0/90/0/90]_S$  CF/PEEK laminate formed using the LTP process.

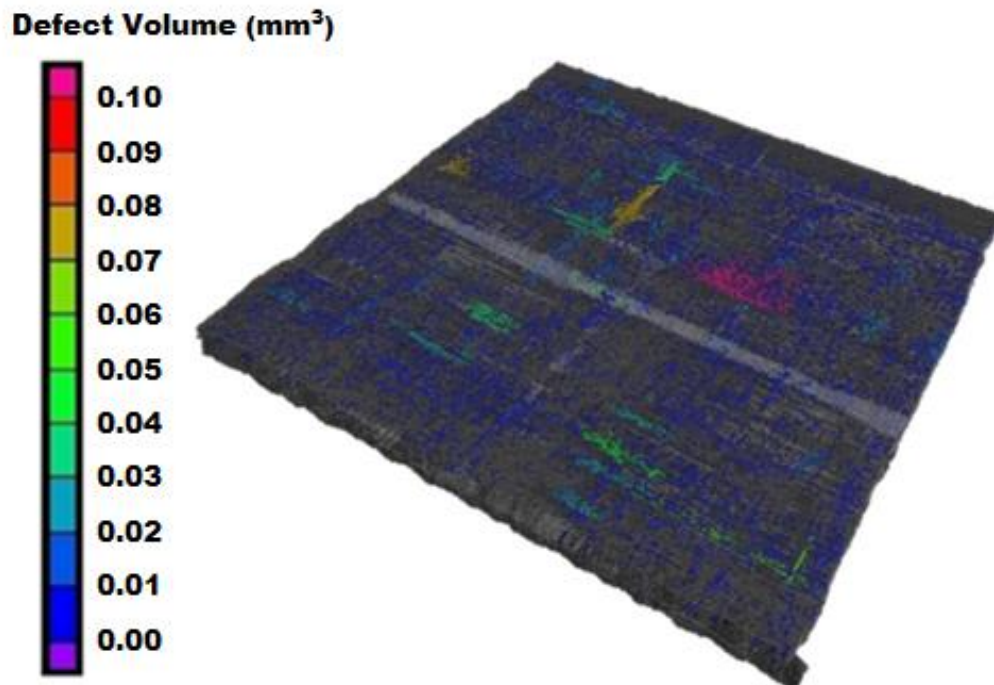
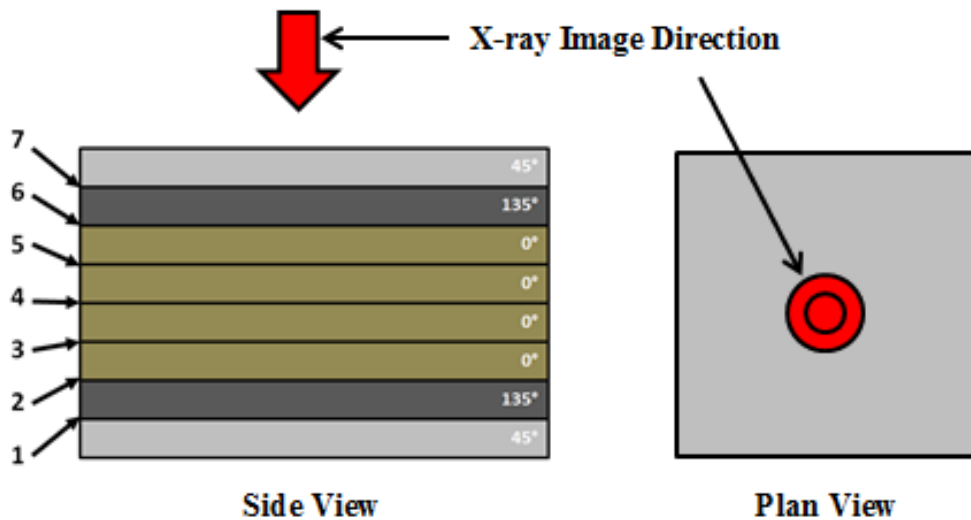


Figure 8.11. Three dimensional rendering of the internal structure of an 8 layer CF/PEEK LTP sample  $[0/90/0/90]_S$  with internal voids and defects highlighted.

Fig. 8.10 shows images from another LATP sample. In this case there is a more uniform tape placement. While there are still darker areas, indicating unbonded regions in layers (5) and (2) between individual layers, this sample is more consistent and demonstrates why the permeability results for the LATP samples are quite varied. Fig. 8.11 shows a three dimensional view of the LATP sample with voids and debond regions highlighted throughout the sample at a number of locations. The volume of the majority of these voids is quite low, and they are thin but long, leading to significantly increased permeability in these regions.



*Figure 8.12. Image direction for the X-ray images of the autoclave CF/PEEK samples.*

In comparison, the quality of the autoclave CF/PEEK laminates is significantly superior to that of the LATP samples. Fig. 8.12 shows an overview of the X-ray image direction for the autoclave CF/PEEK analysis. Fig. 8.13 shows the individual autoclave sample layers with no visible regions of debonding between layers. The samples are uniform and consistent with no visible air gaps, defects, inclusions or voids between samples. The lack of unbonded regions and gaps in the autoclave laminates significantly increases their consistency in regards to material properties and gives them a consistently lower permeability than their LATP counterparts. This is highlighted by the variable nature of LATP permeability results, while the autoclave sample are more uniform with lower permeability coefficients.

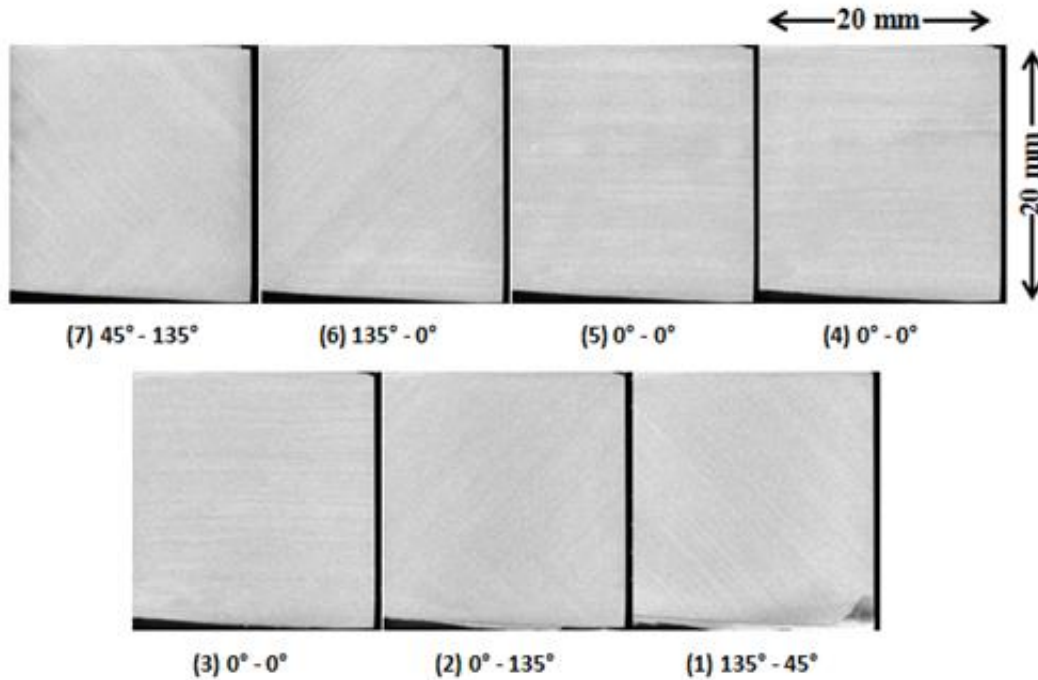


Figure 8.13. Plan view X-ray CT images of the bond between individual layers in an autoclave sample of CF/PEEK.

#### 8.4.2. Effect of LATP Roller Pressure on CF/PEEK Tape Placement

X-ray CT scanning has been used to assess the effects of roller pressure on the consolidation of the CF/PEEK tape to the PEEK substrate during the LATP process. The roller follows the laser and presses the tape into the substrate to improve the bonding of the tape to the surface, with the ability to adjust the roller pressure based on the manufacturer's preference and the materials used. For these trials, two roller pressures were used, 2.5 bar and 4.5 bar. A single layer of CF/PEEK tape was applied to a PEEK plate and then three samples were extracted for X-ray CT scanning.

From the X-ray CT scans of the 2.5 bar samples, Fig. 8.14, regions of debonding are clearly evident between the LATP CF/PEEK tape and the PEEK substrate. Fig. 8.14 has been arranged such that the X-ray CT images from the three samples used to assess the bonding have been placed side-by-side, so that debonding along the length of the tape can be visualised. In Fig. 8.14, the large dark regions indicate areas of

improper bonding/delamination between the LATP applied CF/PEEK tape and the PEEK substrate. These unbonded regions run parallel to the direction of application of the tape and are predominantly located along the edges of an applied tape section. These regions seem to be prevalent throughout the entire part.

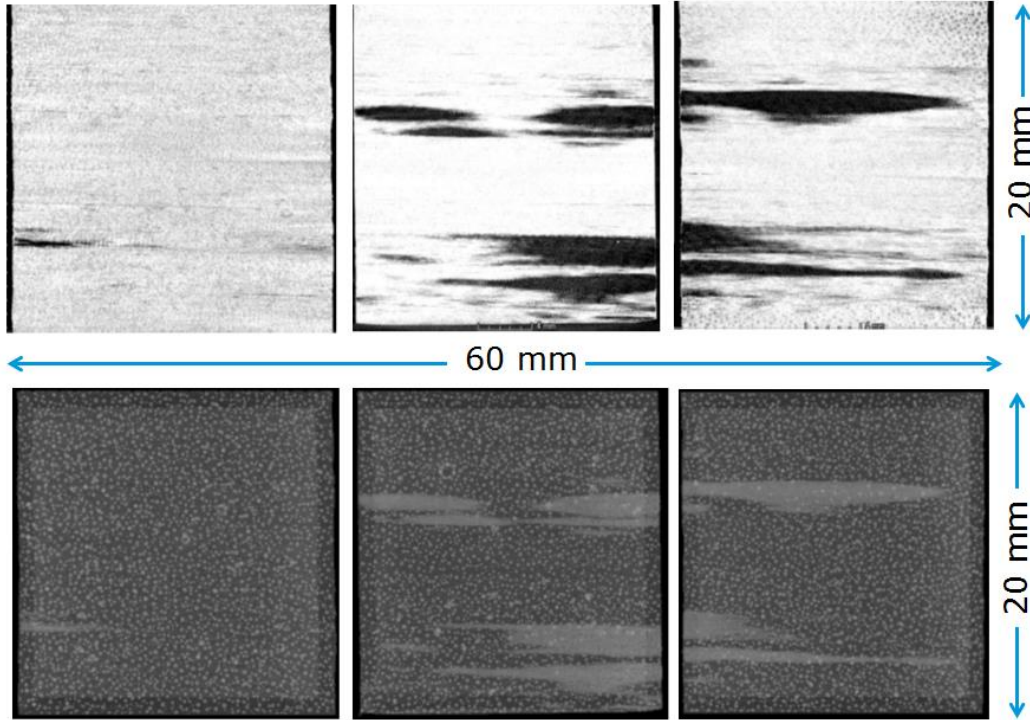


*Figure 8.14. X-ray images in solid and transparent view of unbonded regions in a CF/PEEK-PEEK sample due to improper consolidation during the LATP process with a roller pressure of 2.5 bar.*

X-ray CT images were also taken of a CF/PEEK tape applied to a PEEK laminate using the LATP process and a 4.5 bar roller pressure. Intuitively, the increased pressure is expected to increase contact, and hence bonding, between the CF/PEEK tape and the PEEK laminate but, as seen in Fig. 8.15, the results are very similar to the 2.5 bar samples. Large unbonded regions, highlighted in black, are still present. Hence, roller pressure has little effect on improving consolidation between the tape and substrate. Again, the location of the unbonded regions seems to localise around the applied tape edge, with multiple unbonded regions running parallel to the tape length.

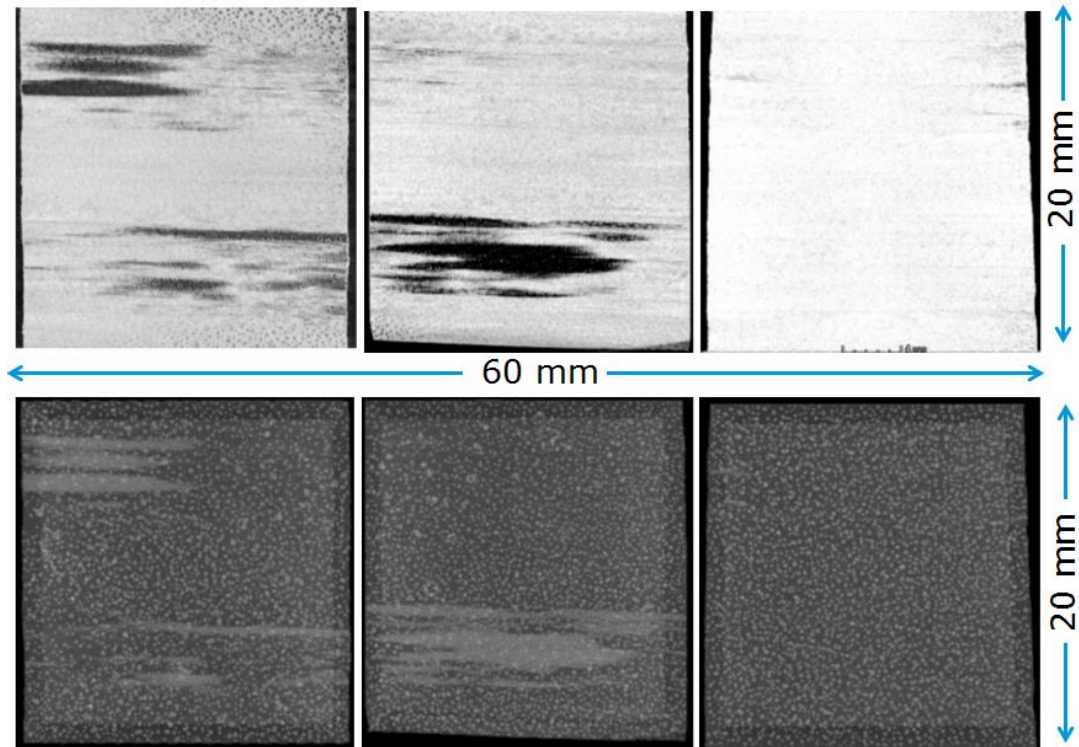


*Figure 8.15. X-ray images in solid and transparent view of unbonded regions in a PEEK-CF/PEEK sample due to improper consolidation during the L ATP process with a roller pressure of 4.5 bar.*

### **8.4.3. X-ray CT Scans of L ATP Tape-Laid Samples**

X-ray CT scans were also taken of the bond region between the 8 layer L ATP liner-tape-laid samples. Fig. 8.16 shows the bond region for three samples, before and after 50 cryogenic cycles. The dark regions are visible in every sample, indicating areas of significant debonding in the internal laminate structure. This signifies a lack of consolidation between the CF/PEEK tape and PEEK liner. However, as shown in Fig. 8.16, the CF/PEEK remained bonded to the PEEK liner, even after 50 cycles, with little to no visible change in the bonded regions. This shows that the bonded regions have a good resistance to debonding under cryogenic cycling. In Fig 8.16, a cross-like pattern of bonding can also be seen at the liner-overwrap interface. This indicates that the application of the second layer of CF/PEEK tape on the PEEK surface has re-melted the liner surface beneath the first layer and caused consolidation of the liner to the tape-laid material along these regions. This is evidenced by the width between parallel lines being between 12 and 14 mm, i.e. the width of an individual CF/PEEK tape.

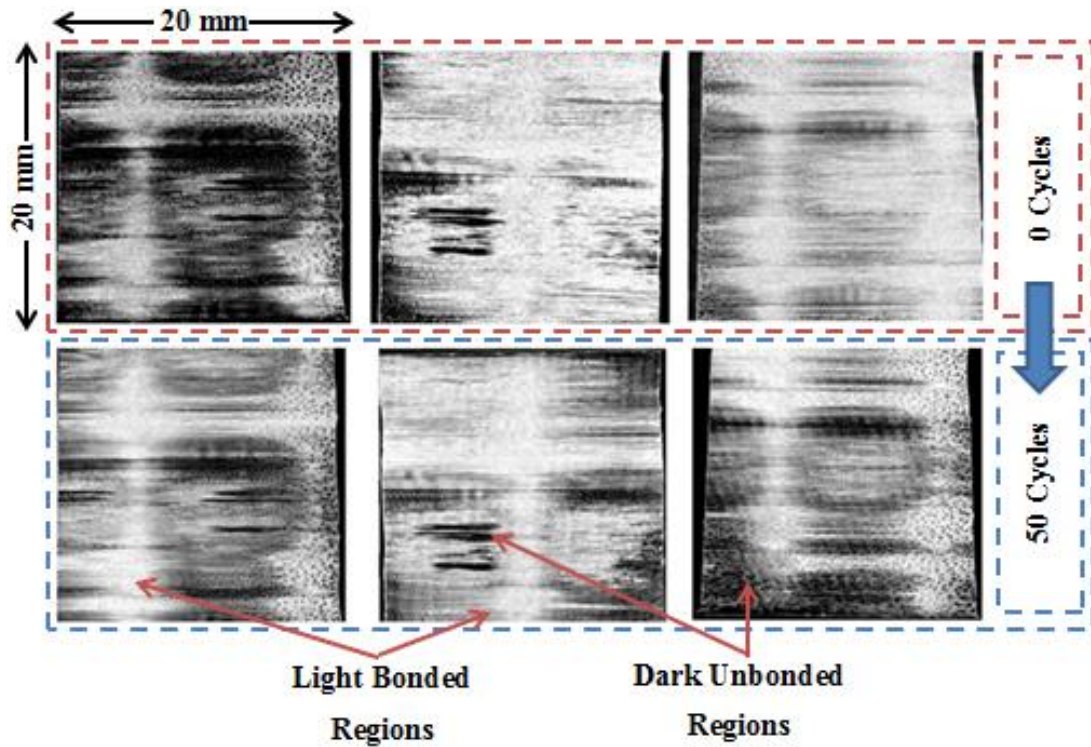


Figure 8.16. X-ray CT images of the LAMP bond region between the CF/PEEK tape and the PEEK liner before and after cryogenic cycling for three different samples.

#### 8.4.4. The Effects of Cryogenic Cycling on LAMP Laminates

The 8 layer  $[0/90/0/90]_s$  CF/PEEK-PEEK samples (Section 8.2) were cryogenically cycled to assess PEEK liner integrity. Three 20 mm  $\times$  20 mm samples were scanned with the X-ray CT machine before and after cryogenic cycling for interrupted numbers of cycles at 1, 2, 3, 5, 10 and 50 cycles for each sample. The X-ray CT images were used to assess the LAMP tape-laid PEEK liner relative to the hot plate counterparts. Fig 8.17 shows that for two of the three samples there were no cracks after 10 cryogenic cycles. However, after a further 40 cycles, through thickness cracking was observed in the liner as shown in Fig 8.18. Hence the liner integrity is compromised. The crack paths appear to originate from the liner-overwrap bond region with the voids on the liner side of the bond line acting as crack initiation points. Nevertheless, these LAMP samples have outperformed the hot plate samples from Chapter 7 which failed after 1 cycle.

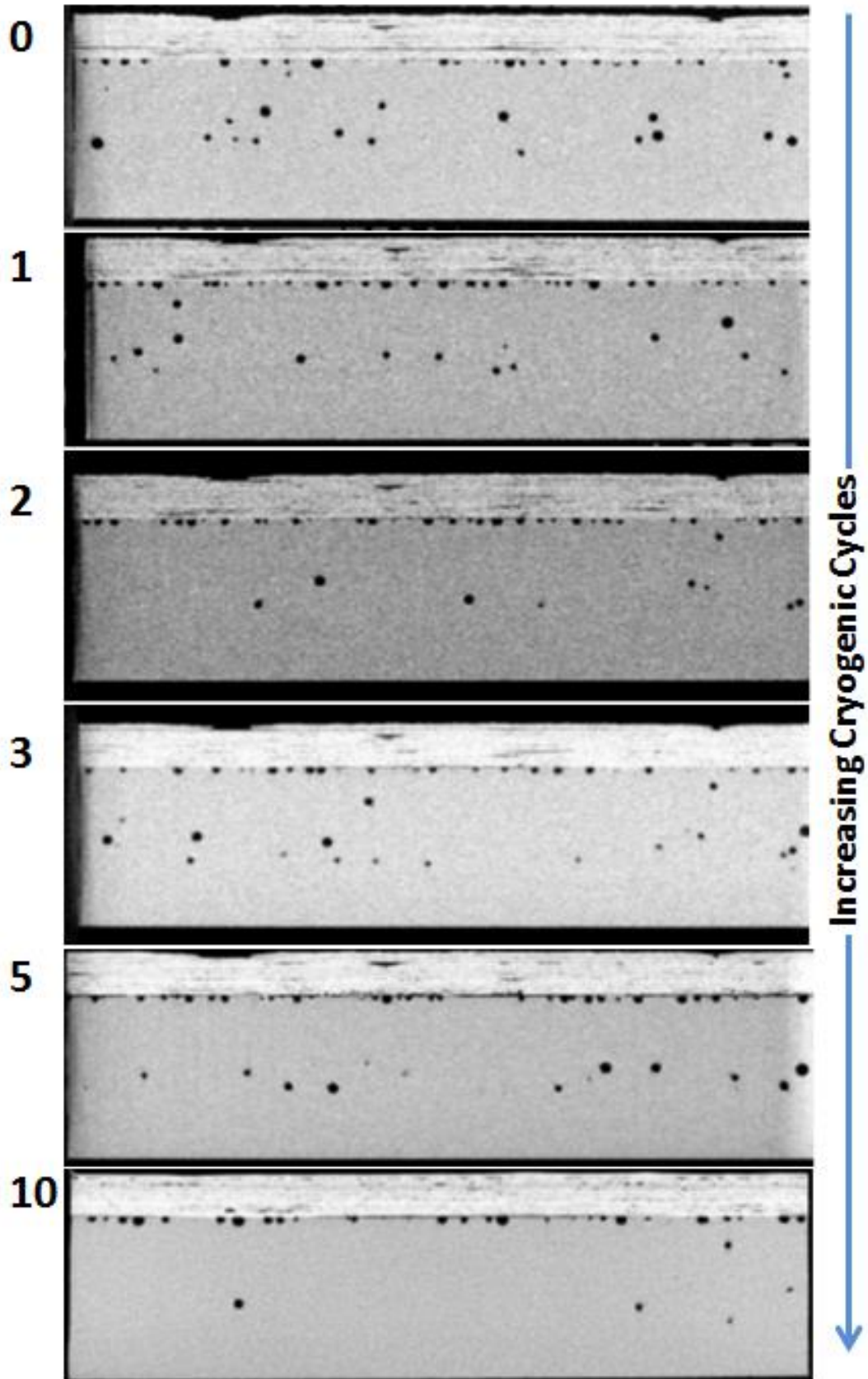
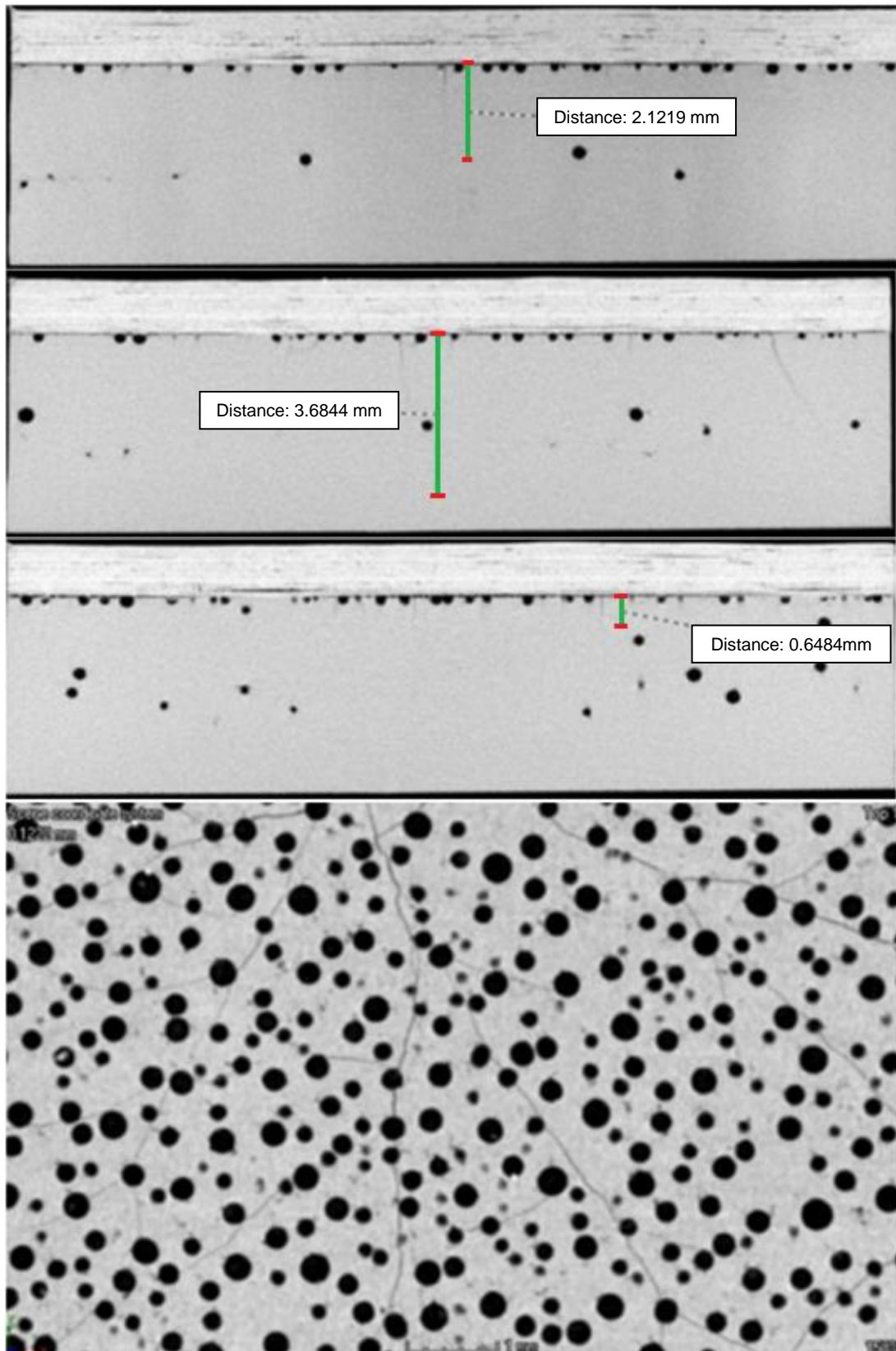


Figure 8.17. Cross sectional images of a cryogenically cycled  $[0/90/0/90]_s$  CF/PEEK-PEEK LATP laminate after 0, 1, 2, 3, 5 and 10 cycles.



*Figure 8.18. Cross sectional images of a cracks in a cryogenically cycled  $[0/90/0/90]_S$  CF/PEEK-PEEK LATP laminate after 50 cycles with a plan view image of crack networking at the liner-overwrap interface through void sections.*

## Cryogenic Cycling and Final Layup Testing

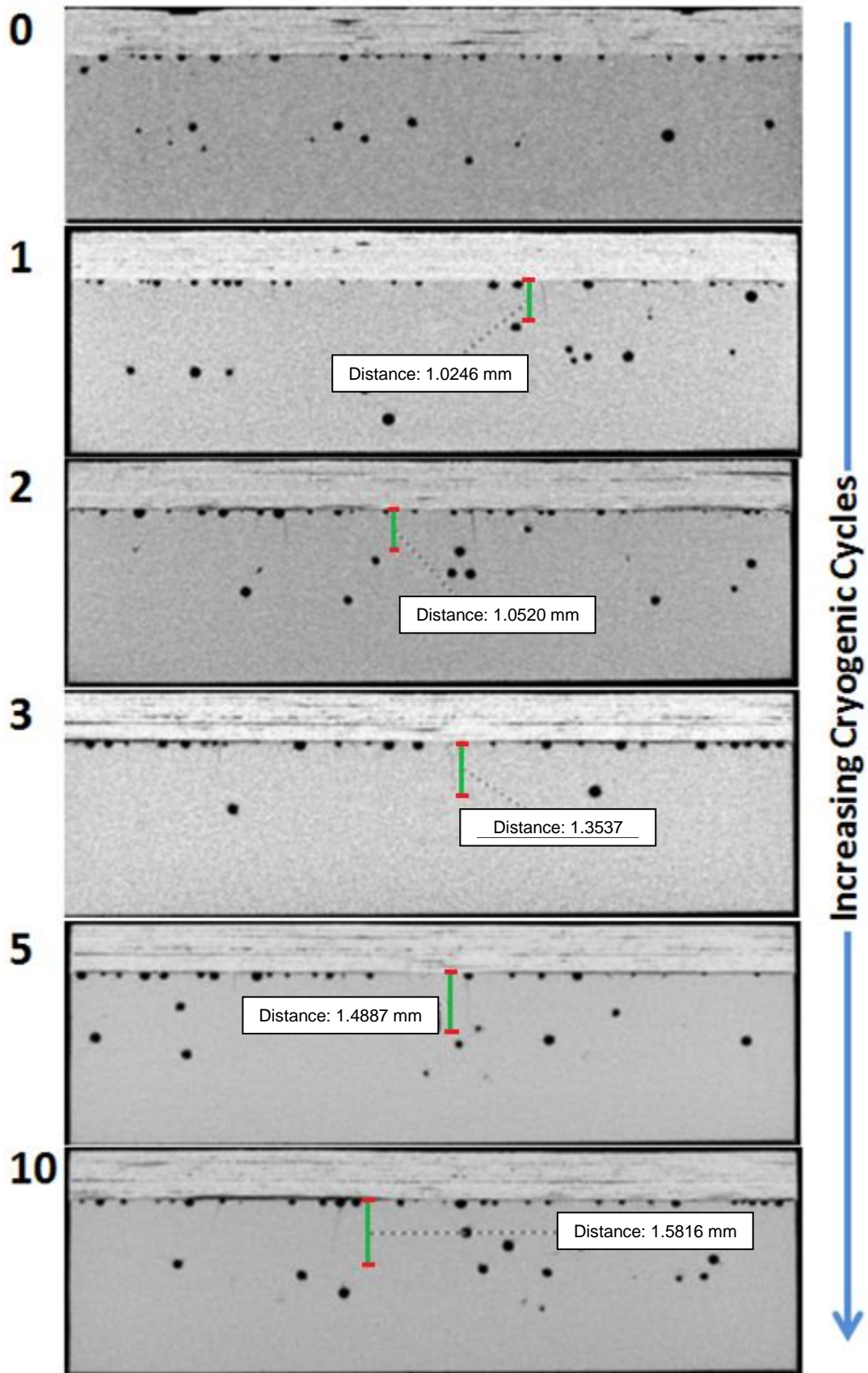
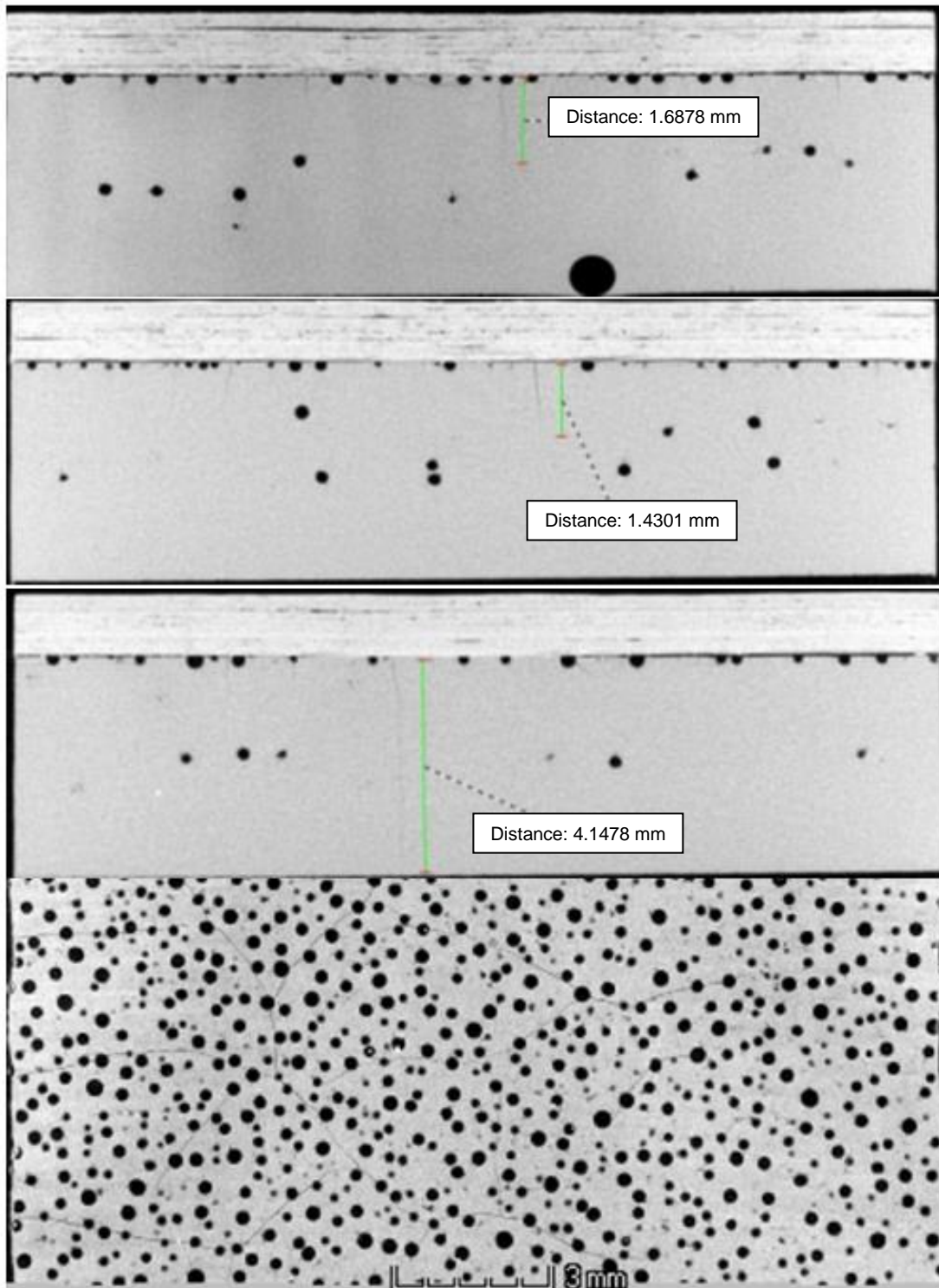


Figure 8.19. Cross sectional images of a cryogenically cycled  $[0/90/0/90]_s$  CF/PEEK-PEEK LATP laminate after 0, 1, 2, 3, 5 and 10 cycles with cracks present.



*Figure 8.20. Cross sectional images of crack growth in a cryogenically cycled  $[0/90/0/90]_S$  CF/PEEK-PEEK LATP laminate after 50 cycles with a plan view image of crack networking at the liner-overwrap interface through void sections.*

The third sample cracked after 1 cycle. This allowed for crack growth to be observed over further cycles to determine the rate of crack growth through the laminate, as shown in Fig. 8.19. It can be seen that the cracks continued to grow in size through the liner thickness with cycling. The cracks after a single cycle had a nominal size of 1.0 mm or less. These cracks grew to almost 1.6 mm in length over the 10 cycles. This is about half the liner thickness and significantly increases the permeability, due to the reduced effective thickness of the liner. Further cycling to 50 total cycles caused crack growth through the entire liner thickness (Fig. 8.20). The removal of the initial voids at the liner-overwrap interface could help to improve cracking resistance at the bond line. The key conclusion from these results is the improvement in crack resistance compared to the hot plate samples.

### **8.5. Microscopy and Nano-Indentation of LATP CF/PEEK-PEEK Welds**

Hot plate formed PEEK polymer liner samples that were tape-laid with 8 layers of CF/PEEK in the LATP process, were analysed using microscopy and nano-indentation techniques to assess the bond line thickness of the LATP process. Small sections were removed and mounted in an epoxy resin and polished with increasingly finer SiC grit papers (from 3200 up to 1200) and then a 0.06  $\mu\text{m}$  alumina suspension as recommended. Fig. 8.21 shows a microscopic image of a typical region of interest in the LATP CF/PEEK to PEEK bond interface region. The laser welding process melts the polymer liner surface during processing to form the bond between the CF/PEEK tape and the PEEK liner surface. An assessment of the effects of the laser welding process on the PEEK liner is presented here using nano-indentation on the sample cross section to determine the change in modulus of the PEEK liner material.

A number of nano-indentation studies have been carried out by other authors on PEEK [280-282] and PEEK composite materials [283-285] with varying test parameters used. For the present study, the nano-indentation parameters used are included in Table 8.4, and they have given a nominal Young's modulus of 5 GPa which is consistent with published results.

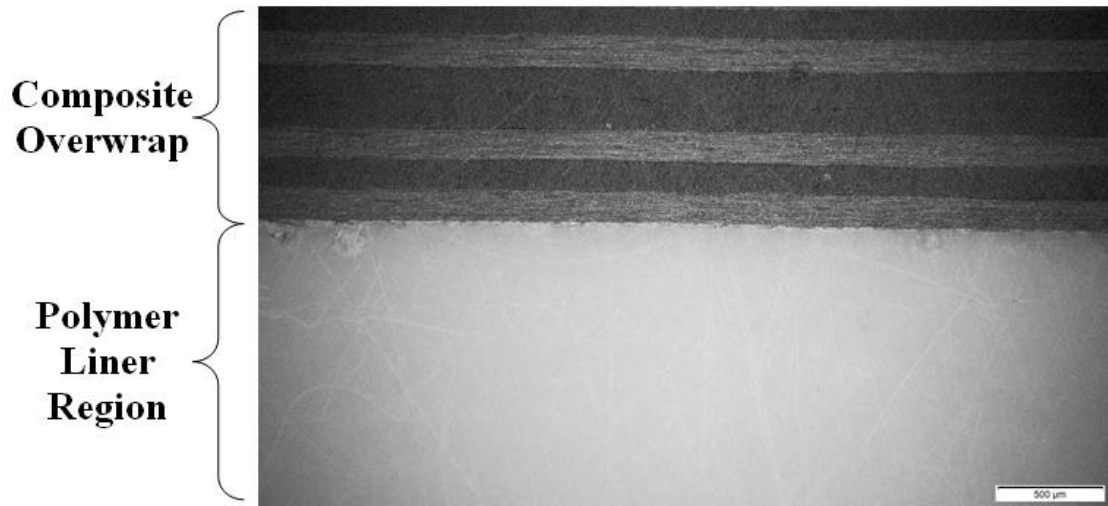


Figure 8.21. Microscopy image of the LAMP CF/PEEK-PEEK samples.

Table 8.4. Nano-indentation test parameters.

Parameter	Value
Applied Load	40 mN
Loading Rate	80 mN/min
Unloading Rate	80 mN/min
Hold Time	20 s
Indent Spacing	75 $\mu\text{m}$

A minimum spacing of 75  $\mu\text{m}$  was maintained between indents to avoid discrepancies due to overlapping fields of elastic deformation. Eleven indents were performed per test in a staggered pattern, as shown in Fig. 8.22. This scheme allowed for the minimum distance between indents to be maintained while incrementally increasing the distance of the indents outward from the bond line between the liner and tape-laid sample. The first indent in every test was a depth calibration to ensure consistent measurements.

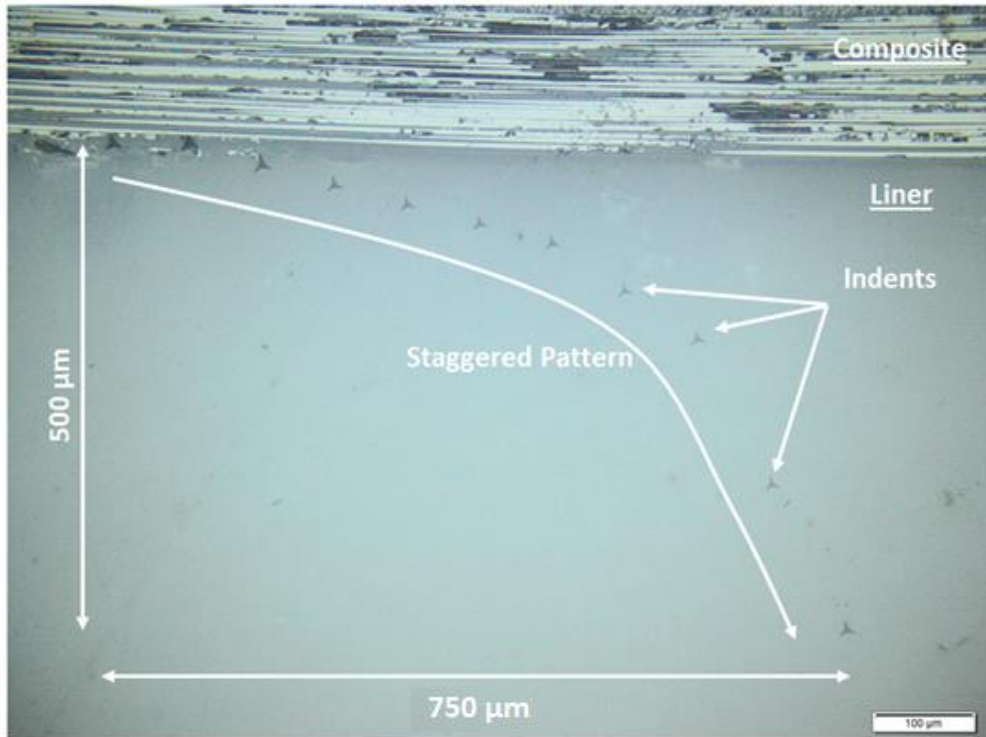


Figure 8.22. Microscopy image of the indentation analysis carried out on the liner-overwrap samples.

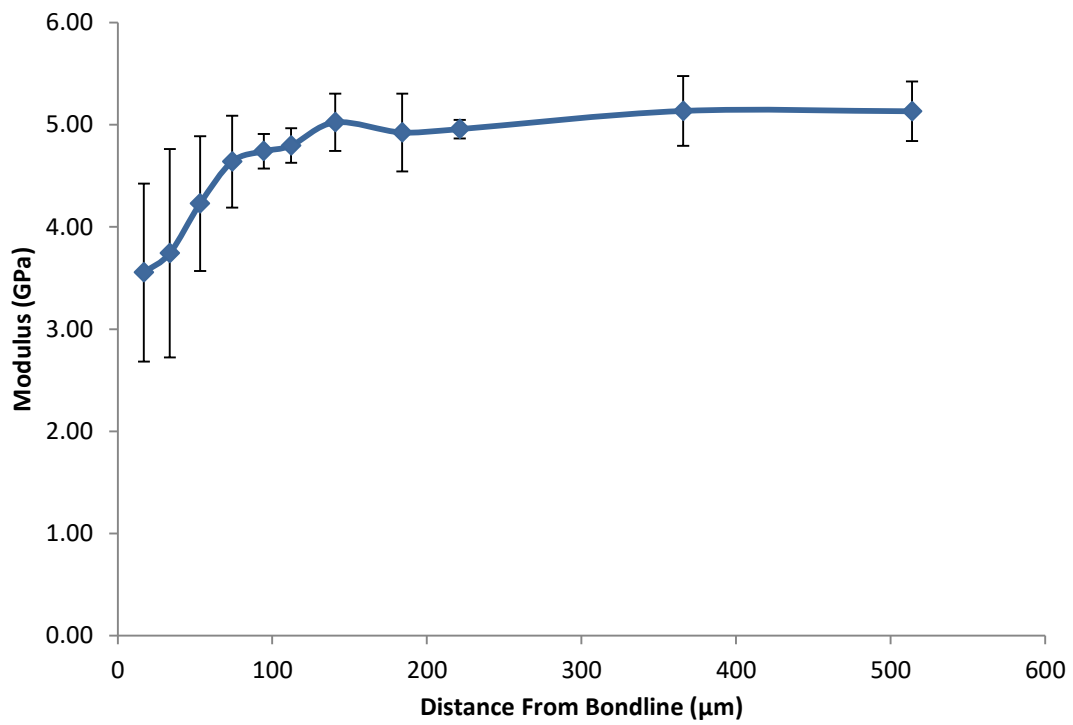


Figure 8.23. Variation in elastic modulus with distance from the liner-overwrap bond line from nano-indentation testing.

Fig. 8.23 shows the modulus results of the individual tests (a minimum of five results were obtained for each data point) showing the change in modulus of the PEEK liner material at the liner-overwrap interface. The PEEK liner material has a significantly lower modulus (at a mean value of 3.5 GPa) near the bond line interface which indicates that the laser welder has caused a reduced modulus in this region to a depth of approximately 100  $\mu\text{m}$  where values settle to around 5 GPa. This suggests that the laser welder has created a more amorphous region at the bond line interface up to a depth of 100  $\mu\text{m}$ . This is due to the rapid heating and cooling effect of the laser welder on the PEEK, leading to an amorphous region of lower crystallinity and hence reduced modulus.

### 8.6. Conclusions

From an analysis of the results the following conclusions can be drawn:

- Rotational moulding of polymer powder materials has been successfully demonstrated for the production of polymer liners for low permeability COPV applications, with equivalent permeability coefficients to hot plate samples
- LATP has been successfully demonstrated for overwrapping PEEK liner materials with CF/PEEK composite tape while maintaining a significant bond strength between the PEEK liner and the composite overwrap
- CF/PEEK-PEEK samples formed using rotational moulding and LATP overwrapping have been shown to have reduced permeability compared to autoclave samples, consistent with permeability predictions
- X-ray CT scanning of hotplate LATP CF/PEEK-PEEK samples has shown resistance to cracking from cryogenic cycling up to 10 cycles. The majority of samples showed no crack formation and the CF/PEEK tape remained bonded to the PEEK polymer liner
- X-ray CT scanning has revealed significant gaps and defects in LATP samples compared to autoclave CF/PEEK samples. Roller pressure was shown to have little effect on laminate consolidation in the range of 2.5 to 4.5 bar
- Cryogenic cycling of rotomoulded LATP CF/PEEK-PEEK samples has resulted in cracking of the PEEK polymer liner

## Cryogenic Cycling and Final Layup Testing

- Cracking was shown to occur after 50 cryogenic cycles, resulting in liner failure
- Nano-indentation of the weld region between the PEEK polymer liner and the CF/PEEK overwrap has allowed for the identification of a region of reduced modulus (with up to a 30% reduction in modulus observed) adjacent to the bond interface, to a depth of approximately 100  $\mu\text{m}$  into the PEEK polymer liner

The successful tape placement of CF/PEEK tape on rotomoulded PEEK liners with the LATP process is a significant step forward for COPV applications. To the authors knowledge, rotomoulding of PEEK polymer has not been used before for the manufacture of COPVs. The use of X-ray CT scanning has provided valuable insight into the LATP bonding process. The ability of tape-laid samples to resist up to 10 cryogenic cycles without failure is promising. Improved control of voids could alleviate the cracking witnessed here. The characterisation of the laser weld zone is also important; the amorphous region at the weld interface may have increased the toughness of the liner at the interface and may be the cause for the reduced crack growth over the 10 cryogenic cycles.

# 9. Conclusions and Future Work

## 9.1. Conclusions

Reducing the costs of sending payloads to space has been a core aim of the aerospace community over the past number of years. New materials and innovative designs for COPVs have been at the forefront of this research, with resources specifically aimed at the development of polymer lined COPVs. This thesis identifies polymer materials which can meet the low permeability requirements of COPVs while also outlining a low cost manufacturing method, in the form of a modified rotational moulding process for polymer liner production and laser assisted thermoplastic tape placement for the overwrapping process. The key achievements of this thesis are as follows:

- Characterisation of polymer materials formed using rotational moulding techniques for suitability as low permeability liner materials for fuel containment in COPV structures
- Development of a modified rotational moulding process for low permeability polymer liner production to demonstrate proof of concept and allow for subsequent viability testing
- The design, development and manufacture of a polymer liner overwrapped with a tape-placed CF/PEEK composite tape in a Laser Assisted Tape Placement process for out-of-autoclave manufacturing

## Conclusions and Future Work

- Testing of demonstrator sections of an LATP tape-laid polymer liner for mechanical properties and permeability rates after cryogenic cycling to prove the viability of the chosen COPV design

A number of powder polymer materials were shown to be capable of meeting the low permeability requirements for the defined COPV. PA11 and PVDF materials provided the best barriers to helium permeation, with PA11 being superior on the basis of its lower density and therefore lower liner weight. PEEK materials were also shown to be capable of the low permeability requirements, but only with increased thickness. Permeability coefficients, adjusted for testing at 1 bar, were proven to successfully predict permeabilities at 5 bar. The higher permeability of the 2000P PEEK material in comparison to its PEEK counterparts is attributed to the increased amount of internal defects found in the sample as shown by X-ray CT scanning.

A finite element permeability prediction model for randomly distributed voids was developed based on the effect of forming temperature, measured void volume fractions and void radii for permeability analysis in rotomoulded polymer liners. Higher void volume fractions are directly related to an increase in permeability. At similar void volume fractions, smaller voids equate to higher permeabilities than larger voids, due to their tendency to distribute more evenly through the sample. Hence, an analysis of forming conditions for COPV liners has shown that higher forming temperatures give lower void volume fractions coupled with larger air voids, creating the optimum conditions for reducing permeability.

A novel modified rotational moulding process was developed to produce rotomoulded polymer liners for testing. The tooling achieved increased wall thickness consistency and dimensional accuracy while proving capable of producing liners from a number of polymer powder materials up to a maximum forming temperature of 450 °C. Thermal imaging was used to confirm the benefits of this segregated heating system. The new rotational moulding system was applied to the rotomoulding of PEEK which is the first of its kind to the authors knowledge.

Hot plate formed liner-tape-laid samples have displayed reduced leak rates over their individual counterparts. However cryogenic cycling of hot plate formed liner-tape-laid samples has shown consistent delamination (Nylon samples) and significant cracking (PEEK samples). This has been attributed to the residual stress build up

## Conclusions and Future Work

from the cooling of samples from their respective forming temperatures down to cryogenic conditions. Attempts to reduce the residual stress build-up have proven unsuccessful with increased cooling rates (leading to decreases in liner crystallinities of up to 4%) and annealing (of up to seven hours) having no effect on decreasing delamination and cracking in hot plate formed samples. Material property testing has shown significant changes in storage modulus and coefficients of thermal expansion for all materials, except PEEK, across the thermal operating range of the COPV.

Rotomoulded polymer liners have shown leak rates and permeability coefficients that are consistent with those of hot plate formed samples. LATP tape-laying of Nylon samples with a thermoplastic CF/PEEK tape has proven unsuccessful, with complete debonding occurring. However, LATP tape-laying of rotomoulded PEEK liners with CF/PEEK tape has been successful. Bonding of the CF/PEEK tape to the PEEK liner is not entirely consistent but has remained bonded over extensive cryogenic cycling (up to 50 cycles). LATP CF/PEEK is not as homogenous as autoclave CF/PEEK samples, with X-ray CT scans and permeability testing showing higher void contents and subsequently higher permeation rates. The majority of microcracking in these laminates occurs during the first cryogenic cycle, as evidenced by the leak rate test results over ten cryogenic cycles, which is consistent with published research. LATP CF/PEEK-PEEK samples have cracked after single cryogenic cycles. However smaller samples have resisted crack growth for up to 10 cycles with cracking only occurring after a further 40 cycles. Nano-indentation testing has shown a reduction in PEEK modulus in a 100  $\mu\text{m}$  deep layer at the liner surface, postulated to be the depth of liner material which is heat-affected by the laser processing. The rapid heating and cooling experienced in this heat effected zone could be the reason for the lower modulus, due to a lower crystallinity, thus giving an increased toughness and crack resistance to the liner-tape-laid configuration.

In future, key performance indicators for polymer liners should centre on an assessment of the melt rheology properties of polymer materials, their glass transition temperatures and their coefficients of thermal expansion with regards to the operating temperature range of the tank. The permeability and expansion coefficients are directly altered when passing through the material's glass transition temperature and a large amount of materials could be removed from future testing by

assessing if the operating range of the tank passes through the glass transition temperature of the polymer material being tested. Melt rheology properties could also be used to assess void characteristics in future rotomoulded parts to determine their ability to be rotomoulded based on their relative melt viscosity and flow properties..

### **9.2. Future Work**

The work conducted here constitutes an initial step towards the realisation of a fully functional thermoplastic-composite polymer lined COPV. However, given the stringent safety standards governing the use of COPVs in space, there is still significant scope for further research. While a number of points have been addressed such as polymer permeability, void content analysis, manufacturing (specifically in regards to rotational moulding and laser assisted tape placement) and environmental testing, a myriad of opportunities still exist to build on the current body of work and move towards the incorporation of polymer lined COPVs in future space missions.

Expanding the permeability analysis to include other powder polymer materials (such as liquid crystal polymers, polyimides and polyethylene terephthalate to name but a few) could potentially uncover even lower permeability materials, which could form the basis for future liners with lower weights and lower permeabilities. Void contents investigated with the X-ray CT scanning show an enhanced view of the internal structure of liner materials. The effect of forming conditions on internal void contents could be assessed with X-ray CT scanning, with the void volume fraction, void radius and void bias being easily measured for different forming temperatures to determine which conditions reduced void contents significantly for future liner production operations.

This void analysis data could then be used to validate and enhance the permeability model developed as part of this thesis. This would allow for the incorporation of variations in void size and shape into the model for a more realistic internal structure analysis. The model updates, in conjunction with minimal permeability testing, could then be used to predict permeabilities through the use of simple equations with results showing the best conditions for low permeability operations. These models could then be used to develop equations for predicting a permeability range (i.e. a

## Conclusions and Future Work

maximum and minimum value) for which the given parts will have a permeability which is within these bounds for specific forming conditions. The LATP overwrap could also be incorporated into the permeability model so that the entire liner-overwrap is assessed, as the overwrap will also impart a reduction in permeability on the wall section. Enhancing the accuracy of this model could also include an assessment of the bond depth region between the liner and overwrap and how this lower crystallinity region will have a higher permeability than the bulk crystalline liner region. The model could also be adapted to assess the permeability of composite materials and how the gaseous helium travels through the matrix and around fibres on a microscale. Factors such as fibre size and volume will affect the tortuosity of the leakage paths and these factors (along with the inclusion of air voids and defects) could enhance knowledge in this area.

The next step for the modified rotational mould tooling would be upscaling the tooling to a cylinder section that could produce cylindrical polymer liners for testing. The inclusion of an internal pressure within the mould tooling, during the cool down phase of the forming process, would also alleviate the formation of voids in the liner cross section and improve material consolidation. The use of a fluorination process on the inner surface of the rotomoulded liner after it has been rotomoulded could also reduce the permeability of the liner even further in a process similar to that currently being used on plastic bottles [286]. PVDF materials may also find more applications in COPV liners if a suitable bonding agent could be identified to bond the PVDF liner to the CF/PEEK overwrap with a sufficient level of strength. PVDF has been successfully bonded to other materials [287] and as such it should be possible to trial a bonded PVDF-CF/PEEK liner overwrap design (as well as a Nylon-CF/PEEK liner-overwrap design formed using similar methods) with an intermediary tie layer

These liners, once fabricated, could then be tape-laid with the LATP process and tested for permeability at a demonstrator level. This would be followed by subsequent permeability testing, after cryogenic cycling of the demonstrator in LN<sub>2</sub>, to determine the ability of the design to withstand the defined environmental conditions. Permeability testing of the COPV design at cryogenic temperatures would also be a step towards further validation of the tank design (as the permeability should be lower than that predicted at room temperature conditions). It

## Conclusions and Future Work

would also be prudent to incorporate modelling of the effects of the cryogenic environment, and the applied maximum operating pressure of 5 bar, on the COPV design to optimise the ability of the chosen design to withstand the stresses generated by the defined operating conditions of the tank.

The thermal control in the tooling could also be overhauled. As it stands, there are only two areas of control in the tooling, the main body and the flange. As has been shown, the use of segmented heating regions allows for the formation of parts with more consistent wall thickness distributions. However, this could be improved further by creating more individual heating zones, particularly at the parting line and vent pipe, as these regions act as cooling fins in the tooling and reduce the pickup of polymer powder during part formation leading to greater part inconsistency. An increase in thermal control in these areas will enhance part quality. Further testing of the capabilities of the modified rotomoulding tooling to create demonstrator parts with tailored material properties through the use of predefined heating and cooling cycles would be beneficial for future liner production. The incorporation of a polar boss insert into the design and an assessment of the stresses generated by this inclusion would then be the next logical step.

Another gap in the research presented here is knowledge of the liner material properties over the entire operating temperature range of the tank. While steps were taken to address this with DMA and TMA testing, a lack of knowledge of the physical properties and behaviour of the materials at cryogenic temperatures will limit the effectiveness of any future models made to predict the stresses generated in the liner-overwrap configuration. Material testing of all materials at cryogenic conditions, coupled with fracture testing of the LATP liner-overwrap configuration (peel testing, double cantilever beam testing and end load split testing) would significantly improve knowledge in this area and allow for the creation of more accurate models in future studies.

Further analysis of the LATP overwrapping process would also be a welcome contribution to the knowledge needed for future projects. While the LATP overwrapping parameters were held constant for this project, varying factors such as laser power (maximum temperature), tape lay down speed and overlap size in conjunction with material property testing will provide recommendations as to the

## Conclusions and Future Work

best forming conditions for laser welding on liner surfaces. The liner-overwrap study presented here is limited by the low number of tests conducted on the formation of these parts. An analysis of quasi-isotropic layups would also be beneficial as these layups would be more indicative of the final overwrap design for a full size COPV tank.

A study which included a structured battery of tests aimed at enhancing material properties in the liner and overwrap formation would allow for the production of better COPV wall configurations. Improvements to the consistency of tape consolidation on the liner surface would also be key, with the removal of air gaps and unbonded regions being the main goal. This could be aided by the use of heated tooling underneath the liner during the overwrap process to enhance the consolidation of the tape. It would also be aided by the development of a proprietary overwrapping tape with a more consistent tape width as variances in the tape width are the main cause of gaps in the overwrap structure.

For the final qualification of a polymer lined COPV, which meets the requirements of a fully functional LH2 storage vessel, the production and testing of a 1:1 scale polymer liner overwrapped with a thermoplastic tape in the LATP process is necessary. PEEK is the only polymer which has been successfully tape laid with the LATP process within this project, and so should form the basis for the liner material studies. Permeability testing at cryogenic conditions which shows a leak rate below that of the acceptable level, without inducing cracking in the liner, would be the optimum outcome and would signify the successful integration of polymer liners into future COPV designs.

### **9.3. Final Conclusions**

The work presented here has contributed significantly to the field of polymer lined COPVs with a focus on polymer permeability evaluation, the effects of cryogenic environments on liner materials, and liner manufacturing techniques. This research provides a framework by which a fully functioning polymer lined COPV can be developed for use in future launches with numerous steps take in this regard, including:

## Conclusions and Future Work

1. Polymer materials are capable of storing highly permeating fuels with leak rates below the acceptable limit for liquid fuel containment in space, specifically for PA11, PVDF and PEEK materials
2. A modified rotational moulding process has been designed and fabricated with the capability of forming polymer liners for COPV applications, including the rotomoulding of PEEK powder materials
3. LATP wrapped PEEK polymer liners are capable of storing highly permeating fuels for up to 10 cryogenic cycles, without failure, with significant scope for improvement
4. The ability of the LATP wrapped PEEK samples to achieve these low permeability requirements is directly related to the reduction in residual stress provided by these manufacturing methods. This is evidenced by the nano-indentation testing which shows the creation of a lower modulus layer in the PEEK liner at the liner-tape interface. This is most likely a laser heat-affected zone with lower crystallinity, and hence higher toughness and more crack resistance, but further testing is needed to confirm this outright
5. Internal air voids and defects cause increased permeation rates by providing leakage paths for the permeating gas in helium permeability tests
6. An air void model has been developed using experimental analyses and finite element tools to predict permeabilities based on internal air void contents for polymer materials

# Appendices

The Appendices have been broken down into a number of sections including:

A.1. Original COPV Designs: Drawings, based on guidelines provided by Airbus Defence and Space, of the COPV structure, the dome ends and the metallic inserts.

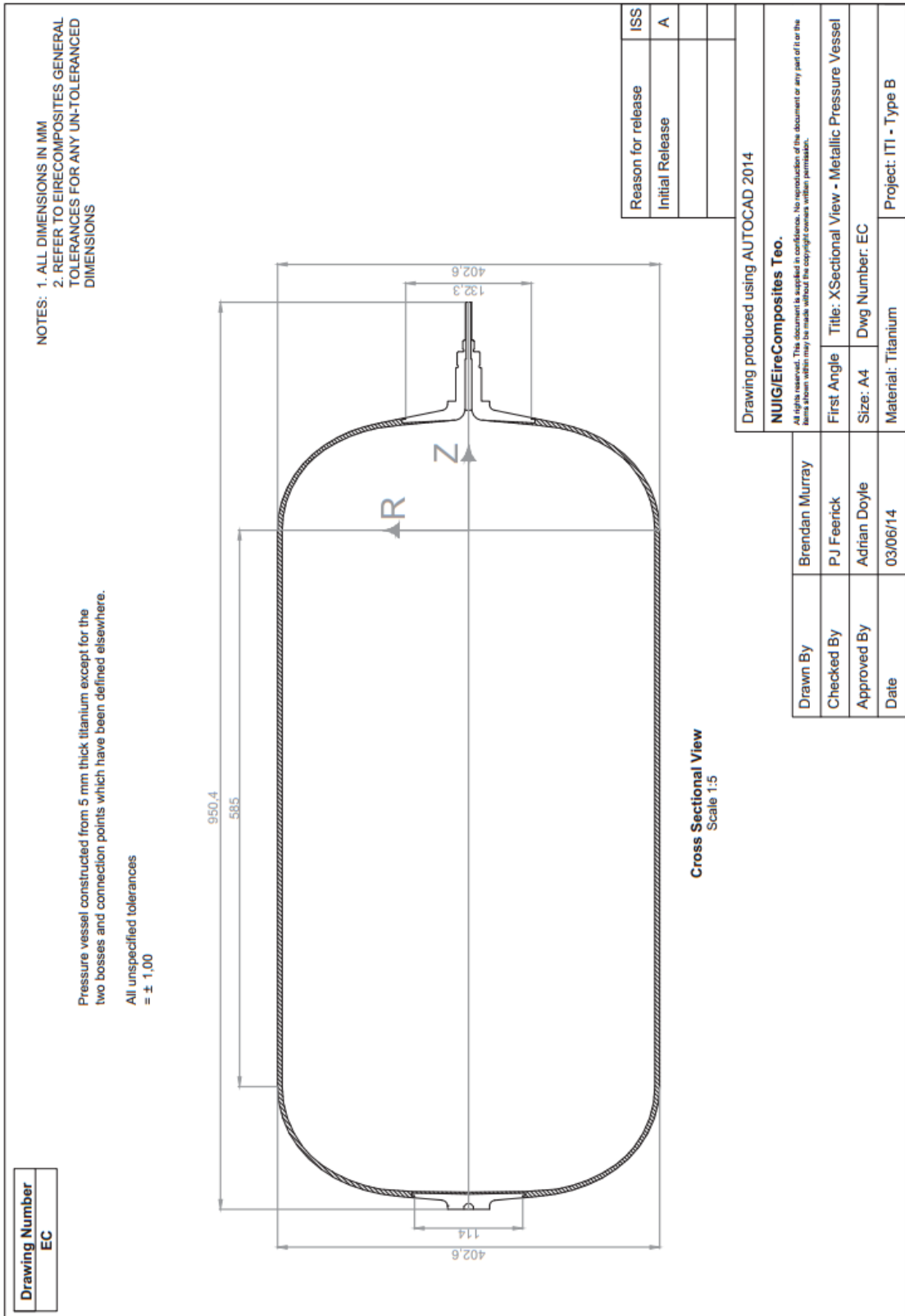
A.2. Rotomoulding Tooling Drawings: Drawings of the tooling fabricated as part of the liner production studies.

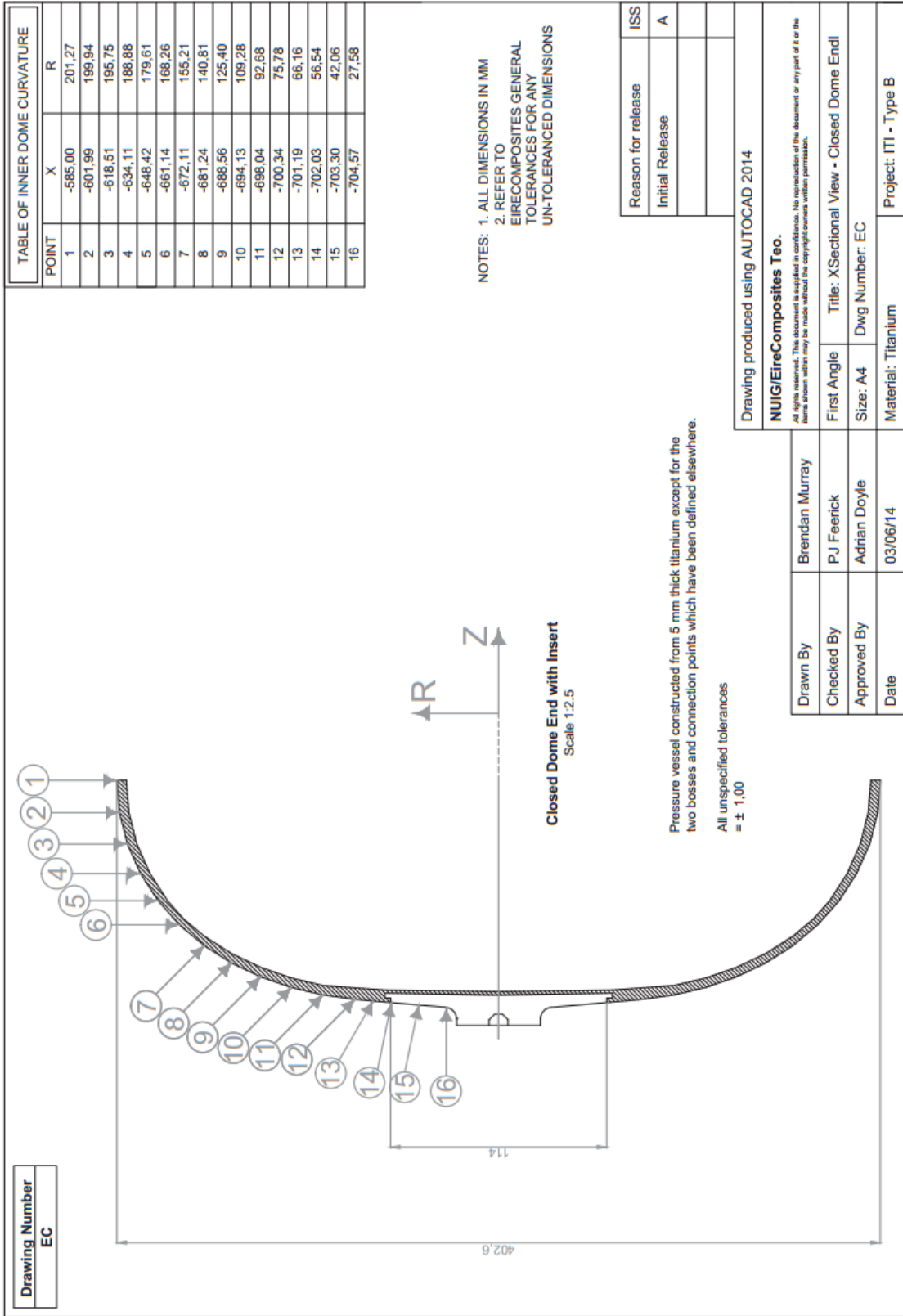
B.1. Python scripting code for random distribution of voids

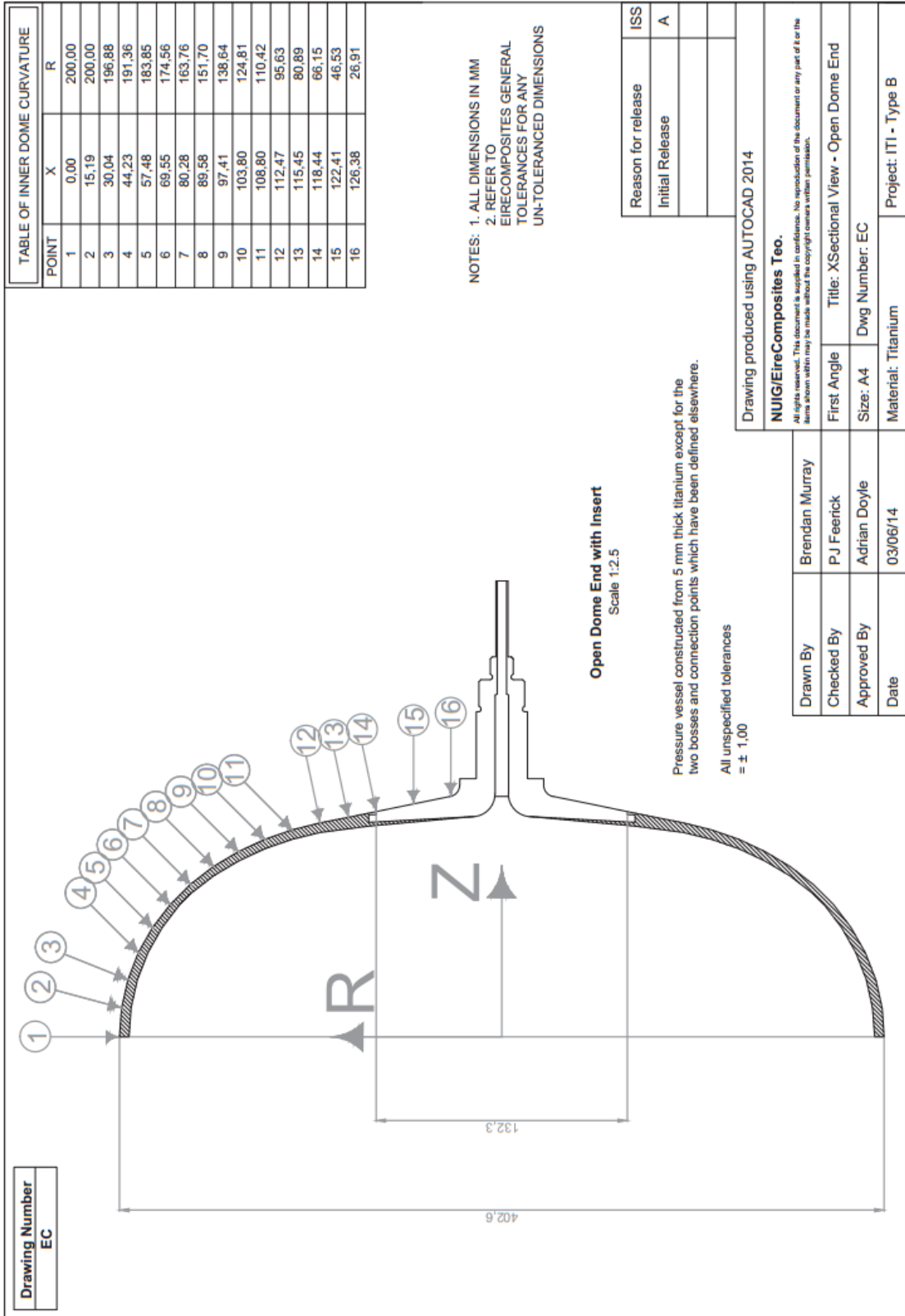
C.1. DMA Test Results: Test results for DMA testing of PEEK150PF, PVDF, PA11, and PA12 polymers in tension and compression.

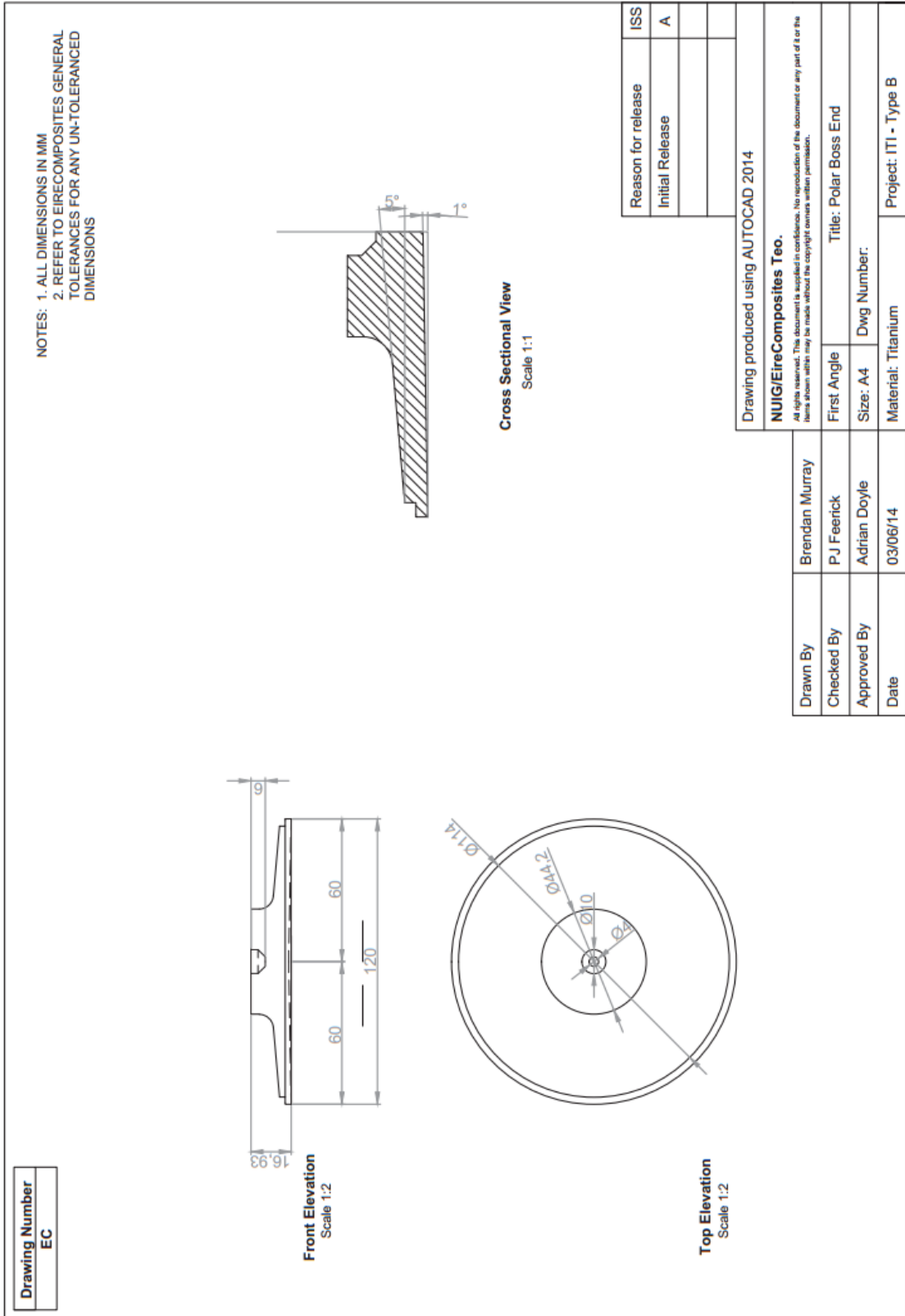
C.2. TMA Test Results: Test results for TMA testing of PEEK150PF, PVDF, PA11, and PA12 polymers.

# A.1. Original COPV Designs



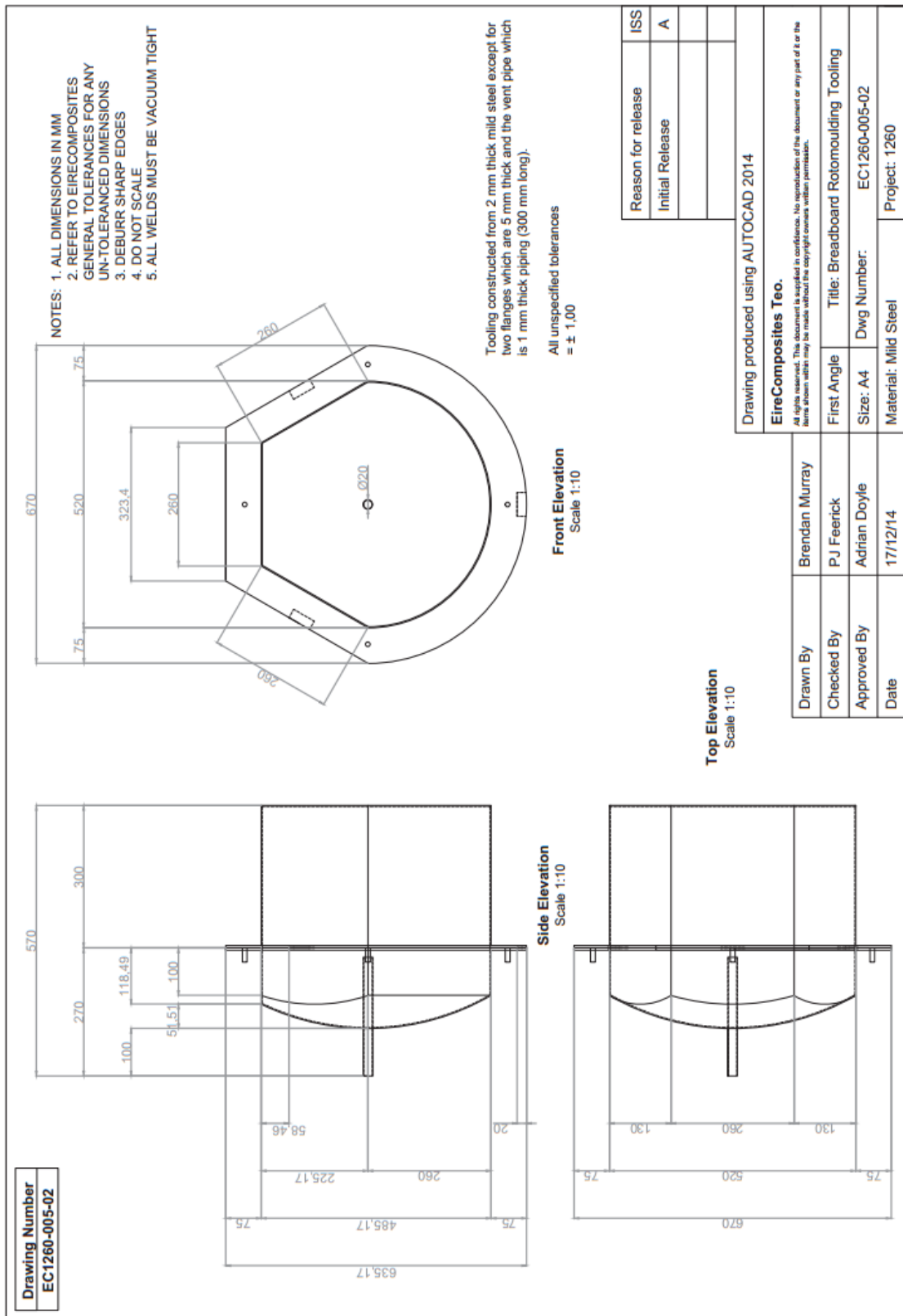


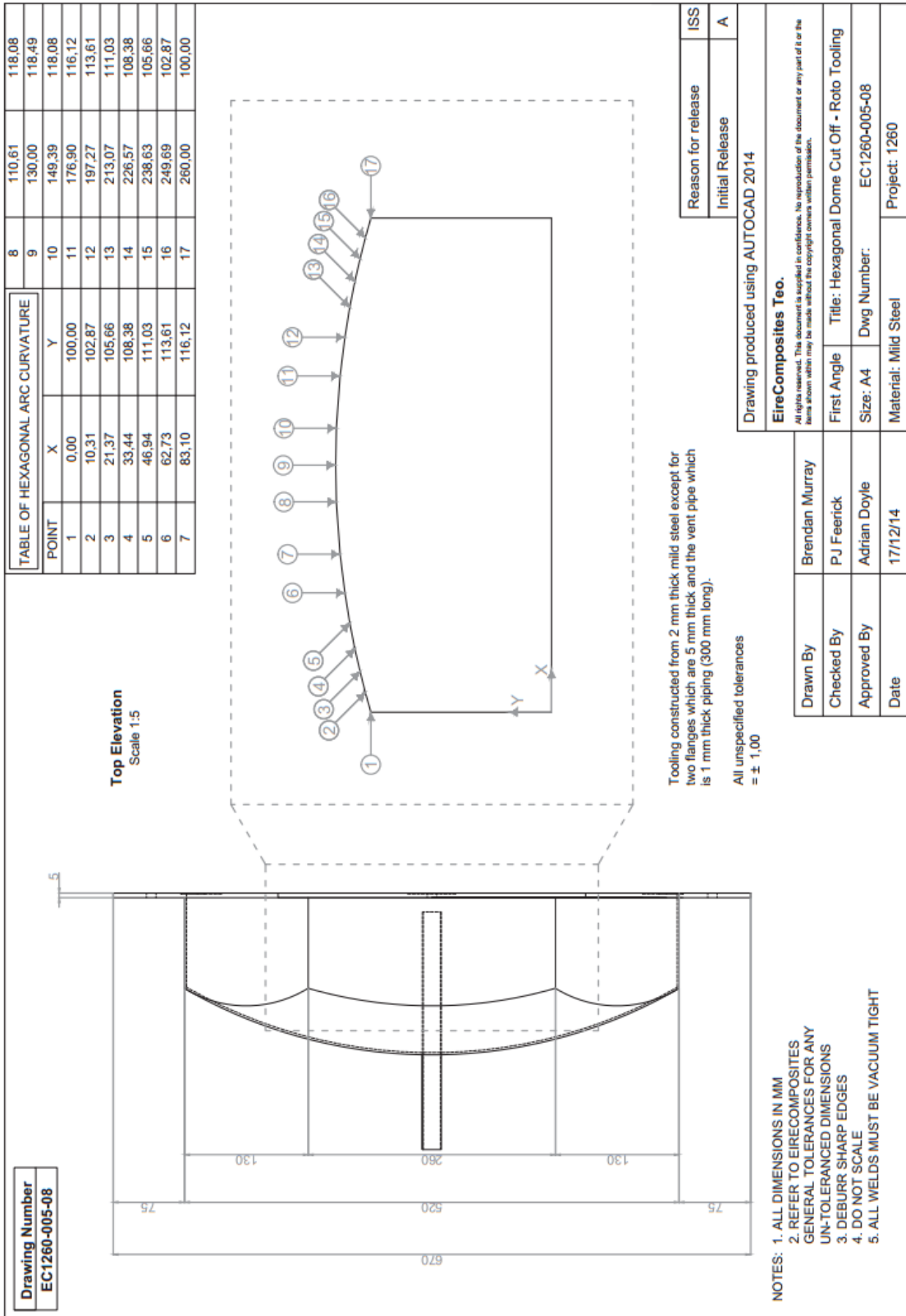






## A.2. Rotomoulding Tooling Drawings





### B.1. DSC Graphs of As-Delivered Powders

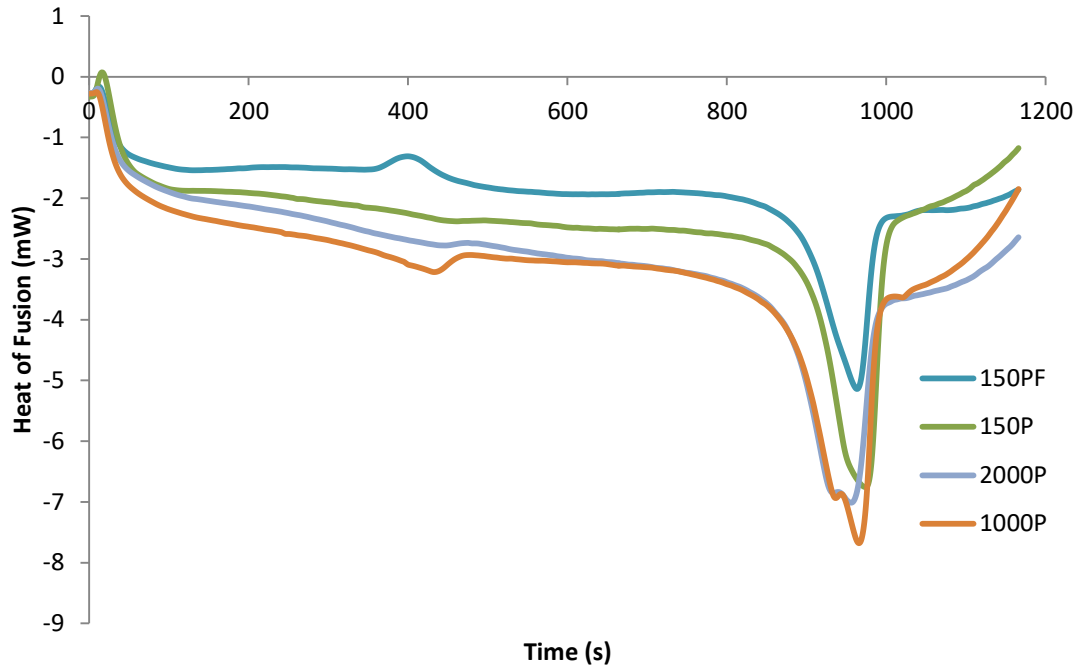


Figure B.1. Typical DSC results for the PEEK powder materials in their as-delivered form.

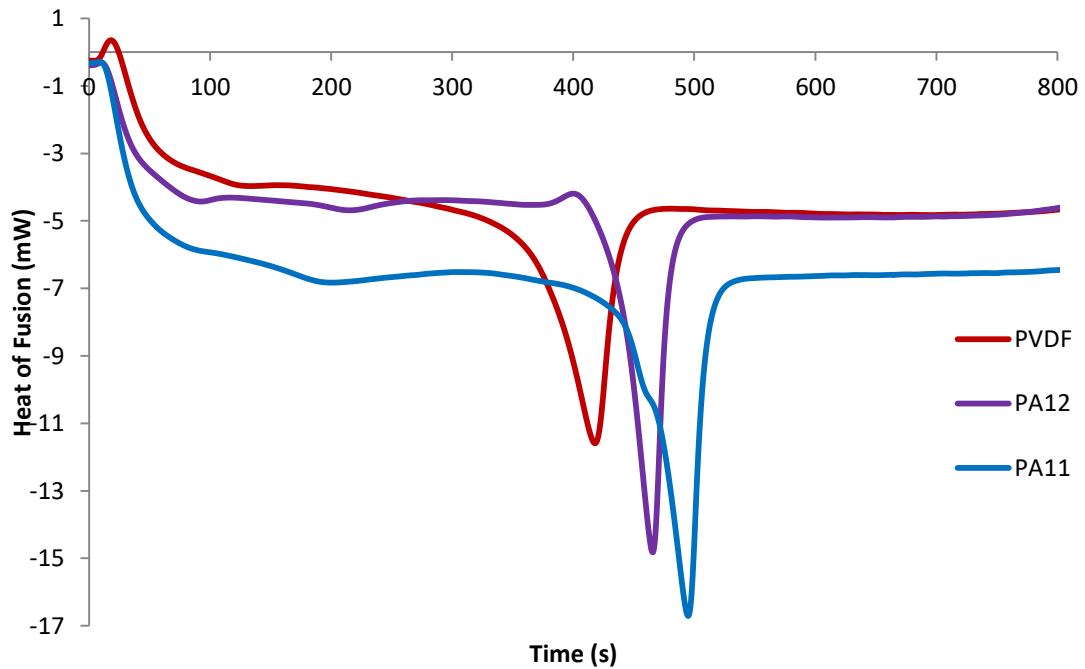


Figure B.2. Typical DSC results for the PVDF, PA12, and PA11 powder materials in their as-delivered form.

## C.1. Python Scripting Code

```

#-----
# VARIABLE DEFINITIONS
#-----

from part import *
from material import *
from section import *
from assembly import *
from step import *
from interaction import *
from load import *
from mesh import *
from job import *
from sketch import *
from visualization import *
from connectorBehavior import *
import random
import math

#-----
# VARIABLE DEFINITIONS
#-----

SPHERE_RAD = 0.1
VOLUME_FRAC = 0.1
PART_LENGTH = 1.00
PART_WIDTH = 1.00
PART_THICK = 1.00
SHEET_SIZE = 1.5*PART_LENGTH
PI = 3.14159265359

print 'The Finite Element model variables have been defined....!'

#-----
# CUBE CONSTRUCTION
#-----

# CREATE CUBE FROM WORKING MODEL

mdb.models['Model-1'].ConstrainedSketch(name='__profile__', sheetSize=SHEET_SIZE)

mdb.models['Model-1'].sketches['__profile__'].sketchOptions.setValues(decimalPlaces=4)

mdb.models['Model-1'].sketches['__profile__'].rectangle(point1=(0.0, 0.0),
point2=(PART_LENGTH, PART_WIDTH))

mdb.models['Model-1'].Part(dimensionality=THREE_D, name='Part-1',
type=DEFORMABLE_BODY)

mdb.models['Model-1'].parts['Part-1'].BaseSolidExtrude(depth=PART_THICK,
sketch=mdb.models['Model-1'].sketches['__profile__'])

del mdb.models['Model-1'].sketches['__profile__']

print 'The Cube FE model has been created....!'

```

## Appendices

```
#-----  
# REVOLVE SEMI-CIRCLES TO CREATE SPHERES IN CUBE  
#-----  
  
# Volume of spheres  
PART_VOLUME = PART_LENGTH*PART_WIDTH*PART_THICK  
TOT_SPH_VOL = PART_VOLUME*VOLUME_FRAC  
  
# Number of spheres  
ONE_SPH_VOL = (4.00/3.00)*SPHERE_RAD*SPHERE_RAD*SPHERE_RAD*PI  
  
NUM_SPHERES = TOT_SPH_VOL/ONE_SPH_VOL  
  
n = int(round(NUM_SPHERES,0))  
  
print 'The number of voids present is....'  
  
print n  
  
#Create n instances of the sphere  
for i in range(2, (n+2)):  
  
    #Create Spheres  
    PartName = 'Part-' + str(i)  
  
    mdb.models['Model-1'].ConstrainedSketch(name='__profile__', sheetSize=SHEET_SIZE)  
    mdb.models['Model-1'].sketches['__profile__'].ConstructionLine(point1=(0.0, -1.0),  
point2=(0.0, 1.0))  
    mdb.models['Model-1'].sketches['__profile__'].FixedConstraint(entity=mdb.models['Model-  
1'].sketches['__profile__'].geometry[2])  
    mdb.models['Model-1'].sketches['__profile__'].ArcByCenterEnds(center=(0.0, 0.0),  
direction=CLOCKWISE, point1=(0.0, -SPHERE_RAD), point2=(0.0, SPHERE_RAD))  
    mdb.models['Model-1'].sketches['__profile__'].Line(point1=(0.0, -SPHERE_RAD),  
point2=(0.0, SPHERE_RAD))  
    mdb.models['Model-  
1'].sketches['__profile__'].VerticalConstraint(entity=mdb.models['Model-  
1'].sketches['__profile__'].geometry[4])  
    mdb.models['Model-1'].Part(dimensionality=THREE_D, name=PartName,  
type=DEFORMABLE_BODY)  
    mdb.models['Model-1'].parts[PartName].BaseSolidRevolve(angle=360.0,  
flipRevolveDirection=OFF, sketch=mdb.models['Model-1'].sketches['__profile__'])  
  
    del mdb.models['Model-1'].sketches['__profile__']  
  
print 'Multiple spheres have been created....!'  
  
#-----  
# MATERIAL DEFINITIONS  
#-----  
  
mdb.models['Model-1'].Material(name='HDPE')  
mdb.models['Model-1'].materials['HDPE'].Diffusivity(table=((7e-10, 0.0), ))  
mdb.models['Model-1'].materials['HDPE'].Solubility(table=((1.0, ), ))  
mdb.models['Model-1'].Material(name='AIR')  
mdb.models['Model-1'].materials['AIR'].Diffusivity(table=((5e-05, 0.0), ))  
mdb.models['Model-1'].materials['AIR'].Solubility(table=((1.0, ), ))  
mdb.models['Model-1'].HomogeneousSolidSection(material='HDPE', name='Section-1'  
, thickness=None)  
mdb.models['Model-1'].HomogeneousSolidSection(material='AIR', name='Section-2',  
thickness=None)
```

## Appendices

```
print 'All materials have been defined.....'

#-----
# SECTION ASSIGNMENT
#-----

# Section assignment for cube material

mdb.models['Model-1'].parts['Part-1'].SectionAssignment(offset=0.0,
    offsetField="", offsetType=MIDDLE_SURFACE, region=Region(
    cells=mdb.models['Model-1'].parts['Part-1'].cells.getSequenceFromMask(
    mask=('#1 ]', ), ), ), sectionName='Section-1', thicknessAssignment=
    FROM_SECTION)

for i in range(2, (n+2)):

    # Section assignment for spheres in for loop for ease/time

    PartName = 'Part-' + str(i)

    mdb.models['Model-1'].parts[PartName].SectionAssignment(offset=0.0,
        offsetField="", offsetType=MIDDLE_SURFACE, region=Region(
        cells=mdb.models['Model-1'].parts[PartName].cells.getSequenceFromMask(
        mask=('#1 ]', ), ), ), sectionName='Section-2', thicknessAssignment=
        FROM_SECTION)

print 'All materials have been assigned a section.....'

#-----
# INSTANCE DEFINITIONS
#-----

mdb.models['Model-1'].rootAssembly.DatumCsysByDefault(CARTESIAN)

for i in range(1, (n+2)):

    #Create Spheres
    PartName = 'Part-' + str(i)
    PartName2 = 'Part-' + str(i) + '-1'

    mdb.models['Model-1'].rootAssembly.Instance(dependent=ON, name=PartName2,
        part=mdb.models['Model-1'].parts[PartName])

print 'All parts have been instanced.....'

#-----
# TRANSLATE SPHERES
#-----

# Translate spheres into cube

#Euclidean Distance Measure
def euclidean_py(x, y):

    if len(x) != len(y):
        raise ValueError, "vectors must be same length"
    sum = 0
    for i in range(len(x)):
        sum += (x[i]-y[i])**2
```

## Appendices

```
return math.sqrt(sum)

spherelist = []
sphereinstancelist = []

for i in range(2, (n+2)):

    PartName = 'Part-' + str(i) + '-1'

    print PartName

    maxtries = 1000

    while len(spherelist) < i-1:
        maxtries -= 1
        if maxtries < 1:
            print 'Maximum tries exceeded, restart!'
            break;

        VECPOSITION = [(SPHERE_RAD + (random.random()*(PART_LENGTH-
(2*SPHERE_RAD)))), (SPHERE_RAD + (random.random()*(PART_WIDTH-
(2*SPHERE_RAD)))), (SPHERE_RAD + (random.random()*(PART_THICK-
(2*SPHERE_RAD))))]
        for pos in spherelist:
            if euclidean_py(pos,VECPOSITION) < 2*SPHERE_RAD:
                break
        else:
            spherelist.append(VECPOSITION)
            print VECPOSITION
            mdb.models['Model-1'].rootAssembly.translate(instanceList=(PartName, ),
                vector=(VECPOSITION))

    print SPHERE_RAD

print 'You have translated all the spheres into the cube, well done!'
#-----
#
#-----
```

### D.1. DMA Test Results

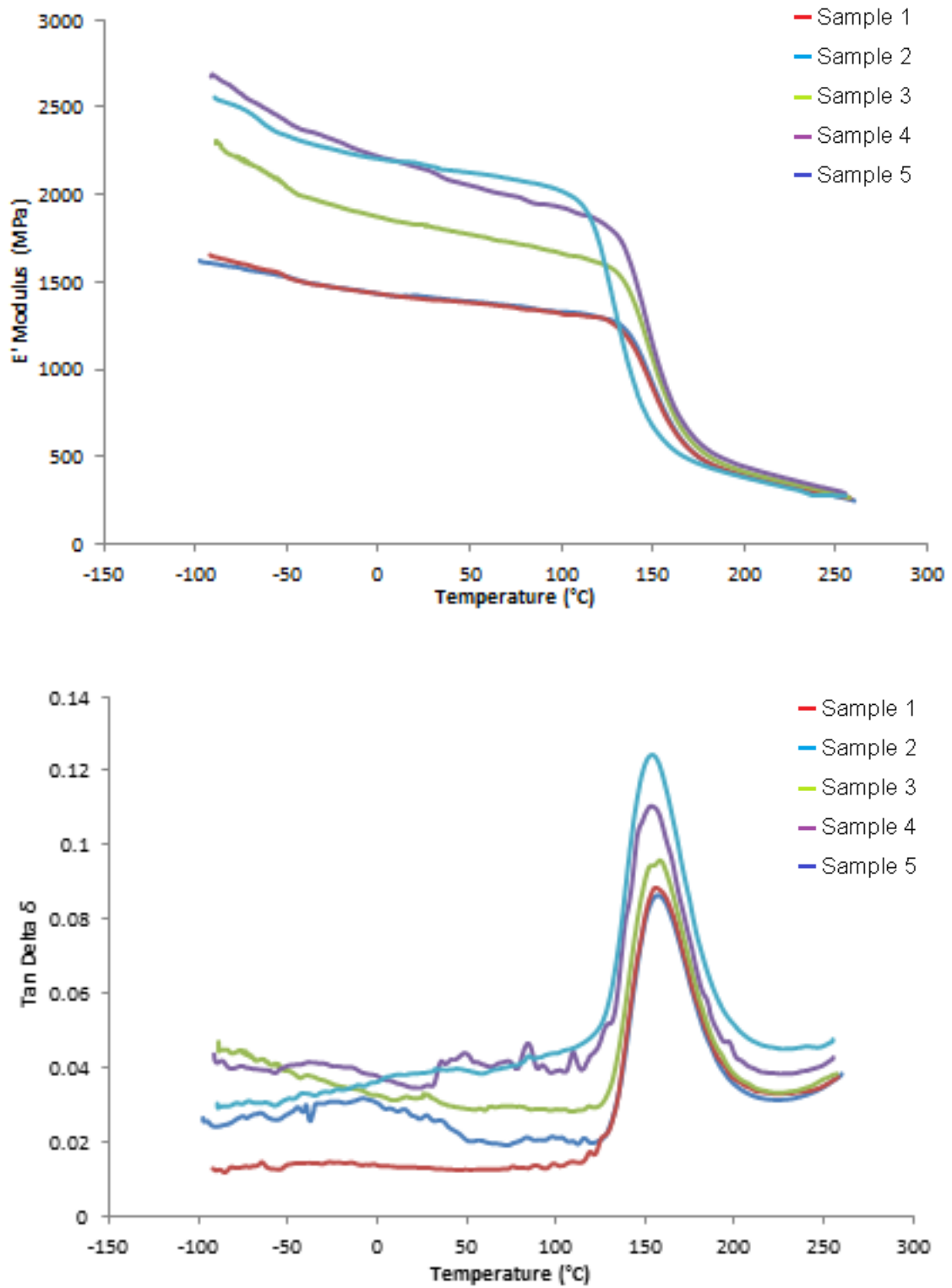


Figure D.1.1. DMA results for the E' Modulus and Tan Delta of Victrex PEEK150PF in tension.

## Appendices

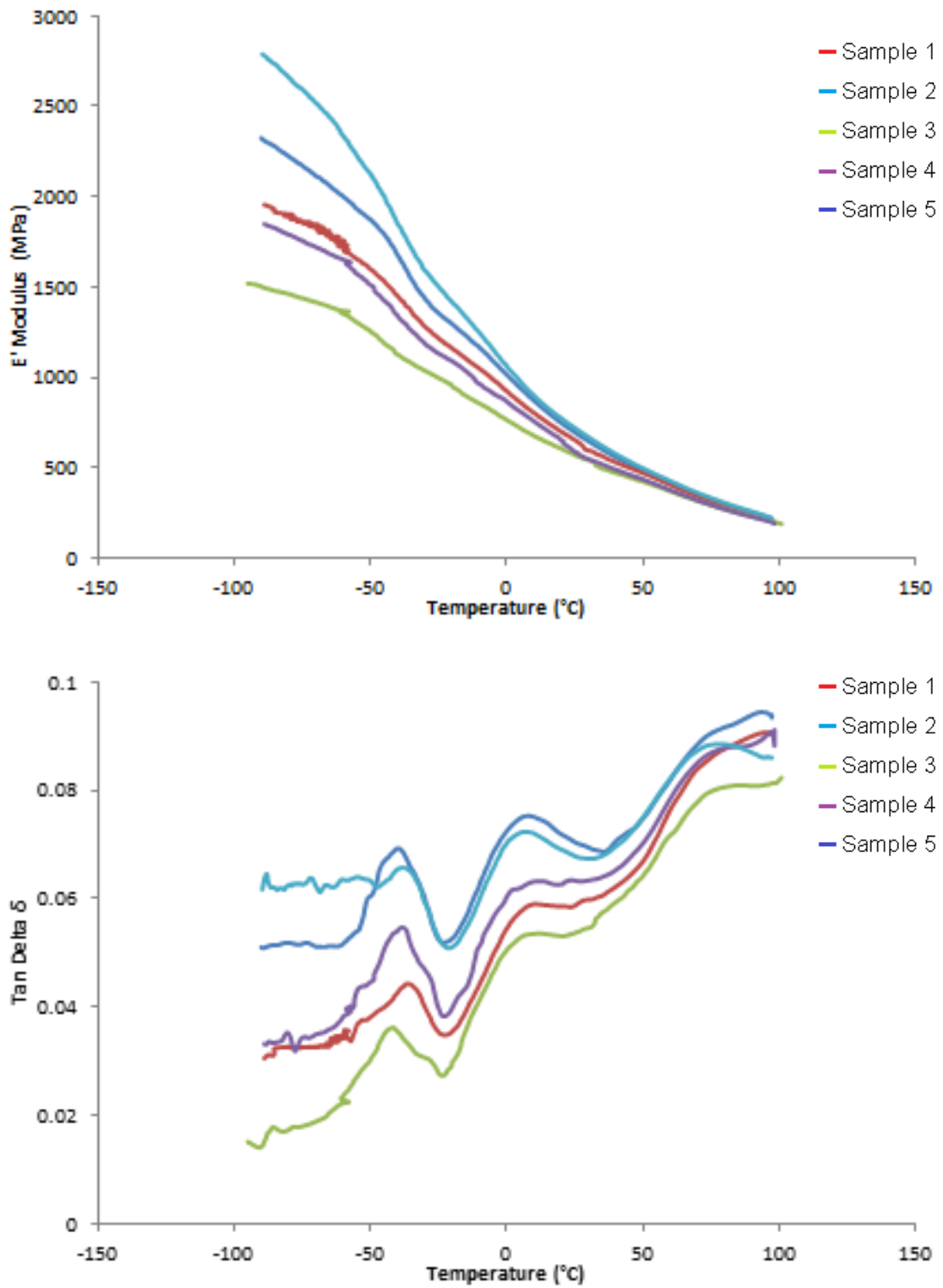


Figure D.1.2. DMA results for the E' Modulus and Tan Delta of Matrix PVDF in tension.

## Appendices

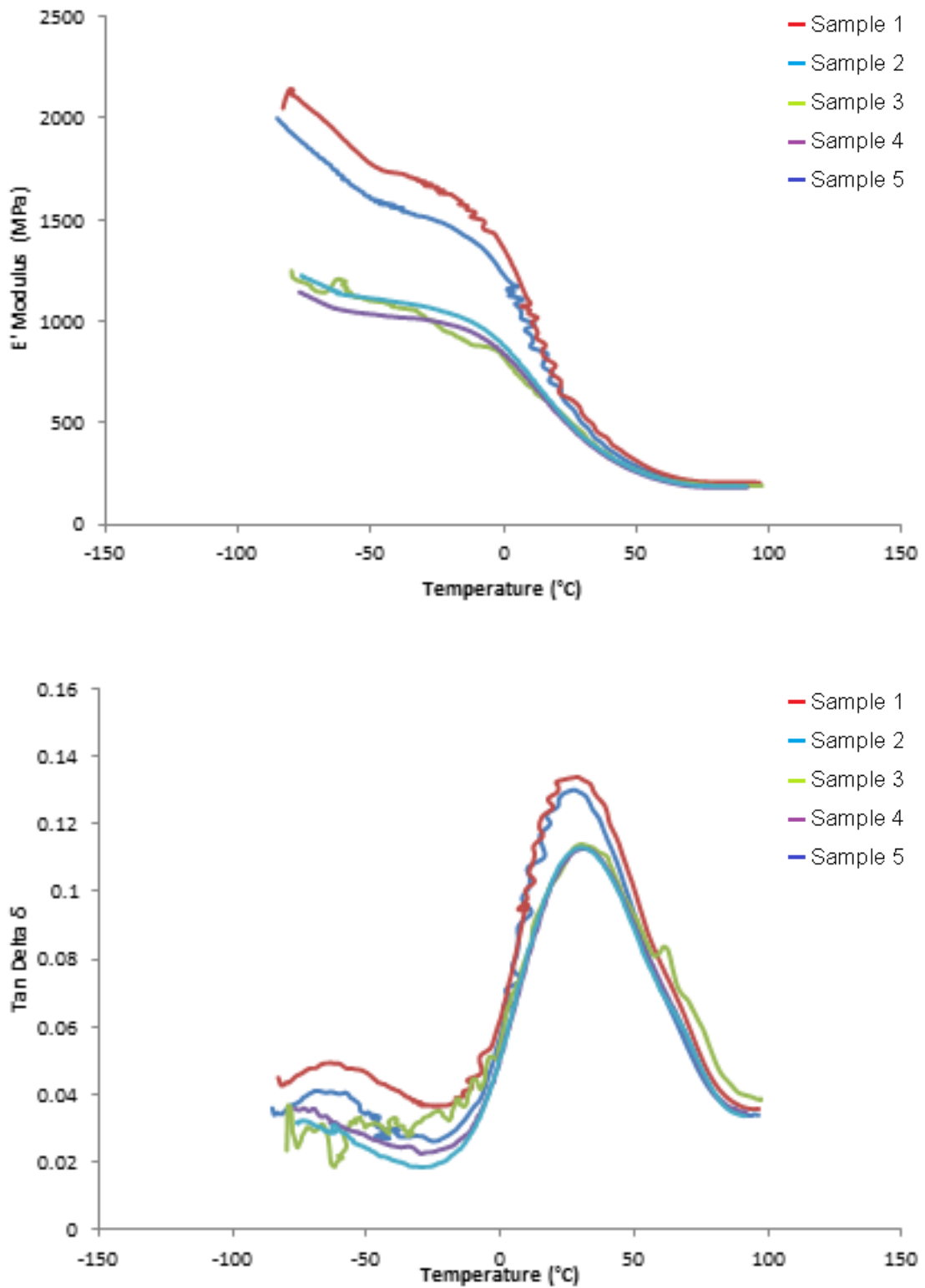


Figure D.1.3. DMA results for the E' Modulus and Tan Delta of Matrix PA11 in tension.

## Appendices

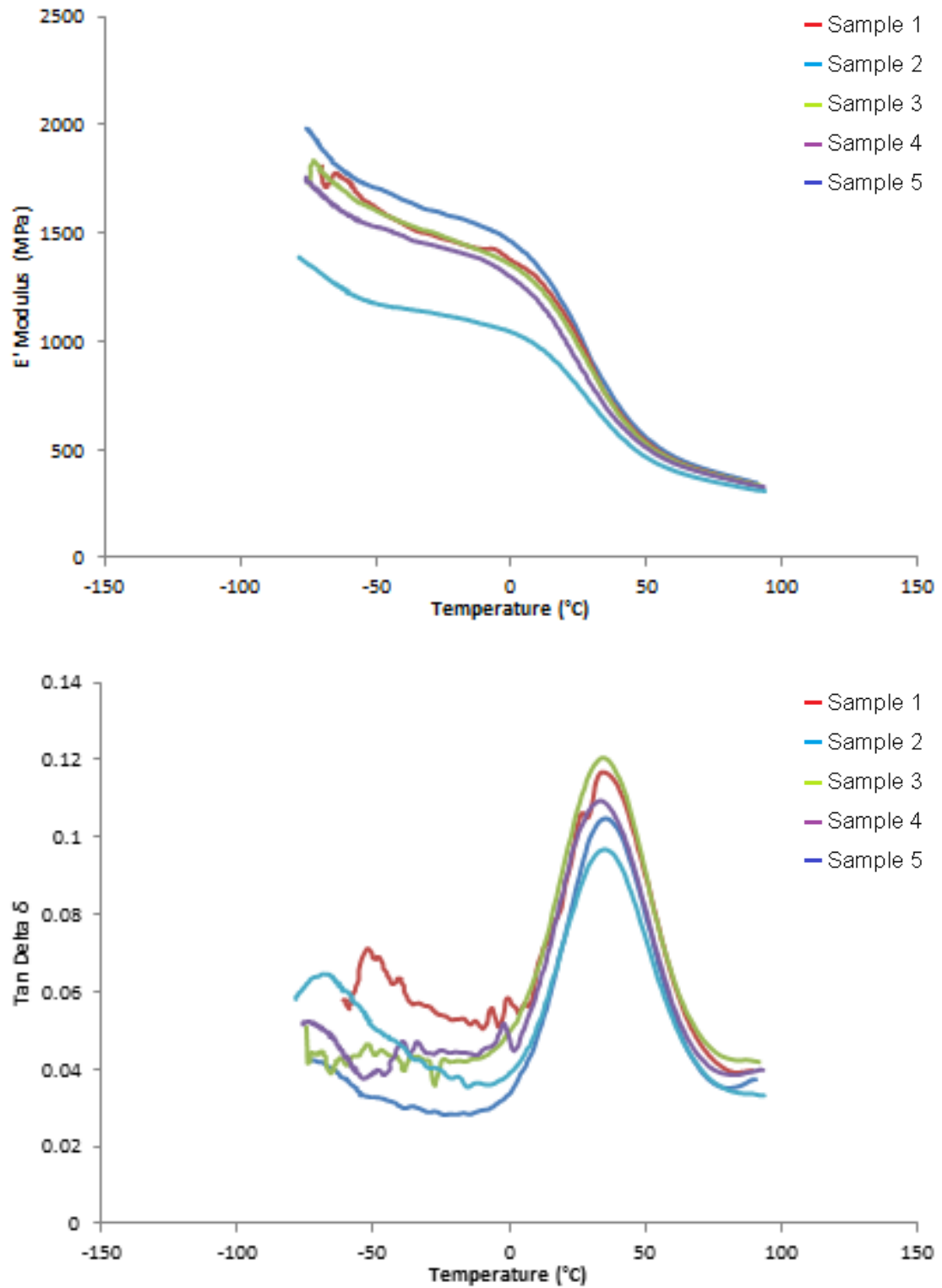


Figure D.1.4. DMA results for the E' Modulus and Tan Delta of Matrix PA12 in tension.

## Appendices

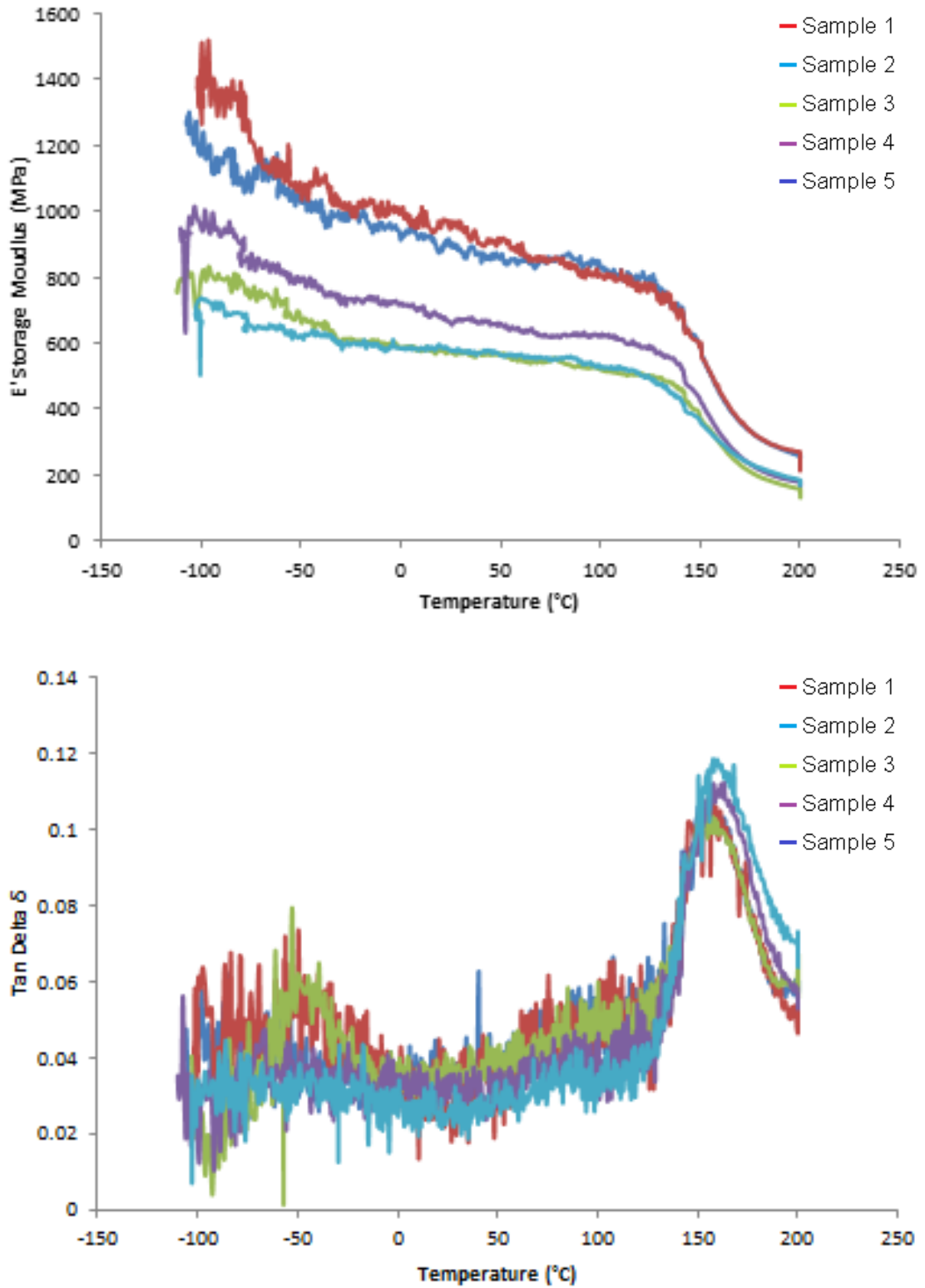


Figure D.1.5. DMA results for the  $E'$  Modulus and Tan Delta of Victrex PEEK150PF in compression.

## Appendices

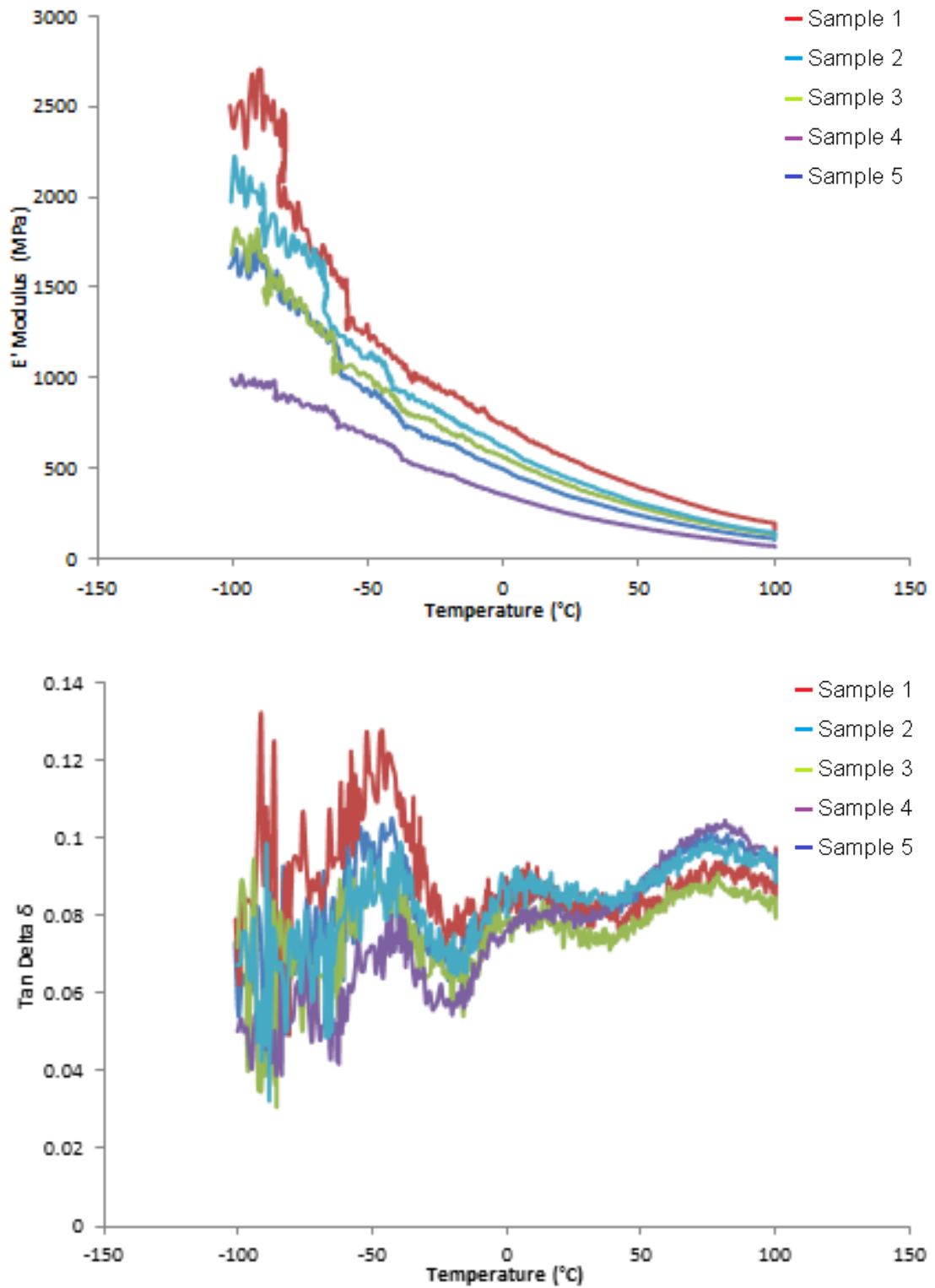
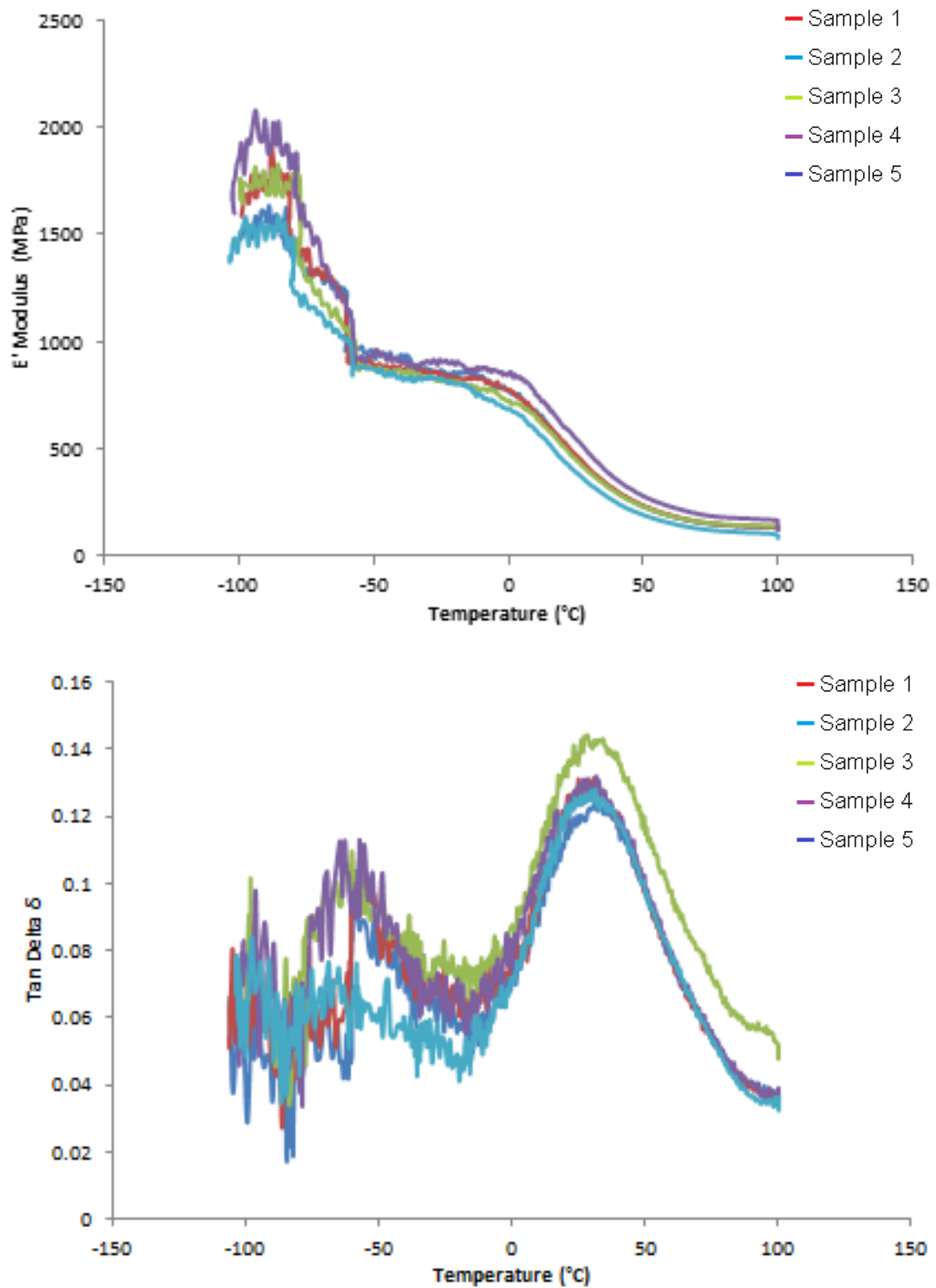


Figure D.1.6. DMA results for the  $E'$  Modulus and Tan Delta of Matrix PVDF in compression.

## Appendices



*Figure D.1.7. DMA results for the E' Modulus and Tan Delta of Matrix PA11 in compression.*

## Appendices

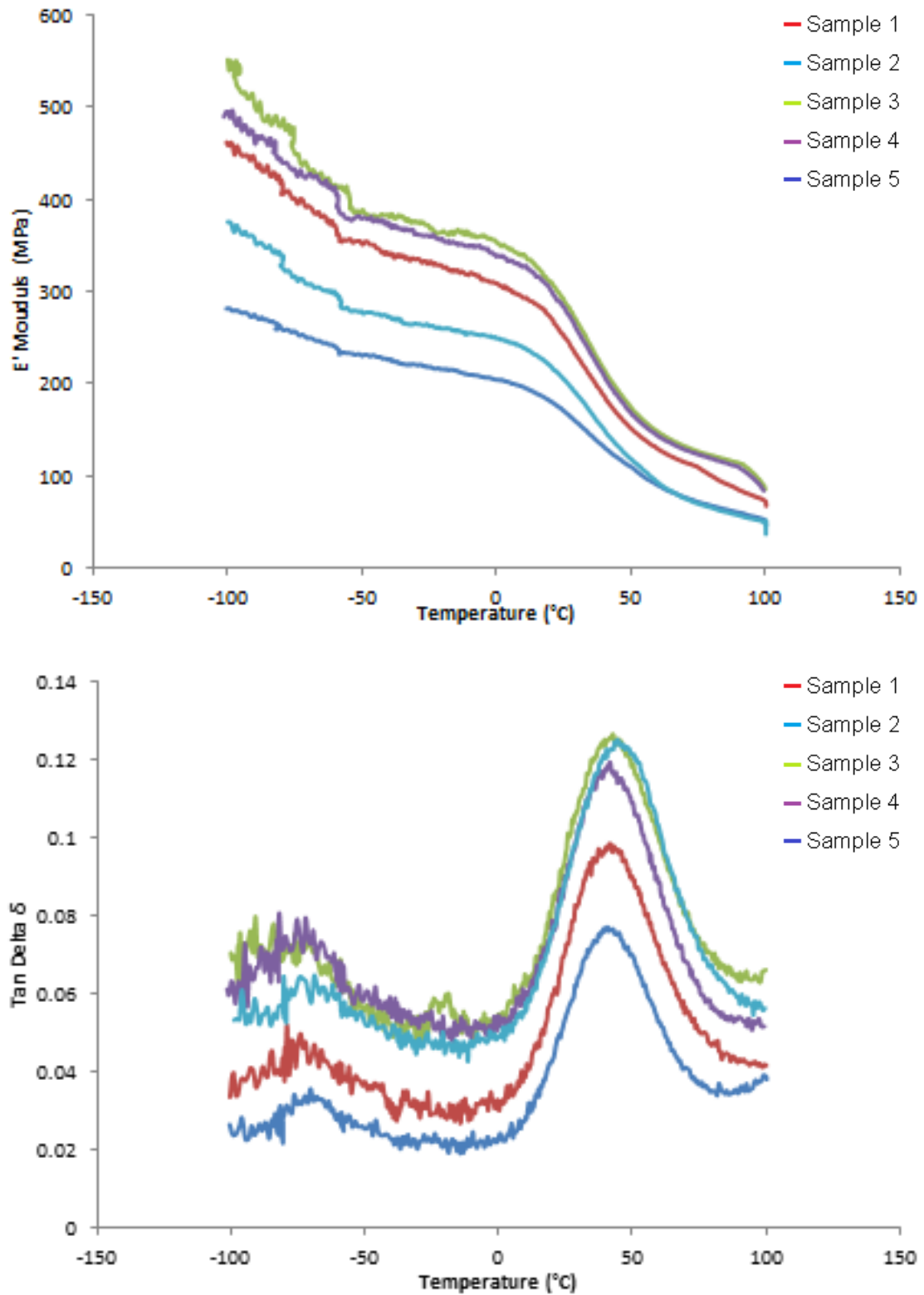


Figure D.1.8. DMA results for the  $E'$  Modulus and Tan Delta of Matrix PA12 in compression.

## D.2. TMA Test Results

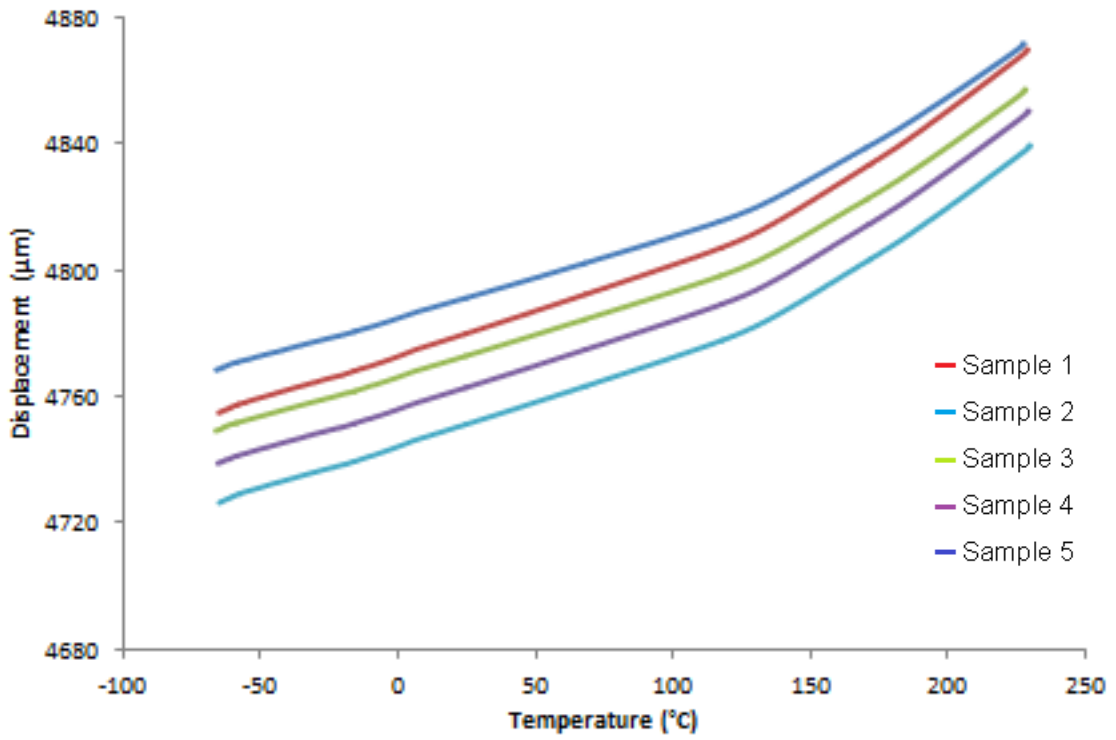


Figure D.2.1. TMA results for Victrex PEEK 150PF.

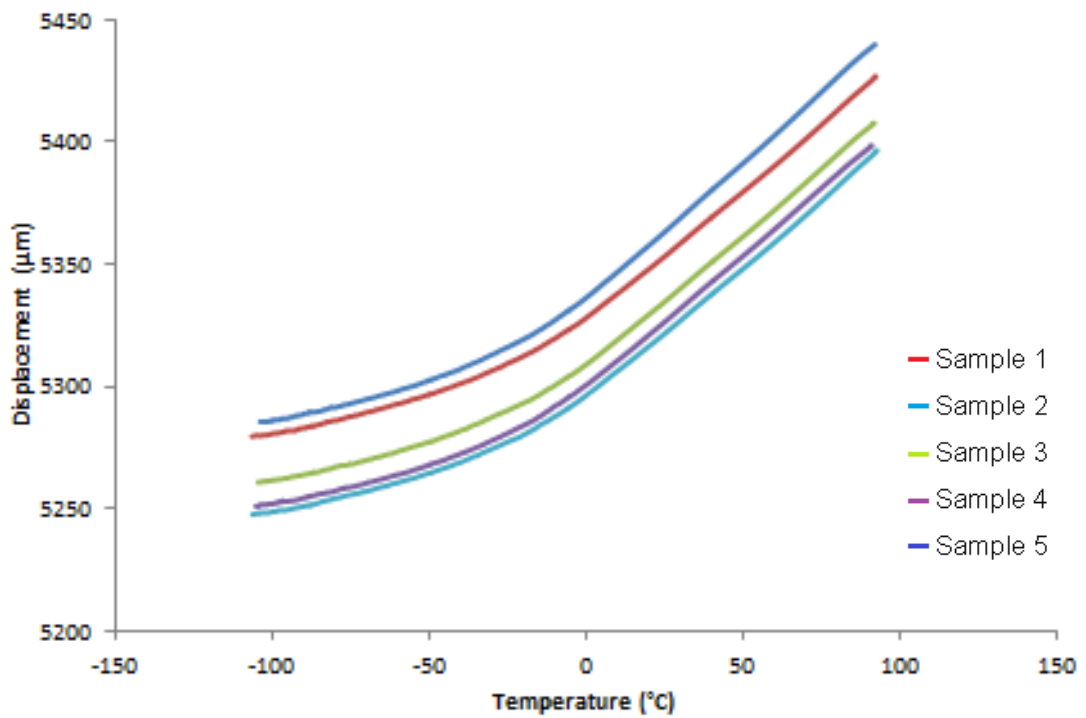


Figure D.2.2. TMA results for Matrix PVDF.

## Appendices

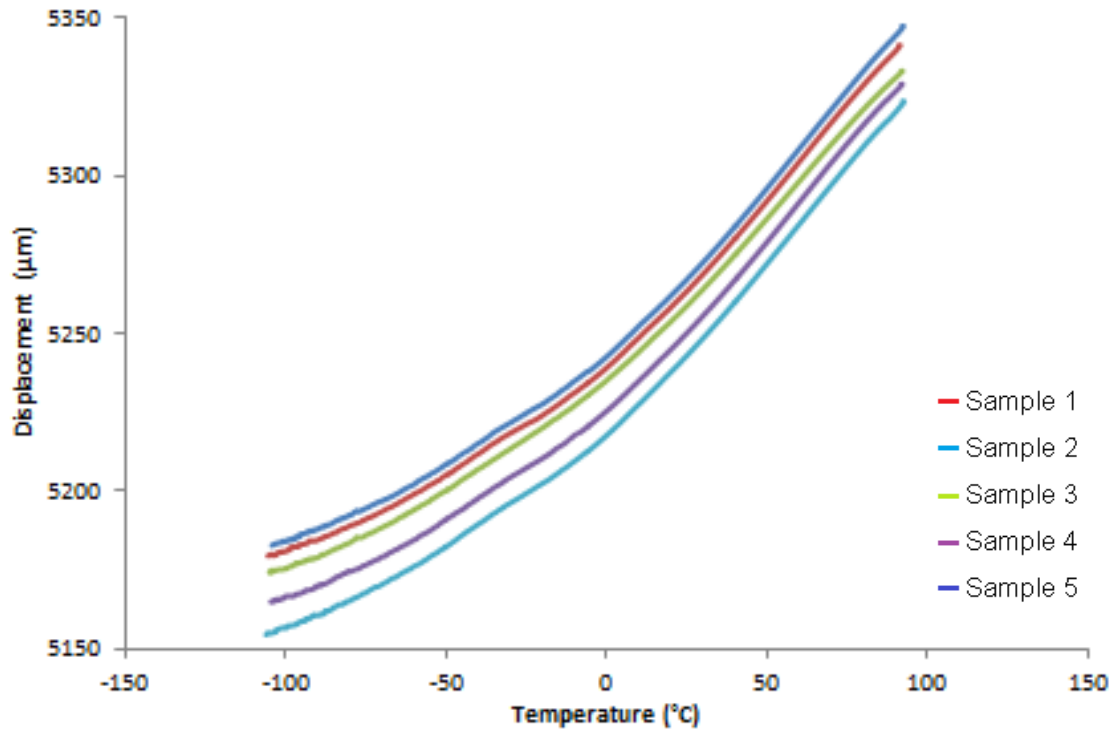


Figure D.2.3. TMA results for Matrix PA11.

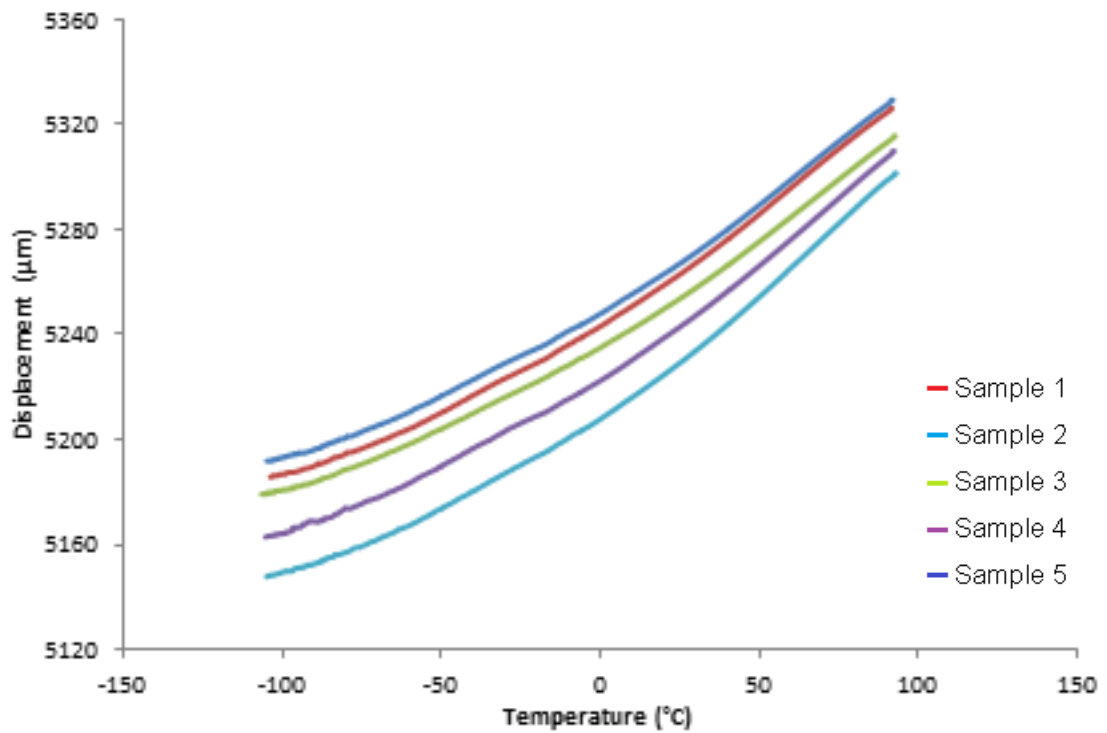


Figure D.2.4. TMA results for Matrix PA12.

# Bibliography

- [1] Y. Mizutani, S. Sugimoto, R. Matsuzaki, and A. Todoroki. Fundamental Study of Integrity Evaluation Method for COPVs by Means of Acoustic Emission Testing. *Journal of Acoustic Emission*, vol. 27, pp. 89-97, 2009.
- [2] H. E. Martinez, J. D. Albright, S. J. D'Amico, J. M. Brewer, and J. C. Melcher. Lessons learned from the design, certification, and operation of the space shuttle integrated main propulsion system (IMPS). *47th AIAA/ASME/SAE/ASEE Joint Propulsion Conference and Exhibit*, California, USA, 2011.
- [3] M. T. Kezirian, K. L. Johnson, and S. L. Phoenix. Composite overwrapped pressure vessels (COPV): Flight rationale for the space shuttle program. *AIAA SPACE 2011 Conference and Exposition*, California, USA, 2011.
- [4] J. C. Thesken, P. L. N. Murthy, S. L. Phoenix, N. Greene, J. L. Palko, J. Eldridge, J. Sutter, R. Saulsberry, and H. Beeson. A theoretical investigation of composite overwrapped pressure vessel mechanics applied to NASA full scale tests. *NASA/TM-2009-215684*, Ohio Aerospace Institute, Ohio, USA, 2009.
- [5] J. B. Chang. On Space Flight Pressure Vessel fracture Control. *Fatigue and Fracture Mechanics: 28th Volume. ASTM STP 1321*. ASTM International, Pennsylvania, USA, 1997.
- [6] W. Tam, M. Hersh, and I. Ballinger. Hybrid propellant tanks for spacecraft and launch vehicles. *39th AIAA Propulsion Conference*, Alabama, USA, 2003.
- [7] G. Kawahara and S. F. McCleskey. Titanium Lined, Carbon Composite Overwrapped Pressure Vessel. *32nd AIAA/ASMA/SAE/ASEE Joint Propulsion Conference*, Florida, USA, 1996.
- [8] P. L. N. Murthy. Reliability of COPV's Accounting for Margin of Safety on Design Burst. *NASA/TM-2012-217638*. NASA Glenn Research Center, Ohio, USA, 2012.

## Bibliography

- [9] W. H. Tam, P. S. Griffin, and A. C. Jackson. Design and manufacture of a composite overwrapped pressurant tank assembly. *38th AIAA/ASME/ASME Joint Propulsion Conference*, Indiana, USA, 2002.
- [10] J. C. Thesken, P. L. N. Murthy, and S. L. Phoenix. Composite Overwrap Pressure Vessels: Mechanics and Stress Rupture Lifting Philosophy, *NASA/TM-2009-215683*, Ohio Aerospace Institute, Ohio, USA, 2009.
- [11] [www.rmtanks.com/images/COPV%20Cross%20Section%20Small.jpg](http://www.rmtanks.com/images/COPV%20Cross%20Section%20Small.jpg) – Accessed 07/09/14.
- [12] <http://www.psi-pci.com/images/Pressuranttanks1.jpg> - Accessed 07/09/14.
- [13] L. M. Alves, P. Santana, H. Moreira, and P. A. F. Martins. Fabrication of metallic liners for composite overwrapped pressure vessels by tube forming. *International Journal of Pressure Vessels and Piping*, vol. 111-112, pp. 36-43, 2013.
- [14] L. M. Alves, M. B. Silva, and P. A. F. Martins. Fabrication of small size seamless reservoirs by tube forming. *International Journal of Pressure Vessels and Piping*, vol. 88, pp. 239-247, 2011.
- [15] H. S. Lee, J. H. Yoon, J. S. Park, and Y. M. Yi. A study on failure characteristic of spherical pressure vessel. *Journal of Materials Processing Technology*, vol. 164-165, pp. 882-888, 2005.
- [16] R. Funck and M. Neitzel. Improved thermoplastic tape winding using laser or direct-flame heating. *Composites Manufacturing*, vol. 6, pp. 189-192, 1995.
- [17] W. J. B. Grove, L. L. Warnet, and R. Akkerman. Critical assessment of the mandrel peel test for fiber reinforced thermoplastic laminates. *Engineering Fracture Mechanics*, vol. 101, pp.96-108, 2013.
- [18] Z. Qureshi, T. Swait, R. Scaife, and H. M. El-Dessouky. In situ consolidation of thermoplastic prepreg tape using automated tape placement technology: Potential and possibilities. *Composites: Part B*, vol. 66, pp. 255-267, 2014.
- [19] R. E. Smylie. NASA development of firefighter protective equipment. *NASA-TM-X-70347*. NASA Manned Spacecraft Center, Texas, USA, 1972.

## Bibliography

- [20] J. T. Hamilton. Technology Utilization Program Report. *NASA-SP-5115*. NASA Technology Utilization Office, Washington D. C., USA, 1974.
- [21] P. B. McLaughlan and M. A. Carson. The NASA firefighter's breathing system program: A status report. *NASA-TM-X-70343*. Lyndon B. Johnson Space Center, Texas, USA, 1974.
- [22] W. B. Wood. NASA firefighters breathing system program report. *NASA TN D-8497*. Lyndon B. Johnson Space Center, Texas, USA, 1977.
- [23] F. J. Hernandez, H. Martinez, A. Ryan, S. Westover, and F. Davies. Selected lessons learned in space shuttle orbiter propulsion and power subsystems. *JSC-SN-24467*. NASA Johnson Space Center, Texas, USA, 2011.
- [24] J. K. Sutter, B. J. Jensen, T. S. Gates, R. J. Morgan, J. C. Thesken, and S. L. Phoenix. Material issues in space shuttle composite overwrapped pressure vessels. *NASA/TM-2006-0020264*, NASA Glenn Research Center, Ohio, USA, 2006.
- [25] [mix.msfc.nasa.gov/IMAGES/HIGH/0102619](http://mix.msfc.nasa.gov/IMAGES/HIGH/0102619) – Accessed 07/09/14.
- [26] L. Grimes-Ledesma, P. L. N. Murthy, S. L. Phoenix, and R. Glaser. A comparison of various stress rupture life models for orbiter composite pressure vessels and confidence intervals. *NASA/TM-2007-214808*. Jet Propulsion Laboratory, California, USA, 2007.
- [27] <http://www.dfrc.nasa.gov/Gallery/Photo/X-33/Large/ED98-44831-4.jpg> - Accessed 27-2-14.
- [28] D. Rohrabacher and B. Gordon. Space Transportation: Status of the X-33 reusable launch vehicle program. *GAO/NSIAD-99-176*, United States General Accounting Office Report to Congressional Requesters, Washington D. C., USA, 1999.
- [29] Letchworth G. X-33 reusable launch vehicle demonstrator, spaceport and range. *AIAA Space Conference*, California, USA, 2011.
- [30] H. K. Rivers, J. G. Sikora, and S. N. Sankaran. Detection of micro-leaks through complex geometries under mechanical load and at cryogenic

## Bibliography

- temperature. *42nd AIAA/ASME/ASCE/AHS/ASC Structures, Structural Dynamics, and Materials Conference and Exhibition*, Washington, USA, 2001.
- [31] R. Goetz, R. Ryan, and A. F. Whitaker. *Final report of the X-33 liquid hydrogen tank test investigation team*. Marshall Space Flight Center, Alabama, USA, 2000.
- [32] P. B. McLaughlan, and L. R. Grimes-Ledesma. Composite Overwrapped Pressure Vessels, A Primer. *NASA/SP-2011-57*, Johnson Space Center, Texas, USA, 2011.
- [33] P. L. N. Murthy, and S. L. Phoenix. Designing of a Fleet-Leader Program for Carbon Composite Overwrapped Pressure Vessels. *NASA/TM-2009-215685*, Glenn Research Center, Ohio, USA, 2009.
- [34] P. Xu, J. Y. Zheng, and P. F. Liu. Finite element analysis of burst pressure of composite hydrogen storage vessels. *Materials and Design*, vol. 30, pp. 2295-2301, 2009.
- [35] J. A. Salem, B. Lerch, J. C. Thesken, J. Sutter, and R. Russell. Strength, fatigue, and fracture toughness of Ti-6AL-4V liner from a composite overwrapped pressure vessel. *NASA/TM-2008-215147*, Glen Research Center, Ohio, USA, 2008.
- [36] D. S. Dawicke and J. C. Lewis. Fracture test methods for plastically responding COPV liners. *50th AIAA/ASME/ASCE/AHS/ASC Structures, Structural Dynamics and Materials Conference*, California, USA, 2009.
- [37] K. L. Carver, R. L. Saulsberry, C. T. Nichols, P. R. Spencer, and R. E. Lucero. Research and development of automated eddy current testing for composite overwrapped pressure vessels. *JSC-CN-27021*, NASA-JSC White Sands Test Facility, New Mexico, USA, 2012.
- [38] M. R. Leifeste. Interrelationship of nondestructive evaluation methodologies applied to testing composite overwrapped pressure vessels. *2nd IAASS Conference - Space Safety in a Global World*, Illinois, USA, 2007.

## Bibliography

- [39] L. M. Alves, T. C. D. Pardal, and P. A. F. Martins. Nosing thin-walled tubes into axisymmetric seamless reservoirs using recyclable mandrels. *Journal of Cleaner Production*, vol. 18, pp. 1740-1749, 2010.
- [40] S. L. Phoenix and M. T. Kezirian. Analysis of potential for titanium liner buckling after proof in a large Kevlar/epoxy COPV. *50th AIAA/ASME/ASCE/AHS/ASC Structures, Structural Dynamics and Materials Conference*, California, USA, 2009.
- [41] J. B. Chang. Implementation Guidelines for ANSI/AIAA S-081: Space Systems Composite Overwrapped Pressure Vessels. SMC-TR-03-07. Space and Missile Systems Center Air Force Space Command, Los Angeles Air Force Base, California, USA, 2003.
- [42] Y. Ni and J. B. Chang. COPV standard requirements implementation issues. *51st AIAA/ASME/ASCE/AHS/ASC Structures, Structural Dynamics and Materials Conference*, Florida, USA, 2010.
- [43] H. T. Yolken and G. A. Matzkanin. Nondestructive evaluation of advanced fiber reinforced polymer matrix composites. *NASA/CR-2009-215566*, Technology Assessment. Texas Research Institute, Texas, USA, 2009.
- [44] J. R. Reeder. Prediction of long-term strength of thermoplastic composites using time-temperature superposition. *NASA/TM-2002-211781*, Langley Research Center, Virginia, USA, 2002.
- [45] L. R. Grimes-Ledesma, S. L. Phoenix, H. Beeson, T. Yoder, and N. Greene. Testing of carbon fibre composite overwrapped pressure vessel stress-rupture lifetime. *ASC/ASTM 21st Annual Technical Conference of the American Society for Composites*, Michigan, USA, 2006.
- [46] N. J. Greene, R. L. Saulsberry, M. R. Leifeste, T. B. Yoder, C. P. Keddy, S. C. Forth, and R. W. Russell. Composite overwrapped pressure vessel (COPV) Stress rupture testing. *4th IAASS Conference: Making Safety Matter*, Alabama, USA, 2010.
- [47] P. L. N. Murthy, S. L. Phoenix, and L. Grimes-Ledesma. Fiber breakage model for carbon composite stress rupture phenomenon: Theoretical development and

## Bibliography

- applications. *NASA/TM-2010-215831*, Glenn Research Center, Ohio, USA, 2010.
- [48] W. Tam, I. Ballinger, and D. E. Jaekle. Review and History of ATK Space Systems Commerce - The Past 15 Years. *Internal Report*, ATK Space Systems, Commerce, California, USA, 2008.
- [49] G. Remy, F. Bénédic, and C. Le Floch. The thermoplastic liner: a breakthrough in high pressure vessel technology. *IAASS COPV Safety and Integrity Workshop*, Rome, Italy, 2008.
- [50] R. J. Crawford and M. P. Kearns. *Practical Guide to Rotational Moulding*. Rapra Technology Ltd., Queen's University Belfast, UK, 2003.
- [51] R.J. Crawford. *Plastics Engineering*. 3rd Edition, Butterworth Heinemann, Oxford, 1998.
- [52] J. P. McEvoy, C. G. Armstrong, and R. J. Crawford. Simulation of the Stretch Blow Molding Process of PET Bottles. *Advances in Polymer Technology*, vol. 17, pp. 339-352, 1998.
- [53] F. Awaja and D. Pavel. Injection stretch blow moulding process of reactive extruded recycled PET and virgin PET blends. *European Polymer Journal*, vol. 41, 2614–2634, 2005.
- [54] Anonymous. Standard general requirements for safe design and operation of pressurized missile and space systems. *MIL-STD-1552A*. Department of Air Force, Washington D.C., USA, 1984.
- [55] T. P. Coffey, T. C. Betterton, M. D. Griffin, J. F. Janni, K. D. Sullivan, P. G. Wilhelm, and L. B. Gray. *Mars Observer Mission Failure Investigation Board Report*. Department of the Navy, Naval Research Laboratory, Washington D.C., USA, 1994.
- [56] O. McSpadden, R. M. Foster, M. Mulgveen, J. J. Zipay, and A. R. Burkey. Fracture Control Requirements for Space Station. International Space Station. *SSP 30558*. National Aeronautics and Space Administration, Space Station Program Office, Lyndon B. Johnson Space Center, Texas, USA, 2001.

## Bibliography

- [57] Anonymous. *Range safety and user requirements manual volume 3 – Launch vehicles, payloads and ground support system requirements*. Air Force Space Command, 2004.
- [58] Anonymous. *Range safety and user requirements manual volume 6 – Launch personnel, equipment, systems, and material operations safety requirements*. Air Force Space Command, 2004.
- [59] M. G. Ryschkewitsch. Fracture control requirements for spaceflight hardware. *NASA-STD-5019*. National Aeronautics and Space Administration, Washington D.C., USA, 2008.
- [60] Anonymous. Space Systems- Composite Overwrapped Pressure Vessels (COPVs). *AIAA-S-081A-2006*. American Institute of Aeronautics and Astronautics (AIAA). Virginia, USA, 2006.
- [61] D. R. Cooke. Commercial Crew Transportation System Certification Requirements for NASA Low Earth Orbit Missions. *ESMD-CCTSCR-12.10*. National Aeronautics and Space Administration, Washington D.C., USA, 2010.
- [62] Anonymous. ISS Crew Transportation and Services Requirements Document. *CCT-REQ-1130-Draft 3.0*. NASA Commercial Crew Program, John F. Kennedy Space Center, Florida, USA, 2011.
- [63] R. J. Crawford and J. L. Throne. *Rotational Molding Technology*. Plastics Design Library, William Andrew Publishing, New York, USA, 2002.
- [64] B. R. Murray, S. B. Leen, and C. M. Ó Brádaigh. Void distributions and permeability prediction for rotationally moulded polymers. 9, vol. 229(5), pp. 403-418, 2015.
- [65] M. Kearns, D. Doyle, P. J. Feerick, C. Daly, and R. J. Crawford. Comparison of cycle times and heating efficiency for direct electrically heated and conventional gas fired rotomoulding machines. *Rotation Magazine*, vol. 13(6), pp. 18-25, 2004.

## Bibliography

- [66] M. McCourt. *Grinding Course Notes. Rotational Moulding Hands-On Training Seminar*. The Polymer Processing Research Centre, Queen's University Belfast, April, 2013.
- [67] J. McDaid and R. J. Crawford. The grinding of polyethylene for use in rotational moulding. *ARM Conference Report*. Vienna, Austria, 1996.
- [68] J. McDaid and R. J. Crawford. Effects of temperature during the grinding of polyethylene powders. *Internal Communication*, The Plastics Development Centre, Newry, Northern Ireland.
- [69] M. A. Rao, and J. L. Throne. Principles of Rotational Moulding. *Polymer Engineering and Science*, vol. 12, iss. 4, pp. 237-264, 1972.
- [70] A. G. Spence, and R. J. Crawford. The effect of processing variables on the formation and removal of bubbles in rotationally molded products. *Polymer Engineering and Science*, vol. 36, iss. 7, pp. 993-1009, 1996.
- [71] G. Gogos. Bubble removal in rotational molding. *Polymer Engineering and Science*, vol. 44, iss. 2, pp. 388-394, 2004.
- [72] P. Y. Kelly. A microscopic examination of rotomoulded polyethylene. DuPont Inc., Toronto, Canada, 1981.
- [73] R. J. Crawford. Recent advances in the manufacture of plastic products by rotomoulding. *Journal of Materials Processing Technology*, vol. 56, pp. 263-271, 1996.
- [74] R. J. Crawford, M. C. Cramez, M. J. Oliveira, and A. G. Spence. The importance of monitoring mold pressure during rotational molding. *Journal of Engineering Manufacture*, vol. 218, pp. 1683-1693, 2004.
- [75] A. G. Spence, and R. J. Crawford. Removal of pinholes and bubbles from rotationally moulded products. *Journal of Engineering Manufacture*, vol. 210, pp. 521-533, 1996.
- [76] G. W. G. McDowell. The reduction of cycle times in the rotational moulding of plastics. *PhD Thesis*. Queen's University Belfast, Northern Ireland, UK, 2002.

## Bibliography

- [77] P. Nugent. Venting of molds for rotational molding. *ARM 20th Annual Spring Conference*. Florida, USA, 1996.
- [78] P. Mitchell. *Tool and Manufacturing Engineers Handbook: Plastic Part Manufacturing*. Volume 8, Chapter 10, 4th Edition, Society of Manufacturing Engineers, 1996.
- [79] R. J. Crawford. *Rotational Moulding of Plastics*. 2nd Edition. John Wiley & Sons Ltd., New York, USA, 1996.
- [80] M. Z. Abdullah, S. Bickerton, D. Bhattacharyya, R. J. Crawford, and E. Harkin-Jones. Rotational molding cycle time reduction using a combination of physical techniques. *Polymer Engineering and Science*, vol. 49, iss. 9, pp. 1846-1854, 2009.
- [81] S. O'Neill and R. J. Crawford. Investigation of Cooling during Rotational Moulding. *ARM Spring Conference Report*, Texas, USA, 1997.
- [82] H. H. Chuah, D. Lin-Vien and U. Soni. Poly(trimethylene terephthalate) molecular weight and Mark – Houwink equation. *Polymer*, vol. 42, pp. 7137-7139, 2001.
- [83] U. Bianchi and A. Peterlin. Intrinsic viscosity of polymers of low molecular weight. *Journal of Polymer Science Part B: Polymer Physics*, vol.6, iss. 10, pp.1759-1772, 1968.
- [84] D. W. van Krevelen and K. te Nijenhuis. *Properties of Polymers: Their Correlation with Chemical Structure; their Numerical Estimation and Prediction from Additive Group Contributions*. 4th Edition, Elsevier B.V. Oxford, UK, 2009.
- [85] A. Hartono. Effect of mechanical treatment temperature on electrical properties and crystallite size of PVDF film. *Advances in Material Physics and Chemistry*, vol. 3, pp. 71-76, 2013.
- [86] M. Nishida. Strain rate dependence of yield condition of polyamide 11. *Dynamic Behaviour of Materials, Volume 1. Conference Proceedings of the Society of Experimental Mechanics Series*. Springer. pp. 121-127, 2014.

## Bibliography

- [87] S. S. Kim. Tribological properties of short glass fiber reinforced polyamide 12 sliding on medium carbon steel. *Wear*, vol. 274-275, pp. 34-42, 2012.
- [88] L. B. Nohara. Processing of high performance composite based on PEEK by aqueous suspension prepregging. *Materials Research*, vol. 13(2), pp. 245-252, 2010.
- [89] L. H. Sperling. *Introduction to Physical Polymer Science*. 4th Edition, John Wiley & Sons Ltd., Pennsylvania, USA, 2006.
- [90] A. Rudin. *Elements of Polymer Science and Engineering*. 2nd Edition, Academic Press, University of Waterloo, San Diego, 1999.
- [91] J. Brandrup, E. H. Immergut, and E. A. Grulke. *Polymer Handbook*. 4th Edition. Wiley-Interscience. 2003.
- [92] S. Kanehashi and K. Nagai. Analysis of dual-mode model parameters for gas sorption in glassy polymers. *Journal of Membrane Science*, vol. 253, pp. 117-138, 2005.
- [93] M. N. Fukuya, K. Senoo, M. Kotera, M. Yoshimoto, and O. Sakata. Enhanced oxygen barrier property of poly(ethylene oxide) films crystallite-oriented by adding cellulose single nanofibers. *Polymer*, vol. 55, pp. 5843-5846, 2014.
- [94] E. A. McGonigle, J. J. Liggat, R. A. Pethrick, S. D. Jenkins, J. H. Daly, and D. Hayward. Permeability of N<sub>2</sub>, Ar, He, O<sub>2</sub> and CO<sub>2</sub> through biaxially oriented polyester films – dependence on free volume. *Polymer*, vol. 42, pp. 2413-2426, 2001.
- [95] A. Eisenberg and J. S. Kim. *Introduction to Ionomers*. John Wiley & Sons Inc. 1998.
- [96] H. Odani and T. Uyeda. Theories of Sorption and Transport in Polymer Membrane. *Polymer Journal*, vol. 23, iss. 5, pp. 467-479, 1991.
- [97] T. Graham. Notice of the singular inflation of a bladder. *Quarterly Journal of Science, Literature and Art*, vol. 28, pp. 88- 89, 1830.

## Bibliography

- [98] T. Graham. On the Law of Diffusion of Gases. *The London and Edinburgh Philosophical Magazine and Journal of Science*, vol. 2, pp. 175- 190, 269-276, 351-358, 1833.
- [99] T. Graham. On the Adsorption and Dialytic Separation of Gases by Colloid Septa. *The London, Edinburgh and Dublin Philosophical Magazine and Journal of Science*, vol. 156, pp. 399- 439, 1866.
- [100] K. Ghosal and B. D. Freeman. Gas separation using polymer membranes: an overview. *Polymers for Advanced Technologies*, vol. 5, pp. 673- 697, 1994.
- [101] I. Blume, E. Smit, M. Wessling, and C. A. Smolders. Diffusion through rubbery and glassy polymer membranes. *Makromolekulare Chemie. Macromolecular Symposia*, vol. 45, iss. 1, pp. 237- 257, 1991.
- [102] G. B. van den Berg and C. A. Smolders. Diffusional phenomena in membrane separation processes. *Journal of Membrane Science*, vol. 73, pp. 103-118, 1992.
- [103] C. J. Cornelli. Physical and gas permeation properties of a series of novel hybrid inorganic composites based on a synthesized fluorinated polyimide. *PhD Thesis*. Virginia Polytechnic Institute, Virginia, USA, 2000.
- [104] S. Kim, K. T. Woo, J. M. Lee, J. R. Quay, M. K. Murphy, and Y. M. Lee. Gas Sorption, Diffusion and Permeation in Thermally rearranged poly(benzoxazole-co-imide) membranes. *Journal of Membrane Science*, vol. 453, pp. 556- 565, 2014.
- [105] R.W. Baker. *Membrane Technology and Applications*. 2nd Edition, John Wiley & Sons Ltd., New Jersey, USA, 2004.
- [106] J. G. Wijmans and R. W. Baker. The solution-diffusion model: a review. *Journal of Membrane Science*, vol. 107, pp. 1- 21, 1995.
- [107] T. W. Pechar. Fabrication and Characterisation of Polyimide-based Mixed Matrix Membranes for Gas Separation. *PhD Thesis*. Virginia Polytechnic Institute, Virginia, USA, 2004.

## Bibliography

- [108] A. E. Fick. Ueber Diffusion. *Annalen der Physik*, vol. 170, iss. 1, pp. 59–86, 1855.
- [109] J.B. Fourier. *Théorie analytique de la chaleur*. Chez Firmin Didot, Père et Fils, Paris, France, 1822.
- [110] J. Crank. *The Mathematics of Diffusion*, 2nd Edition, Brunel University, Clarendon Press, Oxford, England, 1975.
- [111] J. Comyn. *Polymer Permeability*. Chapman and Hall Inc., London, UK. 1985.
- [112] H. A. Daynes. The process of diffusion through a rubber membrane. *Philosophical Transactions of the Royal Society of London*, vol. 97, iss. 685, pp. 286-307, 1920.
- [113] M. H. Cohen and D. Turnbull. Molecular transport in liquids and glasses. *The Journal of Chemical Physics*, vol. 31, iss. 5, pp. 1164-1169, 1959.
- [114] R. J. Pace, A. Datyner. Statistical mechanical model for diffusion of simple penetrants in polymers. I. Theory. *Journal of Polymer Science*, vol. 17, pp. 437-451, 1979.
- [115] H. Fujita. Diffusion in polymer diluent-systems. *Advances in Polymer Science*, vol. 3, pp. 1-47, 1961.
- [116] J. S. Vrentas and J. L. Duda. Diffusion in polymer-solvent systems. I. Re-examination of the free-volume theory. *Journal of Polymer Science*, vol. 15, pp. 403-416, 1977.
- [117] P. Neogi. *Diffusion in Polymers*, Marcel Dekker Inc., New York, USA. 1996.
- [118] S. Kim. High permeability/high diffusivity mixed matrix membranes for gas separations. *PhD Thesis*, Virginia Polytechnic Institute, Virginia, USA, 2007.
- [119] E. Smit, M. H. V. Mulder, C. A. Smolders, H. Karrenbeld, J. van Eerden, and D. Feil. Modelling of the diffusion of carbon dioxide in polyimide matrices by computer simulation. *Journal of Membrane Science*, vol. 73, pp. 247-257, 1992.

## Bibliography

- [120] N. Stadie. Synthesis and thermodynamic studies of physisorptive energy storage materials. *PhD Thesis*, California Institute of Technology, California, USA, 2013.
- [121] D. Schultheiß. Permeation barrier for lightweight liquid hydrogen tanks. *PhD Thesis*, Universität Augsburg, Augsburg, Germany, 2007.
- [122] E. Magner. Porosimetry and Particle Size Analysis. *Course Notes for Advanced Material Characterisation Techniques*, University of Limerick, Limerick, Ireland, 2012.
- [123] D. R. Paul. Fundamentals of Transport Phenomena in Polymer Membranes. *Comprehensive Membrane Science and Engineering*, vol. 1, pp. 75-90, 2010.
- [124] K. Tanaka, H. Kita, M. Okano, and K. Okamoto, Permeability and permselectivity of gases in fluorinated and non-fluorinated polyimides. *Polymer*, vol. 33, iss. 3, pp. 585-592, 1992.
- [125] K. Okamoto, K. Tanaka, H. Kita, M. Ishida, M. Kakimoto, and Y. Imai. Gas permeability and permselectivity of polyimides prepared from 4,4'-diaminotriphenylamine. *Polymer Journal*, vol. 24, iss. 5, pp. 451-457, 1992.
- [126] K. Tanaka, M. Okano, H. Toshino, H. Kita, and K. Okamoto. Effect of methyl substituents on permeability and permselectivity of gases in polyimides prepared from methyl-substituted phenylenediamines. *Journal of Polymer Science*, vol. 30, pp. 907-914, 1992.
- [127] M. H. Klopffer and B. Flaconnéche. Transport Properties of Gases in Polymers: Bibliographic Review, *Oil & Gas Science Technology*, vol. 56, iss. 3, pp. 223-244, 2001.
- [128] R. E. Kesting and A. K. Fritzsche. *Polymeric gas separation membranes*. Wiley Interscience, New York, 1993.
- [129] E.C. Suloff. Sorption behaviour of an aliphatic series of aldehydes in the presence of poly(ethylene terephthalate) blends containing aldehyde scavenging effects. *PhD Thesis*, Virginia Polytechnic Institute, Virginia, USA, 2002.

## Bibliography

- [130] J. C. Maxwell. *A Treatise on Electricity and Magnetism. Vol. I.* Macmillan and Co., London, UK, 1873.
- [131] J. C. Maxwell. *A Treatise on Electricity and Magnetism. Vol. II.* Dover Publications, Inc., New York, USA, 1954.
- [132] D. A. G. Bruggeman. Berechnung verschiedener physikalischer konstanten vonheterogenen substanzen, *Annalen der Physik*, vol. 24, pp. 636–679, 1935.
- [133] R. Pal. On the Lewis-Nielsen model for thermal/electrical conductivity of composites. *Composites: Part A*, vol. 39, pp. 718-726, 2008.
- [134] T. B. Lewis and L. E. Nielsen. Dynamic mechanical properties of particulate-filled composites. *Journal of Applied Polymer Science*, vol. 14, iss. 6, pp. 1449-1471, 1970.
- [135] L. Nielsen. Thermal conductivity of particulate filled composites. *Journal of Applied Polymer Science*, vol. 17, pp. 3819-3820, 1973.
- [136] J. D. Felske. Effective thermal conductivity of composite spheres in a continuous medium with contact resistance. *International Journal of Heat and Mass Transfer*, vol. 47, pp. 3453-3461, 2004.
- [137] R. Pal. Thermal conductivity of three-component composites of core-shell particles. *Materials Science and Engineering A*, vol. 498, pp. 135-141, 2008.
- [138] E. E. Gonzo. Estimating correlations for the effective thermal conductivity of granular materials. *Chemical Engineering Journal*, vol. 90, pp. 299-302, 2002.
- [139] J. Wang, J. K. Carson, M. F. North, and D. J. Cleland. A new approach to modelling the effective thermal conductivity of heterogeneous materials. *International Journal of Heat and Mass Transfer*, vol. 49, pp. 3075-3083, 2006.
- [140] T. T. Moore and W. J. Koros. Non-ideal effects in organic-inorganic materials for gas separation membranes. *Journal of Molecular Structure*, vol. 739, pp. 87-98, 2005.

## Bibliography

- [141] Y. Li, T. Chung, C. Cao, and S. Kulprathipanja. The effects of polymer chain rigidification, zeolite pore size and pore blockage on polyethersulfone (PES)-zeolite A mixed matrix membranes. *Journal of Membrane Science*, vol. 260, pp. 45-55, 2005.
- [142] B. Shimekit, H. Mukhtar, and T. Murugesan. Prediction of the relative permeability of gases in mixed matrix membranes. *Journal of Membrane Science*, vol. 373, pp. 152-159, 2011.
- [143] M. A. Aroon, A. F. Ismail, T. Matsuura, and M. M. Montazer-Rahmati. Performance studies of mixed matrix membranes for gas separation: A review. *Separation and Purification Technology*, vol. 75, pp. 229-242, 2010.
- [144] R. Pal. Permeation models for mixed matrix membranes. *Journal of Colloid and Interface Science*, vol. 317, pp. 191-198, 2008.
- [145] S. A. Hashemifard, A. F. Ismail, and T. Matsuura. Prediction of gas permeability in mixed matrix membranes using theoretical models. *Journal of Membrane Science*, vol. 347, pp. 53-61, 2010.
- [146] R. Mahajan and W. J. Koros. Mixed matrix membrane materials with glassy polymers. Part 1. *Polymer Engineering and Science*, vol. 42, iss. 7, pp. 1420-1431, 2002.
- [147] R. Mahajan and W. J. Koros. Factors controlling successful formation of mixed-matrix gas separation materials. *Industrial Engineering and Chemical Research*, vol. 39, pp. 2692-2696, 2000.
- [148] E. E. Gonzo, M. L. Parentis, and J. C. Gottifredi. Estimating models for predicting effective permeability of mixed matrix membranes. *Journal of Membrane Science*, vol. 277, pp. 46-54, 2006.
- [149] R. H. B. Bouma, A. Checchetti, G. Chidichimo, and E. Drioli. Permeation through a heterogeneous membrane: the effect of the dispersed phase. *Journal of Membrane Science*, vol. 128, pp. 141-149, 1997.

## Bibliography

- [150] S. A. Hashemifard, A. F. Ismail, and T. Matsuura. A new theoretical gas permeability model using resistance modeling for mixed matrix membrane systems. *Journal of Membrane Science*, vol. 350, pp. 259-268, 2010.
- [151] C. Park, W. H. Jo, H. C. Park, and Y. S. Kang. Morphological effect of dispersed phase on gas permeation properties through heterophase polymer membrane: theoretical and experimental approaches. *Polymer*, vol. 41, pp. 1765-1771, 2000.
- [152] K. S. Kwan, C. N. P. Subramaniam, and T. C. Ward. Effect of penetrant size and shape on its transport through a thermoset adhesive: I. n-alkanes. *Polymer*, vol. 44, pp. 3061-3069, 2003.
- [153] K. S. Kwan, C. N. P. Subramaniam, and T. C. Ward. Effect of penetrant size, shape and chemical nature on its transport through a thermoset adhesive: II. Esters. *Polymer*, vol. 44, pp. 3071-3083, 2003.
- [154] S. C. George and S. Thomas. Transport phenomena through polymeric systems. *Progress in Polymer Science*, vol. 26, pp. 985-1017, 2001.
- [155] H. Fujita, A. Kishimoto, and K. Matsumoto. Concentration and temperature dependence of diffusion coefficients for systems polymethyl acrylate and n-alkyl acetates. *Transactions of the Faraday Society*, vol. 56, pp. 424-437, 1960.
- [156] S. Choi and B. V. Sankar. Gas permeability of various graphite/epoxy composite laminates for cryogenic storage system. *Composites: Part B*, vol. 39, pp. 782-791, 2008.
- [157] A. T. Nettles. Permeability Testing of Composite Material and Adhesive Bonds for the DC-XA Composite Feedline Program. *NASA TM-108483*, Marshall Space Flight Center, Alabama, USA, 1995.
- [158] D. R. Lide. *CRC Handbook of Chemistry and Physics*. Internet Version 2005. CRC Press. Florida, USA. 2005.
- [159] J. Humpenodör. Gaspermeation von Faserverbunden mit Polymermatrices\*. *PhD Thesis*. Universität Karlsruhe, Karlsruhe, Germany, 1997.

## Bibliography

- [160] M. Galizia, Z. P. Smith, G. C. Sarti, B. D. Freeman, and D. R. Paul. Predictive calculation of hydrogen and helium solubility in glassy and rubbery polymers. *Journal of Membrane Science*, vol. 475, pp. 110-121, 2015.
- [161] M. J. Robinson, J. D. Eichinger, and S. E. Johnson. Hydrogen permeability requirements and testing for reusable launch vehicle tanks. *43rd AIAA/ASCE/AHS/ASC Structures, Structural Dynamics, and Materials Conference*. Colorado, USA, 2002.
- [162] M. J. Robinson. Determination of allowable hydrogen permeation rates for launch vehicle propellant tanks. *Journal of Spacecraft and Rockets*, vol. 45, iss. 1, pp. 82-89, 2008.
- [163] N. Cohen. Flammability and Explosion Limits of H<sub>2</sub> and H<sub>2</sub>/CO: A Literature Review. *AD-A264 896*. Space and Missile Systems Center Air Force Material Command, Los Angeles Air Force Base, California, USA, 1992.
- [164] V. Schroeder and K. Holtappels. Explosion characteristics of hydrogen-air and hydrogen-oxygen mixtures at elevated pressures. *International Conference of Hydrogen Safety*, Pisa, Italy, 2005.
- [165] S. Woods, S. McDougle, W. Stewart, L. Starritt, and M. Maes. Hydrogen hazards assessment protocol for components and systems. *WSTF-IR-1117-001-08*. Lyndon B. Johnson Space Center, White Sands Test Facility, New Mexico, USA, 2008.
- [166] E. H. Stokes. Hydrogen permeability of a polymer based composite tank material under tetra-axial strain. *5th Conference on Aerospace Materials, Processes and Environmental Technology*. Von Braun Center, Alabama, USA, 2002.
- [167] A. T. Nettles. Permeability testing of impacted composite laminate for use on reusable launch vehicles. *NASA/TM-2001-210799*. Marshall Space Flight Center, Alabama, USA. 2001.
- [168] H. Kumazawa, T. Aoki, and I. Susuki. Influence of Stacking Sequence on Leakage Characteristics through CFRP composite laminates. *Composites Science and Technology*, vol. 66, pp. 2107-2115, 2006.

## Bibliography

- [169] H. Kumazawa, H. Hayashi, I. Susuki, and T. Utsunomiya. Damage and Permeability Evolution in CFRP Cross-Ply Laminates. *Composites Structures*, vol. 76, pp. 73-81, 2006.
- [170] D. Grogan, C. M. Ó Brádaigh, and S. B. Leen. A combined XFEM and cohesive zone model for composite laminate microcracking and permeability. *Composite Structures*, vol. 120, pp. 246-261, 2015.
- [171] B. W. Grimsley, R. J. Cano N. J. Johnson, A. C. Loos, and W. M. McMahon. Hybrid composites for LH2 fuel tank structure. *Technical Report 20040086019*. NASA Langley research Center, Virginia, USA. 2001.
- [172] H. M. Herring. Characterisation of thin film polymers through dynamic mechanical analysis and permeation. *NASA/CR-2003-212422*. Lockheed Martin Engineering & Sciences, Virginia, USA, 2003.
- [173] B. Flaconnéche, J. Martin, and M. H. Klopffer. Permeability, Diffusion and Solubility of Gases in Polyethylene, Polyamide 11 and Poly(vinylidene fluoride), *Oil & Gas Science Technology*, vol. 56, iss. 3, pp. 261-278, 2001.
- [174] C. W. Extrand and L. Monson. Gas permeation resistance of a perfluoroalkoxy-tetrafluoroethylene copolymer. *Journal of Applied Polymer Science*, vol. 100, pp. 2122-2125, 2006.
- [175] L. Monson, S. I. Moon, and C. W. Extrand. Gas permeation resistance of various grades of perfluoroalkoxy-polytetrafluoroethylene copolymers. *Journal of Applied Polymer Science*, vol. 111, pp. 141-147, 2009.
- [176] L. Monson, S. I. Moon, and C. W. Extrand. Permeation resistance of poly(ether ether ketone) to hydrogen, nitrogen and oxygen gases. *Journal of Applied Polymer Science*, vol. 127, iss. 3, pp. 1637-1642, 2013.
- [177] N. Amanat, A. F. Nicoll, A. J. Ruys, D. R. McKenzie, and N. L. James. Gas permeability reduction in PEEK film: Comparison of tetrahedral amorphous carbon and titanium nanofilm coatings. *Journal of Membrane Science*, vol. 378, pp. 265–271, 2011.

## Bibliography

- [178] F. Benedic, J. P. Leard, and C. Lefloch. Helium high pressure tanks at EADS space transportation new technology with thermoplastic liner. *1<sup>st</sup> Symposium on Potentially Disruptive Technologies and their Impact in Space Programs*, Marseille, France, 2005.
- [179] G. Remy, F. Benedic, and C. Lefloch. The thermoplastic liner: a breakthrough in high pressure vessels technology. *IAASS COPV Safety and Integrity Workshop*, Rome, Italy, 2008.
- [180] A. Mataloni, F. Betti, M. Biagioni, and M. Motta. Elastomeric liner for cryogenic application. *FIAT AVIO-Comprensorio NTEESA 10007 Iss.:2.*, Italy, 2005.
- [181] S. Claudel, A. Repellin, L. Jageunaud, D. Lacour, A. Bergerot, and B. Defoort. Advanced and affordable thermoplastic based composite tank for cryogenic fluid storage. *SAMPE Conference*, Washington State Convention Center, Seattle, USA, 2010.
- [182] C.M. Stokes-Griffen, P. Compston, T. I. Matuszyk, and M. J. Cardew-Hall. Thermal modelling of the laser-assisted thermoplastic tape placement process. *Journal of Thermoplastic Composite Materials*, pp. 1-18, 2013.
- [183] A. J. Comer, D. Ray, W. O. Obande, D. Jones, J. Lyons, I. Rosca, and R. M. O'Higgins, M. A. McCarthy. Mechanical characterisation of carbon fibre-PEEK manufactured by laser-assisted automated-tape-placement and autoclave. *Composites: Part A*, vol. 69, pp. 10-20, 2015.
- [184] D. Ray, A. J. Comer, J. Lyons, W. Obande, D. Jones, R. M. O'Higgins, and M. A. McCarthy. Fracture toughness of carbon fiber/polyether ether ketone composites manufactured by autoclave and laser-assisted automated tape placement. *Journal of Applied Polymer Science*, vol. 132, iss. 11, 41643 (pp. 1-10), 2015.
- [185] M. A. Khan, P. Mitschang, and R. Schledjewski. Identification of some optimal parameters to achieve higher laminate quality through tape placement process. *Advances in Polymer Technology*, vol. 29, iss. 2, pp. 98-111, 2010.

## Bibliography

- [186] Z. Qureshi, T. Swait, R. Scaife, and H. M. El-Dessouky. In situ consolidation of thermoplastic prepreg tape using automated tape placement technology: potential and possibilities. *Composites: Part B*, vol. 66, pp. 255-267, 2014.
- [187] R. Lichtinger, P. Hörmann, D. Stelzl, and R. Hinterhölzl. The effects of heat input on adjacent paths during automated fibre placement. *Composites: Part A*, vol. 68, pp. 387-397, 2015.
- [188] R. Funck, and M. Neitzel. Improved thermoplastic tape winding using laser or direct-flame heating. *Composites Manufacturing*, vol. 6, pp. 189-192, 1995.
- [189] C.M. Pistor, and S.I. Güçeri. Crystallinity of on-line consolidated thermoplastic composites. *Journal of Composite Materials*, vol. 33, iss. 4, pp. 306-324, 1999.
- [190] W. Grouve. Weld strength of laser-assisted tape-placed thermoplastic composites. *PhD Thesis*. University of Twente, Enschede, the Netherlands, 2012.
- [191] C. M. Stokes-Griffen and P. Compston. Optical characterisation and modelling for oblique near-infrared laser heating of carbon fibre reinforced thermoplastic composites. *Optics and Lasers in Engineering*, vol. 72, pp. 1-11, 2015.
- [192] C. M. Stokes-Griffen and P. Compston. A combined optical-thermal model for near-infrared laser heating of thermoplastic composites in an automated tape placement process. *Composites: Part A*, vol. 75, pp. 104-115, 2015.
- [193] Victrex PEEK 150P Datasheet. <http://www.victrex.com/en/datasheets> - Accessed 05/03/15.
- [194] J. Chu and M. Schultz. The influence of microstructure on the failure behaviour of PEEK. *Journal of Materials Science*, vol. 25, iss. 8, pp. 3746-3752, 1990.
- [195] B. S. Hsiao and B. B. Sauer. Glass transition, crystallization, and morphology relationships in miscible poly(aryl ether ketones) and poly(ether imide) blends. *Journal of Polymer Science Part B: Polymer Physics*, vol. 31, iss. 8, pp. 901-915, 1993.

## Bibliography

- [196] Victrex PEEK 150PF Datasheet. <http://www.victrex.com/en/datasheets> - Accessed 05/03/15.
- [197] Evonik VESTAKEEP 1000P Datasheet. [http://industrial.vestakeep.com/sites/dc/Downloadcenter/Evonik/Product/VESTAKEEP/en/product-information/VESTAKEEP\\_1000P\\_Product\\_information.pdf](http://industrial.vestakeep.com/sites/dc/Downloadcenter/Evonik/Product/VESTAKEEP/en/product-information/VESTAKEEP_1000P_Product_information.pdf) - Accessed 05/03/15.
- [198] Evonik Manual “VESTAKEEP<sup>®</sup> PEEK-Polyether Ether Ketone Compounds” - <http://corporate.evonik.com/en/Pages/default.aspx> - Accessed 08/08/16.
- [199] Evonik Manual “VESTAKEEP<sup>®</sup> PEEK-Polyether Ether Ketone Powders” - <http://corporate.evonik.com/en/Pages/default.aspx> - Accessed 08/08/16.
- [200] Evonik VESTAKEEP 2000P Datasheet. [http://industrial.vestakeep.com/sites/dc/Downloadcenter/Evonik/Product/VESTAKEEP/en/product-information/VESTAKEEP\\_2000P\\_Product\\_information.pdf](http://industrial.vestakeep.com/sites/dc/Downloadcenter/Evonik/Product/VESTAKEEP/en/product-information/VESTAKEEP_2000P_Product_information.pdf) - Accessed 05/03/15.
- [201] C. Harper. *Handbook of Plastics Technologies*. The McGraw Hill Companies Inc., New York, USA, 2006.
- [202] C. M. Gilmore. *Materials Science and Engineering Properties*. Cengage Learning, Connecticut, USA, 2015.
- [203] Matrix Polymers REVOLVE Rilsan PA11. <http://www.matrixpolymers.com/Content/Resources/files/publications/Revolve%20Roto%2011.pdf> - Accessed 05/03/15.
- [204] Matrix Polymers REVOLVE PA12 ARVO 950 TLD. <http://www.matrixpolymers.com/Content/Resources/files/publications/ARVO%20950%20TLD.pdf> - Accessed 05/03/15.
- [205] Matrix Polymers Explore PVDF. <http://www.matrixpolymers.com/Content/Resources/files/publications/Explore%20PVDF.pdf> - Accessed 05/03/15.
- [206] ENSIGNER TECAVINYL PVC Product Sheet. <http://docs-europe.electrocomponents.com/webdocs/0510/0900766b80510f13.pdf> - Accessed 07/04/15.

## Bibliography

- [207] Suprem T product sheet. Delivered with materials. Unknown Availability.
- [208] A. Lystrup and T. L. Anderson. Autoclave consolidation of fibre composites with a high temperature thermoplastic matrix. *Journal of Material Processing Technology*, vol. 77, pp. 80-85, 1998.
- [209] I. Fernández., F. Blas., and M. Frövel. Autoclave forming of thermoplastic composite parts. *Journal of Material Processing Technology*, vol. 143-144, pp. 266-269, 2003.
- [210] “ASTM D1921-12. Particle Size (Sieve Analysis) of Plastic Materials,” *ASTM International*, West Conshohocken, PA, USA, 2006, DOI: 10.1520/D1921-12.
- [211] A. A. Aissa, C. Duchesne, and D. Rodrigue. Polymer powders mixing part I: Mixing characterization in rotating cylinders. *Chemical Engineering Science*, vol. 65, pp. 786-795, 2010.
- [212] DIN EN ISO 11357-1, “Plastics – Differential Scanning Calorimetry (DSC). Part 1: General Principles ,” *DIN Deutsches Institut für Normung e.V.*, Berlin, Germany, 1997.
- [213] “ASTM D3418-12. Transition Temperatures and Enthalpies of Fusion and Crystallisation of Polymers by Differential Scanning Calorimetry,” *ASTM International*, West Conshohocken, PA, USA, 2012, DOI: 10.1520/D3418-12E01.
- [214] R. L. Blaine. THERMAL APPLICATIONS NOTE – Polymer Heats of Fusion. TN048. TA Instruments, Denver, USA. [http://www.tainstruments.com/main.aspx?n=2&id=181&main\\_id=367&siteid=11](http://www.tainstruments.com/main.aspx?n=2&id=181&main_id=367&siteid=11) [Accessed 24/03/15].
- [215] “ASTM D1434-82. Determining Gas Permeability Characteristics of Plastic Film and Sheeting,” *ASTM International*, West Conshohocken, PA, USA, 2009, DOI: 10.1520/D1434-82R09E01.
- [216] Choi S. Micromechanics, Fracture Mechanics and Gas Permeability of Composite Laminates for Cryogenic Storage Systems. *PhD Thesis*, University of Florida, Florida, USA, 2005.

## Bibliography

- [217] J. Vanpelt. Effect of strain rate on the gas permeability of composite laminates. *Master's Thesis*. University of Florida, Florida, USA, 2006.
- [218] BOC Product Code and Product Listings 2009. [http://www.boconline.ie/internet.lg.lg.irl/en/images/pure-gas-product-code-and-listings674\\_39560.pdf](http://www.boconline.ie/internet.lg.lg.irl/en/images/pure-gas-product-code-and-listings674_39560.pdf) - Accessed 24/03/15.
- [219] R. M. Barrer, J. A. Barrie, and M. G. Rogers. Permeation through a membrane with mixed boundary conditions. *Transactions of the Faraday Society*, vol. 58, pp. 2473-2483, 1962.
- [220] Leybold UL 200 Helium Leak Detector Manual. <http://www.pascaltechnologies.com/files%5CLeak%20Detectors%5CLeybold%5CLeybold%20UL-200%20Manual.pdf> – Accessed 19-03-15.
- [221] W. Umrath. *Fundamentals of Vacuum Technology*. Oerlikon Leybold Vacuum Brochure. Cologne, Germany, June 2007.
- [222] A. T. Nettles. Permeability after impact testing of composite laminates. *SAMPE Symposium and Exhibition*, California, USA, 2003.
- [223] V. T. Bechel, M. B. Fredin, S. L. Donaldson, R. Y. Kim, and J. D. Camping. Effect of stacking sequence on micro-cracking in a cryogenically cycled carbon/bismaleimide composite. *Composites: Part A*, vol. 34, pp. 663-672, 2003.
- [224] V. T. Bechel and R. Y. Kim. Damage trends in cryogenically cycled carbon/polymer composites. *Composites Science and Technology*, vol. 64, pp. 1773-1784, 2004.
- [225] D. M. Grogan, S. B. Leen, C. O. A. Semprimoschnig, and C. M. Ó Brádaigh. Damage characterisation of cryogenically cycled carbon fibre/PEEK laminates. *Composites: Part A*, vol. 66, pp. 237-250, 2014.
- [226] K. P. Menard. *Dynamic Mechanical Analysis*. CRC Press LLC. Boca Raton, Florida, USA, 1999.

## Bibliography

- [227] “ASTM D5026-15. Plastics: Dynamic Mechanical Properties: In Tension,” *ASTM International*, West Conshohocken, PA, USA, 2015, DOI: 10.1520/D5026-15.
- [228] “ASTM D5024-15. Plastics: Dynamic Mechanical Properties: In Compression,” *ASTM International*, West Conshohocken, PA, USA, 2015, DOI: 10.1520/D5024-15.
- [229] ASTM Standard E831-14, 2014, “Linear Thermal Expansion of Solid Materials by Thermomechanical Analysis,” *ASTM International*, West Conshohocken, PA, 2014, DOI: 10.1520/E0831-14.
- [230] Mettler Toledo. PVC, TMA Curves as a Function of Applied Load. [http://us.mt.com/dam/mt\\_ext\\_files/Editorial/Generic/6/tma\\_pvc\\_0x000249470002547400066fef\\_files/pvc\\_tma.pdf](http://us.mt.com/dam/mt_ext_files/Editorial/Generic/6/tma_pvc_0x000249470002547400066fef_files/pvc_tma.pdf). - Accessed 08/09/15.
- [231] “ASTM E2546-15. Standard Practice for Instrumented Indentation Testing,” *ASTM International*, West Conshohocken, PA, USA, 2015, DOI: 10.1520/E2546-15.
- [232] R. Neghabat Shirazi, Y. Rochev, and P. McHugh. Nanoindentation of solvent-cast and compression-moulded poly(lactic-co-glycolic acid) to determine elastic modulus and hardness. *Polymer Testing*, vol. 50, pp. 111-118, 2016.
- [233] R. Neghabat Shirazi, F. Aldabbagh, A. Erxleben, Y. Rochev, and P. McHugh. Nanomechanical properties of poly(lactic-co-glycolic) acid film during degradation.” *Acta Biomaterialia*, vol. 10, pp. 4695-4703, 2014.
- [234] D. J. Shuman, A. L. M. Costa, and M. S. Andrade. Calculating the elastic modulus from nanoindentation and microindentation reload curves. *Materials Characterisation*, vol. 58, pp. 380-389, 2007.
- [235] W. C. Oliver, and G. M. Pharr. Measurement of hardness and elastic modulus by instrumented indentation: Advances in understanding and refinements to methodology. *Journal of Materials Research*, vol. 19, no. 1, pp. 3-20, 2004.

## Bibliography

- [236] P. J. Rae, E. N. Brown, and E. B. Orler. The mechanical properties of poly(ether-ether-ketone) with emphasis on the large compressive strain response. *Polymer*, vol. 48, pp. 598-615, 2007.
- [237] R. Pop-Iliev, G. Liu, C. B. Park, S. D'Uva, and J.A. Lefas. Comparison of dry blending-based and melt compounding based rotomoulding techniques for LLDPE foams. *SPE/ANTEC Conference Proceedings*. New York City, USA, May 2nd-6th, 2009.
- [238] S. Kanehashi, A. Kusakabe, S. Sato, and K. Nagai. Analysis of permeability; solubility and diffusivity of carbon dioxide; oxygen; and nitrogen in crystalline and liquid crystalline polymers. *Journal of Membrane Science*. vol. 365, pp. 40-51, 2010.
- [239] A. Guinault, C. Sollogoub, V. Ducruet, and S. Domenek. Impact of crystallinity of poly(lactide) on helium and oxygen barrier properties. *European Polymer Journal*. 2012; 48: 779-788.
- [240] M. Labriet M, and L. Poluet. The missing step to building a lunar spaceport. *AIAA SPACE 2013 Conference and Exposition*. California, USA, September 10-12, 2013.
- [241] J. A. Angelo. *Space Technology*. Greenwood Press, Westport, Connecticut, USA, 2003.
- [242] I. Demirdzic, A. Ivankovic, and N. O'Dowd. *Computational Continuum Mechanics Lecture Notes*. University College Dublin, Ireland, 2010.
- [243] T. R. Chandrupatla and A. D. Belegundu. *Introduction to Finite Elements in Engineering*. 3rd Edition. Prentice Hall, New Jersey, USA, 2002.
- [244] R. W. Lewis, P. Nithiarasu, and K. N. Seetharamu. *Fundamental of the Finite Element Method for Heat and Fluid Flow*. John Wiley & Son, West Sussex, England, 2004.
- [245] ABAQUS/Standard User's Manual, v. 6.10. Hibbitt, Karlsson & Sorensen. Inc. Pawtucket, Rhode Island, USA, 2010.

## Bibliography

- [246] S.T. Oyama, D. Lee, P. Hacıoğlu, and R. F. Saraf. Theory of hydrogen permeability in nonporous silica membranes. *Journal of Membrane Science*. 2004; 244: 45–53.
- [247] Y.A. Cengel. *Heat and Mass Transfer A Practical Approach*. 3rd Edition, McGraw-Hill, University of Nevada, Reno, USA, 2006.
- [248] “ASTM C297. Standard test method for flatwise tensile strength of sandwich constructions,” *ASTM International*, West Conshohocken, PA, USA, 2010, DOI: 10.1520/C0297\_C0297M-04R10.
- [249] P. P. Parlevliet, H. E. N. Bersee, and A. Beukers. Residual stresses in thermoplastic composites – A study of the literature – Part I: Formation of residual stress. *Composites: Part A*. vol. 37, pp. 1847-1857, 2006.
- [250] M.E. Yurchenko, J. Huang, A. Robisson, G. H. McKinley and P.T. Hammond. Synthesis, mechanical properties and chemical/solvent resistance of crosslinked poly(aryl-ether-ether-ketones) at high temperatures. *Polymer*. vol. 51, pp. 1914-1920, 2010.
- [251] S. Berretta, K. E. Evans and O. Ghita. Processability of PEEK, a new polymer for high temperature laser sintering (HT-LS). *European Polymer Journal*. vol. 68, pp. 243-266, 2015.
- [252] Z. Liu, P. Maréchal, and R. Jérôme. DMA and DSC, investigations of the  $\beta$  transition of poly(vinylidene fluoride). *Polymer*. vol. 38, iss. 19, pp. 4925-4929, 1997.
- [253] E. K. Oikonomou, S. Tencé-Girault, P. Gérard and S. Norvez. Swelling of semi-crystalline PVDF by a PMMA-based nanostructured diblock copolymer: Morphology and mechanical properties. *Polymer*. vol. 76, pp. 89-97, 2015.
- [254] S. Huang, M. Wang, T. Liu, W. Zhang, W.C. Tiju, C. He and X. Lu. Morphology, Thermal, and Rheological Behaviour of Nylon11/Multi-Walled

## Bibliography

- Carbon Nanotube Nanocomposites Prepared by Melt Compounding. *Polymer Engineering and Science*. pp. 1063-1068, 2009.
- [255] L. Mancic, R. F. M. Osman, A. M. L. M. Costa, J. R. M. d'Almeida, B. A. Marinkovic, and F. C. Rizzo. Thermal and mechanical properties of polyamide 11 based composites reinforced with surface modified titanate nanotubes. *Materials & Designs*. vol. 83, pp. 459-467, 2015.
- [256] T. Liu, K. P. Lim, W.C. Tjiu, K. P. Pramoda, and Z. Chen. Preparation and characterisation of nylon11/organoclay nanocomposites. *Polymer*. vol. 44, pp. 3529-3535, 2003.
- [257] A. R. Bhattacharyya, P. Potschke, M. Abdel-Goad, and D. Fischer. Effect of encapsulated SWNT on the mechanical properties of melt mixed PA12/SWNT composites. *Chemical Physics Letters*. vol. 392, pp. 28-33, 2004.
- [258] D. Yan, X. Li, H. Ma, X. Tang, Z. Zhang, and Z. Yu. Effect of compounding sequence on localization of carbon nanotubes and electrical properties of ternary nanocomposites. *Composites: Part A*. vol. 49, pp. 35-41, 2013.
- [259] J. Bai, R. D. Goodridge, R. J. M. Hague, M. Song, and M. Okamoto. Influence of carbon nanotubes on the rheology and dynamic mechanical properties of polyamide-12 for laser sintering. *Polymer Testing*. vol. 36, pp. 95-100, 2014.
- [260] Balseal. Coefficient of Thermal Expansion for Various Materials at Different Temperatures. Technical Report TR-18 (Rev. F). Balseal, Amsterdam, the Netherlands, 2004.
- [261] J. Kilroy. New Carbon Fibre/PEEK Composites for Space Applications. Final Test Report. CTL Tástáil Teo. Galway, Ireland. 2006.

## Bibliography

- [262] D. M. Esterly. Manufacturing of Poly(vinylidene fluoride) and Evaluation of its Mechanical Properties. Master's Thesis, Virginia Polytechnic Institute, USA, 2002.
- [263] V. M. K. Akula and M. K. Shubert. Analysis of debonding of filament wound composite pressure vessels. *American Society for Composites 28th Technical Conference*. Pennsylvania, USA, Sept 9-11, 2013.
- [264] M. Chen and S. C. Chao. Thermal stability and nonisothermal crystallisation of short fiber reinforced poly(ether ether ketone) composites. *Journal of Polymer Science: Part B: Polymer Physics*, vol. 36, pp. 2225-2235, 1998.
- [265] M. Chen and C. T. Chung.. Crystallinity of isothermally and nonisothermally crystallised poly(ether ether ketone) composites. *Polymer Composites*, vol.19, no. 6, pp. 689-697, 1998.
- [266] S. L. Gao, and J. K. Kim. Cooling rate influences in carbon fibre/PEEK composites. Part 1. Crystallinity and interface adhesion. *Composites: Part A*, vol. 31, pp. 517-530, 2000.
- [267] S. A. Sabzevari, M. Sadeghi, and A. Mehrabani-Zeinbad. A multi-structural model for prediction of effective gas permeability in mixed-matrix membranes. *Journal of Macromolecular Chemistry and Physics*, vol. 214, pp. 2367-2376, 2013.
- [268] C. Henaff-Gardin, M. C. Lafarie-Frenot, and D. Gamby. Doubly periodic matrix cracking in composite laminates Part 2: Thermal biaxial loading. *Composite Structures*, vol. 36, pp. 131-140, 1996.
- [269] R. D. Crouch, S. B. Clay, and C. Oskay. Experimental and computational investigation of progressive damage accumulation in CFRP composites. *Composites: Part B*, vol. 48, pp. 59-67, 2013.
- [270] J. Kastner, B. Plank, A. Reh, D. Salaberger, and C. Heinzl. Advanced X-ray tomographic methods for quantitative characterisation of carbon fibre

## Bibliography

- reinforced polymers. *4<sup>th</sup> International Symposium on NDT in Aerospace 2012*. Augsburg, Germany, November 13-15, 2012.
- [271] P. J. Schilling, B. R. Karedla, A. K. Tatiparthi, M. A. Verges, and P. D. Herrington. X-ray computed microtomography of internal damage in fiber reinforced polymer matrix composites. *Composites Science and Technology*, vol. 65, pp. 2071-2078, 2005.
- [272] S. Roy, and M. Benjamin. Modeling of permeation and damage in graphite/epoxy laminates from cryogenic fuel storage. *Composites Science and Technology*, vol. 64, pp. 2051-2065, 2004.
- [273] A. Nair, and S. Roy. Modelling of permeation and damage in graphite/epoxy laminates for cryogenic tanks in the presence of delaminations and stitch cracks. *Composites Science and Technology*, vol. 67, pp. 2592-2605, 2007.
- [274] V. T. Bechel, J. D. Camping, and R. Y. Kim. Cryogenic/elevated temperature cycling induced leakage paths in PMCs. *Composites: Part B*, vol. 36, pp. 171-182, 2005.
- [275] V. T. Bechel, M. Negilski, and J. James. Limiting the permeability of composites for cryogenic applications. *Composites Science and Technology*, vol. 66, pp. 2284-2295, 2006.
- [276] T. Yokozeki, T. Aoki, T. Ogasawara, and T. Ishikawa. Effects of layup angle and ply thickness on matrix crack interaction in contiguous plies of composite laminates. *Composites: Part A*, vol. 36, pp. 1229-1235, 2005.
- [277] T. Yokozeki, T. Ogasawara, and T. Ishikawa. Evaluation of gas leakage through composite laminates with multilayer matrix cracks: Cracking angle effects. *Composites Science and Technology*, vol. 66, pp. 2815-2824, 2006.
- [278] D. M. Grogan, S. B. Leen, C. M. Ó Brádaigh. An X-FEM based methodology for fatigue delamination and permeability of composites. *Composites Structures*, vol. 107, pp. 205-218, 2014.

## Bibliography

- [279] D. M. Grogan, C. M. Ó Brádaigh, J. P. McGarry, S. B. Leen. Damage and permeability in tape-laid thermoplastic composite cryogenic tanks. *Composites: Part A*, vol. 78, pp. 390-402, 2015.
- [280] R. C. Powles, D. R. McKenzie, S. J. Meure, M. V. Swain, and N. L. James. Nanoindentation response of PEEK modified by mesh-assisted plasma immersion ion implantation. *Surface & Coating Technology*, vol. 201, pp. 7961-7969, 2007.
- [281] T. Iqbal, B. J. Briscoe, and P. F. Luckham. Surface plasticization of poly(ether ether ketone). *European Polymer Journal*, vol. 47, pp. 2244-2258, 2011.
- [282] W. Kaczorowski, D. Batory, W. Szymanski, and P. Niedzielski. Evaluation of the surface properties of PEEK substrate after two-step plasma modification: Etching and deposition of DLC coatings. *Surface & Coatings Technology*, vol. 265, pp. 92-98, 2015.
- [283] A. Molazemhosseini, H. Tourani, M. R. Naimi-Jamal, and A. Khavandi. Nanoindentation and nanoscratching responses of PEEK based hybrid composites reinforced with short carbon fibers and nano-silica. *Polymer Testing*, vol. 32, pp. 525-534, 2013.
- [284] J. R. Gregory, and S. M. Spearing. Nanoindentation of neat and in situ polymers in polymer-matrix composites. *Composites Science and Technology*, vol. 65, pp. 595-607, 2005.
- [285] M. Sattari, A. Molazemhosseini, M. R. Naimi-Jamal, and A. Khavandi. Nonisothermal crystallization behaviour and mechanical properties of PEEK/SCF/nano-SiO<sub>2</sub> composites. *Materials Chemistry and Physics*, vol. 147, pp. 942-953, 2014.
- [286] A. P. Kharitonov. Direct fluorination of polymers – From fundamental research to industrial applications. *Progress in Organic Coatings*, vol. 61, pp. 192-204, 2008.
- [287] D. Silagy, P. Bussi, G. Marrot. Technology and material design in PVDF protected thermoplastic substrates. *Journal of Fluorine Chemistry*, vol. 104, pp. 79-86, 2000.